Volume 6, Issue 2, 2020

Journal of Biomedical Photonics & Engineering

Special Issue

Years in Biophotonics: 60-th Anniversary of Profs. I. V. Minin and O. V. Minin

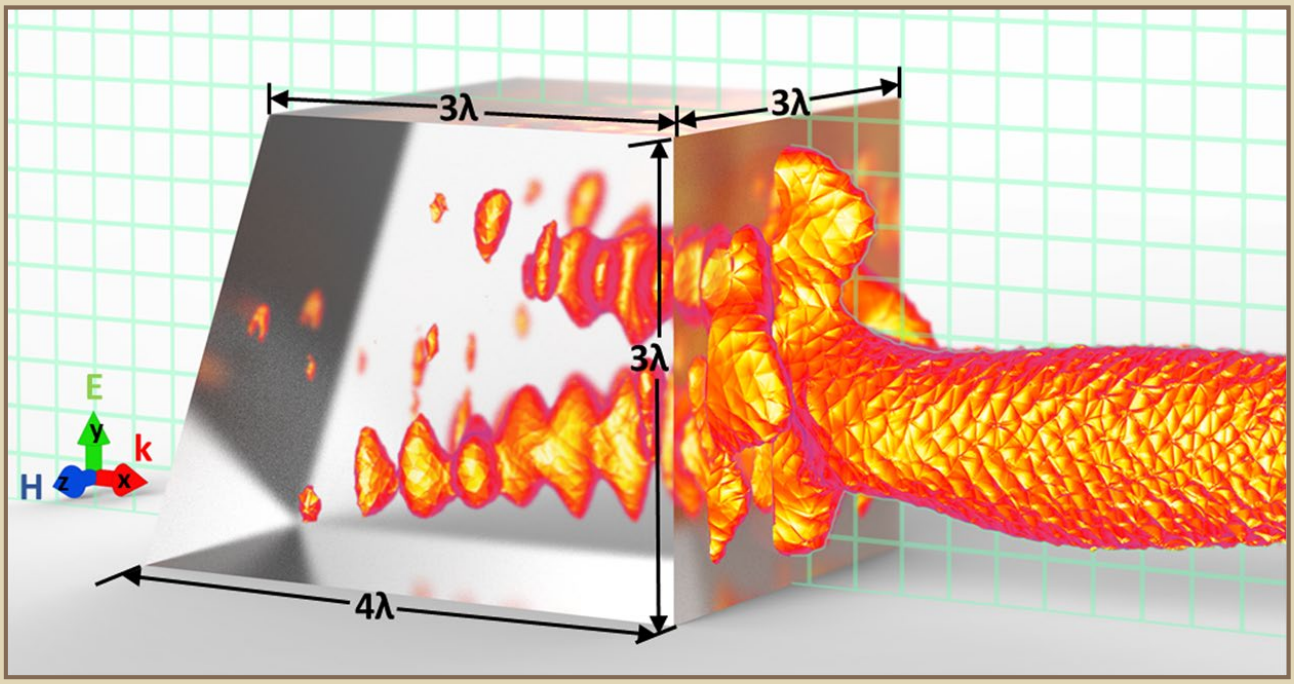


Figure reprinted under CC BY from A.S. Ang et al. *SciRep* 8, 2029 (2018) https://doi.org/10.1038/s41598-018-20224-4

Special Issue Editors:

Kirill I. Zaytsev, Pavel F. Baranov, and Dmitry S. Ponomarev

© 2020 J-BPE

 doi: 10.18287/JBPE20.06.020001

Journal of Biomedical Photonics & Engineering

by Samara National Research University

Volume 6, Issue 2 (June 2020)

Editorial Board

Editor-In-Chief

Valery V. Tuchin - Saratov National Research State University, Russian Federation;
Institute of Precision Mechanics and Control RAS, Russian Federation; a corr.-member of RAS

Deputy Editor-In-Chief

Valery P. Zakharov - Samara National Research University, Russian Federation

Editorial Board

Stefan Andersson-Engels (Tyndall National Institute, Ireland), **Alexey N. Bashkatov** (Saratov National Research State University, Russia), **Ekaterina Borisova** (Institute of Electronics, Bulgarian Academy of Sciences, Bulgaria), **Wei Chen** (University of Central Oklahoma, USA), **Arthur Chiou** (National Yang-Mind University, Taiwan), **Elina Genina** (Saratov National Research State University, Russia), **Min Gu** (Swinburne University, Australia), **Dror Fixler** (Bar-Ilan University, Ramat Gan, Israel), **Vyacheslav Kalchenko** (The Weizmann Institute of Science, Israel), **Nikolay G. Khlebtsov** (Institute of Biochemistry and Physiology of Plants and Microorganisms RAS, Russia), **Juergen Lademann** (Charite University Clinic, Germany), **Kirill V. Larin** (University of Houston, USA), **Martin Leahy** (University of Galway, Ireland), **Qingming Luo** (Hainan University, China), **Stephen J. Matcher** (University of Sheffield, Great Britain), **Aleksandra M. Mayorova** (Samara Branch of P.N. Lebedev Physical Institute of Russian Academy of Sciences, Russia), **Igor Meglinski** (University of Oulu, Finland), **Vladimir S. Pavelyev** (Image Processing Systems Institute RAS, Russia), **Francesco Pavone** (University of Florence, Italy), **Roberto Pini** (Institute of Applied Physics, Italy), **Igor A. Platonov** (Samara National Research University, Russia), **Juergen Popp** (Institute of Photonic Technology, Germany), **Alexander V. Priezzhev** (Moscow State University, Russia), **David Sampson** (The University of Western Australia, Australia), **Alexander Savitsky** (Institute of Biochemistry RAS, Russia), **Alexander P. Shkurinov** (Moscow State University, Russia, a corr.-member of RAS), **Peter So** (Massachusetts Institute of Technologies, USA), **Janis Spigulis** (University of Latvia, Latvia), **Ilya V. Turchin** (Institute of Applied Physics RAS, Russia), **Lihong V. Wang** (California Institute of Technology, USA), **Ruikang Wang** (University of Washington, USA), **Xunbin Wei** (Shanghai Jiao Tong University, China), **Dan Zhu** (Britton Chance Center for Biomedical Photonics, Huazhong University of Science and Technology, China).

Postal address:
39B Lukacheva st., room #301
Samara 443086, Russian Federation

 © 2020 J-BPE

doi: 10.18287/JBPE20.06.020001

Special Issue

“Years in Biophotonics: 60-th Anniversary of Profs. I. V. Minin and O. V. Minin”

Special Issue Editors

Kirill I. Zaytsev
Head of Laboratory of Broadband Dielectric Spectroscopy,
Prokhorov General Physics Institute of RAS, Moscow, Russia

Pavel F. Baranov
Head of division, National Research Tomsk Polytechnic University, Tomsk, Russia

Dmitry S. Ponomarev
Deputy Director, V.G. Mokerov Institute of Ultra-High Frequency Semiconductor Electronics of RAS, Moscow, Russia

© 2020 J-BPE

Contents

Introduction

In the 60-th jubilee of Professors of Tomsk Polytechnic University
Igor V. Minin and Oleg V. Minin 020101
Kirill I. Zaytsev, Pavel F. Baranov, and Dmitry S. Ponomarev

Reviews

Prospects of terahertz technology in diagnosis of human brain tumors – A review 020201
Guzel R. Musina, Pavel V. Nikitin, Nikita V. Chernomyrdin, Irina N. Dolganova, Arsenii A. Gavdush, Gennadiy A. Komandin, Dmitry S. Ponomarev, Alexander A. Potapov, Igor V. Reshetov, Valery V. Tuchin, and Kirill I. Zaytsev

Articles

Recent Trends in Optical Manipulation Inspired by Mesoscale Photonics and Diffraction Optics 020301
Igor V. Minin and Oleg V. Minin

Raman Spectroscopy of Hemoglobin and Dielectrophoresis of Erythrocytes in the Diagnosis of the Resistant Arterial Hypertension 020302
Margarita V. Kruchinina, Andrey A. Gromov, Vladimir N. Kruchinin, Vladimir A. Volodin, and Vladimir M. Generalov

Evaluating the Number of Ligand Binding Sites on Protein from Tryptophan Fluorescence Quenching under Typical Experimental Conditions 020303
Alexey V. Gayer, Boris P. Yakimov, Gleb S. Budylin, and Evgeny A. Shirshin

Terahertz optical and mechanical properties of the gelatin-starch-glycerol-bentonite biopolymers 020304
Tianmiao Zhang, Maria Zakharova, Anna Vozianova, Aleksandr Podshivalov, Maria Fokina, Ravshanjon Nazarov, Anna Kuzikova, Petr Demchenko, Mayya Uspenskaya, and Mikhail Khodzitsky

Study by optical techniques of the dependence of aggregation parameters of human red blood cells on their deformability 020305
Anastasia I. Maslianitsyna, Petr B. Ermolinsky, Andrei E. Lugovtsov, and Alexander V. Priezzhev

Hyperspectral Holography and Laser Diffractometry of Erythrocytes 020306
Andrei E. Lugovtsov, Vladislav D. Ustinov, Georgy S. Kalenkov, Sergey G. Kalenkov, and Alexander V. Priezzhev

UV-NIR efficiency of the refractive index matching mechanism on colorectal muscle during treatment with different glycerol osmolarities 020307
Nelma Gomes, Valery V. Tuchin, and Luís M. Oliveira

Optical Clearing of Human Skin Using Polyethylene Glycols 020308
Kirill V. Berezin, Konstantin N. Dvoretskiy, Vladimir V. Nechaev, Anatoliy M. Likhter, Ilmira T. Shagautdinova, and Valery V. Tuchin

Optical Biopsy and Optical Pathology: Affordable Health Care Under Low-Resource Settings 020309
Swathi Rao, Reena John, Ajeetkumar Patil, Unnikrishnan V. K., Sajan D. George, Keerthilatha M. Pai, Ravikiran Ongole, Tom Devasia, V. B. Kartha, and Santhosh Chidangil

 © 2020 J-BPE

1540 nm LIBS Investigation of Healthy and Pathological Human Nails 020310
Andrey V. Belikov, Sergey N. Smirnov, Andstasia D. Tavalinskaya, and Victoria S. Pomazanova

Letters

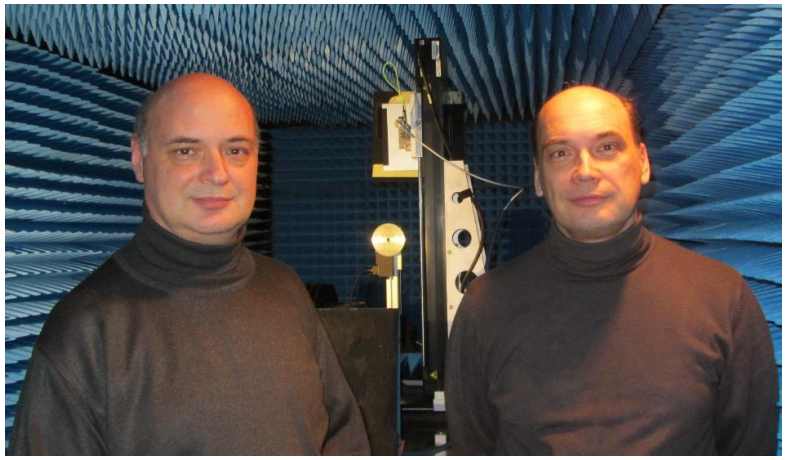
Temperature Dependencies of the Aggregation Properties of RBC in Dextran Solutions *In Vitro* 020501
Petr B. Ermolinskiy, Anastasia I. Maslyanitsina, Andrei E. Lugovtsov, and Alexander V. Priezzhev

 © 2020 J-BPE

 doi: 10.18287/JBPE20.06.020101

In the 60th jubilee of Professors of Tomsk Polytechnic University Igor V. Minin and Oleg V. Minin

The guest editors represent this Special Issue of the Journal of Biomedical Photonics & Engineering in the Honor 60th jubilee of **Profs. Igor V. Minin** and **Oleg V. Minin**, DSc, Corr.-Ms of Russian Academy of Metrology and Russian Academy of Natural History who have made a significant contribution to the field of mesoscale diffraction optics and nanophotonics. **Profs. I.V. Minin** and **O.V. Minin** were born on the 22nd of March in 1960 in Novosibirsk Academytown. They graduated from Novosibirsk State University in 1982. **I.V. Minin** defended his Ph.D. thesis at St. Petersburg Electrotechnical Institute in 1986 while **O.V. Minin** upheld his candidate dissertation at Tomsk Institute of Atmospheric Optics, in 1987. They defended their Dr.Sc. theses at the Novosibirsk State Technical University, in 2004. The brothers began their scientific work at the Institute of Applied Physics in Novosibirsk starting from Lab Assistants to Leading Researches. Now they are Professors at Tomsk Polytechnic University.



Professors of Tomsk Polytechnic University
Prof. Igor V. Minin (left) and **Prof. Oleg V. Minin** (right) standing beside the echoless chamber.

Profs. I.V. Minin and **O.V. Minin** have 300 joint research publications in peer-reviewed journals indexed in Web of Science and Scopus, more than 120 patents on invention, and 18 monographs. Among the monographs we should mention the well-known issues: "Diffractive optics of millimeter waves", IOP Publisher, London-Boston, in 2004; "Three Dimensional Fresnel Antennas", Research Signpost, Kerala, India, in 2005; "Basic Principles of Fresnel Antenna Arrays", Springer, in 2008, and "Diffractive Optics and Nanophotonics", Springer International Publishing, Cham, in 2016.

The biographical data of **Profs. I.V. Minin** and **O.V. Minin** is included in Marquis "Who's Who in the World" in 2003; Russian reference book "Scientists of Russia" in 2004; in the encyclopedia "Scientists of Russia", in 2008; "Who's Who in Russia" in 2010. They were awarded the diploma from the monthly published magazine Laser Focus World in 2003 for a series of publications in the field of telecommunication technologies and counter-terrorism. **Profs. I.V. Minin** and **O.V. Minin** hold the Certificate of Honor of the Ministry of Engineering and the Presidium of the Central

 doi: 10.18287/JBPE20.06.020101

Committee of the USSR Trade Union, and the Certificate of the Minister of Defense of the Russian Federation for their scientific contribution during 1997–2000.

Profs. I.V. Minin and **O.V. Minin** are currently the experts of the International Program COST 284 "Innovative Antennas for Emerging Terrestrial & Space-based Applications" and IASTED as well. Also, they are the experts in different Federal programs and foundations as Russian Foundation for Basic Research, Russian Science Foundation. They both are the SPIE members, and have been the members of various International conferences and meetings from 2008–2020. **Profs. I.V. Minin** and **O.V. Minin** are the members of the Editorial board of several recognized journals.

For a long time, they have been the Invited Professors to many companies and Universities: DaimlerChrysler AG (Germany); Doiche Aerospace (Germany); Technische Universitat Munchen, Germany; Harbin Institute of Technology, China; Samsung Electronics, Korea; National University of Singapore; MMW State Key Lab, Nanjing, China; Universidad Tecnica Federico Santa Maria, Chile, NJUST; Bieijing Institute of Technology, China; Capital Normal University, China; CRC, Canada; Helsinki University, Finland, etc.

Profs. I.V. Minin and **O.V. Minin** have established strong research foundations in different branches of physics, having a global priority, such as shock wave focusing by diffractive optics, explosive plasma antennas, subwavelength structured light and hypercumulative shaped charge. They have developed new types of 3D diffraction lenses, antennas and antenna arrays for telecommunication systems and millimetre-wave and THz imaging systems. Their main interest in mesoscale photonics and plasmonics focuses on terajets, acoustic jets and plasmonic jets. They discovered numerically a new curved beam, a photonic hook, for free space, acoustics and surface plasmon waves, which are much easier to produce compared to the Airy-family beams. Recently, the photonic hook phenomenon has been experimentally verified.

This Special Issue in the honor 60th jubilee of **Profs. I.V. Minin** and **O.V. Minin** provides a multidisciplinary reflection on their career, indicating some of their scientific interests and contributions.

The guest editors of this Special Issue would like to thank all authors for their efforts in preparing their contributions and thank all the reviewers for their help in reviewing these papers. Last but not least, we would like to thank the editorial staff of the Journal of Biomedical Photonics & Engineering for the opportunity to organize this Special Issue.

Special Issue Editors:

Kirill I. Zaytsev
Head of Laboratory of Broadband Dielectric Spectroscopy,
Prokhorov General Physics Institute of RAS, Moscow, Russia
E-mail: kirzay@gmail.com

Pavel F. Baranov
Head of division, National Research Tomsk Polytechnic University, Tomsk, Russia
E-mail: bpf@tpu.ru

Dmitry S. Ponomarev
Deputy Director, V.G. Mokerov Institute of Ultra-High Frequency Semiconductor Electronics of RAS, Moscow, Russia
E-mail: ponomarev_dmitr@mail.ru

Prospects of terahertz technology in diagnosis of human brain tumors – A review

Guzel R. Musina[1], Pavel V. Nikitin[2], Nikita V. Chernomyrdin[1], Irina N. Dolganova[3,4], Arsenii A. Gavdush[1], Gennadiy A. Komandin[1], Dmitry S. Ponomarev[5], Alexander A. Potapov[2], Igor V. Reshetov[6], Valery V. Tuchin[7,8], and Kirill I. Zaytsev[1,9*]

[1] Prokhorov General Physics Institute of the Russian Academy of Sciences, 38 Vavilova str., Moscow 119991, Russia
[2] Burdenko Neurosurgery Institute, 1 4-ya Tverskaya-Yamskaya str., Moscow 125047, Russia
[3] Institute of Solid State Physics of the Russian Academy of Sciences, 2 Academika Osipyana str., Chernogolovka, Moscow Region 142432, Russia
[4] Institute for Regenerative Medicine, Sechenov University, 19/1 Bolshaya Pirogovskaya str., Moscow 119146, Russia
[5] V.G. Mokerov Institute of Ultra High Frequency Semiconductor Electronics of the Russian Academy of Sciences, 7 Nagorniy proezd, Moscow 117105, Russia
[6] Institute for Cluster Oncology, Sechenov University, 19/1 Bolshaya Pirogovskaya str., Moscow 119146, Russia
[7] Saratov State University, 83 Astrakhanskaya str., Saratov 410012, Russia
[8] Institute of Precision Mechanics and Control of the Russian Academy of Sciences, 24 Rabochaua str., Saratov 410028, Russia
[9] Bauman Moscow State Technical University, 5/1 2-ya Baumanskaya str., Moscow 105005, Russia

*** e-mail:** kirzay@gmail.com

Abstract. Terahertz (THz) waves feature high sensitivity to the content and state of water in biological tissues. Therefore, during the past decades, THz technology has attracted significant attention in biophotonics, including diagnosis of malignant and benign neoplasms with different nosologies and localizations. The pathophysiological features of malignant tumors of the central nervous system determine appearance of several morphological phenomena, such as increased vascularity, edema, necrosis. These phenomena cause water content increase in the studied tissues and, thus, open new ways for the THz technology applications in the intraoperative neurodiagnosis, including delineation of tumor margins. This research area is rather novel and, despite the small amount of accumulated research material, is undoubtedly extremely promising for creation of new diagnostic approaches. In this review, available results in the considered exciting branch of THz technology are summarized, and potential projections of this topic into the future are constructed. © 2020 Journal of Biomedical Photonics & Engineering.

Keywords: terahertz radiation; terahertz Biophotonics; terahertz spectroscopy; terahertz imaging; brain tumors; glioma; meningioma; neurodiagnostics; neurosurgery.

Paper #3375 received 3 Jun 2020; accepted for publication 18 Jun 2020; published online 28 Jun 2020. doi: 10.18287/JBPE20.06.020201.

1 Introduction

Malignant gliomas, which represent the largest proportion of malignant tumors of the central nervous system (CNS), are an important problem in modern oncology [1]. Neurosurgical intervention remains the most effective method of glioma treatment, while patient prognosis is largely determined by the gross-total resection of a tumor [2]. At the same time, there are several factors limiting the possibilities of radical

resection, among which we would mention the two most important ones [3]:

- high risk of adverse functional outcomes with severe neurological deficiency,
- a problem of determining the true margins of a tumor due to its infiltrative growth.

If the first problem can be mitigated using electrophysiological methods and functional magnetic resonance imaging, the second one is left to the urgent histological examination, which is characterized by relatively low information content and a high percentage of errors [4]. Therefore, development of fundamentally novel intraoperative diagnostic approaches to identify the tumor margins remains an important one.

Few experimental methods have been introduced recently based on the different physical and metabolic characteristics of the tumor tissues, in order to determine the true margins of a tumor. In particular, the metabolic aspect is based on the use of 5-AminoLevulinic Acid (5-ALA)-induced fluorescence of Protoporphyrin IX, which is most actively accumulated in the tumor tissue due to a higher level of metabolism, allowing us for assessing the brain tumor margins. However, the sensitivity and specificity of this method is significantly reduced due to aberrant accumulation of 5-ALA in non-tumor tissues with inflammation, increased vascular permeability, edema, and other causes, as well as to its poor accumulation in low-grade gliomas [5]. At the same time, other methods are vigorously explored nowadays. There are Raman spectroscopy and imaging [6], photoacoustic imaging [7], multiphoton microscopy and optical coherence tomography (OCT) [8, 9]. Nevertheless, application of these techniques in neurosurgical practice is still difficult, so they remain instruments of basic research. Therefore, further development of new tools for the intraoperative delineation of tumor margins is a challenging problem.

Thanks to a high sensitivity of the terahertz (THz) waves to the content and state of water in tissues, THz spectroscopy and imaging can be applied for the label-free differentiation between healthy tissues and neoplasms with different nosologies and localizations. Among all applications of THz technology in oncodiagnosis, during the last few years, it attracted attention as a tool for the intraoperative delineation of brain tumor margins. Despite quite a small amount of research material accumulated in this exciting branch of THz technology, it is undoubtedly extremely promising for creation of new diagnostic approaches. In this review, modern research results in the area of intraoperative THz diagnosis of brain tumors are discussed.

2 Terahertz biophotonics

Progress in femtosecond laser technologies and creation of new methods for the THz-wave generation and detection have been contributed to the recent development of THz spectroscopy and imaging [10]. As shown in Fig. 1, THz radiation belongs to the frequency range of 0.1–3.0 THz or to the wavelength range of 3 mm–100 μm. Since the end of the XX century, THz spectroscopy and imaging have been the subject of research to create a fundamentally new approach to non-invasive and invasive oncodiagnostics. This approach has been successfully implemented on neoplasms of the skin [11], mucous [12], colon [13], breast [14], stomach [15], liver [16], etc. Most recently, high potential of THz technology was demonstrated in differentiation of intact (healthy) tissue and tumors of the brain [17].

Let us start with fundamental aspects of the THz-radiation – biological tissues interactions. As shown in Fig. 2, structural elements of tissues (such as microfibrils, separate cells and their agglomerates, cell organelles, etc.) are too small at the scale posed by THz wavelengths. Conventional THz imaging systems, which mostly rely on the diffraction limited lens- or mirror-based optics, provide the spatial resolution up to $\sim\lambda$ and, thus, do not allow to resolve such small scale tissue components. As a result, only the effective response of tissues at THz frequencies, which is averaged within $> \lambda^2$ area of the THz beam spot, can be studied using THz spectroscopy and imaging [18]. In this way, the electrodynamic properties of tissues in the THz range are usually described using the frequency-dependent effective complex dielectric permittivity

$$\tilde{\varepsilon} = \varepsilon' - i\varepsilon'', \tag{1}$$

which includes both real ε' and ε'' imaginary parts. At the same time, it can be represented by a frequency-dependent complex refractive index

$$\tilde{n} = n' - in'' \equiv n - i\frac{c}{2\pi\upsilon}\alpha \equiv \sqrt{\tilde{\varepsilon}}, \tag{2}$$

where $n \equiv n'$ and n'' are real and imaginary parts, $c = 3\times10^8$ m/s is the speed of light in a free space, υ is an electromagnetic wave frequency in [Hz], and α is absorption coefficient (by field) in [cm^{-1}].

Biological liquids and tissues, water and its solutions do not feature resonant spectral absorption peaks in the THz range. The main factor determining the THz dielectric response of healthy and pathological tissues (either *in vivo* or freshly-excised (non-dehydrated) specimens *ex vivo*) is the content of free and bound water in tissues [18]. The THz-wave – tissue interactions can be completely described in the frameworks of electrodynamics using the relaxation models of complex dielectric permittivity (such as the Debye, Gavrilyak-Negami, Cole-Cole, Davidson-Cole models [19–24]), while the double-Debye model remains the most frequently-applied one in THz biophotonics [18, 23, 24]

$$\tilde{\varepsilon} = \varepsilon_\infty + \frac{\Delta\varepsilon_1}{1 + i\,2\pi\upsilon\,\tau_1} + \frac{\Delta\varepsilon_2}{1 + i\,2\pi\upsilon\,\tau_2}, \tag{3}$$

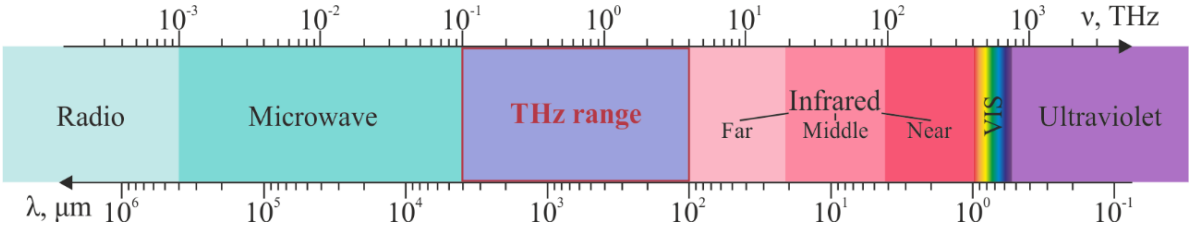


Fig. 1 THz range of the electromagnetic spectrum. Courtesy of G.R. Musina.

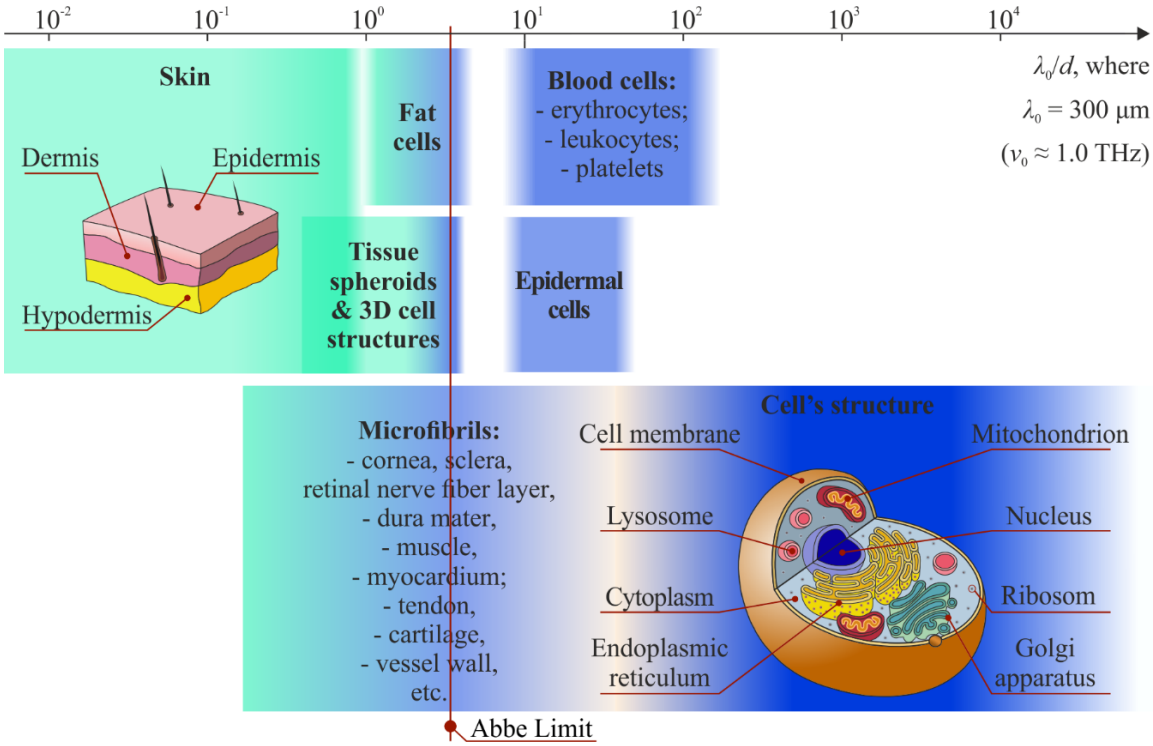


Fig. 2 Dimensions of tissue structural elements δ as compared to the THz wavelength of $\lambda_0 = 300$ μm (it corresponds to the frequency of $\nu_0 = 1.0$ THz). By vertical red line, the $\lambda/2$ Abbe diffraction limit is shown. Courtesy of K.I. Zaytsev.

here, ε_∞ is a dielectric permittivity at infinitely-high frequencies as compared to the considered frequency band); τ_1 and τ_2 are relaxation times (in [ps]) corresponding to the "slow" and "fast" processes; $\Delta\varepsilon_1$ and $\Delta\varepsilon_2$ regulate contributions of "slow" and "fast" Debye relaxation terms to the complex dielectric response function [18]. This double-Debye model allows for convenient parameterization of the tissue dielectric properties in the entire THz range by using only 5 independent constants: ε_∞, $\Delta\varepsilon_1$, $\Delta\varepsilon_2$, τ_1, and τ_2. However, this model is not physically rigorous, since it does not fulfill the summation rule, and it approximates the experimental data by the two broad absorption bands, the maxima of which are centered at the frequencies $\sim\tau_1^{-1}$, $\sim\tau_2^{-1}$ located outside (or at the edges) of the analyzed spectral range. Thus, the considered double-Debye model implies extrapolation of the experimental data. However, this model provides quite an effective parameterization tool, and it also can be applied for physically reasonable differentiation of tissues [23–27].

Majority of biological tissues possesses high content of water due to several histogenetic reasons. For example, fibrous tissues contain significantly large amount of water, as compared to that in adipose tissues. High water content strongly affects the THz dielectric properties of tissues. Since water molecule is very polar, both liquid and tissue water strongly absorbs THz waves, thus, reducing the depth of THz-wave penetration in tissues. The depth of tissues probing by THz radiation can be as large as tens or hundreds of microns, depending on the considered frequency and the tissue type. Such a small penetration depth forms a key limitation of THz technology use for studying biological tissues in various branches of biophotonics. In order to obtain reliable results, response of tissue at THz frequencies is usually studied in reflection geometry [28].

There are several factors that determine the ability to differentiate intact and tumor tissue in the THz range. The key one is the different water content. Due to higher level of metabolism, edema and increased vascular permeability, tumor tissues contain more water than normal ones, which leads to higher refractive index

and absorption coefficient of a tumor in the THz range [17]. At the same time, there are other factors that impact the THz response of tissues tissue and that can be of considerable practical interest. In particular, the presence of necrotic debris, which is a morphological sign for many malignant tumors (for example, glioblastoma), is among such factors [29]. Furthermore, additional changes in the THz dielectric response of tissues can be attributed to some mutational changes, the systematic study of which is of great practical interest [30].

The complex dielectric permittivity $\tilde{\varepsilon}$ (see Eq. (1)) or the complex refractive index $\tilde{n}$ (see Eq. (2)) completely describe the THz-radiation – biological tissues interactions in the framework of classical electrodynamics. Such a complete description allows us to:

- model analytically the THz-wave propagation through multi-layer media, including biological tissues, using the plane wave approximation, the Fresnel formulas, and the modified Bouguer-Lambert-Beer law, which is of crucial importance for THz spectroscopy [17];
- simulate numerically the THz-wave interaction with biological objects, featuring complex geometry and heterogenous character, using computational method of electrodynamics [23] or statistical Monte Carlo techniques [31];
- apply the complex dielectric permittivity, related derived quantities or even parameter of relaxation dielectric permittivity models (see Eq. (3)) for the discrimination between different tissue types [17, 27].

It is worth noting that biological tissues can possess significant heterogeneity and complexity of the internal structure even at the scale posed by THz wavelength (see Fig. 2), which is not taken into account in the effective medium theory formalism and which could not be described by the effective dielectric response function (see Eq. (6)). As examples of such heterogenous tissues, one can consider results of THz microscopy of individual fat cells embedded into fibrous connective mammary gland *ex vivo*, as well as muscle fibers of the tongue *ex vivo* from Ref. [32]. For such structural inhomogeneities of tissues, one can expect Mie scattering of THz waves [33], in contrast to the Rayleigh scattering regime considered in the effective medium theory [34]. Dispersion, absorption and scattering properties of such tissues should be simultaneously taken into account in order to form novel approach for describing the THz-wave – tissue interactions [33], while the radiation transfer theory should be considered as a theoretical basis for this purpose [35]. Nevertheless, problems of studying the scattering properties of tissue and of developing the radiation transfer theory in the THz range remain unaddressed.

With a rapid progress in THz pulsed spectroscopy and imaging observed at the end of the XX century, THz technology are extensively applied in biology and medicine, but it is still far from clinical practice owing to several reasons [18, 36]. In the next few sections, modern research results in the area of THz diagnostics of brain tumors are analyzed, and problems and difficulties that stand in the way of THz technology translation into a practical plane are discussed.

3 Terahertz spectroscopy and imaging of brain tumors

Let us start with one of the first research papers in THz neurodiagnosis [37]. Using THz pulsed spectroscopy in conjunction with a closed cycle cryostat, the authors of this work demonstrated an ability for differentiation between intact and pathologically altered frozen human brain tissue with amyloid plaques *ex vivo*, which are inherent to the Alzheimer's disease. Thanks to tissue freezing, THz-wave absorption by tissue water is strongly suppressed [17], which allows revealing non-water-related differences in the THz dielectric properties of normal and pathologically altered tissues, such as the amyloid plaque proteins. Next, THz spectroscopy was applied for studying a mouse model of the Alzheimer's disease [38], and the observed data for dehydrated brain tissues *ex vivo* confirmed earlier-reported results and indicated a significant effect of the Alzheimer's disease-related amyloid proteins on the THz dielectric response of tissues.

An ability of using THz technologies for the diagnosis of human brain tumors is attracted considerable attention most recently, starting from tumor models in mice and rats [29, 39].

3.1 Glioma models in mice and rats

The orthotopic rat glioma model was studied using the THz pulsed spectrometer equipped with a raster scan unit in Ref. [29], where 9 week old male rats received 9L/lacZ cells, and the tumor was grown for 3–4 weeks to a volume of ~1.0 cm^3 [40]. A distinctive feature of this model is a clear boundary between the tumor and intact brain tissues that simplifies their visualization and discrimination. After extraction, the rat brains were divided into equal parts. Then, THz images of tissue specimens were collected and formed at each point using peak values of the THz waveforms (see Fig. 3) [29]. The tumor margins revealed by such THz imaging are well comparable with that obtained by magnetic-resonance tomography and white light imaging. The results of this study have highlighted ability for the intraoperative diagnosis of brain tumors using THz technology.

At the same time, it seems to be important to study other factors, besides water content in tissues that underlie the contrast between tumor and intact brain tissues in the THz range. For this aim, it is necessary to eliminate water from biological tissues that was achieved in Ref. [29] by paraffin embedding of tissues. By further THz imaging of paraffin-embedded tissues and by comparing the obtained patterns with the results of microscopic examination of the same tissue specimens stained with Hematoxylin and Eosin (H&E),

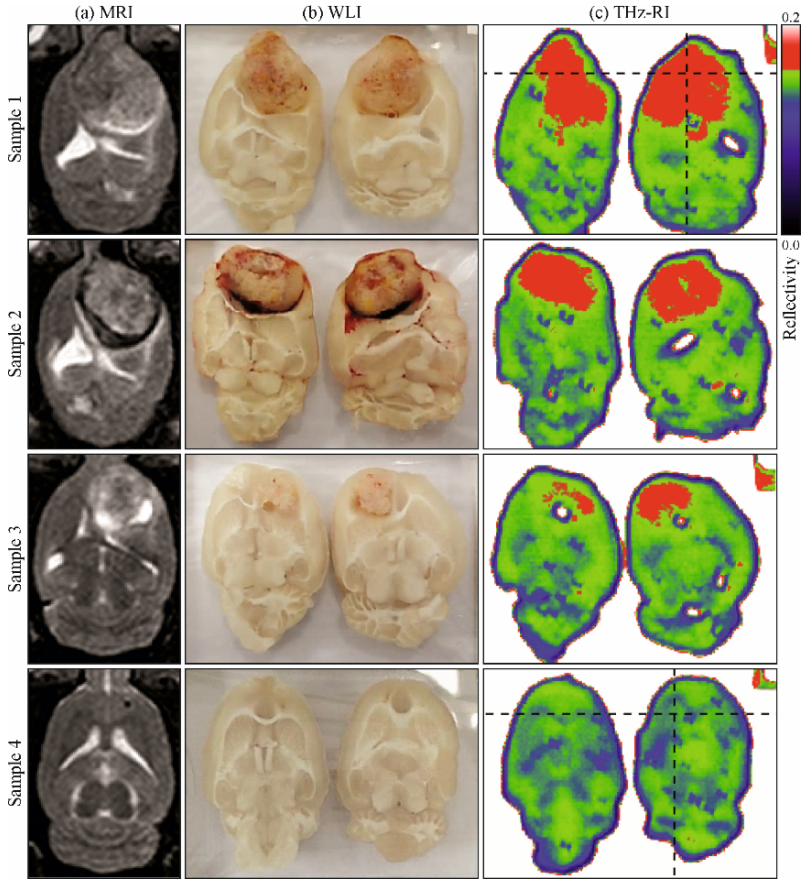


Fig. 3 (a) Magnetic resonance images (MRI), (b) white light images (WLI), and (c) THz reflection-mode images (THz-RI) of freshly-excised whole rat brain tissues, both with orthotopic glioma model (rows 1–3) and without a tumor (row 4). Adapted with permission from Ref. [29]. © The Optical Society of America.

it was found that a differences between intact and pathologically altered tissues are still presented in THz images, but this difference is several tines lower that that observed for the freshly-excised rat brain tissues *ex vivo*. In some cases, the determination of true tumor margins relying on THz images of paraffin-embedded tissues was impossible. It should be noticed that THz refractive index of paraffin-embedded samples was higher near the tumor margins, which can be attributed to a higher cell density in this area as compared to the neoplasm core. Thus, in addition to free water, other factors affect the response of tissues in the THz range. A possible influence of necrotic debris in tumor tissues on their THz response was also indicated in Ref. [29].

In Ref. [29], by using a rat brain model *ex vivo*, it was shown that THz dielectric properties of white matter and gray matter differs, which can be attributed to various content of myelin in these two types of brain tissues. Myelin forms a shell of axons, providing conditions for an adequate conduction of an impulse along them. Therefore, it is presented in a higher amount in white matter that leads to changes in its THz optical properties, as compared to that of a gray matter. This study has an important consequence in relation to pathological changes in brain tissue associated with changes in myelin content. THz technologies have good prospects for implementation in the diagnosis of multiple sclerosis. Nevertheless, the difference in the THz dielectric properties associated with myelin does not affect the possibility of detecting the tumor margins in both gray matter and white matter [41].

In Ref. [39], similar study was carried out using a glioma model in mice. For this aim, the GL261 glioma cell line was implanted into the brain of 6 week old mouse. The tumor was grown for 20 days, after which the brain was removed, cut into pieces and embedded into paraffin blocks. By studying these paraffin-embedded tissues, the authors of Ref. [39] were able to clearly differentiate normal tissue and tumor using THz spectroscopy. In later studies, capabilities of THz technology in the intraoperative diagnostics of brain tumors was confirmed using THz pulsed spectroscopy and different types of gliomas. Particularly, freshly excised tissues of C6 glioma cell line *ex vivo* and human glioblastoma spheroids were studied in Refs. [42, 43]. At the same time, the observed results of THz spectroscopy and imaging of various glioma models require additional validation based on studies of the human brain gliomas.

3.2 Human brain gliomas

In order to mitigate this challenge, in Ref. [43], THz reflectometry was applied for studying *ex vivo* the human brain gliomas of the World Health Organization

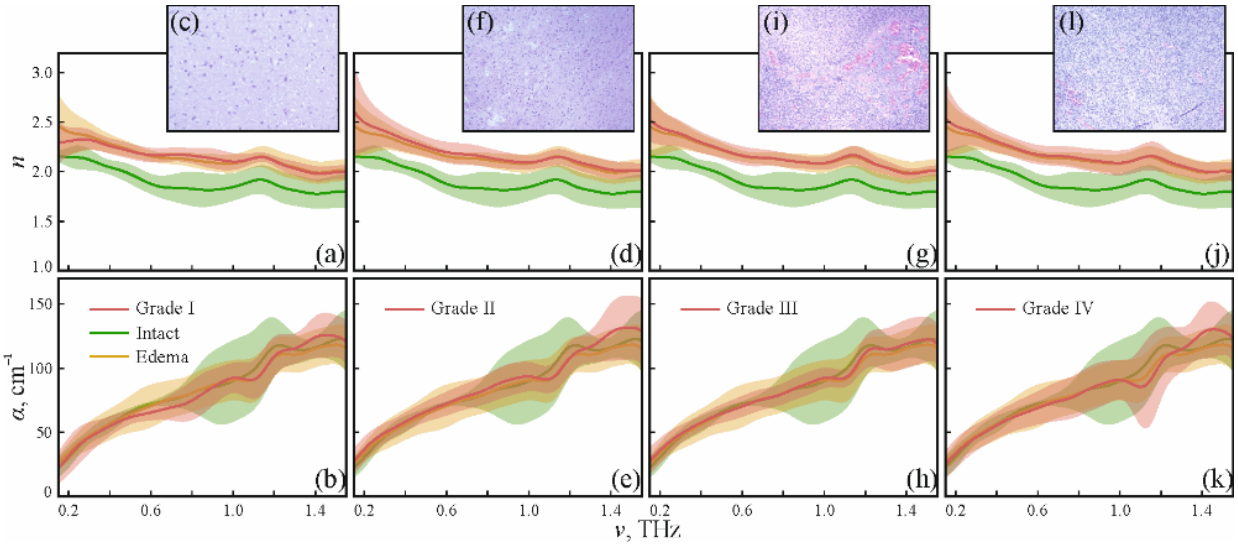


Fig. 4 THz optical properties (i.e. refractive index n and absorption coefficient α) and H&E-stained histology of gelatin-embedded human brain gliomas *ex vivo* of different WHO grade: (a)–(c) Grade I; (d)–(f) Grade II; (g)–(i) Grade III; (j)–(l) Grade IV. The error bars represent the 95% confidential interval of measurements. Adapted from Ref. [17]), published by SPIE under a Creative Commons (CC BY) license.

(WHO) Grades II (6 samples), III (4 samples), and IV (4 samples) at 0.5 THz, thereby emphasizing the potential of THz reflection imaging for brain tumor diagnosis. At the same time, THz spectroscopy in a wide spectral range will open new prospects for the use of THz radiation for subsequent studies. It should be mentioned that THz spectroscopy and imaging may have a higher potential for determining the true tumor margins as compared to the 5-ALA-guided fluorescence spectroscopy and imaging. It was shown that in a cohort of patients with glioblastomas the tissue fluorescence was clearly observed only in half of the cases, while THz technology allowed us to determine the tumor margins in all the considered cases [44].

Next, in Ref. [45], intact tissues and human brain gliomas of WHO Grades I–IV were studied *ex vivo* using THz pulsed spectroscopy, while gelatin embedding of tissues was applied in order to prevent their hydration/dehydration and, thus, to sustain their THz dielectric response unaltered (as compared to that of freshly excised tissues *ex vivo*) over the entire period of tissue transportation and THz measurements. Moreover, fragments of perifocal brain tissue, including those in the edematous state, were also found in the investigated samples. After THz measurements, tissue fragments were fixed in formalin and sent to a routine histopathological study using the H&E stained histology [17]. To study the THz response of human brain tissue, a reflection-mode THz pulsed spectrometer was used, the THz beam path of which was purged by nitrogen gas in order to suppress an impact of water vapors on the measured THz data. Details of brain tissue characterization can be found in Ref. [17].

In Fig. 4, the measured THz refractive index n and absorption coefficient α are shown for the intact and edematous tissues, as well as human brain gliomas of different WHO Grades, while the insets show representative examples of tissue histology [17]. The error bars showed in Fig.4 accounts for fluctuations of the THz optical properties of tissue both within each tissue sample and within each tissue class, representing the 95% confidential interval of measurements. The statistical difference between the THz response of intact tissues and brain gliomas [17] (see Fig. 4) is fully consistent with the results of preliminary studies using glioma models from rats and mice [17, 39, 42, 43] (for example, see Fig. 3). A label-free contrast between the THz refractive index of intact tissues and tumors is observed [17, 43], while the refractive index is higher for a tumor. At the same time, distinguishing between edematous tissues and tumors, as well as between different WHO Grades of a tumor using THz spectroscopy, appears to be a daunting task. From Fig. 4, significant variations of the THz optical properties within each tissue class are clearly observed, which is usual for most modalities of the label-free tissue spectroscopy and imaging. A possible reason for such a high dispersion in the THz response of intact tissues can be due to the lack of differentiation between white matter and gray matter in the considered study (they form a single class of intact tissues in Fig. 4).

The results of Ref. [17] confirmed a strong potential of THz technology in the intraoperative diagnosis of human brain gliomas, where both THz spectroscopy and imaging can be applied for the label free detection of the tumor margins during surgery in order to ensure its gross total resection.

3.3 Human brain meningiomas

Other brain tumors were not spared. For example, in Ref. [44], it was shown that THz spectroscopy yields differentiation of intact brain tissues and meningiomas, as illustrated in Fig. 5. Nevertheless, the need of bringing THz technology to a clinical practice for

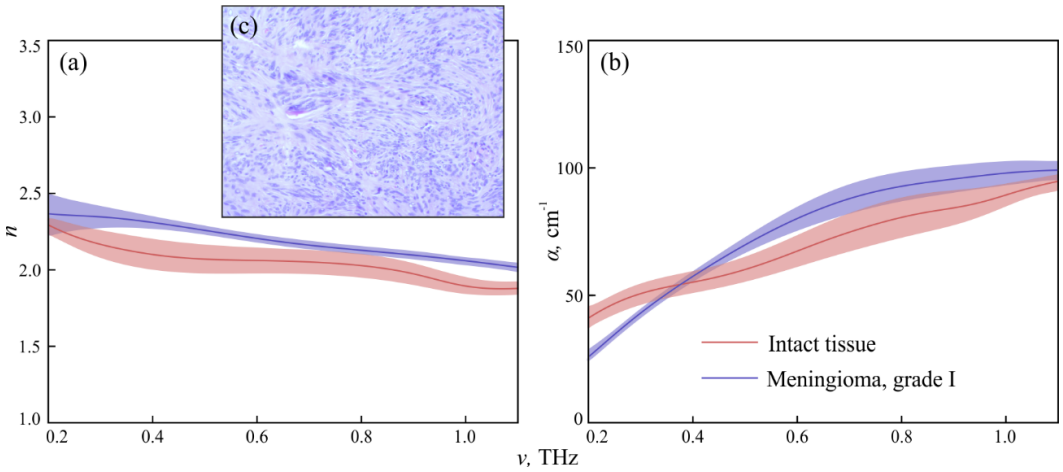


Fig. 5 Results of THz pulsed spectroscopy of gelatin-embedded human brain meningioma *ex vivo* of WHO Grade I: (a) refractive index n; (b) absorption coefficient α, (c) H&E-stained histology. Courtesy of K.I. Zaytsev.

diagnosis of other types of brain tumors (besides gliomas) remains a debatable issue, considering high costs of THz instruments.

3.4 Determination of molecular characteristics of tumors

THz technology can focus not only on the content and state of tissue water, but also on other molecular components, for example, myelin. There are other features of the molecular spectrum, which are reflected in the dielectric properties of tissues in the THz range. THz spectroscopy reveals the nucleotide composition of DNA and RNA. Changes in the composition of nucleotides and conformational changes in the DNA molecule generate low-frequency molecular vibrations that can be determined by THz spectroscopy. In principle, it is possible to determine the qualitative and quantitative composition of nucleotides using THz spectroscopy, since each of the four nucleotides has different absorption coefficients in the THz range [46, 47]. THz spectroscopy was used for the qualitative and quantitative analysis of various types of nucleic acids. It was shown that when the qualitative composition of the DNA chain is changed by one nucleotide, the spectral properties of the DNA molecule is changed in the THz range that indicates the possibility of detecting DNA point mutations using THz spectroscopy [48].

This potential of THz technology may be extremely useful for intraoperative diagnosis of brain tumors. There are a number of mutational changes, including point mutations, which are not only specific for certain types of CNS tumors, but also important factors that determine the patients prognosis. For example, point mutations of the *IDH1* and *IDH2* genes are specific among CNS tumors for some diffuse gliomas: diffuse astrocytoma (Grade II), anaplastic astrocytoma (Grade III) and a special kind of glioblastoma (Grade IV) [49]. Moreover, the presence of this mutation determines a more favorable prognosis of the survival for patients with diffuse gliomas [50]. Another example is the presence of the *BRAF* V600E point mutation, which is a characteristic of pleomorphic xanthoastrocytoma and ganglioglioma and is an important prognosis factor also [51]. The genetic profile of these mutations indicates the fundamental possibility of their detection using THz technology that may have a direct impact not only on the verification of tumor histogenesis, but also on further tactics of surgical treatment.

However, numerous research efforts are required in order to make THz molecular diagnosis possible. Indeed, strong impact of free and bound water on the THz dielectric response of tissues should be suppressed, thus, unmasking spectral fingerprints of other endogenous molecular markers of a tumor.

3.5 Multimodal diagnosis of brain tumors

In general, the variability and heterogeneity of the resulting THz spectroscopy and imaging data somewhat reduce the sensitivity and specificity of these novel tools of intraoperative neurodiagnosis [18]. In order to increase the efficiency of THz technology in diagnosis of brain tumors, multimodal approaches may be applied by combining several modalities of tissue spectroscopy and imaging. In particular, it was shown in Ref. [43] that a favorable combination of preoperative Magnetic Resonance Imaging (MRI), White-Light Imaging (WLI), Green Fluorescence Protein (GFP) imaging, H&E-stained histology, Optical Coherence Tomography (OCT), THz imaging and 5-ALA-induced fluorescence navigation allows to boost the performance of resultant system and to improve the tissue differentiation; see Fig. 6.

It is worth noting that pathogenetic links that determine the features of the distribution of water in the tumor tissue and, as a result, the characteristic features in the THz image, can arise not only in the framework of the oncological process. One of the common variants of brain pathology, accompanied by similar pathogenetic changes, is brain injury. On the one hand, this creates opportunities for the diagnosis of traumatic changes in brain tissue during surgery, which has been

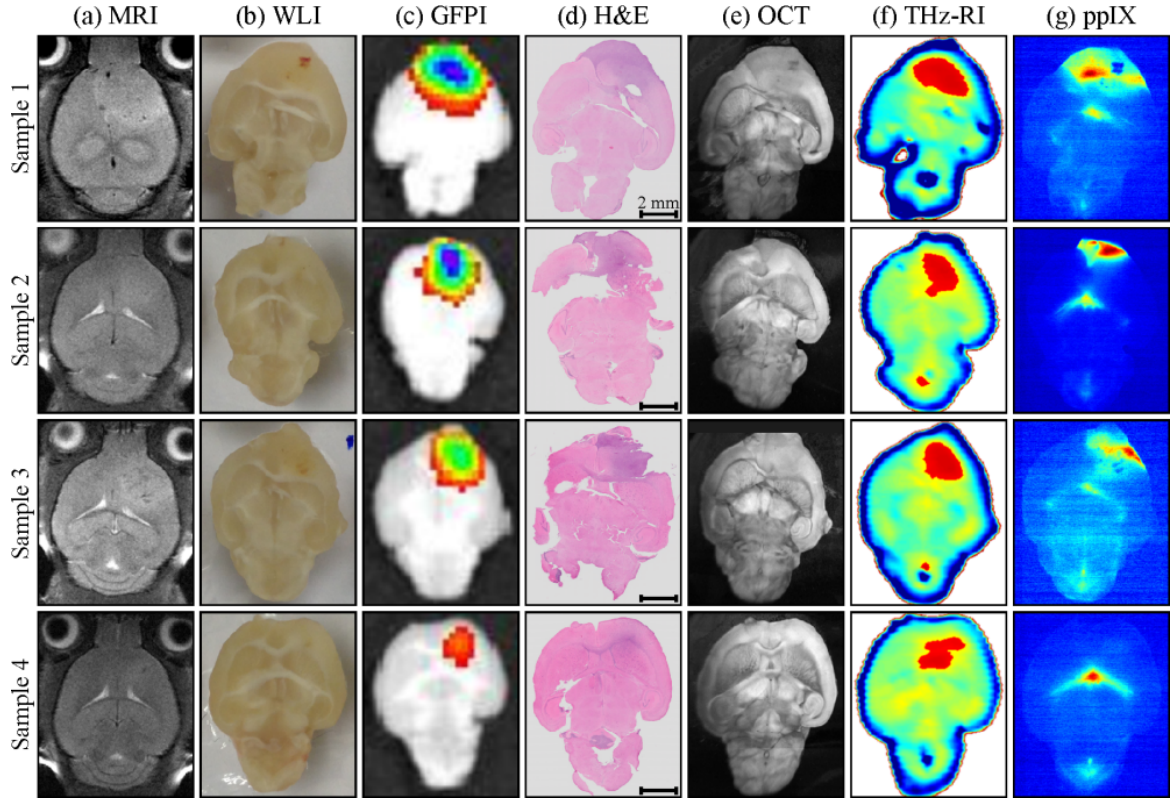


Fig. 6 Various imaging modalities of tissue imaging applied for differentiation between intact tissue and glioma models from 4 samples of whole mouse brain: (a) preoperative Magnetic Resonance Imaging (MRI); (b) White Light Imaging (WLI); (c) Green-Fluorescent Protein (GFP) imaging; (d) Hematoxylin and Eosin (H&E)-stained histology; (e) Optical Coherence Tomography (OCT); (f) THz Reflection-mode Imaging (THz-RI); (g) 5-ALA-induced protoporphyrin IX fluorescence (ppIX) imaging. Adapted from Ref. [43], published by Springer Nature under a Creative Commons (CC BY) license.

proven in Ref. [52]. However, on the other hand, this intersection of pathogenetic links between traumatic injury and brain tumors makes it difficult to verify the pathological process, this difficulty can also be overcome using a multimodal approach for the pathology assessment.

4 Conclusions

In this review, fundamental possibility of using THz technology for the intraoperative diagnosis of CNS neoplasms was considered. Some problems that stand in the way of the implementation of the discussed technique in clinical practice are discussed. Most of these problems are fundamental and require continuation to clinical and paraclinical trials of THz technology in neurooncology. At the same time, advantages of THz diagnostics predetermine the prospect of further work on the translation of available fundamental developments in practice. Further progress in this area and deeper penetration of THz technologies into practice will be accompanied by the emergence of new problematic issues directly related to the clinical and medical aspects of the new diagnostic approach, including the ergonomics of THz equipment for surgery rooms, its biological safety and financial viability. The solution of all the questions posed at different stages of the THz diagnostic development in medicine requires further extensive research and engineering efforts.

Disclosures

The authors declare that there are no conflicts of interest related to this article.

Acknowledgments

The work was supported by the Russian Science Foundation (RSF), Project # 18-12-00328.

References

1. Q. Ostrom, H. Gittleman, G. Truitt, A. Boscia, C. Kruchko, and J. Barnholtz-Sloan, "CBTRUS statistical report: Primary brain and other central nervous system tumors diagnosed in the United States in 2011–2015," Neuro-Oncology 20(Suppl4), iv1–iv86 (2018).
2. E. F. Chang, A. Clark, R. L. Jensen, M. Bernstein, A. Guha, G. Carrabba, D. Mukhopadhyay, W. Kim, L. M. Liau, S. M. Chang, J. S. Smith, M. S. Berger, and M. W. McDermott, "Multiinstitutional validation of the University of California at San Francisco low-grade glioma prognostic scoring system," Journal of Neurosurgery 111(2), 203–210 (2009).
3. M. Hefti, H. Mehdorn, I. Albert, and L. Dorner, "Fluorescence-guided surgery for malignant glioma: a review on aminolevulinic acid induced protoporphyrin ix photodynamic diagnostic in brain tumors," Current Medical Imaging Reviews 6(4), 254–258 (2010).
4. F. N. Obeidat, H. A. Awad, A. T. Mansour, M. H. Hajeer, M. A. Al-Jalabi, and L. E. Abudalu, "Accuracy of Frozen-Section Diagnosis of Brain Tumors: An 11-Year Experience from a Tertiary Care Center," Turkish Neurosurgery 29(2), 242-246 (2019).
5. W. Stummer, U. Pichlmeier, T. Meinel, O. D. Wiestler, F. Zanella, and H.-J. Reulen, "Fluorescence-guided surgery with 5-aminolevulinic acid for resection of malignant glioma: a randomised controlled multicentre phase III trial," The Lancet Oncology 7(5), 392–401 (2006).
6. M. Jermyn, J. Desroches, J. Mercier, K. St-Arnaud, M.-C. Guiot, F. Leblond, and K. Petrecca, "Raman spectroscopy detects distant invasive brain cancer cells centimeters beyond MRI capability in humans," Biomedical Optics Express 7(12), 5129–5137 (2016).
7. B. Liang, W. Liu, Q. Zhan, M. Li, M. Zhuang, Q. Huo, and L. J. Yao, "Impacts of the murine skull on high-frequency transcranial photoacoustic brain imaging," Journal of Biophotonics 12(7), e201800466 (2019).
8. F. Vase, N. MacKinnon, D. Farkas, and B. Kateb, "Review of the potential of optical technologies for cancer diagnosis in neurosurgery: a step toward intraoperative neurophotonics," Neurophotonics 4(1), 011010 (2016).
9. I. Dolganova, P. Aleksandrova, S.-I. Beshplav, N. Chernomyrdin, E. Dubyanskaya, S. Goryaynov, V. Kurlov, I. Reshetov, A. Potapov, V. Tuchin, and K. Zaytsev, "Wavelet-domain de-noising of OCT images of human brain malignant glioma," Proceedings of SPIE 10717, 107171X (2018).
10. Y.-S. Lee, Principles of Terahertz Science and Technology, Springer, 340 (2009).
11. K. Zaytsev, N. Chernomyrdin, K. Kudrin, I. Reshetov, and S. Yurchenko, "Terahertz spectroscopy of pigmentary skin nevi in vivo," Optics and Spectroscopy 119(3), 404–410 (2015).
12. Y. Sim, J. Park, K.-M. Ahn, C. Park, and J.-H. Son, "Terahertz imaging of excised oral cancer at frozen temperature," Biomedical Optics Express 4(8), 1413–1421 (2013).
13. C. Reid, A. Fitzgerald, G. Reese, R. Goldin, P. Tekkis, P. O'Kelly, E. Pickwell-MacPherson, A. Gibson, and V. Wallace, "Terahertz pulsed imaging of freshly excised human colonic tissues," Physics in Medicine & Biology 56(14), 4333–4353 (2011).
14. A. Fitzgerald, V. Wallace, S. Pinder, A. Purushotham, P. O'Kelly, and P. Ashworth, "Classiffication of terahertz-pulsed imaging data from excised breast tissue," Journal of Biomedical Optics 17(1), 016005 (2012).
15. Y. Ji, C. Park, H. Kim, S.-H. Kim, G. Lee, S. Noh, T.-I. Jeon, J.-H. Son, Y.-M. Huh, S. Haam, S. Oh, S. Lee, and J.-S. Suh, "Feasibility of terahertz reflectometry for discrimination of human early gastric cancers," Biomedical Optics Express 6(4), 1398–1406 (2015).
16. H. Chen, S.-H. Ma, W.-X. Yan, X.-M. Wu, and X.-Z. Wang, "The diagnosis of human liver cancer by using THz fiber-scanning near-field imaging," Chinese Physics Letters 30(3), 030702 (2013).
17. A. Gavdush, N. Chernomyrdin, K. Malakhov, S.-I. Beshplav, I. Dolganova, A. Kosyrkova, P. Nikitin, G. Musina, G. Katyba, I. Reshetov, O. Cherkasova, G. Komandin, V. Karasik, A. Potapov, V. Tuchin, and K. Zaytsev, "Terahertz spectroscopy of gelatin-embedded human brain gliomas of different grades: a road toward intraoperative THz diagnosis," Journal of Biomedical Optics 24(2), 027001 (2019).
18. O. A. Smolyanskaya, N. V. Chernomyrdin, A. A. Konovko, K. I. Zaytsev, I. A. Ozheredov, O. P. Cherkasova, M. M. Nazarov, J.-P. Guillet, S. A. Kozlov, Yu. V. Kistenev, J.-L. Coutaz, P. Mounaix, V. L. Vaks, J.-H. Son, H. Cheon, V. P. Wallace, Yu. Feldman, I. Popov, and V. V. Tuchin, "Terahertz biophotonics as a tool for studies of dielectric and spectral properties of biological tissues and liquids," Progress in Quantum Electronics 62, 1–77 (2018).
19. K. Cole, R. Cole, "Dispersion and absorption in dielectrics I. Alternating current characteristics," The Journal of Chemical Physics 9(4), 341–351 (1941).
20. K. Cole, R. Cole, "Dispersion and absorption in dielectrics II. Direct current characteristics," The Journal of Chemical Physics 10(2), 98–105 (1942).
21. D. Davidson, "Dielectric relaxation in liquids: I. The representation of relaxation behavior," Canadian Journal of Chemistry 39(3), 571–594 (1961).
22. S. Havriliak, S. Negami, "A complex plane analysis of dispersions in some polymer systems," Journal of Polymer Science Part C: Polymer Symposia 14(1), 99–117 (1966).

23. E. Pickwell, B. E. Cole, A. J. Fitzgerald, V. P. Wallace, and M. Pepper, "Simulation of terahertz pulse propagation in biological systems," Applied Physics Letters 84(12), 2190–2192 (2004).
24. E. Pickwell, A. J. Fitzgerald, B. E. Cole, P. F. Taday, R. J. Pye, T. Ha, M. Pepper, and V. P. Wallace, "Simulating the response of terahertz radiation to basal cell carcinoma using ex vivo spectroscopy measurements," Journal of Biomedical Optics 10(6), 064021 (2005).
25. G. C. Walker, E. Berry, S. W. Smye, N. N. Zinov'ev, A. J. Fitzgerald, R. E. Miles, M. Chamberlain, and M. A. Smith, "Modelling the propagation of terahertz radiation through a tissue simulating phantom," Physics in Medicine & Biology 49(10), 1853–1864 (2004).
26. A. J. Fitzgerald, E. Pickwell-MacPherson, and V. P. Wallace, "Use of finite difference time domain simulations and Debye theory for modelling the terahertz reflection response of normal and tumour breast tissue," PLOS ONE 9, e99291 (2014).
27. B. C. Q. Truong, H. D. Tuan, V. P. Wallace, A. J. Fitzgerald, and H. T. Nguyen, "The potential of the double Debye parameters to discriminate between basal cell carcinoma and normal skin," IEEE Transactions on Terahertz Science & Technology 5(6), 990–998 (2015).
28. E. P. Parrott, S. M. Y. Sy, T. Blu, V. P. Wallace, and E. Pickwell-MacPherson, "Terahertz pulsed imaging in vivo: measurements and processing methods," Journal of Biomedical Optics 16(10), 106010 (2011).
29. S. J. Oh, S.-H. Kim, Y. B. Ji, K. Jeong, Y. Park, J. Yang, D. W. Park, S. K. Noh, S.-G. Kang, Y.-M. Huh, J.-H. Son, and J.-S. Suh, "Study of freshly excised brain tissues using terahertz imaging," Biomedical Optics Express 5(8), 2837–2842 (2014).
30. C. S. Joseph, A. N. Yaroslavsky, M. Al-Arashi, T. M. Goyette, J. C. Dickinson, A. J. Gatesman, B. W. Soper, C. M. Forgione, T. M. Horgan, E. J. Ehasz, R. H. Giles, and W. E. Nixon, "Terahertz spectroscopy of intrinsic biomarkers for non-melanoma skin cancer," Proceedings of SPIE 7215, 72150I (2009).
31. M. Ney, I. Abdulhalim, "Comprehensive Monte-Carlo simulator for optimization of imaging parameters for high sensitivity detection of skin cancer at the THz," Proceedings of SPIE 9721, 97210W (2016).
32. N. V. Chernomyrdin, A. S. Kucheryavenko, E. N. Rimskaya, I. N. Dolganova, V. A. Zhelnov, P. A. Karalkin, A. A. Gryadunova, I. V. Reshetov, D. V. Lavrukhin, D. S. Ponomarev, V. E. Karasik, and K. I. Zaytsev, "Terahertz microscope based on solid immersion effect for imaging of biological tissues," Optics & Spectroscopy 126(5), 560–567 (2019).
33. A. Ishimaru, Electromagnetic wave propagation, radiation, and scattering: From fundamentals to applications, Wiley–IEEE Press, Piscataway, NJ, USA (2017).
34. P. Doradla, K. Alavi, C. Joseph, and R. Giles, "Detection of colon cancer by continuous-wave terahertz polarization imaging technique," Journal of Biomedical Optics 18(9), 090504 (2013).
35. V. Tuchin. Tissue optics: Light scattering methods and instruments for medical diagnostics, Third edition, SPIE Press, Bellingham, Washington, USA (2015).
36. K. I. Zaytsev, I. N. Dolganova, N. V. Chernomyrdin, G. M. Katyba, A. A. Gavdush, O. P. Cherkasova, G. A. Komandin, M. A. Shchedrina, A. N. Khodan, D. S. Ponomarev, I. V. Reshetov, V. E. Karasik, M. Skorobogatiy, V. N. Kurlov, and V. V. Tuchin, "The progress and perspectives of terahertz technology for diagnosis of neoplasms: A review," Journal of Optics 22(1), 013001 (2020).
37. G. M. Png, R. Flook, B.W.-H. Ng, and D. Abbott, "Terahertz spectroscopy of snap-frozen human brain tissue: an initial study," Electronics Letters 45(7), 343–345 (2009).
38. L. Shi, P. Shumyatsky, A. Rodríguez-Contreras, and R. Alfano, "Terahertz spectroscopy of brain tissue from a mouse model of Alzheimer's disease," Journal of Biomedical Optics 21(1), 015014 (2016).
39. K. Meng, T.-N. Chen, T. Chen, L.-G. Zhu, Q. Liu, Z. Li, F. Li, S.-C. Zhong, Z.-R. Li, H. Feng, and J.-H. Zhao, "Terahertz pulsed spectroscopy of paraffin-embedded brain glioma," Journal of Biomedical Optics 19(7), 077001 (2014).
40. S. Doblas, T. He, D. Saunders, J. Pearson, J. Hoyle, N. Smith, M. Lerner, and R. A. Towner, "Glioma morphology and tumor- induced vascular alterations revealed in seven rodent glioma models by in vivo magnetic resonance imaging and angiography," Journal of Magnetic Resonance Imaging 32(2), 267–275 (2010).
41. Y. Zou, J. Li, Y. Cui, P. Tang, L. Du, T. Chen, K. Meng, Q. Liu, H. Feng, J. Zhao, M. Chen, and L.-G. Zhu, "Terahertz spectroscopic diagnosis of myelin deficit brain in mice and rhesus monkey with chemometric techniques," Scientific Reports 7, 5176 (2017).
42. S. Yamaguchi, Y. Fukushi, O. Kubota, T. Itsuji, T. Ouchi, and S. Yamamoto, "Brain tumor imaging of rat fresh tissue using terahertz spectroscopy," Scientific Reports 6, 30124 (2016).
43. Y. B. Ji, S. J. Oh, S.-G. Kang, J. Heo, S.-H. Kim, Y. Choi, S. Song, H. Y. Son, S. H. Kim, J. H. Lee, S. J. Haam, Y. M. Huh, J. H. Chang, C. Joo, and J.-S. Suh, "Terahertz reflectometry imaging for low and high grade gliomas," Scientific Reports 6, 36040 (2016).
44. N. V. Chernomyrdin, A. A. Gavdush, S.-I. T. Beshplav, K. M. Malakhov, A. S. Kucheryavenko, G. M. Katyba, I. N. Dolganova, S. A. Goryaynov, V. E. Karasik, I. E. Spektor, V. N. Kurlov, S. O. Yurchenko, G. A. Komandin, A. A. Potapov, V. V. Tuchin, and K. I. Zaytsev, "In vitro terahertz spectroscopy of gelatin-embedded human brain tumors: a pilot study," Proceedings of SPIE 10716, 107160S (2018).

45. S. Fan, B. Ung, E. P. J. Parrott, and E. Pickwell-MacPherson, "Gelatin embedding: a novel way to preserve biological samples for terahertz imaging and spectroscopy," Physics in Medicine & Biology 60(7), 2703 (2015).
46. B. M. Fischer, M. Walther, and P. U. Jepsen, "Far-infrared vibrational modes of DNA components studied by terahertz time-domain spectroscopy," Physics in Medicine & Biology 47(21), 3807–3814 (2002).
47. E. Pickwell-MacPherson, V. P. Wallace, "Terahertz pulsed imaging – A potential medical imaging modality," Photodiagnosis and Photodynamic Therapy 6(2), 128–134 (2009).
48. M. Tang, M. Zhang, S. Yan, L. Xia, Z. Yang, C. Du, H. L. Cui, and D. Wei, "Detection of DNA oligonucleotides with base mutations by terahertz spectroscopy and microstructures," PLOS ONE 13(1), e0191515 (2018).
49. P. Wesseling, D. Capper, "WHO 2016 Classification of gliomas," Neuropathology and Applied Neurobiology 44(2), 139–150 (2018).
50. R. Chen, M. Smith-Cohn, A. L. Cohen, and H. Colman, "Glioma Subclassifications and Their Clinical Significance," Neurotherapeutics 14(2), 284–297 (2017).
51. X. Chen, C. Pan, P. Zhang, C. Xu, Y. Sun, H. Yu, Y. Wu, Y. Geng, P. Zuo, Z. Wu, J. Zhang, and L. Zhang, "BRAF V600E mutation is a significant prognosticator of the tumour regrowth rate in brainstem gangliogliomas," Journal of Clinical Neuroscience 46, 50–57 (2017).
52. H. Zhao, Y. Wang, L. Chen, J. Shi, K. Ma, L. Tang, D. Xu, J. Yao, H. Feng, and T. Chen, "High-sensitivity terahertz imaging of traumatic brain injury in a rat model," Journal of Biomedical Optics 23(3), 036015 (2018).

Recent Trends in Optical Manipulation Inspired by Mesoscale Photonics and Diffraction Optics

Igor V. Minin[1,2]* and Oleg V. Minin[1,2]

[1] Siberian State University of Geosystems and Technologies, 10 Plahotnogo Ave., Novosibirsk 630005, Russia
[2] Tomsk State University, 36 Lenina Ave., Tomsk 634050, Russia

***e-mail:** prof.minin@gmail.com

Abstract. The spatial resolution of conventional optics, which is need for non-destructively trapping of microobjects, is limited by diffraction to nearly half the wavelength. Despite this limitation, the use of optical methods is one of the main directions in biological and biomedical researches, since only the use of optical methods has a minimal effect on living organisms. Quick progress in this field is based on a large extent on the development of new optical technologies and significant progress in the mesoscale photonics enabled the researches to obtain novel, previously unachievable information. Below we discussed some recent trends in optical manipulations on wavelength scale based on diffractive elements – mesoscale dielectric particles as a field localization object and classical diffractive optical elements with unusual properties. © 2020 Journal of Biomedical Photonics & Engineering.

Keywords: mesoscale photonics; dielectric particle; optical force; photonic nanojet; photonic hook; particle manipulation; zone plate.

Paper #3349 received 28 Jan 2020; revised manuscript received 24 Feb 2020; accepted for publication 27 Mar 2020; published online 20 Jun 2020. doi: 10.18287/JBPE20.06.020301.

1 Introduction

The possibility of non-destructively trapping and transport of individual sub-micrometer objects are highly benefit in different fields of life sciences [1–4] like microfabrication [5], chemical research [6], optics [7] and biological [8], including the precise control of single biomolecules and drug delivery to living cells. The multidisciplinary nature of optomechanical manipulation of nanoparticles has allowed bringing together seemingly unrelated fields, such as electromagnetic or/and acoustical physics, biology, paving the way for a plethora of emerging applications. The physics of optical trapping is based on the balance of the scattering and gradient optical forces. The gradient optical forces move a target along the gradient of light intensity and the scattering forces push a target in the direction of light propagation [9]. Therefore, an object is pulled to the area of stronger light intensity when the gradient forces are larger than scattering one. It could be noted that for nanoparticles having diameter less than one tenth of wavelength, optical trapping of nanoparticles is challenging due to gradient forces are proportional to the particle volume [10].

However, it is well known that the spatial resolution of conventional optics is determined only by illuminated wavelength and optical objective numerical aperture, and limited by diffraction to nearly half the wavelength. Therefore, the key problem of this achievement is the fundamental diffraction limit that prevents from focusing a light beam down to a subwavelength volume [11].

Especially in the past years, numerous optical structured beams have been proposed to optomechanically act on nanoparticles in subwavelength scale. Below we briefly consider rapidly developing methods for localizing the electromagnetic field based on mesoscale dielectric photonics. The mesoscale dielectric photonics involves the interaction of radiation with dielectric object or material structures of intermediate scale structures (Mie size parameter $q = 2\pi r/\lambda \approx (3–20)\pi$ [12, 13], where λ is illuminating wavelength and r is particle radius) that are too large to be characterized as simple dipoles and too small to be described by geometrical optics.

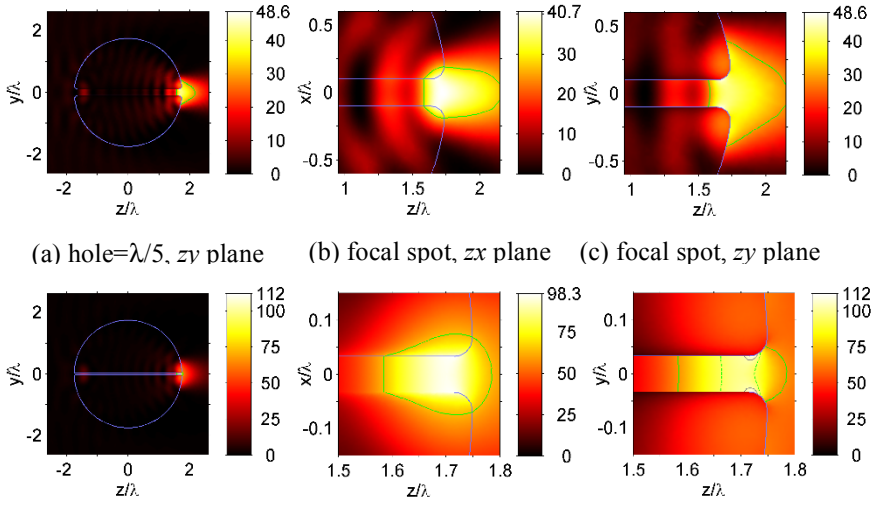
Subwavelength confining and controlling electromagnetic energy usually involves a resonant phenomenon [13, 14]. Below we briefly consider a class of nonresonant diffraction elements (mesoscale

dielectric particles and unusual diffraction zone plates) for nanoparticle manipulations. In this brief review, the nexus of nanophotonics at the mesoscale and particle manipulation science is considered. This nexus offers of novel fundamental effects and interesting applications and can serve for developing groundbreaking technologies at the subwavelength scale as a starting point. Other methods of nanoparticles manipulating are widely covered in the literature and can be found by the reader in relevant reviews [1–4, 7, 8, 10].

2 Nanohole structured dielectric mesoscale particle

To overcome the diffraction limitation, the possibilities of light manipulation based on the mesoscale dielectric structures are becoming attractive to an increasing number of researchers. A diverse range of methods for subwavelength localization of light has been proposed. Among them, photonic crystal-based (PhC) lenses [15–17], 3D diffractive optics [18, 19], and flat nanoslit based on the plasmonic lenses [20–22] have been studied for sharp focusing of light beyond the diffraction limit. Later, in 2017, a conical two-dimensional in-plane nanoslit-based plasmonic-zone plate lens was proposed to realize far-field super-resolution focusing [23] by exciting SPPs and enabling them to couple with radiating propagation modes. The graded PhC lenses with varying-sized air holes were studied in Refs. [24, 25]. It has been reported that by means of graded 3D PhC lens, the focused light beam with full-width at half maximum (FWHM) beam-width of about λ/75 could be achieved [25].

However, the photonic nanojet (PNJ) phenomenon is more attractive due to the simplicity of its implementation and the compact size of the focusing particle. On the other hand, the minimum beam width of PNJ usually is about of λ/3 [12, 13] (where λ is the wavelength of the incident light) and, thus, it is necessary to search for new methods to further reduce the size of the focal spot of the PNJ. For deep subwavelength-scale light focusing deep beyond the solid immersion diffraction limit of λ/2*n* and strong light confinement, in Ref. [26] a nanohole-structured dielectric microsphere was proposed. The field enhancement is due to the permittivity contrast between the nanohole material and the dielectric microparticle material. The proposed nanostructured mesoscale sphere has several unique properties. For example, it could produce a high optical power and electric field intensity in low-index hole materials (air), at levels that cannot be achieved through a conventional PNJ produced by spheres without nanostructure and with the same diameter [12, 13]. It has been shown [26] that the incoming light wave is confined by the dielectric particle inside the nanohole, even when the hole diameter is deeply subwavelength (at least of λ/40), obtaining a resolution near the shadow surface of the particle that is comparable to the nanohole size (beyond the solid immersion diffraction limit). The example of field localization in nanohole structured mesoscale sphere shown in Fig. 1. On the other words, the manufacturing of a nanohole on the rear surface of a dielectric mesoscale particle, allows us to "compress" the field localization characteristic of a PNJ, to the size of this nanohole.



(a) hole=λ/5, *zy* plane (b) focal spot, *zx* plane (c) focal spot, *zy* plane

(d) hole=λ/15, *zy* plane (e) focal spot, *zx* plane (f) focal spot, *zy* plane

Fig. 1 Dielectric microspheres with a through hole, with the hole diameter of (a–c) = λ/5, and (d–f) = λ/15. The sphere diameter and refractive index are set as D_s = 3.5λ and n = 1.5. Contour lines at the value of $0.5I_{max}$, $0.85I_{max}$, and $0.9I_{max}$ are plotted with the green solid lines, green dashed lines, and gray solid lines respectively. Adapted from Ref. [26] with the permission of MDPI under a Creative Commons Attribution (CC BY) license.



Fig. 2 The particle with broken symmetry for PH formation: the morphology of the field localization area depends on the orientation of the particle that resembles the two faces of "Janus bifrons". Adapted from Ref. [33].

The manufacture of nanohole is currently possible using one of the known methods [27–29].

Based on these investigations we propose a novel concept of "optical vacuum cleaner" [30] with simple design. The key idea is to use a designed nanohole-structured dielectric mesoscale particle of arbitrary shape for redirecting of optical momentum and achieving the desired optomechanical effects on a metallic target nanoscale object. Based on full wave numerical simulations we show that the optical forces exerted on a gold nanosphere probe are manyfold enhanced near the nanohole in mesoscale particle, that results in efficient nanoparticle propulsion into the nanohole. For example, the analysis of the phase portrait of the nanoparticle motion (focused lens with NA = 0.5 at λ = 600 nm and with the power of 10 W) has shown [30] that after a few milliseconds, the Au nanoparticle relaxes to the final point of its trajectory located approximately 20 nm inside dielectric cubic particle hole opening.

Nanoparticles removing from the surrounding medium is critical in many life fields, including health, air purification systems and air cabin filters [31]. Numerical simulation shows that the proposed nanohole-structured dielectric mesoscale particle can be used for optomechanical trapping and removal of metal nanoparticles, and comparing with traditional optical methods has a great potential in biomedical, chemical and many other technological applications [32].

3 Photonic hook: a new subwavelength self-bending structured light beams

Based on physical principles of photonic nanojet [11, 12] a new type of subwavelength structured light beam which called photonic hook (PH) was discovered in 2015 [33]. Further theoretical and experimental works confirmed this general effect. Photonic hook light does not propagate along straight line but instead follow curved trajectory [33–36]. A curved beam was formed due to diffraction of an electromagnetic wave by a mesoscale dielectric Janus particle (Fig. 2) in the form of a cuboid with broken symmetry [33].

Without the wedge prism, the symmetric cuboid-only structure produced an electric-field enhancement or photonic jet, as expected, along the transmission axis. However, the addition of the wedge creates the asymmetric structure that curves the light upon exiting the cuboid to a degree dependent on the wedge angle. Wavefront analysis of such asymmetric mesoscale structure reveals that the unequal phase of the transmitted plane wave results in the irregularly concave deformation of the wavefront inside the structure that then leads to creation of the PH [33–38], which can be more easily visualized as a light beam with astigmatism on the macro scale. A distinctive feature of the PH are: the radius of curvature of PH is the fraction of illumination wavelength and although the curved profile evokes a similarity with Airy beams, in contrast to Airy beams there are no curved side lobes [34–37], where in the caustic from one side the sidelobes almost parallel to each other. Moreover, in the PH there is an inflexion where the curved beam changes its propagating direction. This property does not possessed by the Airy-like beam. It is important to note that the PH structured field combines the construction simplicity of the PNJ, as well as the curvature produced by Airy-family self-bending beams at subwavelength level. We also note that previously studied curved beams usually require the use of expensive and complicated optical elements, which often make them unsuitable for embedding in an optical system.

Because of the phenomenon of focus bending the dielectric particle is caused by the interference of waves inside it as the phase velocity disperses the shape of the photonic hook. Also, the characteristics of curved near-field beams [34–37] depending on the specific application can be quite exotic due to the control of phase delays across the wavefront by choosing the shape of mesoscale particles (Fig. 3).

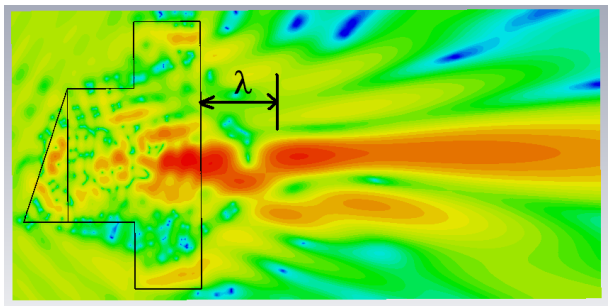


Fig. 3 Example of a photonic hook in the form of subwavelength loop.

Recent studies have investigated the generation of wide families of photonic hook beams, bringing many future opportunities to this fast-moving area including optics [33–35, 37], THz [36], surface plasmon photonics (SPP) [38], acoustics [39] and have boosted the development of mesoscale photonics providing cutting-edge abilities in particle manipulation on subwavelength scales.

The simulations of a multifocal curved beam based on SiO_2 microsphere with a diameter of 433λ (which

does not meet the mesoscale condition and goes beyond the range of PNJ effect existence) in the optical waveband show that it is possible to control the curvature of the beam by adjusting the relative position between an off-axis Gaussian beam and a spherical particle [40]. The PH through a structured dielectric cylinder with embedded a glass cuboid was discussed in [41] based on numerical simulations. Furthermore, specially designed five-layer dielectric cylinder allows to produce double PHs [42]. Also, for the generation of PHs the dielectric particles with symmetry-broken material composed of materials with different refractive indexes were proposed [43, 44] (see Fig. 4) and numerically studied in Refs. [44, 45]. At the same time single light plane wave and twin-ellipse microcylinders were numerically studied to produce twin photonic hook [46].

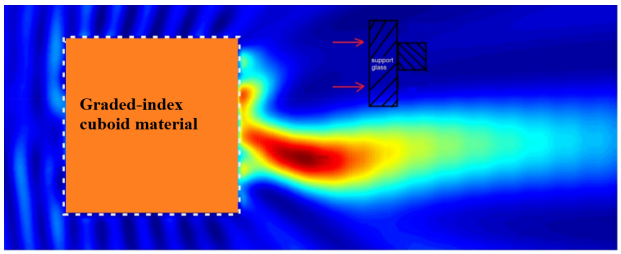


Fig. 4 PH formation by graded-index cuboid Janus particle on substrate. Adapted from Ref. [43].

The generation of curved focus with ultrathin metalens in the visible band was recently reported in Ref. [47]. At the same time, this is not the case of our study because the lens dimensions do not satisfy the mesoscale condition formulated above. In addition, PH features are not observed and cannot be attributed to PH-type beam because its field structure possesses different spatial dependence and physical nature [34–37] and strongly misleads the readers.

In general, these studies have shown the possibility to generate specialized fields that allow for realizing of more varied kinds of optical manipulation beyond trapping. In trapping studies, these investigations led to the concept of optical hook based on the optomechanical manipulator, which refers to the motion of particles on curved trajectory even around dielectric obstacles [35].

Simulations show that in the approximation that the particle is an electric dipole, i.e. Rayleigh particle [48], the target nanoparticle trajectory moves around the dielectric slab obstacle. This allows for better maneuvering of the target nanoparticles around the glass obstacles. On the other hand, the metal (Au) slab completely disrupts the field and the path trajectory of this target nanoparticle [35, 49]. One possible *in vitro* biomedical application of this concept is to guide the cells in a curved trajectory in order to differentiate between them [49]. The photonic hook concept offers the exquisite control over the particle's motion to manipulation and sorting of the cells in “lab-on-a-chip” platforms and microfluidic devices without the need for multiple trapping beam.

Let us note that another interesting area of application of mesoscale dielectric particles is optical traps based on the standing waves. In a standing-wave optical trap nanoparticles localized in the trap antinodes separated along the optical axis of the trap by half the working wavelength from each other. Trapping and manipulating nanoparticles in standing wave (which was generated using counter-propagating two coherent PNJs) in transmitted mode were considered in Ref. [50] and in reflection mode for the first time was investigated in Ref. [51], while the accuracy of trapping is limited by the half-wavelength period of standing waves structure. It could be noted that placing a dielectric particle with a low optical contrast on a dielectric plate with a high optical contrast makes it possible to simultaneously form two regions of field localization - two photonic jets in both reflection and transmission modes.

The applications of long PNJs for atomic cooling and trapping were considered in Ref. [52]. In this application, the Casimir–Polder potential near the surface of microparticles canceled by PNJ. The experimental confirmation of blood cells or DNA trapping and manipulation by PNJs were discussed in [53, 54].

4 Non-standard modification of classical diffraction optics: particle manipulations

The optical trapping based on the application of diffractive optical element (DOE) [55] can be classified into two main categories depending on the type of trap forces used namely vortex like beams with gradient force with orbital angular momentum (OAM) and gradient force with Gaussian beams [55]. In most optical trapping set up the gradient force of the Gaussian intensity profile [56] is used. On the other hand, the generation of vortex beam can be achieved only using complicated phase elements such as spiral phase plates which are difficult to manufacture [57].

First, we investigate the possibility of designing a spiral phase plate with only three phase levels [58]. The Poynting vector fields for the three-level spiral phase were calculated. We experimentally demonstrated an exotic three-dimensional control of structured light to show the evolution of the Poynting vector in such fields. It has been found that it possesses the orbital angular momentum suitable for optical trapping applications.

Recently, we introduce a family of simple binary DOEs to generate beams with OAM based on zone rotation principle of Fresnel zone plate with chiral focusing characteristics. As example, two different DOEs namely chiral square axicon (CSA) [59] and chiral square Fresnel zone plate (CSFZP) [60] were designed for generating structured beams with gradient force were designed as for generating structured beams with gradient force at the center with OAM surrounding it and as for only OAM for optical trapping applications.

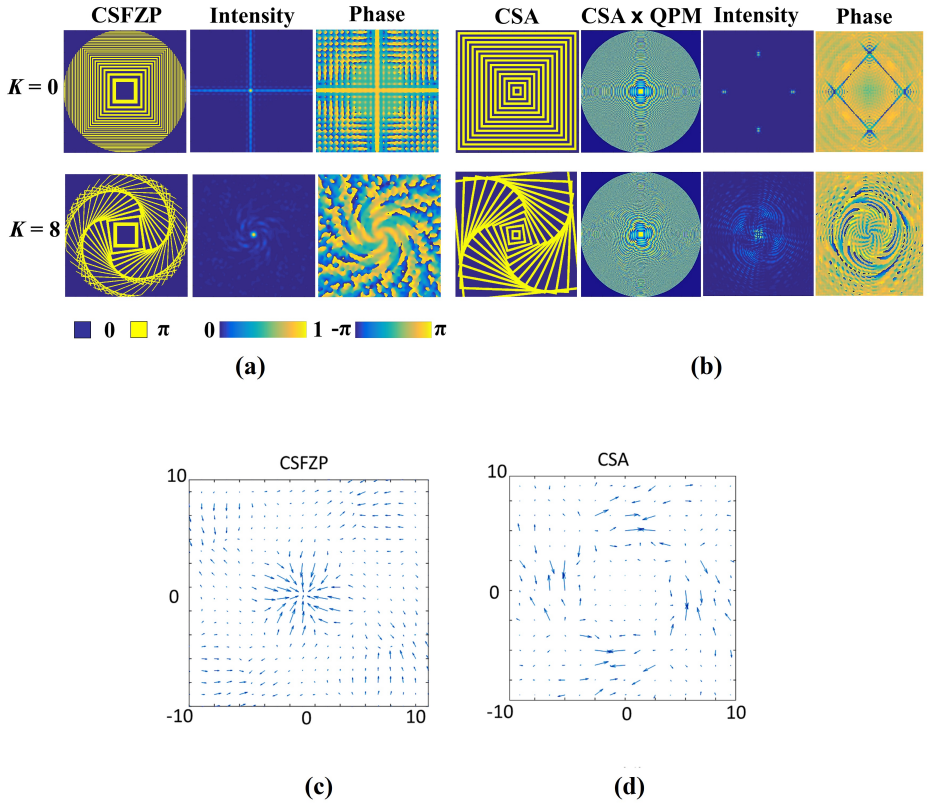


Fig. 5 Simulation of intensity and phase of (a) CSFZP and (b) CSA and Poynting vector plots for CSFZP (c) and CSA (d). The case of $K = 0$ corresponds to classical DOE. Adapted from [65].

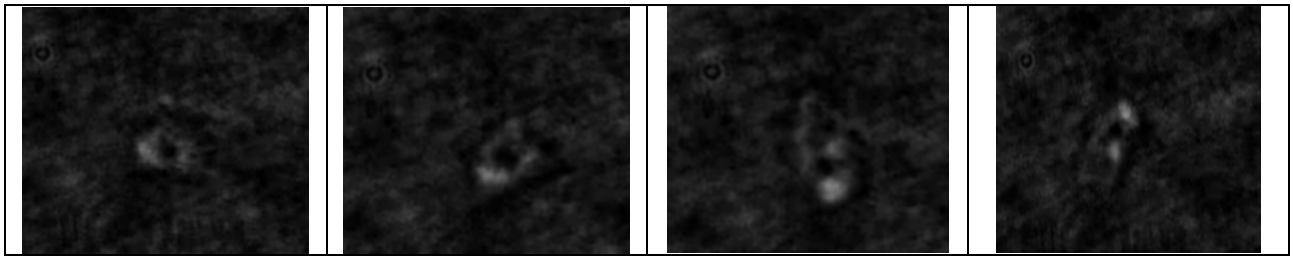


Fig. 6 Counterclockwise rotation of *Candida rugose*. Adapted from Ref. [59]. Experiments were performed in the laboratory of prof. C.-J. Cheng.

It could be noted that for Fresnel zone plate with square zones the boundaries of the zones do not coincide with the boundaries of the zones of the classical zone plate with circular zones [51]. Moreover, as first shown in [18, 33, 62, 63], a zone plate with a focal length less than a wavelength provides a resolution of about λ/3.

The DOEs with binary phase values [0, π] were designed by rotation of the half period zones with respect to one another [64].

In the case of CSA, a quadratic phase function (QPM) was multiplied to it in order to bring the far-field intensity pattern at a finite distance. The intensity and phase profiles generated by these DOEs are shown in Fig. 5. The zone rotation angle θ is $\theta = Km$, where, $m = 2n$ and K is the angular integer step size. From Fig. 5, it is followed, that with an increase of K the phase twist near the optical axis showing the presence of OAM [59, 60, 65]. Secondly, there was a light redistribution from the focal plane of CSFZP to other axial planes that resulted an increase in the focal depth with an increase in K. On the other hand, in the case of CSA, with an increase in K there was a light redistribution to the center creating a vortex. The Poynting vector of CSFZP shows the presence of gradient force at the center and OAM around it due to the presence of twisted side lobes and Gaussian focal spot at the center. Moreover, in CSA, only OAM is presented without gradient force at the center. Important to note that these methods do not involve any additional vortex [0, 2π] phase elements.

The optical tweezer setup consists of two laser sources emitting at wavelengths $\lambda_1 = 532$ nm and $\lambda_2 = 632.8$ nm for trapping and imaging respectively. We have used *Candida rugosa* (ATCC® 200555™) as a specimen for trapping and it is recorded by an imaging

system. The sample was first trapped and then rotated by the OAM of the beam (see Figure 6).

Important to note that CBSA and CSA have some advantages compared to existing DOEs for optical trapping applications [59, 60, 65–69]. The absence of central peak in the optical field expands the applicability of CBSA to highly absorptive optical trapping specimens.

5 Conclusion

Mesoscale dielectric photonics has been developing rapidly lately and we can talk about the beginning of the formation of a new scientific direction – subwavelength structured field [37], despite the fact that the number of published works is extremely limited. Its distinguishing features are its small size (of the order of several wavelengths) and simple implementation. In the field of optomechanical manipulation of nanoparticles, systems based on the mesoscale photonics can be easily integrated into "lab-on-a-chip" platform. Using novel subwavelength structured light may led to the development of 'nanophotonic tweezers,' an exciting new class of 'on-chip' optical traps and can perform new bioscience. Particles can be sorted by refractive index, shape and size. Moreover, we can guide (transport) micro-particles over wavelength scaled distances for sorting sub-cellular biological material, for example, using photonic hook light or acoustical beams. Additionally, different shape of the ultraprecise laser scalpel can be designed based on the photonic hook concept [70]. The integration of a glass microsphere, produced the PNJ, on the tip of the multimode fiber [71] or Fresnel zone plate [72–74] allow to stable trapping of a single nanoparticle.

The successful realization of above briefly discussed methods can lead to fundamental changes of biomedical analysis in subwavelength scale.

Disclosures

All authors declare that there is no conflict of interests in this paper.

Acknowledgence

This work was partially supported by the Russian Foundation for Basic Research (Grant No. 20-57-S52001).

References

1. K. Dholakia, T. Čižmár, "Shaping the future of manipulation," Nature Photonics 5(6), 335–342 (2011).
2. D. Gao, W. Ding, M. Nieto-Vesperinas, X. Ding, M. Rahman, T. Zhang, C. T. Lim, and C.-W. Qiu, "Optical manipulation from the microscale to the nanoscale: fundamentals, advances and prospects," Light: Science & Applications 6(9), e17039 (2017).
3. P. Rodriguez-Sevilla, L. Labrador-Paez, D. Jaque, and P. Haro-Gonzalez, "Optical trapping for biosensing: materials and applications," Journal of Materials Chemistry B 5(46), 9085–9101 (2017).
4. D. G. Kotsifaki, S. N. Chormaic, "Plasmonic optical tweezers based on nanostructures: fundamentals, advances and prospects," Nanophotonics 8(7), 1227–1245 (2019).
5. R. Agarwal, K. Ladavac, Y. Roichman, G. H. Yu, C. M. Lieber, and D. G. Grier, "Manipulation and assembly of nanowires with holographic optical traps," Optics Express 13(22), 8906 (2005).
6. H. T. Li, D. J. Zhou, H. Browne, and D. Klenerman, "Evidence for Resonance Optical Trapping of Individual Fluorophore-Labeled Antibodies Using Single Molecule Fluorescence Spectroscopy," Journal of the American Chemical Society 128(17), 5711–5717 (2006).
7. J. R. Moffitt, Y. R. Chemla, S. B. Smith, and C. Bustamante, "Recent advances in optical tweezers," Annual Review of Biochemistry 77(1), 205–208 (2008).
8. F. M. Fazal, S. M. Block, "Optical tweezers study life under tension," Nature Photonics 5(6), 318–321 (2011).
9. A. Ashkin, J. M. Dziedzic, J. E. Bjorkholm, and S. Chu, "Observation of a single-beam gradient force optical trap for dielectric particles," Optics Letters 11(5), 288 (1986).
10. T. Shoji, Y. Tsuboi, "Plasmonic Optical Tweezers toward Molecular Manipulation: Tailoring Plasmonic Nanostructure, Light Source, and Resonant Trapping," The Journal of Physical Chemistry Letters 5(17), 2957–2967 (2014).
11. E. H. K. Stelzer, "Beyond the diffraction limit?" Nature 417(6891), 806–807 (2002).
12. A. Heifetz, S. Kong, A. Sahakian, A. Taflove, and V. Backman, "Photonic nanojets," Journal of Computational and Theoretical Nanoscience 6(9), 1979–1992 (2009).
13. B. Luk'yanchuk, R. Paniagua-Domínguez, I. V. Minin, O. V. Minin, and Z. Wang, "Refractive index less than two: photonic nanojets yesterday, today and tomorrow," Optical Materials Express 7(6), 1820–1847 (2017).
14. Z. Wang, B. Luk'yanchuk, L. Yue, R. Paniagua-Domínguez, B. Yan, J. Monks, O. V. Minin, I. V. Minin, S. Huang, and A. Fedyanin, "High order Fano resonances and giant magnetic fields in dielectric microspheres," Scientific Reports 9(1), 20293 (2019).

15. B. Wang, L. Shen, and S. He, "Superlens Formed by a One-dimensional Dielectric Photonic Crystal," Journal of the Optical Society of America B 25(3), 391–395 (2008).
16. I. V. Minin, O. V. Minin, Y. R. Triandaphilov, and V. V. Kotlyar, "Focusing properties of two types of diffractive photonic crystal lens," Optical Memory and Neural Networks 17(3), 244–248 (2008).
17. F. Gaufillet, E. Akmansoy, "Design and experimental evidence of a flat graded-index photonic crystal lens," Journal of Applied Physics 114(8), 083105 (2013).
18. I. V. Minin, O. V. Minin, N. Gagnon, and A. Petosa, "FDTD analysis of a flat diffractive optics with sub-Reyleigh limit resolution in MM/THz waveband," Proceeding of the Joint 31st International Conference on Infrared and Millimeter Waves and 14th International Conference on Terahertz Electronics, September 18–22, Shanghai, China (2006).
19. I. V. Minin, O. V. Minin, "3D diffractive lenses to overcome the 3D Abbe subwavelength diffraction," Chinese Optics Letters 12(6), 060014 (2014).
20. Y. Zhu, S. Zhou, Z. Wang, Y. Yu, W. Yuan, and W. Liu, "Investigation on Super-Resolution Focusing Performance of a TE-Polarized Nanoslit-Based Two-Dimensional Lens," Nanomaterials 10(1), 3 (2020).
21. K. R. Chen, "Focusing of light beyond the diffraction limit of half the wavelength," Optics Letters 35(22), 3763 (2010).
22. S. Ishii, A. V. Kildishev, V. M. Shalaev, and V. P. Drachev, "Controlling the wave focal structure of metallic nanoslit lenses with liquid crystals," Laser Physics Letters 8(11), 828–832 (2011).
23. R. G. Mote, O. V. Minin, and I. V. Minin, "Focusing behavior of 2-dimensional plasmonic conical zone plate," Optical and Quantum Electronics 49(8), 271 (2017).
24. L. Jin, Q. Y. Zhu, Y. Q. Fu, and W. X. Yu, "Flat lenses constructed by graded negative index-based photonic crystals with tuned configurations," Chinese Physics B 22(10), 104101 (2013).
25. Y. H. Li, Y. Q. Fu, O. V. Minin, and I. V. Minin, "Ultrasharp nanofocusing of graded index photonic crystalbased lenses perforated with optimized single defect," Optical Material Express, 6(8), 2628–2636 (2016).
26. Y. Cao, Z. Liu, O. V. Minin, and I. V. Minin, "Deep subwavelength-scale light focusing and confinement in nanohole-structured mesoscale dielectric spheres," Nanomaterials 9(2), 186 (2019).
27. T. Sakai, Y. Tanaka, Y. Nishizawa, M. Terakawa, and M. Obara, "Size parameter effect of dielectric small particle mediated nano-hole patterning on silicon wafer by femtosecond laser," Applied Physics A 99(1), 39–46 (2010).
28. J. R. Ong, H. S. Chu, V. H. Chen, A. Y. Zhu, and P. Genevet, "Freestanding dielectric nanohole array metasurface for mid-infrared wavelength applications," Optics Letters 42(13), 2639–2642 (2017).
29. Q. Wang, W. Han, Y. Wang, M. Lu, and L. Dong, "Tape nanolithography: a rapid and simple method for fabricating flexible, wearable nanophotonic devices," Microsystems & Nanoengineering 4(1), 31 (2018).
30. I. V. Minin, O. V. Minin, Y. Cao, Z. Liu, Y. Geints, and A. Karabchevsky, "Optical vacuum cleaner by optomechanical manipulation of nanoparticles using nanostructured mesoscale dielectric cuboid," Scientific Reports 9(1), 12748 (2019)
31. C.-S. Wang, Y. Otani, "Removal of nanoparticles from gas streams by fibrous filters: a review," Industrial & Engineering Chemistry Research 52(1), 5–17 (2013).
32. D. Erickson, X. Serey, Y. F. Chen, and S. Mandal, "Nanomanipulation using near field photonics," Lab on a Chip 11(6), 995 (2011).
33. I. V. Minin, O. V. Minin, Diffractive Optics and Nanophotonics: Resolution Below the Diffraction Limit, Springer, Cham (2016).
34. L. Yue, O. V. Minin, Z. Wang, J. Monks, A. Shalin, and I. V. Minin, "Photonic hook: a new curved light beam," Optics Letters 43(4), 771–774 (2018).
35. A. Ang, A. Karabchevsky, I. V. Minin, O. V. Minin, S. Sukhov, and A. Shalin, "Photonic Hook based optomechanical nanoparticle manipulator," Scientific Reports 8(1), 2029 (2018).
36. I. V. Minin, O. V. Minin, G. Katyba, N. Chernomyrdin, V. Kurlov, K. Zaytsev, L. Yue, Z. Wang, and D. Christodoulides, "Experimental observation of a photonic hook," Applied Physics Letters 114(3), 031105 (2019).
37. K. Dholakia, G. Bruce, "Optical hooks," Nature Photonics 13(4), 229–230 (2019).
38. I. V. Minin, O. V. Minin, D. S. Ponomarev, and I. A. Glinskiy, "Photonic hook plasmons: a new curved surface wave," Annalen der Physik 530(12), 1800359 (2018).
39. C. Rubio, D. Tarrazó-Serrano, O. V. Minin, A. Uris, and I. V. Minin, "Acoustical hooks: a new subwavelength self-bending beam," Results in Physics 16, 102921 (2020)
40. E. Xing, H. Gao, J. Rong, S. Khew, H. Liu, C. Tong, and M. Hong, "Dynamically tunable multi-lobe laser generation via multifocal curved beam," Optics Express 26(23), 30944–30951 (2018).
41. J. Yang, P. Twardowski, P. Gérard, Y. Duo, J. Fontaine, and S. Lecler, "Ultra-narrow photonic nanojets through a glass cuboid embedded in a dielectric cylinder," Optics Express 26(4), 3723–3731 (2018).
42. Y. Huang, Z. Zhen, Y. Shen, C. Min, and G. Veronis, "Optimization of photonic nanojets generated by multilayer microcylinders with a genetic algorithm," Optics Express 27(2), 1310–1325 (2019).

43. I. V. Minin, O. V. Minin, "Subwavelength self-bending structured light beams," Proceeding of the Fourth Russian-Belarusian Workshop "Carbon nanostructures and their electromagnetic properties", April 21–24, Tomsk, 52–57 (2019).
44. I. V. Minin, O. V. Minin, "Dielectric particle-based strategy to design a new self-bending subwavelength structured light beams," Proceedings of the 14th International Forum on Strategic Technology (IFOST 2019), October 14–17, TPU Publishing House, Tomsk (2019).
45. G. Gu, L. Shao, J. Song, J. Qu, K. Zheng, X. Shen, Z. Peng, J. Hu, X. Chen, M. Chen, and Q. Wu, "Photonic hooks from Janus microcylinders," Optic Express 27(26), 37771–37780 (2019).
46. X. Shen, G. Gu, L. Shao, Z. Peng, J. Hu, S. Bandyopadhyay, Y. Liu, J. Jiang, and M. Chen, "Twin photonic hook generated by twin-ellipse microcylinder," IEEE Photonics Journal 12(3), 1–9 (2020).
47. X. Ma, Y. Guo, M. Pu, J.J. Jin, P. Gao, X. Li, and X. Luo, "Tunable Optical Hooks in the Visible Band Based on Ultra-Thin Metalenses," Annalen der Physik 532(1), 1900396 (2019).
48. X. Cui, D. Erni, and C. Hafner, "Optical forces on metallic nanoparticles induced by a photonic nanojet," Optics Express 16(18), 13560–13568 (2008).
49. A. S. Ang, I. V. Minin, O. V. Minin, S. V. Sukhov, A. Shalin, and A. Karabchevsky, "Low-contrast photonic hook manipulator for cellular differentiation," Proceeding of the the 9th International conference on Metamaterials, Photonic crystals and Plasmonics, June 24–July 1, Marseille, France (2018).
50. H. Wang, X. Wu, and D. Shen, "Trapping and manipulating nanoparticles in photonic nanojets," Optics Letters 41(7), 1652 (2016).
51. I. V. Minin, O. V. Minin, V. Pacheco-Peña, and M. Beruete, "Subwavelength, standing-wave optical trap based on photonic jets," Quantum Electronics 46(6), 555–557 (2016).
52. V. Yannopapas, "Photonic nanojets as three-dimensional optical atom traps: a theoretical study," Optics Communications 285(12), 2952–2955 (2012).
53. Y.-C. Li, H.-B. Xin, H.-X. Lei, L.-L. Liu, Y.-Z. Li, Y. Zhang, and B.-J. Li, "Manipulation and detection of single nanoparticles and biomolecules by a photonic nanojet," Light: Science & Applications 5(12), e16176 (2016).
54. Y. Li, H. Xin, X. Liu, Y. Zhang, H. Lei, and B. Li, "Trapping and Detection of Nanoparticles and Cells Using a Parallel Photonic Nanojet Array," ACS Nano 10(6), 5800–5808 (2016).
55. M. Padgett, R. Bowman, "Tweezers with a twist," Nature Photonics 5(6), 343–348 (2011).
56. A. Ashkin, "Acceleration of trapping of particles by radiation pressure," Physical Review Letters 24(4), 156–159 (1970).
57. W. G. Cheong, W. M. Lee, X.-C. Yuan, L.-S. Zhang, K. Dholakia, and H. Wang, "Direct electron-beam writing of continuous spiral phase plates in negative resist with high power efficiency for optical manipulation," Applied Physics Letters 85(23), 5784–5786 (2004).
58. A. Vijayakumar, C. Rosales-Guzmán, M. R. Rai, J. Rosen, O. V. Minin, I. V. Minin, and A. Forbes, "Generation of structured light by multilevel orbital angular momentum holograms," Optics Express, 27(5), 5459 (2019).
59. B. Vinoth, A. Vijayakumar, M. Ratnam Rai, J. Rosen, C.-J. Cheng, O. V. Minin, and I. V. Minin, "Binary square axicon with chiral focusing properties for optical trapping," Optical Engineering 59(4), 041204 (2019).
60. A. Vijayakumar, B. Vinoth, I. V. Minin, J. Rosen, O. V. Minin, and C.-J. Cheng, "Experimental demonstration of square Fresnel zone plate with chiral side lobes," Applied Optics 56(13), F128–F133 (2017).
61. I. V. Minin, O. V. Minin, A. Petosa, and S. Thirakoune, "Improved zoning rule for designing square Fresnel zone plate lenses," Microwave and Optical Technology Letters 49(2), 276–278 (2007).
62. I. V. Minin, O. V. Minin, N. Gagnon, and A. Petosa, "Investigation of the resolution of phase correcting Fresnel lenses with small values of F/D and subwavelength focus," Computer optics 30, 65–68 (2006).
63. I. V. Minin, O. V. Minin, "Experimental verification 3D subwavelength resolution beyond the diffraction limit with zone plate in millimeter wave," Microwave and Optical Technology Letters 56(10), 2436–2439 (2014).
64. I. V. Minin, O. V. Minin, E. Danilov, and G. Lbov, "Parameters optimization algorithm of a new type of diffraction optics elements," Proceedings of 5th IEEE-Russia Conference MEMIA, December 13–15, Novosibirsk, Russia, 177–185 (2005).
65. A. Vijayakumar, M. R. Rai, J. Rosen, B. Vinoth, C.-J. Cheng, O. V. Minin, and I. V. Minin, "Diffractive optical elements with chiral-focusing properties for optical-trapping applications," Chapter in Frontier Research and Innovation in Optoelectronics Technology and Industry, K. Habib and E. Lewis (eds.), Tailor and Francis, London, 461–465 (2019).
66. A. Rohrbach, E. H. K. Stelzer, "Optical trapping of dielectric particles in arbitrary fields," Journal of the Optical Society of America A 18(4), 839–882 (2001).
67. J. Arlt, V. Garces-Chavez, W. Sibbett, and K. Dholakia, "Optical micromanipulation using Bessel light beam," Optics Communications 197(4-6), 239–245 (2001).
68. J. Ng, Z. Lin, and C. T. Chan, "Theory of Optical Trapping by an Optical Vortex Beam," Physical Review Letters 104(10), 103601 (2010).
69. J. Guan, J. Lin, Y. Ma, J. Tan, and P. Jin, "A subwavelength spot and a three-dimensional optical trap formed by a single planar element with azimuthal light," Scientific Reports 7(1), 7380 (2017).

70. O. V. Minin, I. V.Minin, and N. Kharitoshin, "Microcubes Aided Photonic Jet Scalpel Tips for Potential Use in Ultraprecise Laser Surgery," Proceeding of 2015 International Conference on Biomedical Engineering and Computational Technologies (SIBIRCON), October 28–30, Novosibirsk, Russia, 18–21 (2015).
71. X. Tang, Y. Zhang, W. Su, Y. Zhang, Z. Liu, X. Yang, J. Zhang, J, Yang, and L. Yuan, "Super-low-power optical trapping of a single nanoparticle," Optics Letters 44(21), 5165 (2019).
72. A. Asadollahbaik, S. Thiele, K. Weber, A. Kumar, J. Drozella, F. Sterl, A. M. Herkommer, H. Giessen, and J. Fick, "Highly Efficient Dual-Fiber Optical Trapping with 3D Printed Diffractive Fresnel Lenses," ACS Photonics 7(1), 88–97 (2020).
73. R.S. Rodrigues Ribeiro, P. Dahal, A. Guerreiro, P. A. S. Jorge, and J. Viegas, "Fabrication of Fresnel plates on optical fibres by FIB milling for optical trapping, manipulation and detection of single cells," Scientific Reports 7**,** 4485 (2017).
74. L. Ma, J. Guan, Y. Wang, C. Chen, J. Zhang, J. Lin, J. Tan, and P. Jin. "Diffraction-limited axial double foci and optical traps generated by optimization-free planar lens," Nanophotonics 9(4), 841–853 (2020).

Raman Spectroscopy of Hemoglobin and Dielectrophoresis of Erythrocytes in the Diagnosis of the Resistant Arterial Hypertension

Margarita V. Kruchinina[1], Andrey A. Gromov[1], Vladimir N. Kruchinin[2*], Vladimir A. Volodin[2], and Vladimir M. Generalov[3]

[1] Research Institute of Internal and Preventive Medicine – Branch of the Institute of Cytology and Genetics, Siberian Branch of the Russian Academy of Sciences, 175/1 Bogatkova Str., Novosibirsk 630089, Russia

[2] Rzhanov Institute of Semiconductor Physics, SB RAS, 13 Lavrentieva Ave., Novosibirsk 630090, Russia

[3] Federal Budgetary Research Institution "State Research Center of Virology and Biotechnology "Vector", Federal Service for Surveillance on Consumer Rights Protection and Human Well-being, Novosibirsk Region, Koltsovo 630559, Russia

***e-mail:** vladd.kruch@yandex.ru

Abstract. The research aim is to study the associations of changes in the content of hemoglobin complexes by the Raman spectroscopy with electrical and viscoelastic parameters of erythrocytes (using the dielectrophoresis method) among patients with arterial hypertension (AH) (including resistant AH), to evaluate the possibility of using these parameters for diagnostic purposes. Fifty males (54 ± 6 years) with stage 2 of AH have been examined, 24 of them have showed resistant AH. We have determined a significant decrease in the level of hemoglobin-ligand complexes, Hb-NO (II) complexes in patients with resistant AH compared to those among patients with controlled AH and among healthy patients ($p < 0.001 – 0.05$). We have found correlations between intensities of the most important signals of hemoglobin Raman spectra (1325, 1350, 1550, 1580, 1660, 1668 cm^{-1}) and electric and viscoelastic parameters of erythrocytes (amplitude of erythrocytes deformation, summarized indicators of viscosity and rigidity, the magnitude of the dipole moment, polarizability at the frequency 106 Hz, electrical conductivity, index of destruction), the intensity of which had been the biggest one for resistant AH. It has been shown that the combined use of two methods (Raman spectroscopy of hemoglobin and electrical and the studies of erythrocytes by the dielectrophoresis method) allowed to increase the diagnostic accuracy to detect the resistant arterial hypertension up to 88%, sensitivity up to 84.6%, specificity up to 91.7% compared to the data of the combined clinical and instrumental methods of research. The capability of this combination approach exceeds the capabilities of the methods separately. © 2020 Journal of Biomedical Photonics & Engineering.

Keywords: resistant arterial hypertension; diagnostics; Raman spectroscopy; dielectrophoresis; erythrocytes; hemoglobin.

Paper #3352 received 22 Feb 2020; revised manuscript received 8 Mar 2020; accepted for publication 27 Mar 2020; published online 21 Jun 2020. doi: 10.18287/JBPE20.06.020302.

1 Introduction

Diagnostic issues and therapeutic tactics for patients with resistant arterial hypertension (RAH) are very relevant due to its high prevalence (it ranges 3 to 24% among patients receiving antihypertensive therapy [1, 2]), an ambiguity of the mechanisms of refractoriness appearance [3], the role of various factors, such as

endothelium [4], regulatory cytokines, immunological components, blood cells that affect the development of the RAH.

One of the possible pathogenetic factors influencing the development of RAH is a violation of the bioavailability of nitrogen oxide (NO) produced by erythrocytes [5]. There are three main sources of NO in the body, two of which are associated with erythrocytes: there are S-Nitrosothiols of hemoglobin and NO produced by hemoglobin nitrite reductase [6]. The role of erythrocytes as a participant of the vasoregulation is connected with both a direct "liberation" of NO and stimulation of nitrogen oxide liberation by the endothelium through ATP synthesis by involving erythrocytes. The ATP release from erythrocytes occurs in response to their mechanical deformation: declining plasticity of erythrocytes leads to a decrease in ATP levels, and, consequently, to a decrease in the NO synthesis. The aspect of the interplay between erythrocytes and NO for patients with RAH is very promising in terms of existing possibilities to intervene in NO metabolism [7–9].

Modern approaches of the diagnosis of RAH imply the use of a whole set of studies to exclude a pseudo-resistant AH, as well as the factors contributing to resistance of antihypertensive therapy, secondary AH, associated clinical conditions (metabolic syndrome, obesity, smoking, alcohol), genetic characteristics [2, 10]. However, if the resistance persists after the exclusion of the factors described above, possible pathogenetic disorders come to the fore, including the effect of nitrogen oxide levels [11].

Previous pilot studies to identify pathogenetic features of the RAH have proved the promising approach, associated with the assessment of the NO-hemoglobin complexes level for the diagnosis of this pathology [12–14]. At the same time, we have received information about a close association of electrical and viscoelastic parameters of erythrocytes with the development of resistant hypertension [15].

The hypothesis of the present study was the assumption of a possible association of altered levels of hemoglobin complexes with electrical and viscoelastic parameters of erythrocytes that can be used for diagnostic purposes for patients with AH.

This fact has determined our choice of research methods. To determine the content of the NO-hemoglobin complexes of erythrocytes for patients with AH, a modern physical and chemical research method of biological media, namely the coherent Raman scattering spectroscopy (Raman spectroscopy), was used. This method has all the advantages of optical methods that are important for the study of biological objects (high sensitivity, non-destructive nature of impact on biological objects, lack of complex sample preparation) and it has been successfully used for various studies [16, 17].

The study of electrical and viscoelastic parameters of erythrocytes has been performed by the dielectrophoresis method in an non-uniform alternating electric field (NUAEF), which demonstrated high efficiency in the diagnosis of diffuse liver disease, cardiovascular diseases, and cancer processes, being of non-invasive, informative, and low-cost nature [18–23].

Research aim is to identify the dependence of the content of hemoglobin complexes (Raman spectroscopy) on the electrical and viscoelastic parameters of the erythrocytes (dielectrophoresis) for the patients with AH, including the resistant one, and to evaluate the possibility of applying the results for diagnostic purposes.

2 Materials and methods

Fifty males (54 ± 6 years) with 2 AH stage have been examined, 24 of them showed RAH [10]. We have analyzed patients with controlled hypertension (26 persons – group 1) and resistant hypertension (24 persons – group 2) separately. The comparison group consisted of 25 males of comparable age (52 ± 7 years) without hypertension and any other manifesting pathology of internal organs. Criteria for inclusion in the study were as follows: 1) males 40–60 years old with or without stage II of hypertension; 2) signing an informed consent to participate in the study.

The survey was performed with the approval of the Biomedical Ethics Committee of the Research Institute of Internal and Preventive Medicine (session of 15.01.2017).

The patients have undergone a comprehensive clinical, instrumental and laboratory examination, including electrocardiography, heart ultrasound, computed tomography, and electroencephalography.

According to the office measurement, the average blood pressure (BP) of the patients with RAH was 174/100 ± 13/9 mm Hg; the Apnea–Hypopnea Index (AHI) – 63.8 ± 3.6; BMI – 37.5 ± 7.2 kg/m^2. All patients with RAH received multicomponent antihypertensive therapy, including angiotensin-converting enzyme inhibitors, aldosterone receptor antagonists, diuretics, beta-adrenergic blocking agents, calcium antagonists, and centrally acting antihypertensive drugs in maximum or maximum tolerated doses. Patients with RAH had the higher levels of clinically measured systolic and diastolic BP, AHI, longer duration of AH as compared to patients with controlled AH. (12.9 ± 4.8 years vs 5.8 ± 2.5 years, $p < 0.01$) (BP – 141.2/92.4 ± 7.1/4.7 mm Hg; AHI – 28.5 ± 4.2 $p < 0.01$–0.05 in patients with controlled BP, respectively).

The risk stratification of patients with hypertension is presented in Table 1. It shows that in a group of patients with RAH there are no patients with low additional risk, more often there are a high additional risk ($p < 0.01$).

Table 1 Risk stratification for patients with AH.

Additional risk	1st group (controlled AH), n = 26	2nd group (RAH), n = 24
Low, n	2 (no RF)	0
Average, n	16 (1 to 2 RFs)	5 (1 to 2 RFs)*
High, n	8 (3 or more RFs, TODs, MSs or DMs)	19 (3 or more RFs, TODs, MSs or DMs)*

RF – risk factors, TOD – target organ damage, MS – metabolic syndrome, DM – diabetes mellitus;
* Statistically significant result between groups is $p < 0.01$.

Blood samples were obtained on an empty stomach from the ulnar vein using standard single-use sterile vacuum tubes with anticoagulant (citrate buffer of 3.7% in a ratio of 9:1). In groups of patients with AH, as well as among males of the comparison group, the levels of hemoglobin complexes (deoxyhemoglobin (d-Hb), oxyhemoglobin (ox-Hb), hemoglobin complexes with nitrogen oxide (Hb-NO (I, II)) in its aqueous solutions were studied by Raman spectroscopy using a T64000 spectrometer (Horiba Jobin Yvon) with a triple monochromator. Preparation of hemoglobin solutions, conditions and sequence of measurements are described in Ref. [14].

The study of electrical and viscoelastic parameters of erythrocytes was performed by the dielectrophoresis method in an NUAEF using an automated specialized installation [19]. We evaluated the electrical conductivity of membranes, indices of aggregation and destruction of erythrocytes, the capacity of the cell membranes, the velocity of erythrocytes to the electrodes, the position of the crossover frequency, the amplitude of deformation of erythrocytes, polarizability of cells, summarized indices of viscosity and rigidity, the magnitude of induced dipole moment. The original CELLFIND software package was used for computer data processing. The error of the method assay reproducibility is equal to 7–12%.

Statistical data processing was performed using the software SPSS ver. 17. The distribution of quantitative characteristics was determined by the Kolmogorov-Smirnov test. In the case of a normal distribution, the average value (M) and the standard error of the mean (m) were calculated. The significance of the difference values was assessed by the Student's and Pearson's criteria (in a normal distribution), and nonparametric tests (Mann-Whitney U-test, Kolmogorov-Smirnov test) were used in cases of deviation from the normal distribution. The criterion χ^2 was used for evaluating qualitative features. The relationships between features were evaluated using the partial correlation analysis. In all statistical analysis procedures, the critical significance level of the null hypothesis (p) was assumed to be equal to 0.05. To assess the significance of the parameters of Raman spectroscopy and dielectrophoresis in terms of differential diagnosis of controlled and resistant hypertension, ROC analysis was used with the construction of characteristic curves (ROC curves).

3 Results and discussion

The Fig. 1 shows a typical spectrum of an aqueous hemoglobin solution obtained using the Raman spectroscopy. It allows one to evaluate changes in porphyrin conformation and levels of hemoglobin complexes (d-Hb, ox-Hb, and Hb-NO) [24]. The literature suggests that the ratio of Raman spectrum peaks I_{1355} / I_{1564} indicates the ability of deoxyhemoglobin (d-Hb) to bind O_2 and NO; the complex with nitrogen oxide without breaking the connection between the protein and hemoporphyrin was estimated by the ratio of peaks I_{1626} / I_{1580}. The Hb complex with nitrogen oxide should regulate the ability of Hb to release O_2 (I_{1668} / I_{1580}) when the protein-hemoporphyrin bond is broken. The peaks I, III correspond to the vibrational frequencies of deoxyhemoglobin molecules; peaks II, IV – of oxyhemoglobin molecules; peaks V, VI – comply with the vibrational frequencies of NO molecules associated with hemoglobin; the ratio (II/III) / (II/IV) reflects the affinity of hemoglobin to O_2.

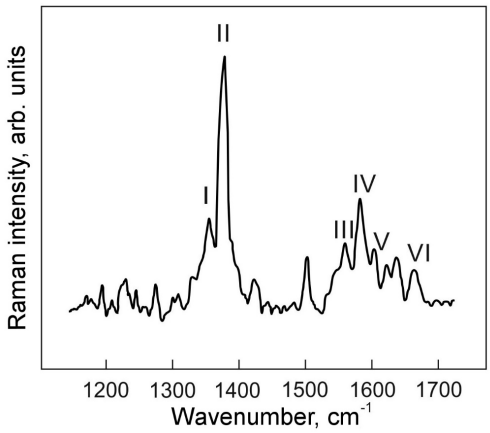


Fig. 1 A typical Raman spectrum of an aqueous hemoglobin solution. I, III – vibrational frequencies of deoxyhemoglobin molecules; II, IV – oxyhemoglobin molecules; V, VI – vibrational frequencies of NO molecules associated with hemoglobin; the ratio (II/III) / (II/IV) reflects the affinity of hemoglobin to O_2 [24].

The hemoglobin complex with nitrogen oxide (Hb-NO) regulates the ability of hemoglobin to release the oxygen when the bond between protein and hemoporphyrin was broken, that is measured by the ratio of Raman peaks I_{1680} / I_{1580}. We determined a

significant decrease in the level of hemoglobin-ligand complexes, Hb-NO (II) complexes in patients with RAH compared to those among patients with controlled AH and among healthy patients ($p < 0.001–0.05$), that probably reflects the reduced reserves of erythrocytic NO and a decrease in O_2 release (Fig. 2). The ratio of signals I_{1680} / I_{1580} in cases of resistant hypertension was the lowest in comparison with that in controlled hypertension and in the comparison group (0.36 ± 0.07 vs 0.45 ± 0.08 in controlled hypertension, $p < 0.01$ and 0.56 ± 0.09 under control, $p < 0.001$), reflecting a decrease in the ability of hemoglobin to give oxygen in RAH. Rodnenkov O. V. et al. [24] have observed a decrease in the level of Hb-NO complexes in cases of coronary heart disease (CHD), hypertension, and circulatory insufficiency. The researchers had explained achieved result by increasing hypoxia in these pathologies; on the contrary, in cases of mountain sickness (hypoxia), an increase in the content of ox-Hb and Hb-NO (II) complexes was observed that increases the exchange of O_2 and probably has a compensatory character.

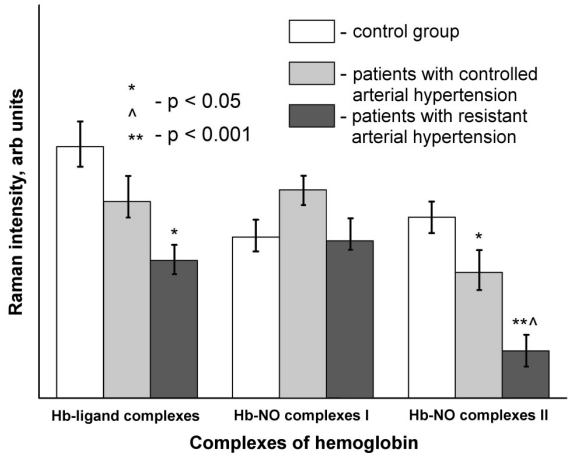


Fig. 2 Hemoglobin complexes levels according to the Raman spectroscopy among patients with RAH, controlled AH, and individuals in the comparison group. Statistically significant results: * – control group: * $p < 0.05$, ** $p < 0.001$; ^ patients with controlled AH: $p < 0.05$.

An insufficiency of the NO production system leading to endothelial dysfunction is to be considered as one of the renal mechanisms of RAH development. During the experiment, it was found that NO-synthase inhibitors were caused systemic and glomerular hypertension, glomerular ischemia, tubulointerstitial injury, and proteinuria. We obtained evidence for the relationship between the decrease in total NO production and renal damage for patients having AH. The NO deficiency develops as a result of an oxidative stress due to inactivation of nitrogen oxide by superoxide anions and due to an exposure to an unpaired NO synthase, resulting in superoxides being produced to a greater extent than NO [25].

Thus, the intra-erythrocyte NO reserves for patients with RAH are reduced and followed by a decrease in the vasodilating NO effects at the microcirculatory level. On the other hand, there are studies that suggest that the levels of NO or NO metabolites in the erythrocytes can directly affect the ability of this cell to release the ATP [6, 7].

A revealed decrease in intra-erythrocyte reserves of nitrogen oxide, and a decrease in its bioavailability associated with changes in the level and composition of intracellular macroergic compounds, viscoelastic parameters of the erythrocytes are probably the pathogenetic factors for the development of resistant hypertension and targets for therapeutic effects.

The study of electrical and viscoelastic parameters of erythrocytes revealed significant differences between groups of patients with controlled and resistant AH. Red cells of patients with controlled AH after conversion to sucrose solution were predominantly discocytic, $22 \pm 4\%$ of the cells acquired the form of a “deflated ball” or spherocytic. The level of non-discocytic forms among patients with RAH increased to $47 \pm 5\%$ ($p < 0.001$), in addition, about a third of the discocytes became spiked. To ensure the integrity of the membrane and the biconcave shape of the erythrocytes, the macroergs’ energy shall be of great importance [26]. Energy support for intracellular homeostasis (and, above all, ion) in erythrocytes is provided by the ATP formed during glycolysis, which is the main way of energy exchange in the erythrocytes [27]. The ATP depletion in erythrocytes leads to a number of disorders; including the interlocking the ionic pumps and changing the ion balance in the medium-cell system. This helps to reduce the ratio of surface area to erythrocytes’ volume and the transformation of cells into hard-to-form spheres, the appearance of spiked processes that complicates the transport of oxygen from the erythrocytes to tissues and exacerbates hypoxia It stimulates the phenomenon of fibrogenesis, leading to internal remodeling of vessel walls [28, 29].

In the group of patients with RAH the levels of electrical conductivity, summarized rigidity, viscosity, aggregation and destruction indices have increased, and the amplitude of cell deformation, polarizability of membranes at a frequency of 10^6 Hz, the speed of cell movement to the electrodes, the dipole moment, and the electrical capacity of erythrocyte membranes have reliably decreased ($p < 0.001–0.05$) compared with the control group and patients with controlled AH (Table 2). Inverse correlations of AH resistance with the strain amplitude ($r = 0.675$, $p = 0.03$) were obtained, as well as direct correlations with summarized parameters of rigidity ($r = 0.527$, $p < 0.001$) and erythrocyte viscosity ($r = 0.493$, $p = 0.005$).

Table 2 Electrical and viscoelastic parameters of the erythrocytes among patients with arterial hypertension (controlled and resistant) and in the comparison group (M ± m).

Viscoelastic and electrical properties of erythrocytes	**Group I of comparison n=25**	**Group II controlled AH, n=26**	**Group III resistant AH, n=24**
The amplitude of Er deformation [m]	$2.7\times10^{-6} \pm 0.6\times10^{-6}$	$0.81\times10^{-6} \pm 0.4\times10^{-6}$ *	$0.62\times10^{-6} \pm 0.22\times10^{-6}$ **^^^
Summarized rigidity [N/m]	$4.4\times10^{-6} \pm 0.6\times10^{-6}$	$6.1\times10^{-6} \pm 0.7\times10^{-7}$*	$8.0\times10^{-6} \pm 0.5\times10^{-7}$ *^^^
Summarized viscosity [Pa · sec]	0.31 ± 0.04	0.58 ± 0.11*	0.75 ± 0.09*^^^
Index of Er aggregation [relative un.]	0.43 ± 0.02	0.66 ± 0.1*	0.82 ± 0.03*^^^
Index of Er destruction [%]	1.07 ± 0.69	5.7 ± 0.5***	8.2 ± 0.3***^^^
Polarization at frequency of 10^6 Hz [m^3]	$5.8\times10^{-15} \pm 0.8\times10^{-15}$	$0.71\times10^{-15} \pm 0.6\times10^{-15}$*	$0.52\times10^{-15} \pm 0.5\times10^{-16}$ ***^^^
Electrical conductivity [Cm/m]	$2.8\times10^{-5} \pm 0.3\times10^{-5}$	$6.1\times10^{-5} \pm 0.4\times10^{-5}$**	$7.3\times10^{-5} \pm 0.1\times10^{-5}$ ***^^^
Cellular membrane capacity [F]	$7.2\times10^{-14} \pm 0.2\times10^{-14}$	$5.1\times10^{-14} \pm 0.4\times10^{-14}$**	$3.9\times10^{-14} \pm 0.2\times10^{-14}$ ***^^^
Velocity of Er motion, [mcm/sec]	13.9 ± 2.5	7.9 ± 2.4	5.4 ± 1.8*^^
Position of crossover frequency [Hz]	$4.7\times10^{5} \pm 0.4\times10^{5}$	$6.2\times10^{5} \pm 0.2\times10^{5}$**	$7.1\times10^{5} \pm 0.3\times10^{5}$ **^^^
Dipole moment [Kl·m]	$1.5\times10^{-21} \pm 0.4\times10^{-21}$	$0.52\times10^{-21} \pm 0.08\times10^{-21}$*	$0.29\times10^{-21} \pm 0.07\times10^{-21}$ *^^

M stands for mean values, m stands for mean error,
* – statistical significance (p) of differences from Group I (* $p < 0.05$, ** $p < 0.02$, *** $p < 0.001$);
^ – statistical significance (p) of differences from Group II (^ $p < 0.05$, ^^ $p < 0.02$, ^^^ $p < 0.0001$);
Dipole moment was calculated at electric field tension of $8.85\cdot10^{-12}$ F/m.

A deterioration of the deformability of the erythrocytes causes a development of stagnation in the microcirculatory bloodstream and, as a consequence, an occurrence of tissue hypoxia [30]. In experiments on an isolated rabbit lung, it was shown that the plasticity of the erythrocytes may affect the blood pressure value in it and the pulmonary oxygen diffusion coefficient [31]. The deformability of the erythrocytes due to an increased convection of their contents is more conducive to oxygen transport than facilitated diffusion [32].

It has been suggested that there should be a unique mechanism for controlling the resistance of pulmonary vessels, according to which the ATP release from the erythrocytes occurs in response to their mechanical deformation, causing stimulation of the synthesis of a NO vasodilator [33].

When identifying associations between the electrical and viscoelastic parameters of erythrocytes and hemoglobin complexes, the most significant correlations were found in the group of patients with resistant AH (Table 3).

It has been found that the closest and most reliable correlations was established between the intensity of peaks reflecting the levels of hemoglobin complexes with nitrogen oxide, and the amplitude of deformation and summarized indicators of viscosity and rigidity. Moreover, the latter association was the strongest one that is probably possible due to the fact that the value of this indicator depends on both the properties of the erythrocyte membrane and its internal content – hemoglobin. The summarized viscosity index is determined by the degree of friction between different cell layers, i.e. it depends on the properties of the entire cell volume [19].

The correlations revealed are obviously not random. It was shown that erythrocytes react with NO synthesized and delivered from the endothelial cells [34]. At the same time, it was found that the erythrocytes have their own NO-synthase for the

Table 3 Correlations between the levels of the coherent Raman scattering peaks of hemoglobin complexes and the values of electrical and viscoelastic parameters of erythrocyte among patients with resistant arterial hypertension.

The position of the peak [cm^{-1}]	The amplitude of Er deformation [m]	Summarized rigidity [N/m]	Summarized viscosity [Pa × sec]	Polarization at frequency of 10^6 Hz [m^3]	Index of Er destruction [%]	Electrical conductivity [Cm/m]	Dipole moment [Kl·m]
1325 (I)	0.312 (0.03)	-0.243 (0.001)	-0.215 (0.05)	0.181 (0.014)	-0.217 (0.03)	-0.169 (0.002)	0.232 (0.002)
1350 (II)	0.401 (0.001)	-0.415 (0.008)	-0.397 (0.043)	0.298 (0.003)	- 0.413 (0.009)	- 0.314 (0.033)	0.362 (0.05)
1550 (III)	0.284 (0.04)	-0.118 (0.008)	-0.239 (0.001)	0.211 (0.023)	-0.262 (0.017)	-0.218 (0.006)	0.301 (0.009)
1580 (IV)	0.378 (0.001)	-0.412 (0.007)	-0.349 (0.004)	0.409 (0.01)	-0.362 (0.04)	-0.422 (0.001)	0.437 (0.05)
1610 (V)	0.435 (0.01)	-0.463 (0.001)	- 0.417 (0.003)	0.354 (0.016)	- 0.330 (0.056)	-0.397 (0.04)	0.428 (0.033)
1680 (VI)	0.571 (0.0001)	-0.610 (0.0001)	-0.466 (0.0001)	0.411 (0.004)	-0.367 (0.05)	-0.429 (0.038)	0.503 (0.008)
I_{1680} / I_{1580}	0.537 (0.007)	-0.560 (0.004)	-0.447 (0.002)	0.463 (0.006)	-0.419 (0.003)	-0.407 (0.005)	0.471 (0.02)

The numbers in brackets in the first column correspond to the main signals of hemoglobin forms and its complexes as indicated in Fig. 1.
The confidence level of the association is indicated in parentheses.

Table 4 Results of the combined assessment of the Raman signals for aqueous solutions of hemoglobin, electrical, viscoelastic parameters of the erythrocytes among patients with AH for detecting resistant and controlled forms of the disease in comparison with the data of combined clinical and instrumental research methods.

Results of a combined study of Raman spectra for aqueous solutions of hemoglobin, electrical, viscoelastic parameters of erythrocytes	Results of clinical and instrumental research methods	
	The group with controlled AH n = 26 cases	The group with resistant AH n = 24 cases
The group with controlled AH n = 24 cases	**True positive** The group with controlled AH n = 22	**False positive** The group with resistant AH n = 2
The group with resistant AH n = 26 cases	**False negative** The group with controlled AH n = 4	**True negative** The group with resistant AH n = 22

Below are calculations of the main characteristics of the method according to Greenhalgh T. [24].

Sensitivity	22 / (22 + 4) × 100% = 84.6%
Specificity	22 / (22 + 2) × 100% = 91.7%
Prognostic value of positive method results	22 / (22 + 2) × 100% = 91.7%
Prognostic value of negative method results	22 / (22 + 4) × 100% = 84.6%
Accuracy index	(22 + 22) / (22 +2 + 22 + 4) × 100 % = 88%

synthesis of their own NO but this process is implemented with a sufficient degree of deformability of the erythrocytes [35]. Based on these data, the plastic erythrocytes are a powerful endogenous source of NO. Therefore, the erythrocytes with reduced deformability and low reserves of intra-erythrocyte NO do not provide sufficient levels of extracellular nitrogen oxide with subsequent vasodilation. Therefore, peripheral resistance will increase, leading to an increase in BP, that is a pathogenetic basis for the development of resistant AH.

It should be noted that the levels of deoxyhemoglobin, oxyhemoglobin, and hemoglobin complexes with NO were significant for the indicator of cell polarizability that reflects the degree of their viability. Reduced intra-erythrocyte reserves of

hemoglobin complexes affect the resistance of the erythrocytes as a likely manifestation of decompensation in RAH, determining a decline of this resistance. This results in excessive hemolysis of the erythrocytes that probably explains the correlation of the destruction index with the peak intensities of hemoglobin compounds. On the other hand, the changed levels of hemoglobin forms and its complexes may affect the mechanisms of their transformations related to the state of cell membranes. Indirectly, this is evidenced by correlations of erythrocyte compounds with the level of electrical conductivity of cell membranes and the value of the dipole moment reflecting the electric charge of the cell [18, 19]. It should be noted that the ratio of Raman signals I_{1680}/I_{1580}, reflecting the ability of hemoglobin to give oxygen, was directly related to the ability of the erythrocytes to be deformed. At the same time, this ratio was correlated with parameters that reflect the charge of cells – the dipole moment, the degree of cell viability – polarizability and the index of destruction. The resulting associations are obviously one of the factors that lead to an increase in tissue hypoxia for patients with RAH [2].

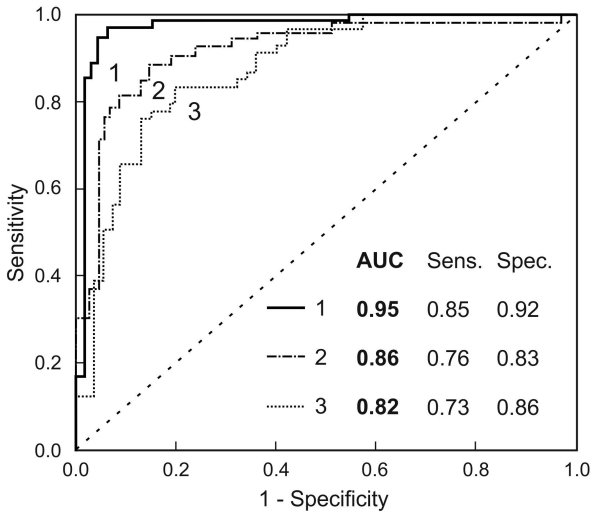


Fig. 3 ROC-curves of signal intensities of Raman spectra of aqueous solutions of hemoglobin, electrical and viscoelastic parameters of erythrocytes for differential diagnosis of resistant and controlled AH. 1 – a ROC-curve when using Raman spectroscopy and dielectrophoresis combined; 2 – a ROC-curve for Raman spectroscopy; 3 – a ROC-curve for erythrocyte dielectrophoresis.

To evaluate the significance of the peak intensities of the Raman spectra for hemoglobin solutions, electrical and viscoelastic parameters of the erythrocytes in terms of differential diagnosis of resistant and controlled hypertension, the ROC analysis has been used by means of the construction of receiving characteristic curves (ROC curves), the results of which are presented in Fig. 3. During the analysis, the first model has been formed from the peak intensities of the coherent Raman scattering spectrum of hemoglobin, the second one from a set of electrical and viscoelastic parameters of the erythrocytes, the third one is a combination of Raman spectroscopy data and of dielectrophoresis. It was turned out that the use of two methods simultaneously increases diagnostic accuracy (88%), sensitivity (84.6%), and specificity (91.7%) in distinguishing resistant from controlled hypertension, as opposed to methods used separately.

Results of the combined assessment of the Raman peaks for aqueous solutions of hemoglobin, electrical, viscoelastic parameters of the erythrocytes among patients with AH for detecting resistant and controlled forms of the disease in comparison with the data of combined clinical and instrumental research methods are presented in Table 4 [36]. Especially, the prospects are important for determining truly positive results for RAH (according to the prognostic value of the negative result) due to the need for a complex of social, therapeutic, and adaptive measures.

4 Summary

Thus, the study of changes in the content of hemoglobin complexes by the Raman spectroscopy, electrical and viscoelastic parameters of the erythrocytes among patients with AH allowed us to draw the following conclusions:

- We have determined a significant decrease in the level of hemoglobin-ligand complexes, Hb-NO (II) complexes in patients with RAH compared to those among patients with controlled AH and among healthy patients ($p < 0.001–0.05$), that probably reflects the reduced reserves of erythrocytic NO and a decrease in O_2 release.
- Among patients with resistant AH, the levels of electrical conductivity, summarized indicators of rigidity, viscosity, the indices of aggregation, and destruction are significantly higher, and the amplitude of cell deformation, polarizability of membranes at a frequency of 10^6 Hz, the speed of cell movement to the electrodes, the dipole moment, and the electrical capacity of erythrocyte membranes are lower than those in the control group and patients with controlled AH ($p < 0.0001–0.05$);
- We have found correlation between the intensities of the most important signals of Raman spectra of hemoglobin (1325, 1350, 1550, 1580, 1660, 1668 cm^{-1}, I_{1680}/I_{1580}) and electric and viscoelastic parameters of erythrocytes (amplitude of deformation of erythrocytes, summarized indicators of viscosity and rigidity, the magnitude of the dipole moment, polarizability at the frequency 10^6 Hz, electrical conductivity, index of destruction), the intensity of which was the biggest one for resistant AH;
- The combined use of two methods (Raman spectroscopy of hemoglobin and electrical and viscoelastic indicators of the erythrocytes) allowed to increase the diagnostic accuracy in detecting RAH up to 88%, sensitivity up to 84.6%, specificity up to 91.7% compared to the data of the combined clinical and

instrumental methods of research, which exceeds the capabilities of the methods separately.

Thus, the combined use of the above methods in clinical practice will reduce the material, time, and labor costs for the diagnosis and treatment of the RAH and its consequences, and will make it possible to identify new targets for therapeutic effects.

Disclosures

All authors declare that there is no conflict of interests in this paper.

Acknowledgence

This work was done within the publicly funded topic in State Assignment No. AAAA-A17-117112850280-2.

References

1. S. A. Boitsov, R. G. Oganov, "Experience in the prevention of cardiovascular diseases in the country," Therapeutic archive 84(9), 4–10 (2012) [in Russian].
2. A. N. Britov, M. M. Bystrova, "Refractory hypertension – modern approaches to diagnostics and treatment," Rational pharmacotherapy in cardiology 6(2), 206–211 (2010) [in Russian].
3. V. A. Dmitriev, E. V. Oschepkova, V. N. Titov, A. N. Rogoza, T. V. Balakhonova, O. A. Pogorelova, V. P. Masenko, and D. M. Ataullakhanova, "C-reactive protein and interleikin-6 in damage of target-organs of patients at early stages of hypertension," Kardiologicheskii vestnik 2(2), 45–49 (2007) [in Russian].
4. E. V. Oschepkova, V. A. Dmitriev, and V. N. Titov, "Non-specific inflammation rates in hypertensive patients," Therapeutic archive 12, 62–67 (2007) [in Russian].
5. S. Spina, C. Lei, R. Pinciroli, and L. Berra, "Hemolysis and kidney injury in cardiac surgery: The protective role of nitric oxide therapy," Seminars in Nephrology 39(5), 484–495 (2019).
6. J. T. Alexander, A. M. El-Ali, J. L. Newman, S. Karatela, B. L. Predmore, D. J. Lefer, R. L. Sutliff, and J. D. Roback, "Red blood cells stored for increasing periods produce progressive impairments in nitric oxide–mediated vasodilation," Transfusion 53, 2619–2628 (2013).
7. J. Carroll, M. Raththagala, W. Subasinghe, S. Baguzis, T. D. A. Oblak, P. Root, and D. Spence, "An altered oxidant defense system in red blood cells affects their ability to release nitric oxidestimulating ATP," Molecular BioSystems 2(6–7), 305–311 (2006).
8. R. S. Sprague, A. H. Stephenson, E. A. Bowles, M. S. Stumpf, and A. J. Lonigro, "Reduced expression of Gi in erythrocytes of humans with type 2 diabetes is associated with impairment of both cAMP generation and ATP release," Diabetes 55(12), 3588–3593 (2006).
9. C. C. Helms, M. T. Gladwin, and D. B. Kim-Shapiro, "Erythrocytes and Vascular Function: Oxygen and Nitric Oxide," Frontiers in Physiology 9, 1–125 (2018).
10. "Working Group for the Treatment of Arterial Hypertension of the European Society of Hypertension. Recommendations for the treatment of arterial hypertension. ESH/ESC 2013," Russian cardiologic journal 1(105), 7–94 (2014) [in Russian].
11. S. T. Halpin, D. M. Spence, "Direct plate-reader measurement of nitric oxide released from hypoxic erythrocytes flowing through a microfluidic device," Analytical Chemistry 82, 7492–7497 (2010).
12. M. V. Kruchinina, A. A. Gromov, Ya. Sh. Shvartz, A. V. Rabko, V. A. Baum, V. M. Generalov, V. N. Kruchinin, S. V. Rykhlitskii, and V. A. Volodin, "Resistant arterial hypertension: some aspects of pathogenesis," Atherosclerosis 11(3), 5–14 (2015) [in Russian].
13. Ya. Sh. Shvartz, M. V. Kruchinina, M. M. Timofeeva, M. I. Rudina, O. M. Dolganova, A. A. Gromov, V. A. Baum, and A. V. Rabko, "Determining the ability of erythrocyte to generate nitric oxide in patients with cardiovascular diseases," International Journal of Applied and Fundamental Research 4(2), 386–391 (2016) [in Russian].
14. M. V. Kruchinina, Ya. Sh. Shvartz, A. A. Gromov, V. N. Kruchinin, V. A. Volodin, and S. V. Rykhlitskii, "Raman-spectroscopy of hemoglobine in diagnostics of resistant arterial hypertension," Atherosclerosis 12(4), 22–29 (2016) [in Russian].
15. M. V. Kruchinina, A. A. Gromov, A. V. Rabko, V. A. Baum, V. M. Generalov, V. N. Kruchinin, S. V. Rykhlitskii, and V. A. Volodin, "Are there any differences in the optical parameters of blood associated with the degree of arterial hypertension?" Atherosclerosis 10(1), 22–31 (2014) [in Russian].
16. S. Uskokovic-Markovic, M. Jelikic-Stankov, I. Holclajtner-Antunovic, and P. Durdevic, "Raman spectroscopy as a new biochemical diagnostic tool," Journal of Medical Biochemistry 32(2), 96–103 (2013).
17. G. W. Auner, S. K. Koya, C. Huang, B. Broadbent, M. Trexler, Z. Auner, A. Elias, K. C. Mehne, and M. A. Brusatori, "Applications of Raman spectroscopy in cancer diagnosis," Cancer and Metastasis Reviews 37(4), 691–717 (2018).
18. V. M. Generalov, M. V. Kruchinina, A. G. Durymanov, A. A. Medvedev, A. S. Safatov, A. N. Sergeev, G. A. Buryak, S. A. Kurilovich, and A. A. Gromov, Dielectrophoresis in the diagnosis of infectious and non-infectious

diseases, V. M. Generalov, M. V. Kruchinina (eds.), CERIS, Novosibirsk (2011) [in Russian]. ISBN 978-5-7007-0256-4.
19. V. M. Generalov, M. V. Kruchinina, A. A. Gromov, and G. V. Shuvalov, Dielectrophoresis in biology and medicine, Publishing office of NGTU, Novosibirsk (2017) [in Russian]. ISBN 978-5-7782-3485-7.
20. M. V. Kruchinina, S. A. Kurilovich, M. I. Voevoda, A. A. Gromov, V. M. Generalov, A. S. Safatov, G. A. Buryak, and K. V. Generalov, "Associations of erythrocyte parameters with viral loadin patients with chronic viral hepatitis C," Vestnik NGU 13(2), 5–17 (2015) [in Russian].
21. M. V. Kruchinina, S. A. Kurilovich, A. A. Gromov, V. M. Generalov, and V. N. Kruchinin, "Peculiarities of erythrocytic parameters in patients with nonalcoholic steatohepatitis," Journal of Analytical Sciences, Methods and Instrumentation 6(1), 6–14 (2016).
22. M. V. Kruchinina, A. V. Starikov, A. A. Gromov, and V. M. Generalov, "Interaction of electrical and viscoelastic parameters with biochemistry parameters in patients with various stages of colorectal cancer," Therapy 3(7), 40–47 (2016) [in Russian].
23. M. V. Kruchinina, A. A. Gromov, M. V. Parulikova, M. G. Golovin, V. A. Baum, V. M. Generalov, K. V. Generalov, and V. N. Kruchinin, "Diagnostic possibilities for rheological disorders in patients with type 2 diabetes," Modern problems of science and education 5 (2017).
24. O. V. Rodnenkov, O. G. Luneva, N. A. Ulyanova, G. V. Maksimov, A. B.Rubin, S. N. Orlov, and E. I. Chazov, "Erythrocyte membrane fluidity and haemoglobin haemoporphyrin conformation: features revealed in patients with heart failure," Pathophysiology 11(4), 209–213 (2005).
25. I. E. Chazova, N. M. Danilov, and A. Yu. Litvin, Refractory arterial hypertension: Monography, Moscow, Atmosphere (2014) [in Russian].
26. A. S. Said, S. C. Rogers, and A. Doctor, "Physiologic Impact of Circulating RBC Microparticles upon Blood-Vascular Interactions," Frontiers in Physiology 8, 1120 (2017).
27. G. J. Bosman, "The involvement of erythrocyte metabolism in organismal homeostasis in health and disease," PROTEOMICS - Clinical Applications 10(8) 774–777 (2016).
28. E. B. Menshikova, V. Z. Lankin, N. K. Zenkov, I. A. Bondar, N. F. Krugovyh, and V. A. Trufakin, Oxidative stress. Prooxidants and antioxidants, Moscow, Slovo (2006) [in Russian].
29. V. V. Novitskij, N. V. Ryazantseva, and E. A. Stepovaya, The physiology and pathophysiology of red blood cells, Publishing office of TGU, Tomsk (2004) [in Russian].
30. M. Becatti, R. Marcucci, A. M. Gori, L. Mannini, E. Grifoni, A. A. Liotta, A. Sodi, R. Tartaro, N. Taddei, S. Rizzo, D. Prisco, R. Abbate, and C. Fiorillo, "Erythrocyte oxidative stress is associated with cell deformability in patients with retinal vein occlusion," Journal of Thrombosis and Haemostasis 14(11), 2287–2297 (2016).
31. A. I. Berezniakova, O. D. Zhemela, "Deformability of the erythrocytes membrane in rats of different age in hypoxia," Fiziolohichnyĭ zhurnal 59(3), 72–77 (2013).
32. M. Tarasev, M. Muchnik, L. Light, K. Alfano, and S. Chakraborty, "Individual variability in response to a single sickling event for normal, sickle cell, and sickle trait erythrocytes," Translational Research 181, 96–107 (2017).
33. Y. Zhao, X. Wang, M. Noviana, and M. Hou, "Nitric oxide in red blood cell adaptation to hypoxia," Acta Biochimica et Biophysica Sinica 50(7), 621–634 (2018).
34. M. Grau, A. Lauten, S. Hoeppener, B. Goebel, J. Brenig, C. Jung, W. Bloch, and F. Suhr, "Regulation of red blood cell deformability is independent of red blood cell-nitric oxide synthase under hypoxia," Clinical Hemorheology and Microcirculation 63(3), 199–215 (2016).
35. O. V. Kosmachevskaya, A. F. Topunov, "Alternate and Additional Functions of Erythrocyte Hemoglobin," Biochemistry (Moscow) 83(12) 1575–1593 (2018).
36. T. Greenhalgh, How to read a paper: the basics of evidence-based medicine, Fifth edition, BMJ Books (2014).

Evaluating the Number of Ligand Binding Sites on Protein from Tryptophan Fluorescence Quenching under Typical Experimental Conditions

Alexey V. Gayer[1], Boris P. Yakimov[1], Gleb S. Budylin[2], and Evgeny A. Shirshin[1,3*]

[1] Department of Physics, M.V. Lomonosov Moscow State University, 1/2 Leninskie gory, Moscow 119991, Russia

[2] National Research University Higher School of Economics, Faculty of Physics, 20 Myasnitskaya str., Moscow 101000, Russia

[3] Institute of spectroscopy of the Russian Academy of Sciences, 5 Fizicheskaya str., Moscow 108840, Russia

*** e-mail:** shirshin@lid.phys.msu.ru

Abstract. Fluorescence quenching technique is extensively applied for the characterization of intermolecular interactions in the solution that is one of the major problems in biochemistry and pharmacology. Using the Stern-Volmer equation, one can obtain a measure of binding affinity calculated under the assumption of static quenching, while the possibility to determine other binding parameters is under discussion. Several mathematical approaches are known, which allow determining the number of binding sites from fluorescence quenching curves. However, they usually require high concentrations of the ligand to obtain saturating binding curves that could be complicated in a number of experimental conditions. In this paper, we present a simple algorithm, which allows to prove that the number of binding sites in the system is equal to one or not and to verify that the quantum yield of the complex is zero. The advantage of the suggested approach is its applicability at typical conditions used in tryptophan fluorescence quenching experiments for the protein-ligand binding. A web interface for automated processing of fluorescence quenching experiments based on the suggested approach is presented. © 2020 Journal of Biomedical Photonics & Engineering.

Keywords: fluorescence quenching; Stern-Volmer; tryptophan fluorescence quenching; protein-ligand binding; number of binding sites; drug discovery.

Paper #3365 received 12 May 2020; accepted for publication 28 May 2020; published online 22 Jun 2020. doi: 10.18287/JBPE20.06.020303.

1 Introduction

Quantitative characterization of binding affinities is a central task of biochemistry and pharmacology [1, 2]. It requires determination of binding sites number and affinity constants for each site. To obtain a binding curve, one should use a method, which is sensitive to a change of a certain physical parameter upon complex formation, e.g. diffusion coefficient, surface plasmon resonance properties, hydrodynamic radius, enthalpy etc. [3]. Among others, optical molecular spectroscopy techniques can be used, including the fluorescence quenching technique (FQT) – in cases when fluorescence is quenched upon binding [4]. In this paper, we will focus on the assessment of protein-ligand binding by analyzing intrinsic protein fluorescence quenching.

Since there is still a confusion in terminology concerning different types of quenching, we will first introduce it according to Ref. [5]. In the systems where fluorophore and quencher are different molecules, two types of quenching could be distinguished: collisional quenching (in which the diffusion is required to bring the quencher close enough to fluorophore) and binding-related (often called “static”) quenching (for which quencher and fluorophore are bound, so that the

quenching process occurs immediately upon excitation) [5]. The efficiency of binding-related quenching, characterized by the quenching constant, depends on the binding affinity, hence, by obtaining the dependence of the fluorescence intensity on the ligand concentration, one can determine binding parameters [4]. However, even under the assumption of binding-related (static) quenching, two distinct cases should be considered: the first is when the fluorescence of protein-ligand complex is negligible in comparison with the protein fluorescence (i.e. complete quenching), and the second when the fluorescence of protein-ligand complex is less, but comparable with the protein fluorescence (i.e. incomplete quenching). Obviously, affinity constants calculated based on fluorescence quenching parameters obtained in the case of incomplete quenching would significantly differ from the real affinity constant. Hence, understanding of fluorophore's quantum yield dependence on the occupied sites number is crucial for correct interpretation of the FQT data. Moreover, several papers point out the errors and pitfalls of FQT application for quantification of binding affinities and determination of the number of binding sites [6–10].

It should be noted that binding of a ligand to protein does not necessarily lead to quenching of fluorescence, and systems with the fluorescence enhancement are also known [11]. Indeed, the variation of fluorescence parameters upon binding ligands to proteins could be rather complex [12], however, in this paper we will focus on the most common case, when the emission intensity of tryptophan residues within a protein decreases upon ligand binding, i.e. fluorescence quenching is observed. A number of methods was suggested in the literature, which allow estimation of the number of binding sites from titration curves [13–15]. Nevertheless, these methods require measurements of several titration curves in the regime when concentration of ligand must be high and significantly exceeds the characteristic dissociation constant of a complex [14–15], that is sometimes hardly possible due to experimental artifacts like the inner filter effect or low quantities of the ligand available. Hence, a simple and reliable test to assess the binding stoichiometry in more realistic experimental conditions is still of interest. In this paper, we suggest an algorithm for the assessment the binding parameters from fluorescence quenching curves, as well as a web-interface implementing this algorithm for on-line data processing.

2 Backgrounds

Consider the case of the 1:1 stoichiometry interaction:

$$\mathrm{P} + \mathrm{Q} \rightleftarrows \mathrm{PQ}, \qquad (1)$$

where P, Q and PQ correspond to protein, quencher and complex, respectively. Relation between equilibrium concentrations in this system can be expressed as

$$\frac{[\mathrm{P}]_\mathrm{T}}{[\mathrm{P}]} = 1 + K_\mathrm{A}[\mathrm{Q}], \qquad (2)$$

where $[\mathrm{P}]_\mathrm{T}$, [P] and [Q] are the total concentration of protein and equilibrium concentrations of protein and quencher, respectively, and K_A is the affinity (binding) constant. The Stern-Volmer equation is derived from (2) under the following assumptions:

(i) the concentration of complex is much less than quencher concentration ([PQ] << [Q]), thus yielding $[\mathrm{Q}] \approx [\mathrm{Q}]_\mathrm{T}$,

(ii) the quantum yield of the complex is approximately zero (complete quenching), thus fluorescence intensity F is proportional to [P].

Under these assumptions Eq. (2) transforms into the Stern-Volmer equation:

$$\frac{F_0}{F} = 1 + K_\mathrm{SV}[\mathrm{Q}]_\mathrm{T}, \qquad (3)$$

where F_0 is the fluorescence intensity in the absence of quencher and K_SV is the Stern-Volmer constant, which is used as a measure of binding affinity in FQ experiments.

The violation of the assumptions (i–ii) may result in discrepancies between K_SV and true binding affinity K_A of the considered ligand-fluorophore system. First, the impact of equilibrium concentration of the complex [PQ] cannot be neglected for large binding constants, when significant part of ligand molecules is bound. This fact becomes especially important when using FQT for studying protein-drug binding, which is usually characterized by high affinity constants [16]. Also, derivation of the Stern-Volmer equation (3) implies that the quantum yield η_complex of the complex is zero, but this is not the case for a number of systems.

Further, in this work it will be shown that based on multiple fluorescence quenching curves, measured at different total fluorophore concentration one may determine (a) if the number of binding sites in the system is equal to one or larger and (b) the quantum yield of the complex in the case of 1:1 stoichiometry.

3 Materials and Methods

3.1 Samples preparation

Bovine serum albumin (BSA), Congo Red (CR), 1-anilino-8-naphthalene sulfonate (ANS), sodium myristate (myr) and thioflavin T (ThT) were purchased in Sigma-Aldrich (Germany) and used without further purification. BSA stock solutions were prepared in phosphate buffered saline (PBS, 0.1M ionic strength) at pH 7.4. To obtain fluorescence quenching curves, stock solutions of Congo Red, ANS, and ThT dyes at a concentration of 100 μM in PBS were prepared, and small volumes of obtained stock solutions were added to the solution with fixed protein concentration.

3.2 Fluorescence measurements

Fluorescence spectra were measured using the FluoroMax-4 (Horiba Jobin Yvon) spectrofluorometer. To avoid the inner-filter effect excitation wavelength

was set to 295 nm that corresponds to the red edge of Trp absorption. Fluorescence emission was measured in the 325–400 nm range that corresponds to the fluorescence of tryptophan residues in BSA. Integral fluorescence values F were calculated as the sum of fluorescence intensity signal in the 325–400 nm spectral range. Changes in fluorescence intensity F due to changes in protein concentration upon titrant addition were corrected for all measurements.

Numerical simulation and experimental data processing were performed using the Python programming language and NumPy, SciPy, Matplotlib libraries. The online service for automatic data processing is available at http://lid.phys.msu.ru/fluorescence-quenching/.

4 Results and Discussion

4.1 Test on the difference between total and equilibrium concentration of the quencher

To take into account that the total quencher concentration is not equal to its equilibrium concentration, one should use nonlinear fitting procedure and modified Stern-Volmer equation [7], which takes into account the assumptions on residuals distribution implied in least-squares procedure [17]. However, an alternative correction procedure that could be applied to experimental data to visually inspect whether the impact of the difference between total and equilibrium concentration is significant could benefit the data quality evaluation.

The equilibrium concentration could be derived using the following expression:

$$[\mathrm{Q}] = [\mathrm{Q}]_\mathrm{T} - [\mathrm{PQ}] = [\mathrm{Q}]_\mathrm{T} - [\mathrm{P}]_\mathrm{T}\left(1 - \frac{[\mathrm{P}]}{[\mathrm{P}]_\mathrm{T}}\right). \quad (4)$$

Still assuming that the quantum yield of complex equals zero, Eq. (3) can be rewritten as

$$y = 1 + K_\mathrm{A}\left([\mathrm{Q}]_\mathrm{T} - [\mathrm{P}]_\mathrm{T}\left(1 - \frac{1}{y}\right)\right), \quad (5)$$

where $y = F_0/F$. Plotting the same FQ curves in the new coordinates (y over $[\mathrm{Q}]_\mathrm{T} - [\mathrm{P}]_\mathrm{T}\left(1 - \frac{1}{y}\right)$ instead of $[\mathrm{Q}]_\mathrm{T}$) thus should result in the correction of nonlinearity of FQ plots caused by differences between total and equilibrium concentrations of quencher Q. The non-modified FQ curves calculated for $K_\mathrm{A} = 10^6\ \mathrm{M}^{-1}$ and different $[\mathrm{P}]_\mathrm{T}$ are presented in Fig. 1a, where significant difference in their slope is clearly seen. This fact is due to violation of the assumption (i) at high $[\mathrm{P}]_\mathrm{T}$, while the proposed correction yields coinciding lines with the slope equal to K_A (Fig 1b).

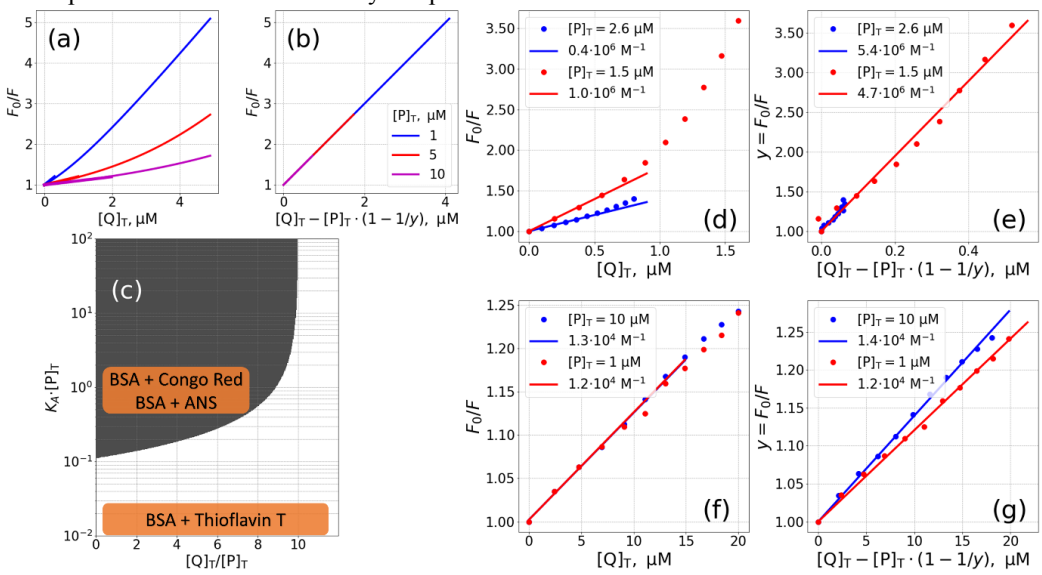


Fig. 1 (a) The FQ curves calculated for $K_\mathrm{A} = 10^6\ \mathrm{M}^{-1}$ and different $[\mathrm{P}]_\mathrm{T}$ using Eq. (2). (b) FQ curves from Fig. 1a corrected for the difference between total and equilibrium concentration of quencher by plotting in the $\left([\mathrm{Q}]_\mathrm{T} - [\mathrm{P}]_\mathrm{T}\left(1 - \frac{1}{y}\right), y\right)$ coordinates. (c) Diagram of 1:1 stoichiometry system parameters $(K_\mathrm{A}\cdot[\mathrm{P}]_\mathrm{T}, [\mathrm{Q}]_\mathrm{T}/[\mathrm{P}]_\mathrm{T})$, where correction for the difference between total and equilibrium concentration of quencher should (gray area) and should not (white area) be considered. The gray area corresponds to $\frac{[\mathrm{Q}]}{[\mathrm{Q}]_\mathrm{T}} < 0.9$, where the assumption $[\mathrm{Q}] \approx [\mathrm{Q}]_\mathrm{T}$ is invalid. The orange areas correspond to parameters of the systems measured in this work. (d)-(e) FQ curves for BSA-CR before (d) and after (e) the correction procedure. BSA-CR FQ curves obtained for different $[\mathrm{P}]_\mathrm{T}$ without correction do not coincide due to significant difference between total and equilibrium concentration of quencher. Correction resulted in the coincidence of two FQ curves measured at different $[\mathrm{P}]_\mathrm{T}$. (f)–(g). FQ curves for BSA-ThT before (f) and after (g) correction procedure. Correction does not affect the FQ curves significantly due to low affinity constant in this system.

As the criterion for significant difference between $[Q]$ and $[Q]_T$ we estimated parameter values of the system where $\frac{[Q]}{[Q]_T} \leq 0.9$ (i.e. $[PQ] > 10\%$ of $[Q]_T$). The results are presented in Fig. 1c, where the gray area corresponds to "forbidden" zone, meaning that at the corresponding parameters the assumption that $[Q] \approx [Q]_T$ is violated and the affinity constant determined from Eq. (3) will be estimated with a high error.

To illustrate the importance of accounting for $[Q] \neq [Q]_T$, we also performed experiments for model systems with high and low affinity constants: (a) BSA and Congo Red, (b) BSA and ThT. One more example with the BSA-ANS system is presented in the text below (Section 4.3). The BSA-CR system has $K_A \sim 10^6\ M^{-1}$ [17, 18], hence, for the total protein concentration varying in range of 1–10 μM the difference between equilibrium and total concentration should be taken into account. While fluorescence quenching curves for different $[P]_T$ differed significantly (Fig. 1d), correction for $[Q] \neq [Q]_T$ using Eq. (5) resulted in their coincidence (Fig. 1e). The slopes of fluorescence quenching curves (i.e. binding affinities) obtained from the non-corrected Stern-Volmer plots (Fig. 1d) varied by an order of magnitude for different protein concentration (4×10^5 M^{-1} for $[P]_T = 2.6$ μM vs. 10^6 M^{-1} for $[P]_T = 1.5$ μM), while for the corrected plots yielded binding affinities of ~$5 \cdot 10^6$ M^{-1} both for $[P]_T = 1.5$ μM and $[P]_T = 2.6$ μM, respectively. Similar correction for the BSA-ThT system had no effect (Fig. 1f–g) because of low binding affinity in this system [18].

4.2 Assessment of fluorescence quantum yield of a protein-ligand complex

Derivation of the SV equation (3) also implies that the quantum yield $\eta_{complex}$ of the complex is zero, i.e. that the quenching is complete. As this assumption is violated in a number of systems, the question is whether it is possible to prove that $\eta_{complex}$ is non-zero. The ratio F_0 / F for the 1:1 complexation in case of non-zero quantum yield can be expressed as:

$$\frac{F_0}{F} = \frac{\eta_{Protein}[P]_T}{\eta_{Protein}[P] + \eta_{PQ}[PQ]} =$$

$$= \frac{[P]_T}{[P]+\eta[PQ]} = \frac{[P]_T}{[P]_T+(\eta-1)[PQ]}, \qquad (6)$$

where $\eta \equiv \frac{\eta_{complex}}{\eta_{Protein}}$ is the relative quantum yield of the complex ($0 \leq \eta < 1$). By measuring $y = \frac{F_0}{F}$ it is possible to estimate the value of $[PQ]$:

$$y = \frac{[P]_T}{[P]_T+(\eta-1)[PQ]} \Rightarrow [PQ] = \frac{[P]_T\left(1-\frac{1}{y}\right)}{1-\eta}. \qquad (7)$$

Concentration of free quencher can be expressed as:

$$[Q] = [Q]_T - [PQ] = [Q]_T - \frac{[P]_T\left(1-\frac{1}{y}\right)}{1-\eta}. \qquad (8)$$

Next, combining Eq. (2) and Eq. (7) yields:

$$y = \frac{F_0}{F} = \frac{[P]_T}{[P]+\eta[PQ]} = \frac{1+K_A[Q]}{1+\eta K_A[Q]}. \qquad (9)$$

Finally, by substituting the Eq. (8) into Eq. (9), one may obtain the following parametric equation:

$$\frac{y-1}{1-\eta y} = K_A\left([Q]_T - [P]_T\frac{1-\frac{1}{y}}{1-\eta}\right). \qquad (10)$$

Eq. (10) describes the dependence of fluorescence quenching ratio F_0 / F on total concentration of fluorophore $[P]_T$ and quencher $[Q]_T$ without the assumptions $[Q] \approx [Q]_T$ and $\eta_{complex} \approx 0$. To determine the values of η and K_A, we suggest to measure at least two FQ for different $[P]_T$, and then simultaneously fit these curves to Eq. (10) to obtain the η and K_A parameters. The main idea of this approach is that the Eq. (10) allows to consider the y values as function $y = y([Q]_T, [P]_T, K_A, \eta)$ with two independent variables $[Q]_T, [P]_T$ and two parameters K_A, η, thus the reliable evaluation of these parameters might be done.

The Eq. (10) could be also rewritten in the form suggested in Ref. [7]. Despite the correctness of the equations in Ref. [7], we found out that using a titration curve for a single concentration of protein could result in poor accuracy in determination of binding constant K_A and relative quantum yield η. To demonstrate this we modelled the fluorescence quenching curves for system with 1:1 stoichiometry and incomplete quenching with $K_A = 2 \times 10^5\ M^{-1}$ and $\eta = 0.3$ for two concentrations of protein $[P]_T = 1$ μM and $[P]_T = 10$ μM with total concentration of quencher Q varied in such region so the F_0 / F ratio was lower than 1.5 for both protein concentrations. It was found that the binding constant and relative quantum yield of complex system obtained at $[P]_T = 1$ μM were equal to $K_A = (1.53 \pm 0.21) \times 10^6$ and $\eta = 0,15 \pm 0.08$, while for $[P]_T = 10$ μM, $K_A = (9 \pm 4) \times 10^5\ M^{-1}$ and $\eta = 0{,}0001 \pm 0{,}0019$ were obtained. At the same time, simultaneous use of two titration curves modelled for two concentrations of protein resulted in $K_A = (1.8 + 0.3) \times 10^6\ M^{-1}$ and $\eta = 0,26 \pm 0.02$ that coincided with the true values within the error. Hence, we emphasize that even using correct equation for analysing a single titration curve could be insufficient to obtain reliable results on binding parameters of the system, and using two titration curves is beneficial.

4.3 Estimation of the number of binding sites

Currently, in order to obtain the number of binding sites from fluorescence quenching curves, the "log-log" Stern Volmer equation is often used. However, it has been demonstrated by several authors that this approach is incorrect [6–8, 10]. The question about the possibility to

obtain the information about stoichiometry using fluorescence methods was reviewed in detail in Refs. [14, 15], and as it was already mentioned, for determination of the exact number of binding sites it is crucial to measure several titration curves with ligand concentrations up to the values that significantly exceed $1/K_A$ [14, 15]. In this work we propose the method for simple FQT data processing in the region of parameters, where saturation is not achieved, to test the hypotheses whether a single binding site ($n = 1$) or multiple binding sites ($n > 1$) are present in the system. The procedure for this can be done as follows.

Step 1. One should measure fluorescence quenching curves for two (or more) titration series for different initial values of $[P]_T$. Theoretically, $[P]_T$ values should be chosen in the way that $K_A[P]_T^{(1)} \ll 1$ and $K_A[P]_T^{(2)} \sim 1$ as for at these values the FQ curves would differ significantly. At the same time, one should find a compromise between two experimental artifacts. On the one hand, low values of $[P]_T$ lead to low intensity signals. On the other hand, high values of $[P]_T$ lead to inner filter effect, which also should be taken into account. For example, for BSA these values can be suggested to be equal to $[P]_T^{(1)} = 1$ μM and $[P]_T^{(2)} = 10$ μM. If the FQ curves measured at different $[P]_T$ values coincide, it can be argued that both assumptions of Stern-Volmer equation (i) and (ii) are fulfilled and further corrections are not necessary.

Step 2. If the FQ curves measured at two $[P]_T$ values differ, the procedure for fluorescence quantum yield estimation, i.e. fitting them to Eq. (10) should be performed. As a result, the values K_A, η will be obtained.

Step 3. If for both FQ curves $R^2 > 0.95$ and the residuals are not correlated (that could be verified visually or by using the Durbin-Watson statistical test) the fitting procedure can be considered successful. In this case, it can be argued that $n = 1$ and the relative quantum yield of complex and binding affinity constant K_A are determined correctly. If $R^2 < 0.95$, or residuals are correlated, it can be concluded that the system is not described by Eq. (10) and $n > 1$.

The described algorithm is visualized in Fig. 2.

To illustrate how this method works, the following systems were selected: the BSA-sodium myristate (myr) system, where $n > 1$ [20, 21]; BSA-ANS, where it is known that number of binding sites is 2 and fluorescence of the complex is not completely quenched [22]; and BSA-Congo Red where $n = 1$ [18, 19]. For all the systems two FQ curves were measured at different $[P]_T$ (Fig. 3a–c), and then the suggested approach was applied. The R^2 value for the BSA-myr system was equal to 0.407, there were clearly visible trends in residuals behavior (Fig. 3d), and the value of the Durbin-Watson's statistics was equal to 0.05 (the value of the Durbin-Watson statistic close to zero means the presence of positive correlation between residuals, a lack of correlation corresponds to the value of Durbin-Watson statistic equal to 2). Hence, it was verified that $n > 1$. Fit of the BSA-ANS data also exhibited poor $R^2 = 0.915$ value and correlated residuals (Fig. 3e).

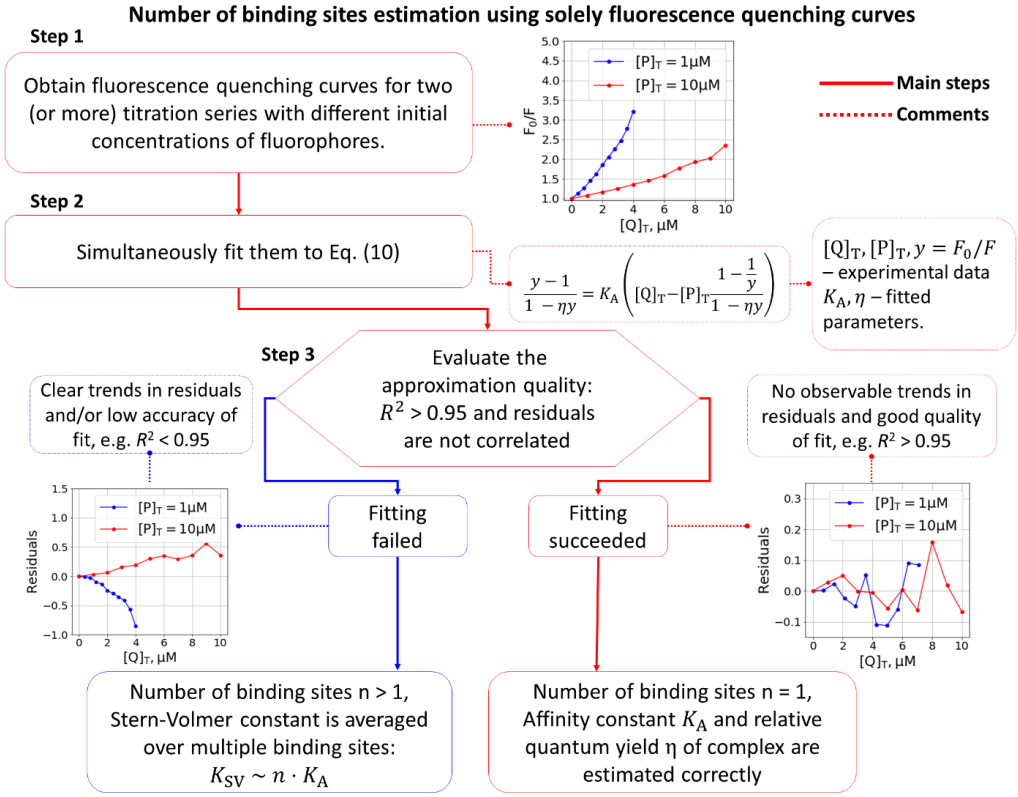


Fig. 2 Schematic representation of steps to be performed to analyze fluorescence quenching curves.

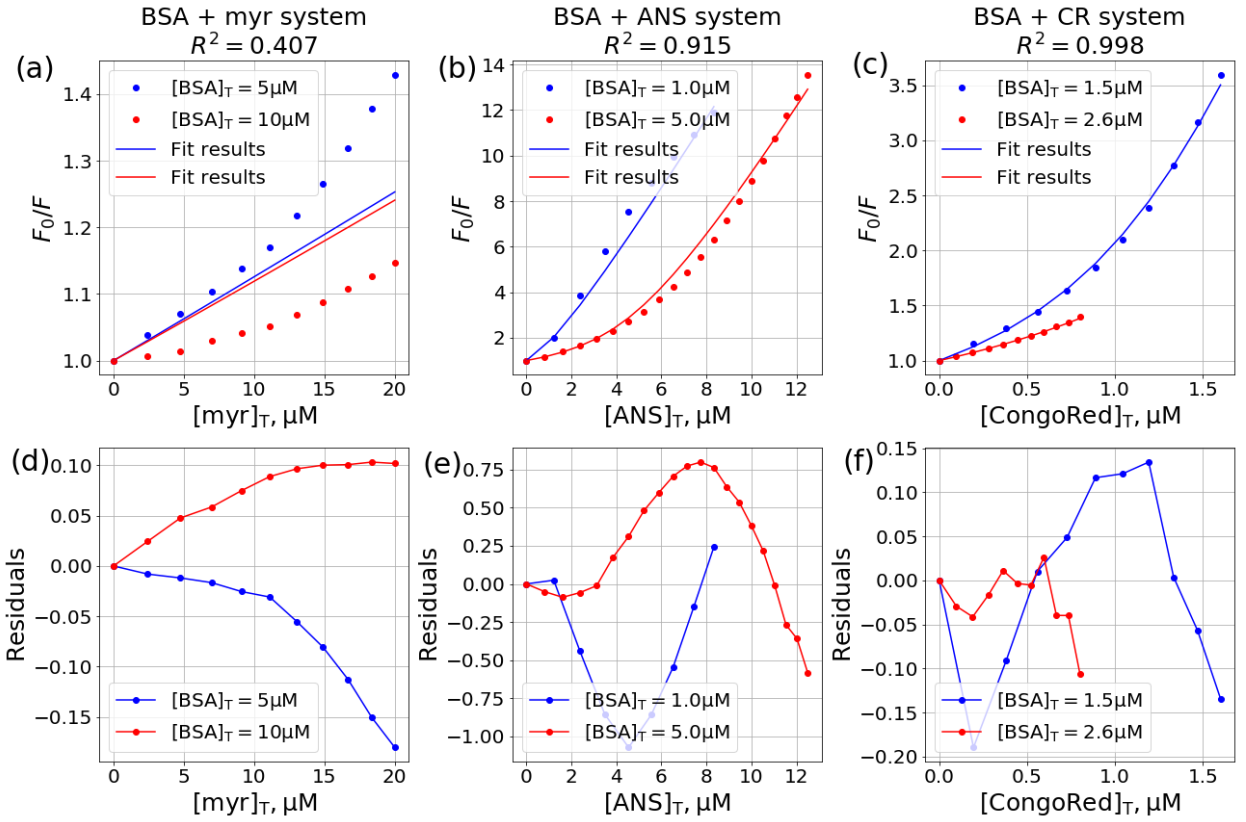


Fig. 3 (a)–(c) Fluorescence quenching curves for the BSA-myr (a), BSA-ANS (b) and BSA-CR (c) systems. (d)–(f) Residuals of fit of FQ curves by Eq. (10) for the BSA-myr (d), BSA-ANS (e), BSA-CR (f). Clearly observable trends in residuals may be noted for BSA-myr and BSA-ANS systems, verifying that number of binding sites is greater than 1 for these systems.

On the contrary, when the proposed algorithm was applied to the BSA-CR system, where n = 1 (Fig. 3c), the R^2 value was equal to 0.998 (Fig. 3f), and the values of the Durbin-Watson's statistics were equal to 1.5. Hence, it can be concluded that n = 1. The values obtained from fitting the FQ curves to Eq. (10) were $K_A = (4.6 \pm 0.4)\times10^6\ M^{-1}$ and $\eta = 0.003 \pm 0.018$, suggesting complete quenching in the system.

The suggested algorithm was also investigated numerically. Several systems were taken into consideration: (a) the system with one binding site and zero quantum yield of the complex, (b) the system with one binding site and non-zero quantum yield of the complex and (c) the system with several binding sites ($n = 2, 3, 4, 5$ and $K_{A_i} = \frac{K_{A_{i-1}}}{2}$, zero quantum yields). For each system the series of FQ experiments (two FQ curves with $[P]_T^{(1)} = 1\ \mu M, [P]_T^{(2)} = 10\ \mu M$) were simulated. To simulate the experimental error, five percent noise with uniform distribution was added to the F values. Then the suggested method for estimation of K_A and quantum yield was applied to fit the simulated data. Overall, 10000 experiments were simulated for all parameters sets. Fig. 4 demonstrates the contingency matrices of algorithm predictions for the system with low and high affinities ($K_A = 5\times10^4\ M^{-1}$ and $K_A = 5\times10^6\ M^{-1}$, respectively). For the high affinity systems the algorithm successfully distinguished three cases: the 1:1 stoichiometry with zero quantum yield of complex, 1:1 complexation with non-zero quantum yield and the $n > 1$ case, yielding almost 100% accuracy. Higher error rates were observed for low affinity systems: classification algorithm was prone to falsely attribute $n = 1$ systems with non-zero quantum yield to systems with $n > 1$. However, firstly, the case of high affinities is of more interest for biochemistry and pharmacology, and, secondly, as it was demonstrated in the section 4.1, FQ curves measured at different $[P]_T$ for low affinity constants coincide before the correction procedure, so one may classify the case of low binding affinities without applying the suggested algorithm.

4.4 Web-interface for the FQ data processing

To simplify the data processing using the suggested approach, the online service for data processing has been developed. (link: http://lid.phys.msu.ru/fluorescence-quenching/). Users can upload their data (two FQ curves), as a result, the procedure application summary is displayed. At first, the cases of $n = 1$ and $n > 1$ are discriminated; then in case of $n = 1$, K_A, η, R^2 values and the values of Durbin-Watson's statistics are shown; in case of $n > 1$ the R^2 value and the values of Durbin-Watson's statistics are displayed.

data, residuals and fits to an Eq. (10) with obtained parameters are presented in plots. Accurate estimation the number of binding sites, affinity constants and quantum yields of each of binding sites cannot be performed using solely fluorescence quenching method without any additional assumptions and restrictions imposed on quantum yields and binding affinities. So other experimental techniques should be used in addition to FQ technique to determine system properties.

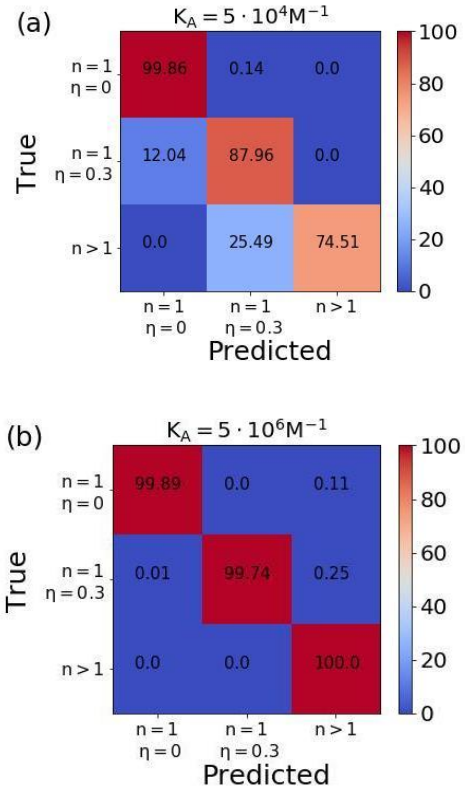


Fig. 4 The results of predictions of the proposed algorithm presented in the form of contingency matrices. Percentage of predicted vs. true parameters of the modeled FQ experiments is presented in each cell. (a) The contingency matrix for the system with low affinity ($K_A = 5{\times}10^4\ M^{-1}$). b) The contingency matrix for $K_A = 5{\times}10^6\ M^{-1}$. It can be noted that the proposed algorithm is better suited for higher values of affinity constants commonly occurring in biochemistry and pharmacology.

5 Conclusion

A number of papers has been devoted to the discussion of fluorescence quenching technique for binding parameters estimation. In this paper, we focused on the case of tryptophan fluorescence quenching in proteins upon binding and tried to suggest a simple algorithm for FQT data processing for the curves measured at typical experimental conditions. As some of the authors before [14–15], we came to the conclusion that measuring more than one fluorescence quenching curve is highly advantageous. That is, even application of the established procedure for assessing the fluorescence quantum yield [7] to a single curve may lead to discrepancy in the determined parameters. On the other hand, the use of some advanced algorithms [14–15] requires reaching a saturation in quenching, i.e. the use of high ligand concentrations, that has certain shortcomings – e.g. high optical density. Here we considered the application of the fluorescence quenching method to determine binding constant, number of binding sites and quantum yield of complex under the most typical experimental conditions. We demonstrated, both theoretically and experimentally, that several procedures can be applied to avoid common pitfalls that are encountered in processing and interpretation of FQ curves. A method was proposed that allows one to estimate the number of binding sites and the relative quantum yield of the complex in case of 1:1 stoichiometry. It was shown that in the case of high affinity constants (~10^6 M^{-1}), the presence of several binding sites can be determined by measuring multiple FQ curves with different initial fluorophore concentrations. Measurement of multiple fluorescence quenching curves is necessary to reliably estimate the effect of differences in the equilibrium and total quencher concentration and to estimate the complex quantum yield. We also present the web-interface for automated processing of fluorescence quenching experiments based on the suggested approach.

Disclosures

All authors declare that there is no conflict of interests in this paper.

References

1. M. E. Burton, L. M. Shaw, J. J. Schentag, and W. E. Evans (eds.), Applied pharmacokinetics & pharmacodynamics: principles of therapeutic drug monitoring, Lippincott Williams & Wilkins, Philadelphia, USA (2006).
2. D. L. Nelson, A. Lehninger, and M. M. Cox, Lehninger – principles of biochemistry, D. Nelson, M. B. Cox (Eds.), Macmillan, London, UK (2008).
3. K. Hirose, "A practical guide for the determination of binding constants," Journal of inclusion phenomena and macrocyclic chemistry 39(3), 193–209 (2001).

4. J. R. Lakowicz (Ed.), Principles of fluorescence spectroscopy, Springer Science & Business Media, Berlin/Heidelberg, Germany (2013).
5. P. R. Callis, "Binding phenomena and fluorescence quenching. I: descriptive quantum principles of fluorescence quenching using a supermolecule approach," Journal of Molecular Structure 1077, 14–21 (2014).
6. M. Van De Weert, "Fluorescence quenching to study protein-ligand binding: common errors," Journal of fluorescence 20(2), 625–629 (2010).
7. M. Van de Weert, L. Stella, "Fluorescence quenching and ligand binding: A critical discussion of a popular methodology," Journal of Molecular Structure 998(1–3), 144–150 (2011).
8. E. Lissi, C. Calderón, and A. Campos, "Evaluation of the number of binding sites in proteins from their intrinsic fluorescence: limitations and pitfalls," Photochemistry and photobiology 89(6), 1413–1416 (2013).
9. T. N. Tikhonova, E. A. Shirshin, G. S. Budylin, V. V. Fadeev, and G. P. Petrova, "Assessment of the europium(III) binding sites on albumin using fluorescence spectroscopy," The Journal of Physical Chemistry B 118(240), 6626–6633 (2014).
10. M. van de Weert, L Stella, "The dangers of citing papers you did not read or understand," Journal of Molecular Structure 1186, 102–103 (2019).
11. Y. Hong, J. W. Lam, and B. Z. Tang, "Aggregation-induced emission," Chemical Society Reviews 40(11), 5361–5388 (2011).
12. M. R. Eftink, Fluorescence methods for studying equilibrium macromolecule-ligand interactions, In Methods in enzymology 278, 221–225 (1997).
13. L. D. Ward, Measurement of ligand binding to proteins by fluorescence spectroscopy, Chapter in Methods in enzymology 117, 400–414 (1985).
14. W. Bujalowski, M. J. Jezewska, and P. J. Bujalowski, "Signal and binding. I. Physico-chemical response to macromolecule-ligand interactions," Biophysical Chemistry 222, 7–24 (2017).
15. W. Bujalowski, M. J. Jezewska, and P. J. Bujalowski, "Signal and binding. II. Converting physico-chemical responses to macromoleculeligand interactions into thermodynamic binding isotherms," Biophysical Chemistry 222, 25–40 (2017).
16. V. Kairys, L. Baranauskiene, M. Kazlauskiene, D. Matulis, and E. Kazlauskas, "Binding affinity in drug design: experimental and computational techniques," Expert opinion on drug discovery 14(8), 755–768 (2019).
17. R. J. Leatherbarrow, "Using linear and non-linear regression to fit biochemical data," Trends in biochemical sciences 15(12), 455–458 (1990).
18. Y.-Z. Zhang, X. Xiang, P. Mei, J. Dai, L.-L. Zhang, and Y. Liu, "Spectroscopic studies on the interaction of Congo Red with bovine serum albumin," Spectrochimica Acta Part A: Molecular and Biomolecular Spectroscopy 72(4), 907–914 (2009).
19. H. M. C. de Paula, Y. L. Coelho, A. J. P. Agudelo, J. de Paula Rezende, G. M. D. Ferreira, G. M. D. Ferreira, A. C. dos Santos Pires, and L. H. M. da Silva, "Kinetics and thermodynamics of bovine serum albumin interactions with Congo red dye," Colloids and Surfaces B: Biointerfaces 159, 737–742 (2017).
20. J. A. Hamilton, D. P. Cistola, J. D. Morrisett, J. T. Sparrow, and D. M. Small, "Interactions of myristic acid with bovine serum albumin: a 13C NMR study," Proceedings of the National Academy of Sciences 81(12), 3718–3722 (1984).
21. E. L. Gelamo, C. H. T. P. Silva, H. Imasato, and M. Tabak, "Interaction of bovine (BSA) and human (HSA) serum albumins with ionic surfactants: spectroscopy and modelling," Biochimica et Biophysica Acta (BBA)-Protein Structure and Molecular Enzymology 1594(1), 84–99 (2002).
22. I. M. Kuznetsova, A. I. Sulatskaya, O. I. Povarova, and K. K. Turoverov, "Reevaluation of ANS binding to human and bovine serum albumins: key role of equilibrium microdialysis in ligand–receptor binding characterization," PLoS One 7(7), e40845 (2012).

Terahertz optical and mechanical properties of the gelatin-starch-glycerol-bentonite biopolymers

Tianmiao Zhang[1*], Maria Zakharova[2], Anna Vozianova[1], Aleksandr Podshivalov[2], Maria Fokina[2], Ravshanjon Nazarov[1], Anna Kuzikova[1], Petr Demchenko[1], Mayya Uspenskaya[2], and Mikhail Khodzitsky[1]

[1] Terahertz Biomedicine Laboratory, ITMO University, Saint Petersburg 199034, Russia

[2] International Scientific and Research Institute of Bioengineering, ITMO University, Saint Petersburg 197101, Russia

*** e-mail:** tmzhang91@gmail.com

Abstract. With the fast development of terahertz technology in medical diagnosis and monitoring, it has become important to investigate the application of THz radiation in the cancer treatment assessment during the therapy. In this paper, a buccal drug delivery system is studied as the first step towards this application. The drug delivery system is based on a gelatin-starch biopolymer matrix filled with plasticizing glycerol and various contents of reinforcing particles of bentonite clay. The biopolymers were subjected to morphology analysis using optical microscopy, analysis of mechanical tensile properties, and analysis of terahertz optical properties, followed by a theoretical approach of the experiment. The results show a visible effect of the bentonite content on both of the mechanical and terahertz optical properties of the biopolymer. These findings allow us to confirm the feasibility of using THz radiation for cancer assessment during therapies. The proposed biopolymer also has the potential to be applied as a substrate when carrying out in-vivo optical property measurement of biotissue in terahertz frequency range. © 2020 Journal of Biomedical Photonics & Engineering.

Keywords: biopolymer; terahertz time-domain spectroscopy; effective medium theory; bentonite; drug delivery system; mechanical properties; optical properties.

Paper #3359 received 1 Apr 2020; revised manuscript received 28 May 2020; accepted for publication 15 Jun 2020; published online 22 Jun 2020. doi: 10.18287/JBPE20.06.020304.

1 Introduction

Terahertz (THz) radiation is attracting scientists' attention around the world because it has been considered as an efficient non-destructive and non-ionizing optical method for biological object investigation. For example, THz imaging has been previously shown to be capable of distinguishing normal (healthy) tissue from its cancerous form [1–4]. Wound assessment of skin burn using THz radiation was also investigated [5]. The THz optical properties of oral tissue and its cancerous form have been measured and potential diagnosis method using THz radiation was given [6]. A THz endoscope system was described in article [7], which made *in vivo* cancer diagnosis possible.

The following potential research topic is to investigate the application of THz radiation in the cancer treatment assessment during the therapy. Applying drug delivery system made by biocompatible/biodegradable polymers (biopolymers) on the surface of cancerous area is a standard treatment protocol of oral and skin cancers [8, 9]. THz radiation needs to penetrate through the biopolymer for the treatment assessment. However, no comprehensive investigation of drug delivery system in the THz frequency range has been done. Its THz optical properties, i.e. the THz waves propagation inside of drug delivery systems, are still unknown.

The drug delivery system based on gelatin-starch biopolymers is chosen as the research object, due to its attractive properties, such as, good solubility in water,

processability by melt methods, high film-forming properties, relatively low cost and availability on the world market [10, 11]. The solid-state materials, which obtained from gelatin-starch systems have such properties as non-toxicity, edibility and digestibility in organisms, biodegradability, higher mechanical properties and vapor-gas barrier properties compared to pure materials [12]. The use of gelatin-starch systems in the shell coat of the micro-capsules for drug delivery [13, 14], soft and hard capsule materials for drugs [15], edible films and coatings for extending the shelf life of food products [12, 16] and orally disintegrating films and carriers embedded vitamins and drugs for buccal drug delivery [17, 18] has been reported in the recent studies.

This work aims to study the THz optical properties of gelatin-starch biopolymers and to evaluate the feasibility of using THz radiation as a medical assessment technique during cancer therapy. We prepared biopolymers based on gelatin-starch-glycerol composition with different content of the bentonite reinforcing particles and various thicknesses. The structural analysis of morphology of the resulting biopolymers was studied using light microscopy and mechanical tensile tests. The refractive index and the absorption coefficient of the biopolymers were studied in the frequency range of 0.2 – 1 THz using THz time-domain spectroscopy (TDS). Three mathematical models known as Complex Refractive Index (CRI), Landau-Lifshitz-Looyenga (LLL) and Bruggeman models, and additionally an iterative method based on Bruggeman model were used to seek for the best mathematical approach to describe the proposed biopolymer. The THz optical properties of the proposed biopolymers were also compared with those of healthy and cancerous oral tissues for the feasibility evaluation of THz medical assessment technique during cancer therapy.

2 Materials and methods

2.1 Materials

Potato starch is from local source (analytical grade) in the form of white powder and food grade gelatin is from local source in form of light-yellow grains were obtained by Vekton (Russia). Glycerol in off-white liquid form is provided by LenReactiv (Russia). Hydrophilic bentonite particles "Nanoclay" with mean particle size of 21 μm (CAS # 1302-78-9) was obtained by Sigma Aldrich (USA).

2.2 Biopolymer preparation

The biopolymers were prepared by casting gel-forming solution and subsequent drying. At first, the single water-biopolymer solution of gelatin and starch with 5 wt.% concentration of dry basis were prepared as the biopolymer matrix. Both gelatin and starch were swollen separately in distilled water in 10 min. Then the solutions were dissolved and homogenized at 60 °C and at 90 °C with continuous stirring for gelatin and starch solution, respectively. After complete homogenization (≈10 minutes), the single biopolymer solution of gelatin and starch was blended with the volume ratio of 90 vol.% and 10 vol.%, respectively. Afterwards, the solution was continuously being stirred for 5 min at 70 °C.

Next, the water and filler suspensions were prepared. The glycerol in count of 30 wt.% from dry basis of main biopolymers was dissolved in distilled water with continuous stirring for 3 min at room temperature. Then bentonite particles with various contents were added to the water-glycerol solution. Then the obtained filler suspensions were homogenized at 70 °C for 10 min with continuous stirring.

After the preparation of the blended biopolymer solutions and filler suspensions, they were mixed and homogenized at 70 °C for 5 min with continuous stirring. The obtained solutions were additionally sonicated using standard ultrasonic homogenizer at 70 °C for 15 min. The final gel-forming solutions were casted into polystyrene Petri dishes in various volumes for the material preparation with different thicknesses. Casted solutions were dried using the drying oven UT-4620 Ulab (Russia) equipped with bubble level holder at 26 ± 2 °C for 48 h.

After complete fabrication of the biopolymers with different thicknesses, their moisture contents were determined using the standard gravimetric method. Based on the concentrations of the components in the solutions and the moisture contents of dried biocomposites, the volume fractions of all components in the fabricated biopolymers were determined depending on φ and presented in Table 1.

Table 1 The volume fractions of the components in the biopolymers depending on φ.

φ (wt.%)	Gelatin (vol.%)	Potato starch (vol.%)	Glycerol (vol.%)	Bentonite (vol.%)	Water (vol.%)
0	74.0	7.4	8.6	0	10 ± 2
3	72.0	7.2	8.1	2.7	10 ± 2
5	70.6	7.0	7.9	4.5	10 ± 2
7	69.0	6.9	7.8	6.3	10 ± 2
9	68.0	6.8	7.7	7.5	10 ± 2

For additional mechanical tests, biopolymers were prepared with an extended range of φ from 1 to 11 wt.% with increment of 2 wt.% from dry basis of main biopolymer matrix.

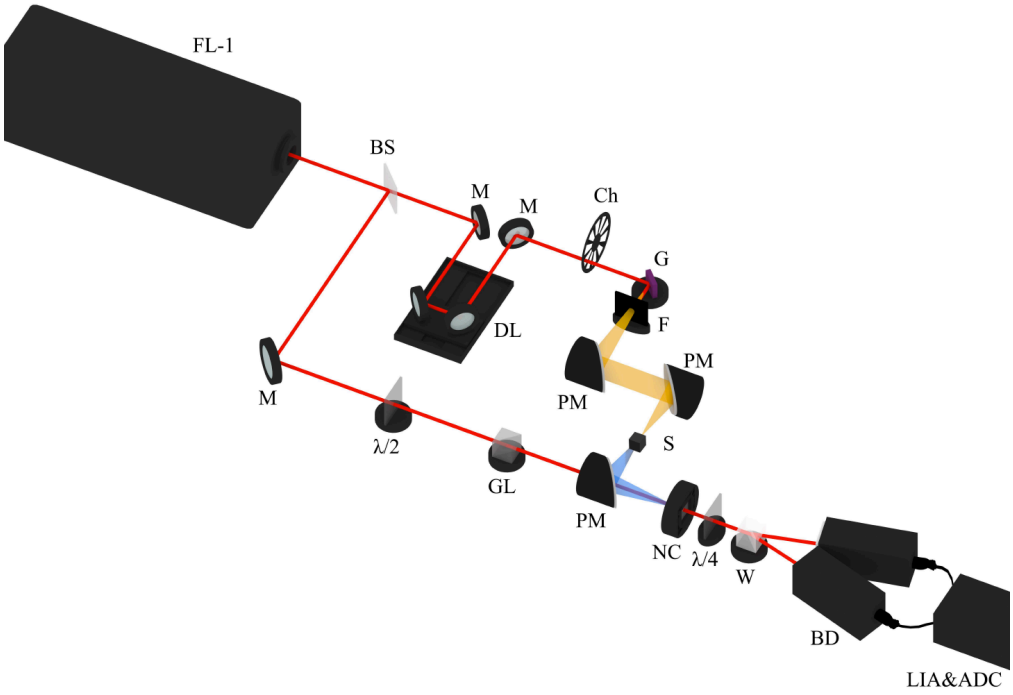


Fig. 1 Scheme of THz time-domain spectrometer (TDS). FL-1 – femtosecond IR laser, M – mirror, BS – beam splitter, λ/2 – half-wave plate, GL – Glan prism, DL – optical delay line, CH – chopper, G – THz-generator (InAs crystal locates inside of the constant magnetic field of 2T), F – Teflon filter, PM – parabolic mirror, S – sample, NC – nonlinear crystal detector (CdTe), λ/4 – quarter-wave plate, W – Wollaston prism, BD – balanced photodiodes, LIA – Lock-in-amplifier, ADC – analog-to-digital converter.

2.3 Investigation methods

Morphology and mechanical properties. The thickness of samples (*d*) was determined at ten different points on each composition using a standard digital micrometer T050011 Tehrim (Russia) with an accuracy of ±5 μm. Tensile properties of the samples, obtained from 15 ml volume of solutions, were determined using the electromechanical testing machine Instron 5966 (USA) equipped with a 10 kN load cell, the pneumatic action grip system and special software Bluehill 3. During the tests 6 film samples of each composition with rectangular shape and dimension of 50×10 mm^2 were subjected to tensile deformation at 50 mm/min rate that conforms to the standard ASTM D882-12. To obtain the micro-transmitted light images of the biopolymer structures, we used an Olympus STM6 microscope.

Terahertz time-domain spectroscopy. Optical properties and spectral characteristics of the samples were measured using the THz-TDS (Fig. 1). The THz signals were recorded using the electro-optical sampling technique.

First, infrared (IR) femtosecond laser beam is divided into a pump beam and a probe beam at 90:10 ratio intensity of beam source, respectively. The pump beam passes through optical delay line (motorized reflector), optical chopper and incidents on indium arsenide (InAs) crystal positioned in the constant magnetic field of 2T. The generation of terahertz radiation using the InAs crystal is based on the Dember effect. Next, THz beam is focused, passes through sample and then incidents on the cadmium tellurium crystal (NC). Meanwhile, the probe beam passes through a half-wavelength plate and a Glan prism to achieve the linear polarization. After that the probe beam also enters in NC through a hole in the parabolic mirror and focusing lens. The CdTe crystal turns to be anisotropic due to the Pockel's effect when there is incidence of THz radiation, and the polarization of the probe beam becomes elliptical. Afterwards, the probe beam passes the quarter-wave plate and the Wollaston prism, after which splits into two orthogonal components (vertical and horizontal polarization). These beams incident on the balanced detector, and it gives analogue signal of the intensity differences between these two polarizations. This difference is proportional to the THz beam amplitude. Then the analogue signal goes into lock-in-amplifier as input, while reference input is given from the chopper. After that result signal gets into analog-to-digital converter (ADC) and then digital signal enters PC. The arrival time of the probe pulse with respect to the THz pulse is varied by moving the optical delay line, and the THz pulse is scanned and its waveform is finally registered. The optical delay line is controlled by PC through a digital-to-analog converter (DAC).

The THz-TDS has the following parameters: the wavelength of femtosecond laser is 1040 nm, the pulse duration ≤200 fs, the average power is up to 1 W; the terahertz radiation output: the pulse duration is around 2.7 ps, the frequency of modulation is 773 Hz, the

frequency range is from 0.2 to 1 THz, the dynamic range is up to 50 dB. In the experiments, the frequency resolution is approximately 50 GHz.

Extraction of optical properties. The optical property measurement of biopolymers was performed in transmission mode. First, the reference signal was obtained while no sample was placed in the TDS setup. Then the samples were placed on the sample mount and were measured at ambient temperature (20 °C) one by one. For each sample, five measurements were performed continuously. Then the averaged waveforms were used to calculate the optical properties of the samples to diminish the system errors. The waveforms were first filtered using the Gaussian window to acquired correct phases [19]. After the filtration, the Fourier transform was done to extract information such as amplitude and phase. The following formulas were then used to calculate the refractive index and absorption coefficient getting from the transmission mode [20–22]:

$$\alpha(\nu) = -\frac{2}{d}\ln\frac{\left|\hat{E}_{sample}(\nu)\right|}{\sqrt{T(\nu)}\left|\hat{E}_{reference}(\nu)\right|}; \quad (1)$$

$$n(\nu) = 1 + \frac{c\left[\psi_{sample}(\nu) - \psi_{reference}(\nu)\right]}{2\pi\nu d}; \quad (2)$$

$$T(\nu) = 1 - R = 1 - [n(\nu) - 1]^2/[n(\nu) + 1]^2, \quad (3)$$

where α – the absorption coefficient of the sample, n – the refractive index of the sample, $\hat{E}_{reference}$, $\hat{E}_{sample}$ – the complex amplitudes of reference and sample signal, respectively, $\psi_{reference}$, ψ_{sample} – the phase of reference and sample signal, respectively, ν – the frequency, d – the thickness of the sample, R – the Fresnel loss (reflectance) at the air-sample interface, c – the speed of light.

The optical property measurement of each component was carried out in reflection mode. One component was mounted on a plastic plate, was covered by a dielectric lossless silicon window with the thickness of 325 μm and the refractive index of 3.425. The THz beam reached the surface of window at normal incidence, then the THz beam was reflected at air-window interface and window-sample interface. Thus in one measurement two pulses were recorded. The first pulse is the reference and the second pulse is the sample signal. The two pulses were extracted using Gaussian windows accordingly. The same as the measurement of biopolymers, for each component five measurements were carried out to calculate the average amplitude of the THz waveform. For the extraction of the optical properties getting from the reflection mode, the following formulas were used [23]:

$$n_S(\nu) = \frac{n_w(1 - A^2)}{1 + A^2 + 2A\cos\psi}; \quad (4)$$

$$\alpha_S(\nu) = \frac{2n_w A\sin\psi}{1 + A^2 + 2A\cos\psi}\cdot\frac{4\pi}{c}; \quad (5)$$

$$A\exp(i\psi) = \\ = \frac{1 - n_w^2}{4n_w}\exp\left[2jn_w\frac{2\pi\nu d_w}{c}\right]\frac{\hat{E}_{sample}(\nu)}{\hat{E}_{reference}(\nu)}, \quad (6)$$

where n_s, n_w – the refractive index of the sample and dielectric window, respectively, α_S – the absorption coefficient of the sample, ν – the frequency, $\hat{E}_{reference}$, $\hat{E}_{sample}$ – the complex amplitudes of reference and sample signal, respectively, A and ψ – the amplitude and the phase of complex expression from Eq. (6), d_w – the thickness of the window, c – the speed of light.

3 Experiment results

3.1 Morphology of biopolymers

Fig. 2 shows the typical morphology of the gelatin-starch-glycerol biopolymer with a phase separation of the components in the form of a continuous major phase of gelatin and a minor starch microdomain phase built into it. Also, microphotographs show dark regions localized mainly close to the interfacial region of biopolymers. These objects belong to the dispersed phase of bentonite filler particles, which absorb visible light. The microphotograph in Fig. 2b shows that an increase in φ to 7 wt.% leads to an increase in the planar area of the dark regions associated with the filler phase. In this case, the localization of the filler is observed more clearly.

3.2 Mechanical properties of biopolymers

Fig. 3 presents the results of mechanical tensile testing of the biopolymers. The particles of bentonite clay in an amount of $\varphi < 5$ wt.% do not significantly change the tensile strength of the materials. However, a further increase in the bentonite content to $\varphi = 7$ wt.% leads to a twofold (to $\sigma = 19$ MPa) reinforcement of the composite polymer matrix. The results in Fig. 3b show that the elongation at break (η) of the biopolymers decreases from $\eta = 81\%$ to $\eta = 51.5\%$ as the concentration of bentonite particles increases from $\varphi = 1$ wt.% to $\varphi = 9$ wt.%. Besides, the subsequent increase of the φ value does not affect the flexibility of the material. As can be seen from Fig. 3c, the stiffness of the biopolymer matrix increases significantly only from $E = 140$ MPa at $\varphi = 7$ wt.% to $E = 447$ MPa at $\varphi = 9$ wt.%.

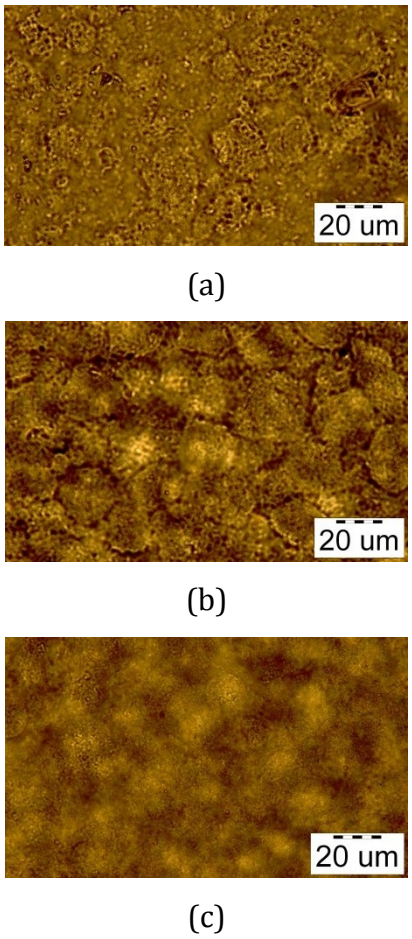


Fig. 2 Optical transmitted-light microphotographs of the biopolymers at (a) φ = 3 wt.%, (b) φ = 7 wt.% and (c) φ = 9 wt.%.

3.3 THz optical properties of biopolymers

First, the biopolymers with the same bentonite content of φ = 9 wt.% but with the different thicknesses were fabricated and measured. As seen in Fig. 4a, the refractive indices of the biopolymers becomes more reproducible in 0.2–1 THz frequency range as the thickness of the biopolymer increases over 186 μm. A resonance can be observed when biopolymer is thin. The absorption coefficient (Fig. 4b) in the frequency range from 0.2 to 1 THz has the same behavior, that by increasing the biopolymer thickness, the absorption coefficient becomes more reproducible.

In general, the THz optical properties of a material should not change no matter how its thickness changes. But in our case, the properties change because the proposed biopolymer with the thicknesses lower than 186 μm is inhomogeneous in the direction of THz wave propagation.

The biopolymers without bentonite were also measured to investigate the influence of bentonite concentration on the THz optical properties of the biopolymers. The results (Fig. 5) show that with an increase of bentonite content, the refractive index increases, while the absorption coefficient has no clear dependency on bentonite concentration.

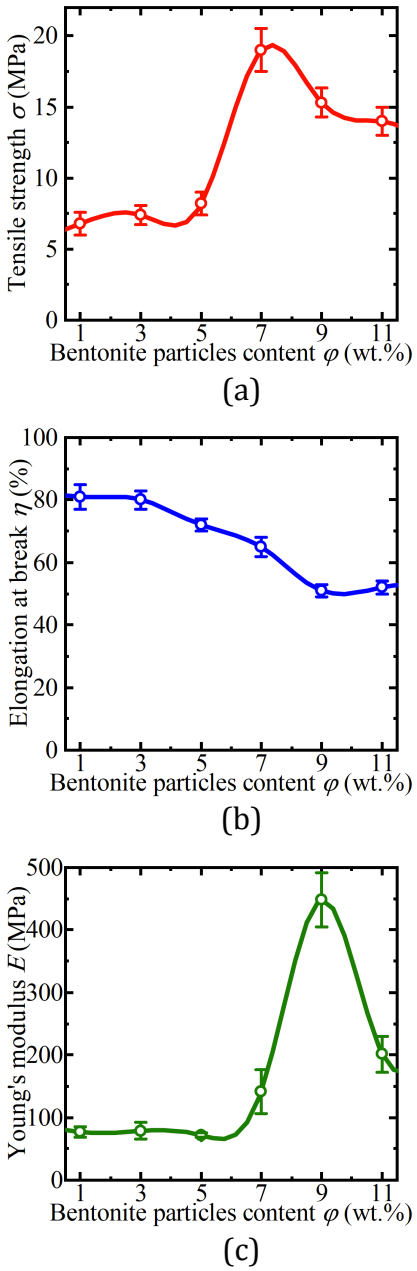


Fig. 3 Behavior of the (a) tensile strength, (b) elongation at break and (c) Young's modulus of the biopolymers depending on φ value.

To study further, more biopolymers with the thicknesses less than 186 μm were also measured in the frequency range from 0.2 to 1 THz. Control variates method was used. First, the thickness of the samples was controlled as 0.125 mm. In Fig. 6a, the refractive indices of the biopolymers increase monotonically as the φ value increases. The absorption coefficients have no clear dependency on bentonite concentration. The results indicate that the influence of bentonite content on the THz optical properties of biopolymers thicker than 186 μm also happens with the biopolymer thinner than 186 μm. The homogeneity of the biopolymer does not change this behavior.

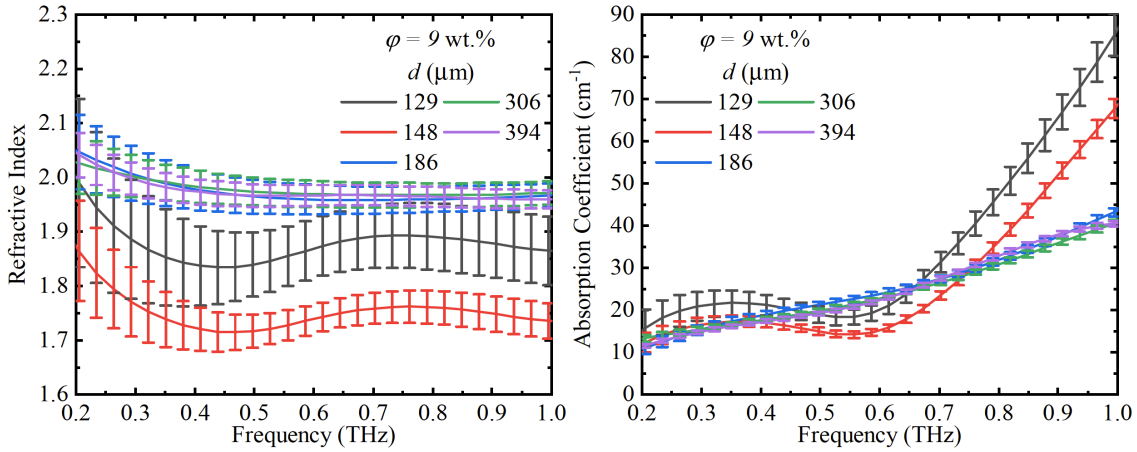


Fig. 4 The dispersion of (a) refractive index and (b) absorption coefficient of the biopolymers at φ = 9 wt.% and different thicknesses in the frequency range of 0.2–1.0 THz.

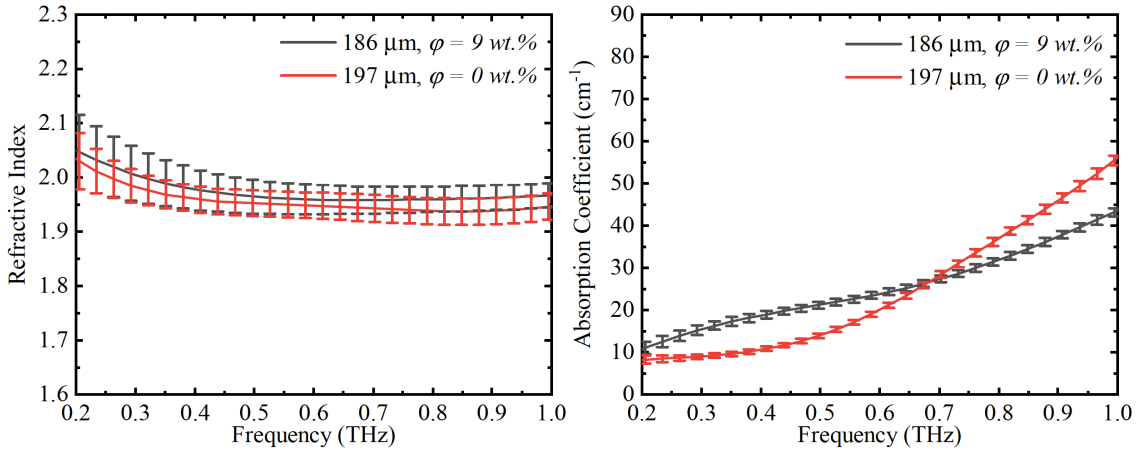


Fig. 5 The dispersion of (a) refractive index and (b) absorption coefficient of the biopolymers at φ = 9 wt.% and φ = 0 wt.% with the similar thicknesses of 186 μm and 197 μm, respectively, in the frequency range of 0.2–1.0 THz.

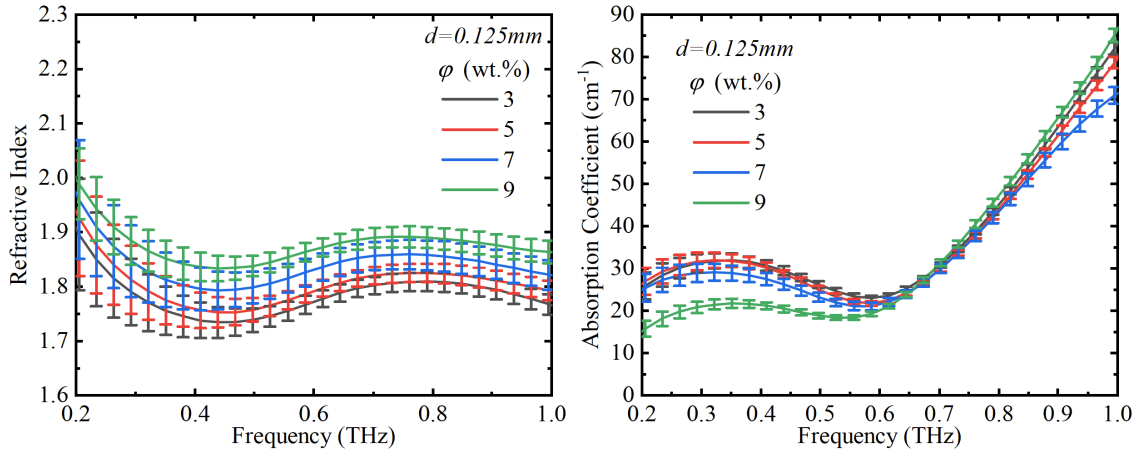


Fig. 6 The dispersion of (a) refractive index and (b) absorption coefficient of the biopolymers at various φ value and the fixed thickness of 125 μm in the frequency range of 0.2–1.0 THz.

3.4 THz optical properties of components

THz optical properties of each components were also measured using THz TDS in reflection mode as shown in Fig. 7. THz optical properties of water were also compared with the published data [24] for the device calibration. The data of each components were then used in the numerical models.

4 Numerical models

Generally, the interaction of terahertz waves with a composite material is described by effective medium theory (EMT), which can be used to estimate the complex permittivity $\hat{\varepsilon}_R$ of a composite material. In this paper, three well-known theoretical models of EMT, namely CRI model [25], LLL model [25] and Bruggeman model [26] generalized for the anisotropic inclusions of N-component mixture, as well as an iterative method [27] based on Bruggeman model were used for the optical property prediction of 5-component mixture.

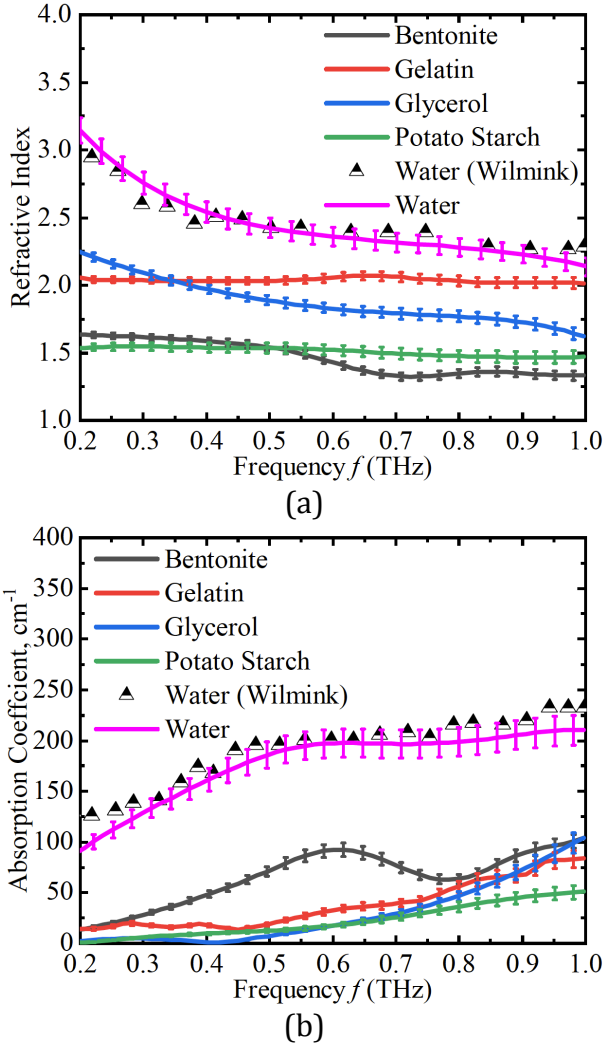


Fig. 7 The dispersion of (a) refractive index and (b) absorption coefficient of all components in the frequency range of 0.2–1.0 THz. The reference data of water are from Ref. [24].

The first EMT theoretical model we decided to use is multi-component CRI model:

$$\hat{n}_R = \sum_{i=1}^{N} f_i \hat{n}_i. \tag{7}$$

Here $\hat{n}_R$ is the complex refractive index of the heterogeneous mixture, f_i is the volume fraction for i-th inclusion of the dispersed component, $\hat{n}_i$ is the complex refractive index of i-th inclusion in the heterogeneous mixture.

The second of considered EMT theoretical model is multi-component LLL model:

$$\sqrt[3]{\hat{\varepsilon}_R} = \sum_{i=1}^{N} f_i \sqrt[3]{\hat{\varepsilon}_i}, \tag{8}$$

where f_i is the volume fraction for i-th inclusion of the dispersed component, $\hat{\varepsilon}_R$ is the complex permittivity of the heterogeneous mixture, $\hat{\varepsilon}_i$ is the complex permittivity of the i-th dispersed component. This model describes a biopolymer matrix with low volume fraction values of the components and applicable to mixtures of irregularly shaped particles.

The third one, is the mostly used EMT theoretical model – Bruggeman model, which explicitly considers the influence of the inclusions shape and orientation as well structure anisotropy and is described by the following equation [28]:

$$\sum_{i=1}^{N} f_i \frac{\hat{\varepsilon}_i - (\hat{\varepsilon}_R)_p}{(\hat{\varepsilon}_R)_p + \nu_{ip}\left[\hat{\varepsilon}_i - (\hat{\varepsilon}_R)_p\right]} = 0, \tag{9}$$

where $\hat{\varepsilon}_R$ is the complex permittivity of the heterogeneous mixture, f_i is the volume fraction for i-th inclusion of the dispersed component, $\hat{\varepsilon}_i$ is the complex permittivity of the i-th dispersed component, ν_{ip} is the depolarization coefficient for the i-th inclusion and p-th principal axis, $(\hat{\varepsilon}_R)_p$ principal values (diagonal elements) of $\hat{\varepsilon}_R$.

For the iterative method proposed in Ref. [27], the complex permittivity of two-component (gelatin-in-water) $\hat{\varepsilon}_{R_1}$ is calculated first by the Eq. (9) for the spherical particles. Further, the obtained value $\hat{\varepsilon}_{R_1}$ is equated to the complex permittivity of matrix inside which the third component (starch) is considered using the Bruggeman equation for the lamellar (disk) particles. By repeating this iteration procedure, first put glycerol (spherical particles) into account, then add bentonite using the formula for disk particles, the complex dielectric constant $\hat{\varepsilon}_R$ of the five component mixture can be estimated. The order of components during the iteration was taken in accordance with the order of sample preparation.

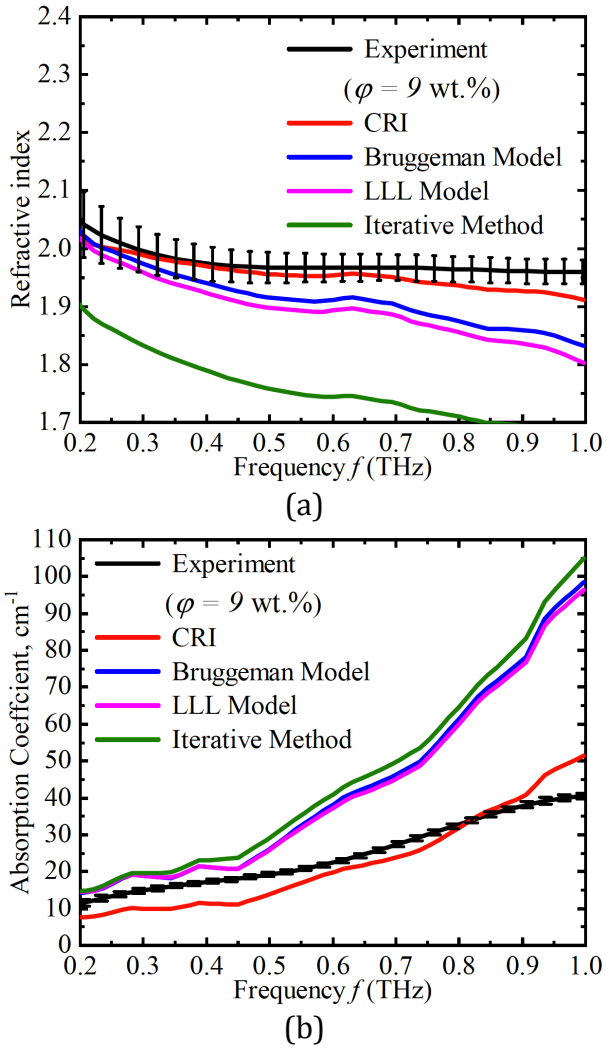


Fig. 8 Numerical simulation results of the dispersion of (a) refractive index and (b) absorption coefficient of the biopolymers at φ = 9 wt.% in the frequency range of 0.2–1.0 THz.

Fig. 8 shows that the refractive index and the absorption coefficient of the biopolymer with the thickness of 306 μm is closer to the estimated THz optical properties obtained using CRI model.

5 Discussion

The visual analysis of the biopolymer morphology using optical microscopy (Fig. 2) shows that the biopolymers have a heterogeneous structure with phase separation of the components (see Section 3.1). The observed effect is a consequence caused by the shear stresses of the gelatin and starch solutions at the drying temperature of the gel-forming solution [29]. We previously found [30] that when the biopolymer solution is thermally dried and the molecular mobility of gelatin's polymer chains is higher than that of starch in solution, which leads to the coalescence of the minor phase drops of the starch solution.

In addition to the phases of the biopolymer matrix, the morphology of the biopolymers shows dark regions at their interface, relates mainly to the localized phase of bentonite clay solid particles. Their localization becomes more pronounced with increasing the φ value. It is seen that at φ = 7 wt.% a dense network of filler particles is observed. Such localization of the filler phase is a consequence not only of the relatively high mobility of the polypeptides in the gelatin compared to starch macromolecules, but also of the increased intermolecular interactions between bentonite-water-starch [31].

A tensile test of the biopolymers was carried out. The result shows that for φ < 5 wt.%, the presence of bentonite particles does not significantly affect the mechanical properties of the material (see Section 3.2). When the concentration of the filler particles rises to φ = 5 wt.%, a strong increase in the σ value is observed. However, a further increase in φ to 9 wt.% does not lead to significant reinforcing of the polymer matrix, while greatly increasing of E value and, accordingly, the stiffness of the material.

This mechanical behavior of the biopolymers is a consequence of their formed morphology. The introduction of bentonite fillers into the polymer matrix at φ = 7 wt.% leads to the excess of the filler content threshold with the formation of a dense uniform reinforcing network, which brings upmost of the deformation stresses inside the material. A further increase in the filler content leads to the strong localization of its particles and the formation of stress centers, which leads to a decrease in the tensile strength and a strong increase in the stiffness of the material.

The resonance peak appeared in the experiment data in the low terahertz frequency range of 0.3–0.6 THz in Fig. 6 is the resonance caused by starch particles. The resonant frequency can be calculated using the whispering gallery modes approach [32, 33]. As mentioned in the Section 3.1, starch formed a microdomain phase inside of the biopolymer which can be seen from the bright clusters of Fig. 2. The quantity of microdomain phases N_s in one cluster should take into account as 4 or 5. Thus the formula should be written as:

$$r_s = \frac{c}{2\pi n_s f_r N_s}, \tag{10}$$

where r_s is the average radius of the starch particles, c is the light speed, n_s is the average refractive index of the starch particles shown in Fig. 7a, and f_r is the resonant frequency shown in Fig. 6. If we substitute, according to the known parameters, N_s = 4 or 5, c = 3×10^8 m/s, n_s = 1.5, f_r = 0.6 THz into the Eq. (10), then we may accordingly get the possible radius of one starch particles is r_s = 13 ± 2 μm, which are very close to the average radius of the bright areas in Fig. 2.

Fig. 9. shows the comparison of the optical properties of the biopolymers with φ = 9 wt.% bentonite and cancerous and healthy oral tissue. The data of oral tissues are from Ref. [6]. It is clear that there are visible diversities between biopolymers and real tissues. Since

the absorption coefficients of biopolymers are relatively low, THz radiation may penetrate through the biopolymer with low losses. Thus, diseased region can be easily monitored in THz frequency range while the biopolymer is being applied as a drug delivery system. In consideration of the obvious differences in refractive indices, a good reflection can be achieved in the interface between biopolymer and tissue, which may give THz devices a good promise to record noise-less reflection signals *in vivo*. Furthermore, on account of its good mechanical properties, it can be used as the substrate for tissue surface leveling when an in-vivo measurement needs to be carried out [34]. Moreover, by the fact that changing the content of bentonite doesn't influence on the absorption coefficient of the biopolymer effectively but greatly affects its refractive index, the drug delivery system based on it can be fabricated with different refractive indices for different drugs accordingly, depending on whether the drug layer needs to be taken into account. According to the published researches [35–37], THz-TDS may distinguish the layers of polymeric materials by detecting the reflection of THz waves and has better resolution than other conventional ultrasonic and optical devices. Thus, the biopolymer may also be used as the potential substrate for *in vivo* THz measurements.

6 Conclusions

In this work, we obtained a solid-state biopolymer material based on gelatin-starch biopolymer matrix filled with plasticizing glycerol and various loadings of reinforcing bentonite clay particles. The biopolymers were subjected to an analysis of the morphology, mechanical tensile properties and optical properties in the THz frequency range. Also, the results of optical measurements were analytically described using Complex Refractive Index model as the best theoretical approach.

It is shown that the morphology of biopolymers has a pronounced heterogeneous structure with phase separation of components and strongly depends on the content of bentonite filler. It is found that the introduction of bentonite up to 7 wt.% leads to the formation of a dense reinforcing network in the structure of the material, which entails its strong hardening. With a further increase of bentonite content to 9 wt.%, filler particles are localized in the interfacial region of the material, which leads to the formation of stress centers and reduces the interfacial interaction of the material. These effects lead to reducing the strength and increasing the fragility of the biopolymers.

The THz TDS measurement results show that the refractive index of the biopolymer tends to increase as the bentonite content increases, while the absorption coefficients does not have the same behavior. The THz optical properties of the biopolymer with the thickness higher than 186 μm are more reproducible and stable, and can be accurately described by the CRI model. The absorption troughs appeared at the frequency around 0.6 THz are caused by the resonant state of starch clusters.

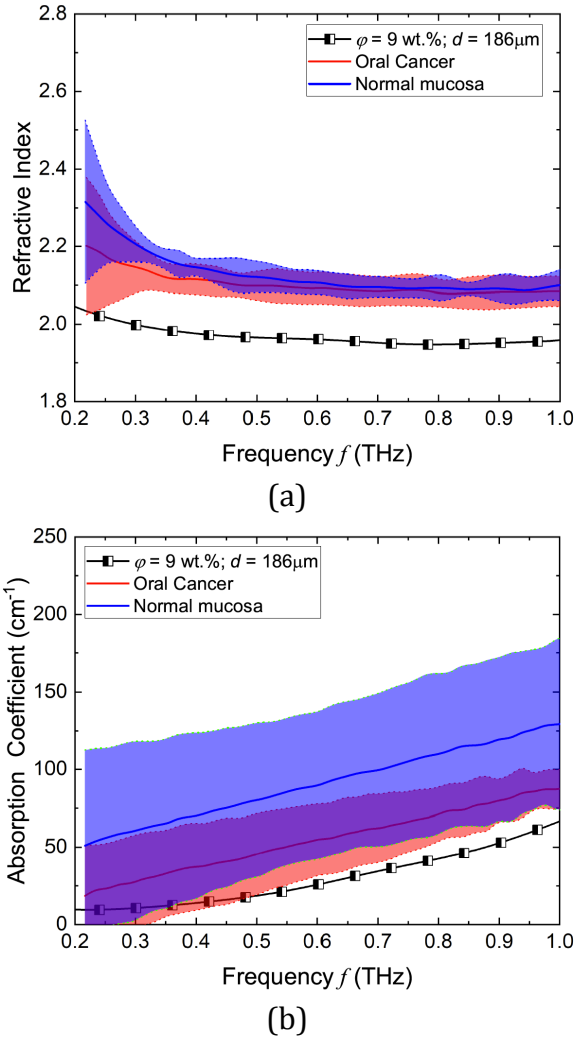


Fig. 9 Comparison of the (a) refractive index and (b) absorption coefficient of the biopolymers at φ = 9 wt.%, cancerous oral tissue [6] and normal mucosa from health oral tissue [6] depending on terahertz frequency.

Due to its relatively lower absorption coefficients, THz radiation may penetrate through the given biopolymer well. Moreover, from the comparison of THz optical properties between the fabricated biopolymer and oral tissues, clear diversities in optical properties can be observed. Such THz optical properties of the biopolymer allow us to confirm the feasibility of using THz radiation for cancer assessment during therapies. The result of our work shows that THz waves should be able to distinguish the buccal drug delivery system (biocomposite), drug layer and oral tissue. The biopolymer may also be used as the potential substrate for in-vivo THz measurements.

Disclosure

All authors declare that there is no conflict of interests in this paper.

Acknowledgement

This research was financially supported by the Government of the Russian Federation (Grant 08-08).

References

1. A. Y. Pawar, D. D. Sonawane, K. B. Erande, and D. V. Derle, "Terahertz technology and its applications," Drug invention today 5(2), 157–163 (2013).
2. J.-H. Son, Terahertz biomedical science and technology, CRC Press (2014).
3. C. Yu, S. Fan, Y. Sun, and E. Pickwell-MacPherson, "The potential of terahertz imaging for cancer diagnosis: A review of investigations to date," Quantitative imaging in medicine and surgery 2, 33–45 (2012).
4. R. Grigorev, A. Kuzikova, P. Demchenko, A. Senyuk, A. Svechkova, A. Khamid, A. Zakharenko, and M. Khodzitskiy, "Investigation of fresh gastric normal and cancer tissues using terahertz time-domain spectroscopy," Materials 13(1), 85 (2020).
5. M. H. Arbab, D. P. Winebrenner, T. C. Dickey, A. Chen, M. B. Klein, and P. D. Mourad, "Terahertz spectroscopy for the assessment of burn injuries in vivo," Journal of Biomedical Optics 18(7), 077004 (2013).
6. Y. C. Sim, J. Y. Park, K.-M. Ahn, C. Park, and J.-H. Son, "Terahertz imaging of excised oral cancer at frozen temperature," Biomedical Optics Express 4(8), 1413–1421 (2013).
7. Y. B. Ji, E. S. Lee, S.-H. Kim, J.-H. Son, and T.-I. Jeon, "A miniaturized fiber-coupled terahertz endoscope system," Optics Express 17(19), 17082–17087 (2009).
8. G. Calixto, J. Bernegossi, B. Fonseca-Santos, and M. Chorilli, "Nanotechnology-based drug delivery systems for treatment of oral cancer: a review," International journal of nanomedicine 9, 3719 (2014).
9. C. Dianzani, G. P. Zara, G. Maina, P. Pettazzoni, S. Pizzimenti, F. Rossi, C. L. Gigliotti, E. S. Ciamporcero, M. Daga, and G. Barrera, "Drug delivery nanoparticles in skin cancers," BioMed research international 2014, 895986 (2014).
10. J. H. Han, Innovations in Food Packaging, Elsevier B.V. (2005).
11. D. Verma, E. Fortunati, Biopolymer processing and its composites, Elsevier Ltd (2019).
12. O. Moreno, À. Gil, L. Atarés, and A. Chiralt, "Active starch-gelatin films for shelf-life extension of marinated salmon," LWT - Food Science and Technology 84, 189–195 (2017).
13. H. Chen, M. Yang, Z. Shan, S. Mansouri, B. K. May, X. Chen, H. Chen, and M. W. Woo, "On spray drying of oxidized corn starch cross-linked gelatin microcapsules for drug release," Materials Science and Engineering: C 74, 493–500 (2017).
14. H. Chen, Z. H. Shan, M. W. Woo, and X. D. Chen, "Preparation and characteristic of gelatine/oxidized corn starch and gelatin/corn starch blend microspheres," International Journal of Biological Macromolecules 94, 326–334 (20170.
15. N. Zhang, H. Liu, L. Yu, X. Liu, L. Zhang, L. Chen, and R. Shanks, "Developing gelatin-starch blends for use as capsule materials," Carbohydrate Polymers 92(1), 455–461 (2013).
16. O. Moreno, L. Atarés, A. Chiralt, M. C. Cruz-Romero, and J. Kerry, "Starch-gelatin antimicrobial packaging materials to extend the shelf life of chicken breast fillets," LWT 97, 483–490 (2018).
17. S. Wannaphatchaiyong, P. W. S. Heng, J. Suksaeree, P. Boonme, and W. Pichayakorn, "Lidocaine loaded gelatin/gelatinized tapioca starch films for buccal delivery and the irritancy evaluation using chick chorioallantoic membrane," Saudi Pharmaceutical Journal 27(8), 1085–1095 (2019).
18. V. A. d. S. Garcia, J. G. Borges, V. B. V. Maciel, M. R. Mazalli, J. d. G. Lapa-Guimaraes, F. M. Vanin, and R. A. de Carvalho, "Gelatin/starch orally disintegrating films as a promising system for vitamin C delivery," Food Hydrocolloids 79, 127–135 (2018).
19. J. Vázquez-Cabo, P. Chamorro-Posada, F. J. Fraile-Peláez, Ó. Rubiños-López, J. M. López-Santos, and P. Martín-Ramos, "Windowing of THz time-domain spectroscopy signals: A study based on lactose," Optics Communications 366, 386–396 (2016).
20. S. L. Dexheimer, Terahertz spectroscopy: principles and applications, CRC press (2007).
21. D. Swinehart, "The Beer-Lambert law," Journal of Chemical Education 39(7), 333 (1962).
22. M. Naftaly, R. E. Miles, "Terahertz time-domain spectroscopy for material characterization," Proceedings of the IEEE 95(8), 1658–1665 (2007).
23. M. Naftaly, Terahertz metrology, Artech House (2015).
24. G. J. Wilmink, B. L. Ibey, B. D. Rivest, J. E. Grundt, W. P. Roach, T. D. Tongue, B. J. Schulkin, N. Laman, X. G. Peralta, C. C. Roth, C. Z. Cerna, B. D. Rivest, J. E. Grundt, and W. P. Roach, "Development of a compact terahertz time-domain spectrometer for the measurement of the optical properties of biological tissues," Journal of Biomedical Optics 16(4), 047006 (2011).

25. M. Scheller, C. Jansen, and M. Koch, "Applications of effective medium theories in the terahertz regime," Chapter in Recent Optical and Photonic Technologies, InTech Rijeka, Croatia, 231–250 (2010).
26. V. A. Markel, "Introduction to the Maxwell Garnett approximation: tutorial," Journal of the Optical Society of America A 33(7), 1244–1256 (2016).
27. R. Nazarov, T. Zhang, M. Khodzitsky, and P. Demchenko, "Comparative study of quantitative methods to determine component concentration for water-free biotissue phantom," SPIE Proceedings 11075, 110750Y (2019).
28. D. Schmidt, M. Schubert, "Anisotropic bruggeman effective medium approaches for slanted columnar thin films," Journal of Applied Physics 114(8), 083510 (2013).
29. H. Firoozmand, B. S. Murray, and E. Dickinson, "Microstructure and rheology of phaseseparated gels of gelatin + oxidized starch," Food Hydrocolloids 23(4), 1081–1088 (2009).
30. A. Podshivalov, M. Zakharova, E. Glazacheva, and M. Uspenskaya, "Gelatin/potato starch edible biocomposite films: Correlation between morphology and physical properties," Carbohydrate Polymers 157, 1162–1172 (2017).
31. F. Xie, E. Pollet, P. J. Halley, and L. Avérous, "Starch-based nano-biocomposites," Progress in Polymer Science 38(10–11), 1590–1628 (2013).
32. V. Klimov, Nanoplasmonics, Pan Stanford (2014).
33. G. C. Righini, Y. Dumeige, P. Feron, M. Ferrari, G. Nunzi Conti, D. Ristic, and S. Soria, "Whispering gallery mode microresonators: fundamentals and applications," La Rivista del Nuovo Cimento 34, 435–488 (2011).
34. K. I. Zaytsev, A. A. Gavdush, N. V. Chernomyrdin, and S. O. Yurchenko, "Highly accurate in vivo terahertz spectroscopy of healthy skin: Variation of refractive index and absorption coefficient along the human body," IEEE Transactions on Terahertz science and Technology 5(5), 817–827 (2015).
35. S. Wietzke, C. Jansen, M. Reuter, T. Jung, D. Kraft, S. Chatterjee, B. M. Fischer, and M. Koch, "Terahertz spectroscopy on polymers: A review of morphological studies," Journal of Molecular Structure 1006(1–3), 41–51 (2011).
36. P. Lopato, T. Chady, "Terahertz detection and identification of defects in layered polymer composites and composite coatings," Nondestructive Testing and Evaluation 28(1), 28–43 (2013).
37. A. Redo-Sanchez, B. Heshmat, A. Aghasi, S. Naqvi, M. Zhang, J. Romberg, and R. Raskar, "Terahertz time-gated spectral imaging for content extraction through layered structures," Nature communications 7(1), 1–7 (2016).

Study by optical techniques of the dependence of aggregation parameters of human red blood cells on their deformability

Anastasia I. Maslyanitsyna[1*], Petr B. Ermolinsky[1], Andrei E. Lugovtsov[1,2], and Alexander V. Priezzhev[1,2]

[1] Physics faculty, Lomonosov Moscow State University, Leninskie Gory 1-2, Moscow 119991, GSP-1, Russian Federation
[2] International Laser Centre, Lomonosov Moscow State University, Leninskie Gory 1-62, Moscow 119991, GSP-1, Russian Federation

*** e-mail:** stasyazavr2000@biomedphotonics.ru

Abstract. Blood microcirculation in human body is greatly dependent on the microrheologic properties of red blood cells. The aim of this work is to identify the relationship between the deformability of these cells and their aggregation properties, both of which are the key factors for the blood flow. Laser diffractometry, diffuse light scattering and laser tweezers were implemented for *in vitro* measurements. Different osmolarity of plasma (150–500 mOsm/l) and concentrations of glutaraldehyde (up to 0.004%) were used to change the deformability of healthy red blood cells *in vitro*. The results show that with the cells becoming more rigid some aggregation parameters (e.g. the fraction of aggregated cells) decrease, while some of them (e.g. the hydrodynamic strength of the aggregate) stay unchanged. For example, after incubation in 0.004% glutaraldehyde solution the erythrocyte deformability drops by 19 ± 2% and this leads to a decrease by 77 ± 4% in the aggregation index. This means that there is a connection between cell deformability and the formation of the aggregates, however the relationship is less pronounced and more complex for the disaggregation process.
© 2020 Journal of Biomedical Photonics & Engineering.

Keywords: blood; erythrocytes; red blood cell aggregation; deformability; laser diffractometry; laser tweezers; diffuse light scattering; glutaraldehyde; osmolarity.

Paper #3359 received 19 May 2020; revised manuscript received 15 Jun 2020; accepted for publication 19 Jun 2020; published online 22 Jun 2020. doi: 10.18287/JBPE20.06.020305.

1 Introduction

The state of human organism largely depends on blood microcirculation that, in turn, depends on the microrheologic properties of red blood cells (RBCs), in particular, the RBC intrinsic properties of deformability and aggregation that some research [1] shows as interdependent.

The RBCs have the ability to be deformed in the blood flow. Usually they elongate in the direction of the flow, but also, they can change their shape dramatically in the vessels that are smaller than the size of the RBCs, for example, capillaries with a 3 to 5 μm radius [2]. A considerable contribution to the deformability comes from the elasticity of the cell membrane, as well as from the hemoglobin solution inside [3]. RBC deformability plays a significant role in the blood circulation. In particular, RBC filtering in narrow circulatory pathways in the human spleen is based on their impaired deformability [4].

Another important process that influences the blood flow is the aggregation of RBCs [5]. It is a reversible process of creation of linear and more complex structures of RBCs. The aggregation happens dominantly inside large vessels [5]. However, the aggregates can become quite large themselves, and if

not their ability to disaggregate to single cells, the blood flow would be impaired.

Socially significant diseases such as arterial hypertension, diabetes mellitus and others are associated with serious changes in the RBC deformability [6, 7]. At the same time a significant change in the aggregation parameters happens. For example, RBC aggregates in the blood of patients suffering from arterial hypertension are stronger and form faster than in the blood of healthy people [8]. Moreover, these pathologies are accompanied by an alteration in the number of RBC involved in the process of spontaneous aggregation [9]. This can be caused by many reasons: a change in the protein composition of plasma, cell membrane changes, different rigidity and age of the cells, as well as the average patient age and their medication, etc. [5].

The aim of this work is to study the effect of RBC deformability on their aggregation properties using optical methods *in vitro*. By establishing this relationship, one can better predict the effect of drugs such as Semax [10] on both of the discussed parameters. Also, it is a small step towards understanding the RBC aggregation process fundamentally.

2 Materials and methods

2.1 Blood samples

The blood was drawn from two healthy individuals who gave informed consent. Blood was stabilized by EDTA anticoagulant. The experiments were carried out within 3 h after the sample collection. The RBCs were separated from the plasma by centrifuging the sample at 170g for 10 min, then the plasma was centrifuged for 10 min at 3000g to remove the buffy coat. After that, two treatments were used to change the deformability of RBC. The first one included washing the RBCs thrice with isotonic phosphate-buffered saline (PBS), incubating them in glutaraldehyde (GA) solutions in a range 0 to 0.004% for 30 minutes at room temperature (according to the protocol in Ref. [11]), washing them three times in PBS again and then adding them to plasma at 40% hematocrit. The second one included mixing the plasma with PBS and NaCl in order to achieve different osmolarities 150 to 500 mOsm/l and then adding RBC at 40% hematocrit. Next, three optical techniques described in more detail in the work [12] were used to study the cells *in vitro*.

2.2 Laser tweezers

A part of the measurements was carried out with laser tweezers using a highly diluted RBC suspension [13]. Two-channel optical tweezers based on a Nd:YAG laser with diode pumping (λ = 1064 nm, 200 mW) allow us to manipulate single cells and measure the forces of interaction between them without a direct mechanical contact [7]. Thus, numerical values of the forces of aggregation and disaggregation on pairs of single RBCs (doublets) were obtained. The aggregation force is the minimum force necessary to prevent spontaneous aggregation and the disaggregation force is the minimum force required to separate a pair of aggregated RBCs. The measurements were performed at room temperature.

2.3 Laser aggregometry

Laser aggregometry was performed using the RheoScan aggregometer (Rheomeditech, Seoul, Korea) [14]. It is based on diffuse light scattering and is applied to whole blood samples in order to retrieve a number of the RBC aggregation properties. By analyzing the scattered light intensity as a function of time during the process of RBC spontaneous aggregation we can evaluate the aggregation index (AI), which characterizes the ratio of aggregated cells during the first 10 sec of the aggregation process [14]. Besides that, the critical shear stress (CSS) that characterizes the balance of aggregation and disaggregation processes was measured. In order to do it, the blood flow conditions were created *in vitro* with varying shear stress, and the light scattered backwards was analyzed. The measurements were performed at 37 °C.

2.4 Laser deformometry

Laser deformometry performed with the RheoScan diffractometer was used to obtain the shear induced deformation parameters of RBCs by processing the light intensity distribution in the diffraction pattern [15]. This pattern is based on diffraction of a laser beam on a highly diluted RBC suspension in a flow channel *in vitro*. The dimensions of the channel are 0.2 mm high × 4.0 mm wide × 40 mm long. We measured the RBC deformability index (DI) that describes the average elongation of the cells by shear stress illuminated by the laser beam induced. The elongation of the cells corresponds to the elongation of the diffraction pattern. Different shear stresses from 20 Pa to 0.5 Pa are applied to the RBC suspension in order to change the shear stress and, consequently, the elongation of the cells. Shear stress is calculated automatically assuming a parabolic velocity profile [11]. The measurements were performed at 37 °C.

2.5 Statistical analysis

This study was conducted on the blood of 2 healthy donors. The values of AI, DI and the forces of RBC interaction were measured 5 times for the same sample. The results were then averaged and the standard deviations from the mean values were calculated.

3 Results and discussion

3.1 RBC deformability changes

The RBC deformability changes are presented in the Fig. 1. Firstly, results in the Fig. 1a show a decrease in the deformability index with the increase of GA

concentration that corresponds to the conclusions from the study [16]. The deformability of all GA treated samples is lower than that of the control sample. The deformability index at the highest shear stress of 20 Pa of the sample with maximum GA concentration (0.004%) is 16 ± 2% lower than the control. For shear stresses less than 6 Pa the relationship is not that clear. This can happen because the viscosity of the cytoplasm inside of the cell plays a role in the deformability at sufficiently high shear stress. As discussed in Ref. [17] GA cross-links the proteins inside the cells. In the study [18] the authors present a dependence of RBC deformability for different GA concentrations measured with ectacytometer LORRCA. It shows a conclusive decrease of deformability in the samples treated with GA at high shear stress similar to that in Fig 1a.

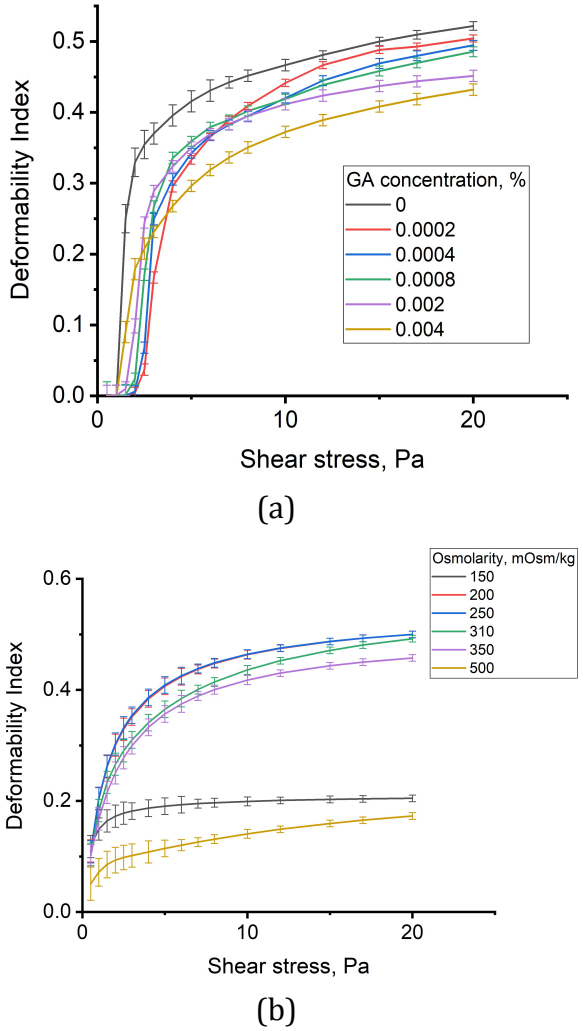


Fig. 1 The deformability index as a function of the shear stress (a) at different glutaraldehyde concentrations and (b) at different osmolarities. The values were measured 5 times for each donor. The averaged values for two donors and the standard deviations from the mean are presented.

Secondly, in a separate experiment, the osmolarity of the suspension was also shown to influence RBC deformability as seen in Fig. 1b. The normal osmolarity of plasma of two healthy volunteers was measured to be 300 mOsm/l. We found that the deformability curve corresponding to the normal osmolarity level does not lie above all other curves, and even at 20 Pa the DI control value is similar to that of 200 and 250 mOsm/l. However, any significant upward or downward variations of osmolarity decrease the RBC deformability dramatically. A similar dependence is described in the following work [19]. A more complicated relationship between osmolarity and deformability is discussed in Ref. [20], where the authors show that the deformability of RBC actually rises again at around 100 mOsm/l.

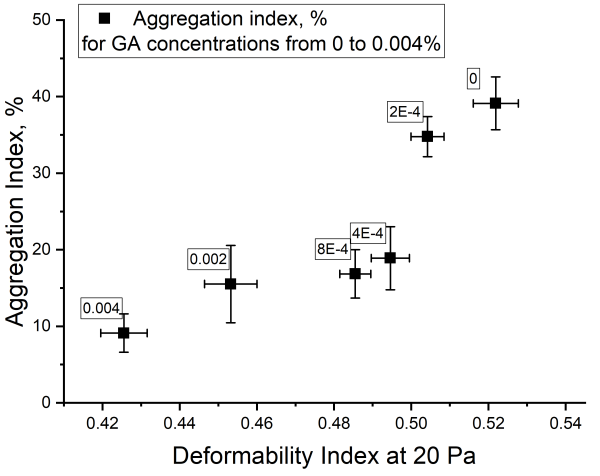
3.2 RBC aggregation changes

The results obtained by laser aggregometry for the samples treated with GA are shown in Fig. 2. The aggregation index significantly drops for samples with low DI, which corresponds to high GA concentration. Namely, the control measurement (0% GA) yields DI equal to 0.522 ± 0.006 and AI equal to 39 ± 4%. For 0.004% GA concentration DI decreases to 0.426 ± 0.006 and AI decreases to 9 ± 3%. This means that at high GA concentrations the process of spontaneous aggregation almost stops.

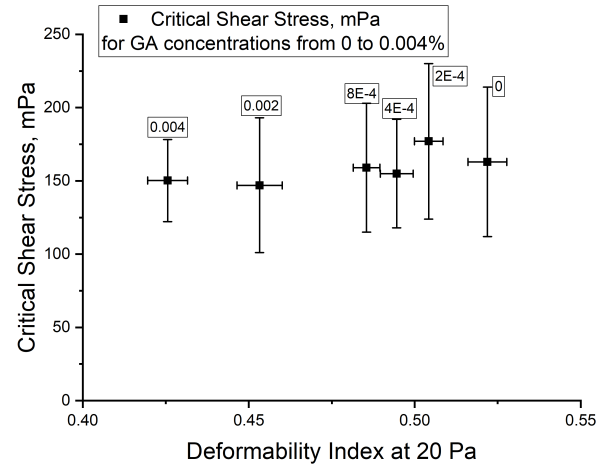
The CSS parameter (Fig. 2b) remains unchanged at 160 ± 40 mPa for all DI levels without any significant differences due to the large deviations of its values. On the one hand, the balance of aggregation and disaggregation in flow conditions obviously depends on the aggregability of RBC, but on the other hand, this method measures the hydrodynamic strength of the aggregates, not their number in the sample. Article [21] suggests that membrane deformability does not influence the aggregate break-up in steady uniform shear flow. Also, the difference between the deformability of interacting RBC within one sample can explain large deviations. The following computer model [22] based on the depletion theory of RBC aggregation shows that cells with different deformabilities have a reduced aggregating tendency in shear conditions.

For the samples suspended in different osmolarities the laser aggregometry method shows similar results (Fig. 3a). Lower deformability corresponds to smaller aggregation index. No statistically significant influence of the deformability on CSS was found.

However, more intriguing results are presented on Fig. 3b. The effect of osmolarity (250 to 500 mOsm/l) on the forces of interaction between RBC in a doublet is more pronounced. The forces are presented in relative units, normalized to the aggregation force with an osmolarity of 300 mOsm/l. This graph clearly shows a decrease in aggregation force at low deformability. At the same time, the disaggregation force also decreases, but very slightly. In the sample with low osmolarity of 250 mOsm/l, the force values are not significantly different from those in the 300 mOsm/l sample. This shows that the disaggregation process is less responsive to changes in the deformability of RBC.



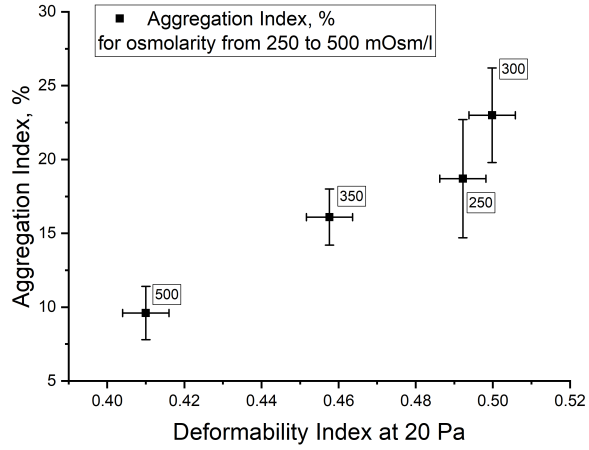
(a)



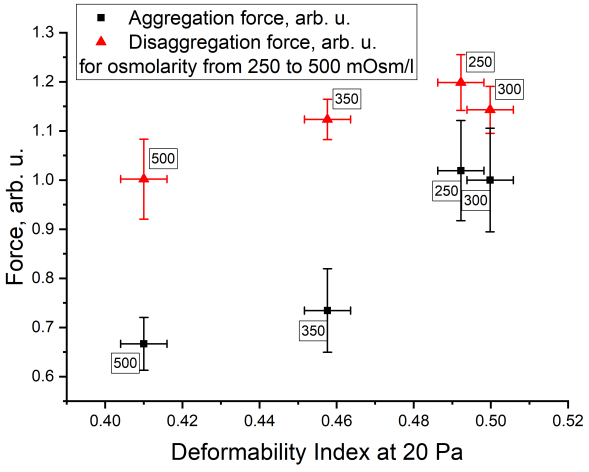
(b)

Fig. 2 (a) The aggregation index and (b) critical shear stress as functions of the deformability index for different glutaraldehyde concentrations (labeled). The values were measured 5 times for each donor. The averaged values for two donors and the standard deviations from the mean are presented.

To sum up, the parameters describing the formation of aggregates (aggregation index and force) decrease significantly for less deformable RBCs. However, the parameters describing the aggregates destruction (critical shear stress and disaggregation force) do not show a strong dependence on the deformability of RBCs. Both of these processes are complex and depend not only on the RBC properties, but also on the composition of the surrounding plasma. It was found that the hydrodynamic strength of the aggregates increases along with simultaneous reduction of RBC deformability and elevation of fibrinogen levels [23]. Research [13] performed with laser tweezers shows that the disaggregation process in large part can be described with a migrating cross-bridging mechanism of cell interaction, while the description of RBC aggregation requires additional factors. Nevertheless, further study with different methods is needed to assess the synergetic effects of protein concentration, deformability and others on aggregation of RBCs.



(a)



(b)

Fig. 3 (a) The aggregation index and (b) forces of aggregation and disaggregation as functions of the deformability index for different osmolarities (labeled). The values were measured 5 times for each donor. The averaged values for two donors and the standard deviations from the mean are presented.

4 Conclusion

Firstly, the method of laser diffractometry confirmed that with addition of glutaraldehyde and with a large change in the osmolarity of the solution, red blood cells become more rigid. Secondly, the methods of laser aggregometry and laser tweezers gave consistent results: with the decreased ability of red blood cells to deform the formation of aggregates becomes impaired. However, the critical shear stress and the disaggregation force remain mostly unchanged. This means that the RBC aggregate formation is dependent on the deformability of the membrane, while the connection to

disaggregation is less pronounced and more complicated in nature.

These results confirm the existence of a complex relationship between the selected microrheologic parameters of blood, and it is necessary to study thoroughly this relationship and keep it in mind when diagnosing and treating various cardiovascular diseases. Of course, these findings are valid only for *in vitro* conditions. Further experiments are needed to correlate this work with *in vivo* studies.

Disclosures

All authors declare that there is no conflict of interests in this paper.

Acknowledgments

This work was supported by the Russian Foundation for Basic Research grant #19-52-51015.

References

1. V. Leftov, S. Regirer, and N. Shadrina, Blood Rheology, Meditsina (1982) [in Russian].
2. V. V. Tuchin (Ed.), Handbook of Optical Biomedical Diagnostics, Vol. 2, second edition, SPIE PRESS, Bellingham, Washington, USA (2016).
3. N. Firsov, A. Priezzhev, N. Klimova, and A. Tyurina, "Fundamental laws of the deformational behavior of erythrocytes in shear flow," Journal of Engineering Physics and Thermophysics 79(1), 118–124 (2006).
4. H. Li, L. Lu, X. Li, P. A. Buffet, M. Dao, G. E. Karniadakis, and S. Suresh, "Mechanics of diseased red blood cells in human spleen and consequences for hereditary blood disorders," Proceedings of the National Academy of Sciences, 115(38), 9574–9579 (2018).
5. O. Baskurt, B. Neu, and H. Meiselman, Red blood cell aggregation, CRC Press (2012).
6. O. Fadyukova, A. Lugovtsov, A. Priezzhev, and V. Koshelev, "Optical study of blood rheological properties for krushinsky–molodkina strain rats with diabetes mellitus and acute disturbances of the cerebral circulation," Series Physics 17, 111–120 (2017) [in Russian].
7. P. Ermolinskiy, A. Lugovtsov, A. Maslyanitsina, A. Semenov, L. Dyachuk, and A. Priezzhev, "Interaction of erythrocytes in the process of pair aggregation in blood samples from patients with arterial hypertension and healthy donors: measurements with laser tweezers," Journal of Biomedical Photonics & Engineering 4(3), 030303, (2018).
8. P. Ermolinskiy, A. Lugovtsov, A. Maslyanitsina, A. Semenov, L. Dyachuk, and A. Priezzhev, "In vitro assessment of microrheological properties of erythrocytes in norm and pathology with optical methods," Series on Biomechanics, 32(3), 20–25 (2018).
9. Yu. Gurfinkel, A. Lugovtsov, P. Ermolinskiy, E. Pavlikova, L. Diachuk, and A. Priezzhev, "Comparative in-vivo and in-vitro study of blood rheological properties in patients with coronary heart disease with laser-optic techniques," Proceedings of SPIE 11065, 110650U (2019).
10. O. Fadyukova, A. Yu. Tyurina, A. E. Lugovtsov, A. V. Priezzhev, L. A. Andreeva, V. B. Koshelev, and N. F. Myasoedov, "Semax increases erythrocyte deformability in the shearing blood stream in intact rats and rats with cerebral ischemia," Doklady Biological Sciences 439, 208–211 (2011).
11. O. Baskurt, M.R. Hardeman, M. Uyuklu, P. Ulker, M. Cengiz, N. Nemeth, S. Shin, T. Alexy, and H. J. Meiselman, "Comparison of three commercially available ektacytometers with different shearing geometries," Biorheology 46(3), 251–264 (2009).
12. A. Lugovtsov, Y. I. Gurfinkel, P. B. Ermolinskiy, A. I. Maslyanitsina, L. I. Dyachuk, and A. V. Priezzhev, "Optical assessment of alterations of microrheologic and microcirculation parameters in cardiovascular diseases," Biomedical Optics Express 10(8), 3974–3986 (2019).
13. K. Lee, M. Kinnunen, M. D. Khokhlova, E. V. Lyubin, A. V. Priezzhev, I. Meglinski, and A. A. Fedyanin, "Optical tweezers study of red blood cell aggregation and disaggregation in plasma and protein solutions," Journal of Biomedical Optics 21(3), 035001 (2016).
14. S. Shin, Y. Yang, and J. Suh, "Measurement of erythrocyte aggregation in a microchip stirring system by light transmission," Clinical Hemorheology and Microcirculation 41(3), 197–207 (2009).
15. S. Shin, J. Hou, J. Suh, and M. Singh, "Validation and application of a microfluidic ektacytometer (RheoScan-D) in measuring erythrocyte deformability," Clinical Hemorheology and Microcirculation 37(4), 319–28 (2007).
16. A. Abay, G. Simionato, R. Chachanidze, A. Bogdanova, L. Hertz, P. Bianchi, E. van den Akker, M. von Lindern, M. Leonetti, G. Minetti, C. Wagner, and L. Kaestner, "Glutaraldehyde – a subtle tool in the investigation of healthy and pathologic red blood cells," Frontiers in Physiology 10, 514 (2019).
17. G. Griffiths, "Fixation for fine structure preservation and immucytochemistry", Chapter in Fine Structure Immunocytochemistry, Springer, 26- 89 (1993).
18. N. Nemeth, F. Kiss, and K. Miszti-Blasius, "Interpretation of osmotic gradient ektacytometry (osmoscan) data: a comparative study for methodological standards," Scandinavian Journal of Clinical and Laboratory Investigation, 75(3), 213- 222 (2015)

19. Y. Liang, Y. Xiang, J. Lamstein, A. Bezryadina, and Z. Chen, "Cell deformation and assessment with tunable "tug-of-war" optical tweezers," Conference on Lasers and Electro-Optics, AM1I.4 (2019).
20. R. Huisjes, A. Bogdanova, W. W. van Solinge, R. M. Schiffelers, L. Kaestner, R. van Wijk, "Squeezing for life – properties of red blood cell deformability," Frontiers in Physiology 9, 514 (2018).
21. P. Snabre, M. Bitbol, and P. Mills, "Cell disaggregation behavior in shear flow," Biophysical Journal, 51(5), 795–807 (1987).
22. M. Ju, S. S. Ye, H. T. Low, J. Zhang, P. Cabrales, H. L. Leo, and S. Kim, "Effect of deformability difference between two erythrocytes on their aggregation," Physical Biology 10(3), 036001 (2013).
23. S. Xue, B. Lee, and S. Shin. "Disaggregating shear stress: The roles of cell deformability and fibrinogen concentration," Clinical Hemorheology and Microcirculation 55(2), 231-240 (2012).

Hyperspectral Holography and Laser Diffractometry of Erythrocytes

Andrei E. Lugovtsov[1,2*], Vladislav D. Ustinov[3], Georgy S. Kalenkov[4], Sergey G. Kalenkov[5], and Alexander V. Priezzhev[1,2]

[1] Department of Physics, M.V. Lomonosov Moscow State University, 1 Leninskie Gory, Moscow 119991, Russia
[2] International Laser Center, M.V. Lomonosov Moscow State University, 1 Leninskie Gory, Moscow 119991, Russia
[3] Moscow Center of Fundamental and Applied Mathematics, M.V. Lomonosov Moscow State University, 1 Leninskie Gory, Moscow 119991, Russia
[4] Institute of Geosphere Dynamics (IDG RAS), 38/1 Leninskiy prospekt, Moscow 119334, Russia
[5] Moscow Polytechnic University, 38 Bolshaya Semyonovskaya str., Moscow 107023, Russia

*** e-mail:** anlug@biomedphotonics.ru

Abstract. Geometrical 3D models of human red blood cells in dry smear were obtained experimentally using hyperspectral holography technique. Corresponding diffraction patterns in the far field diffraction zone were calculated. Visibility values of the diffraction patterns were obtained in cases of low and high red cell distributions width (RDW). Our study reveals that although the visibility is influenced by the cells shapes, this parameter can still be used to assess red cell distribution width in clinical practice.
© 2020 Journal of Biomedical Photonics & Engineering.

Keywords: laser diffractometry; hyperspectral holography; erythrocyte; visibility.

Paper #3368 received 22 May 2020; revised manuscript received 18 Jun 2020; accepted for publication 18 Jun 2020; published online 24 Jun 2020. doi: 10.18287/JBPE20.06.020306.

1 Introduction

Modern medical diagnostics is based on blood tests that allow one to insure diagnosis with high accuracy. Red cell distribution width (RDW) is known as a crucial parameter in case of blood anemia. RDW is a measure of how much the erythrocytes differ from each other in size. RDW is close to zero, when all cells have similar size, and increases when the sizes are different. RDW has been evaluated for decades, and its application field grows rapidly. Recent investigation performed with more than 8000 people shows that RDW serves as a reliable mortality predictor independent of the disease type, see Ref. [1]. Thus, accurate diagnostic instruments for measuring this parameter are in high demand.

There is a number of different methods to measure RDW, each of which has its own advantages and disadvantages [2]. For example, optical microscopy enables one to see the erythrocytes and estimate their sizes visually. This is the most common method and it allows one to investigate the erythrocytes shapes by looking at the image. However, only a few hundreds of cells can be analyzed during a short time. The Coulter cell counter measures about 10000 cells in a few seconds. However, it should be assumed that the shape of the cells is spherical that leads to certain misinterpretation of the results. Thus, more reliable and efficient RDW measurement techniques are still required.

In this article, we continue our research on laser diffractometry of erythrocytes, which has been started by our group several years ago. In this technique, erythrocytes are illuminated by a laser beam and a diffraction pattern is observed in the far-field diffraction zone. One can solve integral equation in which the diffraction pattern is used as an input data and the solution is erythrocyte size distribution [3]. Another strategy is to rely on certain features of the diffraction pattern. For example, the visibility of the pattern reflects the shape and size of particles, see Ref. [4].

In Refs. [5–6], it was shown that the visibility of the diffraction pattern monotonically depends on RDW of the cells in the given blood sample. Thus, laser diffractometry allows one to assess the value of RDW. It is possible to illuminate hundreds of thousands of cells within a moment. Calculation of the visibility parameter can also be performed during less than a second using any modern personal computer. This

makes the method more preferable to others. However, the shape of the cells remains unknown as in the Coulter counter and one has to use some 3D geometrical model of the cells.

In hyperspectral holography (HH), one obtains the phase modulation of the light rays passing through the object with resolution up to half of the incident light wavelength. In previous Refs. [7–8], HH technique has been well developed and successfully tested on biological particles. In the present work, we have applied HH to measure the phase profiles of red blood cells on a glass smear. This enables one to reconstruct the 3D geometrical model of the erythrocytes shape. Although we use the specific technique developed in Refs. [7, 8], one can find other works on the topic, see, for example, Refs. [9, 10].

The main aim of this paper is to enhance laser diffractometry of erythrocytes by using the 3D geometrical model of real cell experimentally obtained using HH method. The visibility of the diffraction pattern depends not only on RDW value but also on the model of the cells shape. In this paper, we validate the dependency of the visibility parameter on RDW comparing different theoretical and experimentally obtained cells models.

Dry blood smears are used worldwide in routine medical tests. There are techniques that enable one to study cells in their original wet environment. In this paper, we consider dry smears in order to be closer to real medical practice.

2 Materials and Methods

The 3D geometrical model was obtained experimentally by using HH method as shown in Fig. 1. The method is described in a separate paper [7]. We have drawn the blood samples from a healthy male donor 35 years old. The dry blood smear was prepared according to a conventional medical protocol. In Fig. 1, the object was an erythrocyte on the glass smear located separately from other cells. The cell can change its normal shape of the biconcave disk during drying. Collecting data from the HH, we were be able to estimate this change precisely.

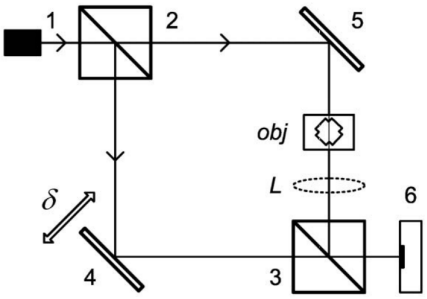


Fig. 1 Principal scheme of the interferometer for hyperspectral holograms registration. Polychromatic light source 1; beam splitter cubes 2, 3; mirrors 4, 5; CCD/CMOS sensor 6; obj – object under the study (erythrocyte); L – objective. See Ref. [7] for more details.

The collected data were used to model laser light scattering by erythrocytes in laser diffractometer. Principal scheme of this device is shown in Fig. 2, see Ref. [6] for more details.

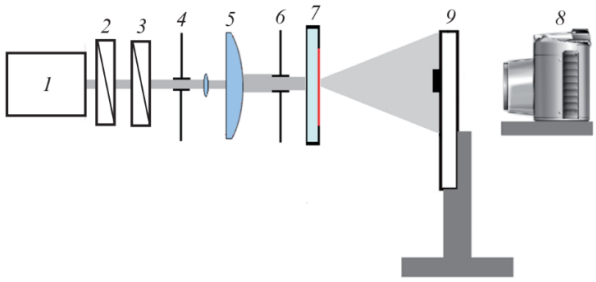


Fig. 2 Laser diffractometer; 1 – He-Ne laser; 2, 3 – polarizers; 4, 6 – apertures; 5 – lens system; 7 – blood smear; 8 – camera; 9 – translucent screen with a laser-beam absorbing plate. See Ref. [6].

Laser beam with wavelength 0.63 μm illuminates the cells on the smear 7. The laser power is controlled by the polarizers. The beam width is controlled by aperture and telescope. The diffraction pattern is detected by the camera on the observation screen. The key points are as follows:

- typical size of erythrocytes is equal to 7.5 μm and is about one order of magnitude higher than the laser wavelength, which insures that forward scattering in Mie regime occurs;
- the light scattering is single due to low concentration of cells, which insures that they do not overlap with each other;
- the observation screen is placed in the far-field diffraction zone.

He-Ne lasers yield a higher visibility of diffraction pattern as compared to a LED sources. Calculation of light scattering by single particle was performed by means of anomalous diffraction approximation. In this approximation, we assume that each ray passing through particle does not refract but gets additional phase modulation. Note, that only forward scattering with small scattering angles up to 15° are computable with high accuracy using this approximation. See Ref. [11] for more details on the application of the anomalous diffraction approximation for laser diffractometry of erythrocytes. The formula for electrical field of scattered light by single particle is as follows:

$$-\frac{i\,e^{ikl}}{\lambda l}\iint_S E_0 \cdot e^{-\frac{ik}{l}x\cdot x_0-\frac{ik}{l}y\cdot y_0}\times$$

$$\times\left(e^{-ikn_0\left(\frac{n_1}{n_0}-1\right)\cdot h(x,y)}-1\right)dxdy = \qquad (1)$$

$$= E(x_0, y_0),$$

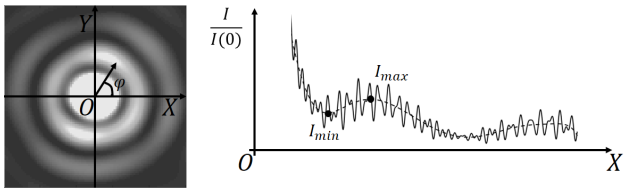
where S is the area bounded by the particles shadow in the laser beam; $k = 2\pi/\lambda$ – wavenumber of incident light, λ – laser wavelength in vacuum, n_0 – absolute refractive index of the medium (absorption is

neglected), n_1 – absolute refractive index of the particle. Point (x, y) goes through the area S, point (x_0, y_0) is fixed on the observation screen. Value $h(x, y)$ determine the particle thickness along the direction of laser beam propagation. Parameter $l = \sqrt{z^2 + x_0^2 + y_0^2}$ is distance from the point $(0, 0)$ on the site S to the point (x_0, y_0) on the observation screen, z – distance between the sample and the observation screen. E_0 – constant electric field complex amplitude of a plane incident wave. $E(x_0, y_0)$ – the desired complex amplitude of the electric field of the wave scattered by a given single particle.

Note that in laser diffractometry one obtains only the intensity of the scattered light $I(x_0, y_0) = |E(x_0, y_0)|^2$ measured by the camera at the observation screen. We refer to the 2D function $I(x_0, y_0)$ as a diffraction pattern. In our model, we assume that each cell has some known shape given by the function of cell thickness $h(x, y)$ in Eq. (1). We use random number generator to place cells uniformly on the plane. We calculate the integral in Eq. (1) for each particle and sum up the results according to the interference of rays coming from different cells to the same points on the observation screen. This enables one to calculate the diffraction pattern $I(x_0, y_0)$ at each point. As the cells have random coordinates, this diffraction pattern has some speckles corresponding to the coordinates and amount of the cells but not their shape geometry.

In the case of an ideal theoretical model, the area S in Eq. (1) is a circle with a given diameter. Otherwise, S is determined by calculating the particle contour from the given experimental HH image. In this case, the size of S is determined as the diameter of a circle with equivalent area. The histogram of the cell sizes represents the function of particle size distribution. In this paper, we assume it to be uniform on some physically meaningful fixed segment. We treat RDW as the standard deviation of the cell size distribution divided by its mean diameter.

Let us introduce visibility v of a diffraction pattern. Fig. 3 helps to explain the situation. Consider the diffraction pattern calculated as described above. As shown in Fig. 3(a), this pattern is non-symmetric because the cells may have irregular shapes and random coordinates. Consider polar coordinates (r, φ) on the observation screen. Let us average the intensities at each polar radii r over all angles φ: $I(r) = \frac{1}{2\pi}\int_0^{2\pi} I(r, \varphi)d\varphi$. This procedure enables one to treat all directions in the diffraction pattern in equivalent way. Function $I(r)$ contains speckles coming from the interference of laser light scattered by different particles with arbitrary positions inside of the laser beam. In order to overcome their influence, we calculate a polynomial of degree 10 best fitting the function $I(r)$ in the segment close to the first interference fringe of the diffraction pattern. In the first dark fringe $I(r)$ has a local minimum and in the first bright fringe $I(r)$ has a local maximum. Denote them by I_{min} and I_{max} respectively. Let visibility be $v = (I_{max} - I_{min})/(I_{max} + I_{min})$ by its definition.

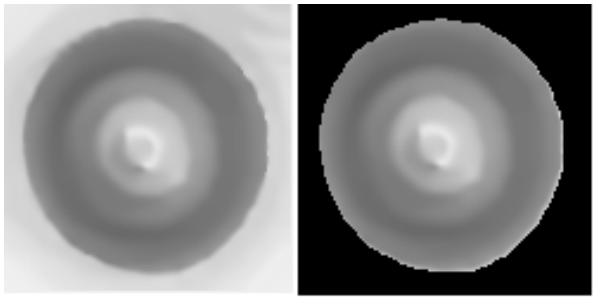


(a) (b)

Fig. 3 Part (a) shows diffraction pattern that corresponds to some non-symmetric cell image. Both Cartesian and polar coordinates are pictured. In part (b), solid line is the function of the intensity after the averaging procedure and the dashed line is the best fitting polynomial. I_{max} and I_{min} are values of first bright and dark interference fringes. One can see them in (a) near the center.

3 Results

Fig. 4(a) shows a typical phase image of red blood cell obtained by the HH method. An automatically extracted contour of a cell is shown in Fig. 4(b). One can see that the cell is non-symmetric that should result in a non-symmetric diffraction pattern. If the cell was an ideal cylinder with a round base, then the visibility of the diffraction pattern would be exactly 1. Even if the cell had a shape of an ideal biconcave disk, the visibility would equal about 0.86. However, our calculations show that for such a particle as in Fig. 4, the visibility is about 0.5. This is mainly due to the contribution of phase non-symmetry inside the particle, and not to its contour. For example, if we set the phase inside of the contour to be constant, the visibility for a single particle remains equal about 0.98.



(a) (b)

Fig. 4 Part (a) shows the phase image of a typical cell obtained by the HH method. Part (b) shows a result of contour recognition procedure applied to image (a). The image is brighter in the middle because the background is not yet subtracted.

4 Discussion

The erythrocytes shape is strongly influenced by the sample preparation and experimental protocols. In this work, we made dry smears placing the cells on a flat

glass surface. The cell concentration was low enough so that it was possible to isolate separately the single cells. However, as one can see from the Function 4 in Fig. 5 the obtained shape changes the visibility value critically. We have to follow such procedure of blood preparation in order to be closer to routine medical blood test in which a dry smear is analyzed using optical microscope. From this point of view, our calculations are far from ideal model but close to medical reality.

In principle, other protocols of blood smear preparation are available for the same purposes. For example, one can add glutaraldehyde into the blood probe and fix the erythrocyte shape, see Ref. [12] for more details. Being in normal conditions, the red cells take the shape of a biconcave disk, and glutaraldehyde will preserve this shape even when the erythrocytes dry up on the glass smear. For the cells prepared in such way, the method becomes much more stable as the main unknown parameter is fixed in advance. However, even in this case, the cells may have different shapes due to some blood diseases. Given such sample, our method should also show decreased value of the diffraction pattern visibility. Thus, the researchers should take into account that the visibility function reflects not only the dependence on RDW but also on the distribution of the cells in shape. To clarify this aspect by strict formulas, additional research is currently undertaken.

Note that placing the cells in a transparent liquid, generally leads to that the cells shape features make lower influence on the diffraction pattern. However, when working with liquid samples one has to take care about fluid evaporation in the sample and additional forces acting on blood cells. These forces may again change cells shapes, which should be taken into account in model calculations in laser diffractometry technique.

Most often in laser diffractometry, the small particles are placed into some liquid in a cuvette that leads to random orientations of the particles in space. In this case, results are still largely dependent on the cells shape as the shape is not uniform in all directions.

Whatever protocol of blood sample preparation one chooses, the basic requirement is that the results of laser diffractometry method may only be compared with the ones, achieved by using the same protocol. As described above, different procedures of blood sample preparation lead to unique typical distortions of the cells shapes and the visibility changes according to them.

5 Conclusion

Geometrical 3D models of human red blood cells in a dry smear were obtained experimentally using hyperspectral holography method. Corresponding diffraction patterns in the far field diffraction zone were calculated. Visibility values of the diffraction patterns were obtained in cases of low and high red cell size distribution width. The results revealed that the visibility is influenced by the cells shapes. Namely, the visibility is always lower when using the model of real cells shape to compare with the case of ideal symmetric shapes. However, the visibility of the diffraction pattern still can be used to assess the red cell distribution width in clinical practice.

Fig. 5 shows four calculated functions representing the main result. The visibility values are plotted along the vertical axis. The horizontal axis corresponds to the values of RDW denoted by δ_R.

Function 1 shows the dependence of visibility on RDW in case when all the cells have an ideal circle base and ideal flat surface. We also assumed that there is no speckle structure in the diffraction pattern in case of Function 1. That is why the function is ideally monotonic. This function was first calculated in Ref. [5]. The Function 2 was calculated in the same conditions as Function 1 but the speckle structure in the diffraction pattern was taken into account. One can see that the Functions 1 and 2 are very close to each other within a small error space of about 5%. This means that randomness of cells coordinates does not make too big impact into our model.

Function 3 represents the case when the shape of the cells was an ideal biconcave disk. Here, the visibility is not 1 even for very low values of RDW. Note that this figure was calculated when the red cells were in the air medium, thus their relative refractive index was 1.4, that is a high value. If the cells were in the transparent liquid medium like water, then Function 3 would be very close to the Functions 1 and 2. This means that the model of the cells shape acts together with optical parameters of the medium in which the cells are located.

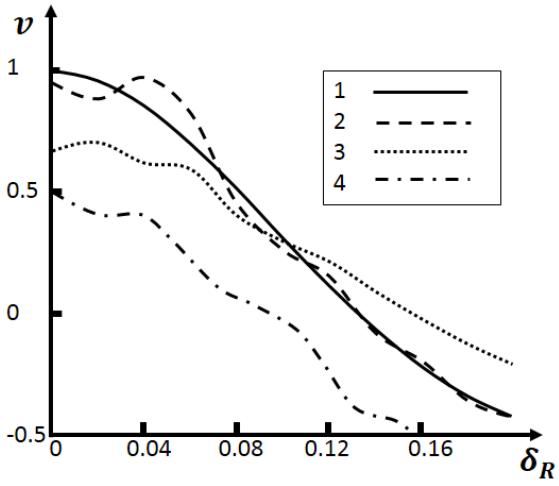


Fig. 5 Dependency of visibility v on RDW δ_R in the cases of 4 different assumptions. 1 – ideal circular cylinders with no speckles, 2 – ideal circular cylinders with speckles, 3 – ideal biconcave disks with speckles, 4 – real 3D models of cells obtained experimentally with speckles.

To calculate the Function 4, we assumed that the cells are described by natural 3D geometrical models taken from the HH experiment as shown in Fig. 4. Cells of 3 typical images were taken as initial data. They were stretched, rotated and located randomly on the plane. One can see from Fig. 5 that taking into account the natural shape we significantly reduce the visibility.

However, the calculated visibility still decreases with δ_R becoming larger. This further leads to a conclusion that the method of laser diffractometry is still applicable in case of natural dry erythrocytes shapes.

Disclosures

All authors declare that there is no conflict of interests in this paper.

Acknowledgments

This work was supported by RFBR grant № 17-29-03507-ofi-m. Authors acknowledge the help of Dr. Alexei N. Semenov in preparing the blood smears and Prof. Sergey Yu. Nikitin for useful discussions.

References

1. K. V. Patel, L. Ferrucci, W. B. Ershler, D. L. Longo, and J. M. Guralnik, "Red blood cell distribution width and the risk of death in middle-aged and older adults," Archives of Internal Medicine 169(5), 515–523 (2009).
2. G. I. Kozinets, V.A. Makarova, The study of the blood system in clinical practice, Triada-X, Moscow (1997) [in Russian].
3. D. L. Black, M. Q. McQuay, and M. P. Bonin, "Laser-based techniques for particle-size measurement: a review of sizing methods and their industrial applications," Progress in energy and combustion science 22(3), 267–306 (1996).
4. W. M. Farmer, "Measurement of particle size, number density, and velocity using a laser interferometer," Applied Optics 11(11), 2603–2612 (1972).
5. S. Yu. Nikitin, A. E. Lugovtsov, A. V. Priezzhev, and V. D. Ustinov, "Relation between the diffraction pattern visibility and dispersion of particle sizes in an ektacytometer," Quantum Electronics 41(9), 843–846 (2011).
6. Yu. S. Yurchuk, V. D. Ustinov, S. Yu. Nikitin, and A. V. Priezzhev, "Scattering of a laser beam on a wet blood smear and measurement of red cell size distribution," Quantum Electronics 46(6), 515–520 (2016).
7. G. S. Kalenkov, S. G. Kalenkov, and A. E. Shtan'ko, "Hyperspectral holographic Fourier-microscopy," Quantum Electronics 45(4), 333–338 (2015).
8. S. G. Kalenkov, G. S. Kalenkov, and A. E. Shtanko, "Hyperspectral holography: an alternative application of the Fourier transform spectrometer," Journal of the Optical Society of America B 34(5), B49–B55 (2017).
9. A. I. Yusipovich, E. Yu. Parshina, N. Yu. Brysgalova, A. R. Brazhe, N. A. Brazhe, A. G. Lomakin, G. G. Levin, and G. V. Maksimov, "Laser interference microscopy in erythrocyte study," Journal of Applied Physics 105(10), 102037 (2009).
10. G. G. Levin, G. N. Vishnyakov, and V. L. Minaev, "An automated interference microscope for measuring dynamic objects," Instruments and Experimental Techniques 56(6), 686–690 (2013).
11. S. Yu. Nikitin, A. V. Priezzhev, and A. E. Lugovtsov, "Laser diffraction by the erythrocytes and deformability measurements," Chapter 6 in Advanced optical flow cytometry: methods and disease diagnoses, V. Tuchin (Ed.), Wiley-VCH, Weinheim, Germany, 133–154 (2011).
12. I. Dulińska, M. Targosz, W. Strojny, M. Lekka, P. Czuba, W. Balwierz, and M. Szymoński, "Stiffness of normal and pathological erythrocytes studied by means of atomic force microscopy," Journal of Biochemical and Biophysical Methods 66(1–3), 1–11 (2006).

UV-NIR efficiency of the refractive index matching mechanism on colorectal muscle during treatment with different glycerol osmolarities

Nelma Gomes[1], Valery V. Tuchin[2,3,4], and Luís M. Oliveira[1,5*]

[1] Department of Physics, Polytechnic of Porto – School of Engineering, 431 Rua Dr. António Bernardino de Almeida, Porto 4249-015, Portugal

[2] Research-Educational Institute of Optics and Biophotonics, Saratov State University, 83 Astrakhanskaya str., Saratov 410012, Russia

[3] Laboratory of Laser Diagnostics of Technical and Living Systems, Institute of Precision Mechanics and Control of the Russian Academy of Sciences, 24 Rabochaya str., Saratov 410028, Russia

[4] Interdisciplinary Laboratory of Biophotonics, Tomsk State University, 36 Lenin Ave., Tomsk 634050, Russia

[5] Centre of Innovation in Engineering and Industrial Technology, 431 Rua Dr. António Bernardino de Almeida, Porto 4249-015, Portugal

*** e-mail:** lmo@isep.ipp.pt

Abstract. The evaluation of the optical clearing mechanisms in tissues provides information about the efficiency of the clearing treatment. One of such mechanisms is the refractive index matching, which is created by the partial replacement of tissue water by an optical clearing agent with higher refractive index, better matched to the index of tissue scatterers. With the objective of evaluating the refractive index matching mechanism for a wide spectral range and comparing its magnitude between treatments with different clearing agent osmolarities, thickness and collimated transmittance measurements were obtained from human colorectal muscle samples under treatment with 20%-, 40% and 60%-glycerol. Such measurements were used in a calculation model to obtain the refractive index kinetics for the interstitial fluid and for the whole tissue. The calculation results show that the refractive index matching has a stronger effect in the ultraviolet and that such matching is more effective for higher agent concentrations in the treating solutions. © 2020 Journal of Biomedical Photonics & Engineering.

Keywords: ultraviolet spectroscopy; refractive index matching; light scattering; tissue water content; optical clearing; colorectal muscle; collimated transmittance.

Paper #3374 received 25 May 2020; revised manuscript received 12 Jun 2020; accepted for publication 14 Jun 2020; published online 26 Jun 2020. doi: 10.18287/JBPE20.06.020307.

1 Introduction and theoretical background

Since its rediscovery about 30 years ago [1], the research related to the Optical immersion Clearing (OC) technique has produced a large number of publications [2], which continues to grow significantly. Some of those studies were made to evaluate, discriminate and characterize the mechanisms of OC [2–8], while others evaluated the diffusion properties of the optical clearing agents (OCAs) in tissues [9–16], or described such diffusion as a molecular-based model [17–18].

The combination of OC treatments with other optical-based methods in clinical practice provides significant improvements, since by reducing light scattering inside tissues, it allows for higher tissue-depth optical probing and imaging, higher contrast and resolution in diagnostic images [19–26]. Some imaging and spectroscopy studies made during OC treatments have allowed to discriminate between normal and pathological tissues. One of those spectroscopy studies was reported by Carvalho et al. [16], where colorectal

cancer was identified by evaluating the different content of mobile water in normal and pathological tissues. Imaging methods have also been applied to identify tumor locations in tissues after clearing [19, 21–23]. One of such studies was reported by Lagerweijt et al. [26], where fluorescence confocal imaging, two-photon imaging, photoacoustic imaging and image reconstruction of optically cleared tissues have allowed to discriminate between normal and infiltrating glioblastoma brain tumors in rats.

As a result of OC evaluation and characterization studies, it is known that tissue transparency increases during treatments as a result of three major mechanisms, commonly designated as: tissue dehydration, refractive index (RI) matching and protein dissociation [2, 27–30]. Tissue dehydration occurs when interstitial water flows out as a result of the osmotic pressure that the OCA creates inside the tissue. Such water flux leads to a more compact and better organized distribution of the other tissue components (scatterers) [2]. As the water flows out, the OCA, with a higher RI, flows into the interstitial locations to partially replace the leaving water and provide the RI matching mechanism [3]. Considering that water, tissue scatterers and OCAs have a decreasing behavior with increasing wavelength [2, 31–34], it is expected that the RI matching will have a higher effect on scattering in the ultraviolet (UV) range. The third OC mechanism, designated as protein dissociation, has also been observed as a result of the interaction of the OCA molecules with protein connections [27]. Since proteins have a strong absorption band in the deep-UV (200–230 nm) [31, 35–36], such dissociation also leads to a higher RI matching in this wavelength range. Such fact was recently reported by Carneiro et al. [37], where two OC-induced transparency windows were observed in the UV, with central peaks at 230 and 300 nm. This study also demonstrated that the magnitude of these windows increases with the OCA concentration in the treating solution [37], which suggests that higher OCA concentrations provide a higher magnitude RI matching in the UV range.

It has been demonstrated that all the three OC mechanisms are completely reversible, provided that the OCA is later washed out by subsequent tissue rehydration [2, 27, 38]. Such rehydration occurs naturally *in vivo*, since water from adjacent areas of the tissue flows into the treated area and the OCA is completely expelled out [2]. For the *ex vivo* situation, washing out of the OCA can be provided by immersing the treated tissue in saline.

Tissue spectroscopy is a powerful tool in the study of OC treatments, since it provides data for a wide spectral range. One of the benefits of using sensitive spectroscopy measurements from tissues during OC treatments for a range between the UV and the near infrared (NIR), is that comparison of the induced variations can be made between the UV, visible and NIR.

In a previous study by our group [39], we have evaluated the RI matching mechanism in the visible-NIR range in skeletal muscle under treatment with glucose and ethylene glycol solutions, showing that both the RI of the interstitial fluid (ISF) and of the whole tissue increase as a result of the applied OC treatments.

With the objective of studying the RI matching mechanism and compare its magnitude between the UV, visible and NIR ranges, the present study was conducted with human colorectal muscle under treatment with different glycerol osmolarities.

2 Materials and methods

The present study consisted only of the calculation of the RI matching mechanism in human colorectal muscle for a wide spectral range during treatments with glycerol in different osmolarities. The samples and collimated transmittance (T_c) measurements used in these calculations are the same that were used in a previous study that reported the discovery of two OC-induced tissue windows in the UV range [37]. Sub-section 2.1 presents a resumed description of tissue collection, sample preparation and measurement procedure, which were used in that study. The following sub-sections describe the calculation procedure adopted to obtain the RI kinetics of colorectal muscle during treatments.

2.1 Tissue samples and measurement procedure

The tissue samples used to obtain the measurements necessary for this study were obtained from surgical resections of patients under treatment at the Portuguese Oncology Institute of Porto, Portugal. The collection of surgical resections and sample preparation were performed according to the guidelines of the Ethics Committee of that Institution and after obtaining a written consent from the patients to use surgical specimens for diagnostic and research purposes.

The muscle layer of the colorectal wall was retrieved from the surgical resections and a cryostat (Leica Biosystems, model CM 1850 UV) was used to prepare the samples for the study with approximate circular slab-form, having diameter $\phi = 1$ cm and 0.5 mm thickness.

Three of these samples were submitted to T_c measurements during the OC treatments with aqueous solutions containing 20%-, 40%- or 60%-glycerol (one sample per treatment) [37]. The setup to perform T_c measurements is presented in Fig. 1 of Ref. [37], where an optical fiber cable delivers a collimated beam of 1 mm from a broadband light source into a cuvette that contains the tissue sample. A similar optical fiber collects the collimated transmitted beam to deliver it to the spectrophotometer. For measurements during treatment, the solution is introduced inside the cuvette to immerse the sample. The volume of the solution is about 10× higher than the sample volume to guarantee a continuous flux of the OCA into the tissue during the treatment. The samples used in the study of Ref. [37]

had low blood content, which resulted in low magnitude for the absorption bands of hemoglobin. To obtain more realistic results in the present study, ten other muscle samples, from which we recently measured the native T_c spectra and presented well-defined Soret and Q-bands, were used to perform calculations.

Thickness measurements were also made during treatment with the same glycerol solutions, using a precision micrometer as described in Fig. 1B of Ref. [39]. Nine muscle samples were used in these measurements, three per treatment with each glycerol osmolarity, to obtain more precise mean thickness kinetics.

2.2 Recovery of T_c kinetics

Since we had previously measured kinetics data for the T_c spectra during the treatments with various glycerol osmolarities to use in the study reported in Ref. [37], we needed to retrieve the time dependence variations created by those treatments to use in the calculations of the RI kinetics intended for the present study.

As indicated above, the T_c kinetics reported in Ref. [37] were obtained from muscle samples with low blood content. Since we intended to present more realistic results, for tissues that have some absorption bands, and to show the effect of such bands in tissue dispersion and following kinetics, we needed to adjust the previous T_c kinetics [37] to tissues that had such spectral signatures.

The recovery of the T_c kinetics and their recalculation for treatments with more realistic tissues was made in the following way for each treatment:

I. In the study presented in Ref. [37], the OC efficiency was calculated as:

$$\mathrm{OC}_{eff}\left(\lambda,t\right)=\frac{T_c\left(\lambda,t\right)-T_c\left(\lambda,t=0\right)}{T_c\left(\lambda,t=0\right)}\times 100\%, \quad (1)$$

where $T_c(\lambda, t = 0)$ represents the spectrum of the untreated sample and $T_c(\lambda, t)$ represents the spectrum measured at each time of treatment t. The resulting $\mathrm{OC}_{eff}(\lambda, t)$ contains information about the T_c variations for colorectal muscle in each treatment, which can be retrieved to use with other native T_c spectrum from the same tissue under the same OC treatments.

II. Using recent T_c spectra, which were measured from similar colorectal muscle samples that had higher blood content and better-defined hemoglobin bands, we calculated the mean and standard deviation (SD) for the native $T_c(\lambda)$ of the muscle. The calculated mean $T_c(\lambda)$ for the native muscle was used in Eq. (2) as a replacement of $T_c(\lambda, t = 0)$ to calculate the time dependence variations in $T_c(\lambda)$:

$$T_c\left(\lambda,t\right)=\frac{\mathrm{OC}_{eff}\left(\lambda,t\right)\times T_c\left(\lambda,t=0\right)}{100\%}+T_c\left(\lambda,t=0\right). \quad (2)$$

This means that the $T_c(\lambda, t)$ spectra obtained with this calculation for each treatment contains the same spectral signatures for hemoglobin as the recent measured samples and the corresponding kinetics that were obtained by measurement in the study of Ref. [37]. As a result, using this data will produce more realistic RI kinetics data.

2.3 Calculation of optical properties for the native colorectal muscle

To perform the calculations to obtain the RI kinetics for each treatment, it was also necessary to obtain the optical properties of the untreated tissue, namely the absorption coefficient ($\mu_a(\lambda)$), the scattering coefficient ($\mu_s(\lambda)$) and tissue dispersion ($n_{\mathrm{muscle}}(\lambda)$).

The calculation of these properties was performed according to the following procedure:

I. Using the sample thickness (d = 0.5 mm) and the mean $T_c(\lambda)$ that was obtained from the recent measurements, we calculated the attenuation coefficient ($\mu_t(\lambda) = \mu_a(\lambda) + \mu_s(\lambda)$) using the Bouguer-Beer-Lambert equation [40]:

$$\mu_t\left(\lambda,t=0\right)=\frac{-\ln\left(T_c\left(\lambda,t=0\right)\right)}{d}. \quad (3)$$

II. The wavelength dependence for μ_s is described in literature [41] as a combination of Rayleigh and Mie scattering regimes:

$$\mu_s\left(\lambda\right)=a'\times\left(\begin{array}{l} f_{\mathrm{Ray}}\times\left(\dfrac{\lambda}{500(\mathrm{nm})}\right)^{-4}+ \\ +\left(1-f_{\mathrm{Ray}}\right)\times\left(\dfrac{\lambda}{500(\mathrm{nm})}\right)^{-b_{\mathrm{Mie}}} \end{array}\right), \quad (4)$$

where a' is a multiplying factor that establishes the magnitude of μ_s at 500 nm, λ is the wavelength (nm), f_{Ray} is the Rayleigh scattering fraction and b_{Mie} represents the decreasing power for the Mie scattering component [41].

After obtaining the optimal curve for $\mu_s(\lambda)$ through Eq. (4), with appropriate estimated values for a', f_{Ray} and b_{Mie}, we subtracted it to $\mu_t(\lambda)$ to obtain $\mu_a(\lambda)$.

III. After obtaining the wavelength dependence for μ_a, we could calculate the dispersion for the colorectal muscle. Refs. [42–43] describe a set of transformation relations to obtain the real and imaginary parts of the RI from the optical properties of a medium. Such relations are known as the Kramers-Kronig (K-K) relations. The relation to calculate the real part of the RI, which is the one we need, is described as [42–43]:

$$n_{\mathrm{muscle}}\left(\lambda\right)=1+\frac{2}{\pi}\int_0^{\infty}\frac{\lambda}{\Lambda}\cdot\frac{\lambda}{\Lambda^2-\lambda^2}\kappa\left(\lambda\right)\mathrm{d}\Lambda, \quad (5)$$

where Λ represents the integrating variable over a wavelength spectral range under consideration and λ is a fixed wavelength in that range that can be tuned for better adjustment of the calculated dispersion. κ(λ) represents the imaginary part of the RI, which can also be calculated by another K-K relation [42–43], or in a simpler way if we have $\mu_a(\lambda)$ [42]:

$$\kappa(\lambda)=\frac{\lambda}{4\pi}\mu_a(\lambda). \quad (6)$$

Since we have already calculated $\mu_a(\lambda)$, we used it in Eq. (6) to obtain κ(λ) for the range between 200 and 1000 nm, which was then used in Eq. (5) to calculate $n_{muscle}(\lambda)$ for the same range. To check the accuracy of this calculation, we compared $n_{muscle}(\lambda)$ with the previous dispersion that we have calculated form direct RI measurements at different wavelengths in the visible-NIR range [44]. Both curves matched perfectly in the visible-NIR range, showing differences only in the UV range, where significant absorption bands occur and where we had no experimental RI data to use in the previous estimation. Such agreement indicates that the dispersion estimation from K-K relations is good and more precise in the UV range.

2.4 Calculation of tissue dispersion kinetics

Once we have obtained all the necessary optical properties for the native muscle and the kinetics measurements for thickness and T_c during the treatments, we could calculate the RI kinetics for the colorectal muscle and for its ISF, according to a model described in literature [39, 44–46].

Such model considers that for short-time treatments the OCA will only partially replace the interstitial water, without any interaction with the scatterers, meaning that the scatterers will keep their hydration, RI and absolute volume [45]. Due to this fact, the RI of tissue scatterers ($n_{scat}(\lambda)$), which remains unchanged during treatment, needs to be calculated. Such calculation was previously made [44], based on experimental RI data obtained at wavelengths within the visible-NIR range. To get more realistic data that accounts for the wide spectral range between 200 and 1000 nm, we performed a simple calculation. The ISF is known to be composed mainly by water and some dissolved salts, proteins and minerals [2, 45, 47–48]. This way, the wavelength dependence for its RI ($n_{ISF}(\lambda)$), can be described as a combination of the dispersions of water ($n_{H2O}(\lambda)$) and dry matter (completely dehydrated muscle, $n_{dry}(\lambda)$), through the Gladstone and Dale equation [39, 44–47, 49–54]:

$$\begin{aligned} &n_{ISF}(\lambda)=f_{H_2O}\times n_{H_2O}(\lambda)+f_{dry}\times n_{dry}(\lambda);\\ &f_{H_2O}+f_{dry}=1. \end{aligned} \quad (7)$$

To perform such calculation, it was first necessary to obtain $n_{dry}(\lambda)$. Assuming that the total water content in colorectal muscle is 73%, which is a similar value to the total water in neighbor tissues of the colorectal wall [46], we used the Gladstone and Dale equation to calculate $n_{dry}(\lambda)$:

$$n_{dry}(\lambda)=\frac{n_{muscle}(\lambda)-f_{H_2O}\times n_{H_2O}(\lambda)}{1-f_{H_2O}}, \quad (8)$$

where f_{H2O} was replaced by 0.73, $n_{muscle}(\lambda)$ was calculated by Eq. (5) and $n_{H2O}(\lambda)$ represents the water dispersion between 200 and 1000 nm as reported for 20 ºC [55].

Finally, to obtain $n_{scat}(\lambda)$, the same equation can be applied for the entire tissue, using the volume fractions (VFs) for the ISF and scatterers [44]:

$$n_{scat}(\lambda)=\frac{n_{muscle}(\lambda)-f_{ISF}\times n_{ISF}(\lambda)}{1-f_{ISF}}, \quad (9)$$

where f_{ISF} is the VF of the ISF, $1-f_{ISF}$ is the VF of scatterers (f_{scat}) and $n_{ISF}(\lambda)$ is calculated with Eq. (7). Since we know from previous study [44] that $f_{ISF}=0.6$ and $f_{scat}=0.4$, all these calculations can be made, ultimately depending on the values of f_{H2O} and f_{dry} in Eq. (7), which are unknown. When performing calculations with Eq. (7) we tried some combinations for these VFs in Eq. (7) and for the combination with $f_{H2O}=84\%$ and $f_{dry}=16\%$, the calculated dispersions for the ISF and scatterers matched the ones we previously calculated based on experimental RI data in the visible-NIR range. These graphs are presented in Section 3.

The following step consisted on calculating the kinetics for the VFs. Since the scatterers keep their absolute volume unchanged, we started by calculating it from the untreated sample volume ($V_{sample}(t=0)$) [39]:

$$V_{scat}=V_{sample}(t=0)\times f_{scat}(t=0)\ \text{cm}^3, \quad (10)$$

where $f_{scat}(t=0)$ is 0.4. The untreated sample volume was calculated considering the sample slab-form radius (ϕ = 1 cm) and thickness (d = 0.5 mm) as:

$$V_{sample}(t=0)=(\pi\times 0.5^2)\times 0.05\ \text{cm}^3. \quad (11)$$

Since V_{scat} does not change during treatment, but V_{sample} will change, we calculated the time dependence for f_{scat} considering the variations in sample thickness ($d(t)$) as:

$$f_{scat}(t)=\frac{V_{scat}}{(\pi\times 0.5^2)\times d(t)}. \quad (12)$$

Since from Gladstone and Dale law (Eq. (7)), the sum of VFs equals 1, we could calculate $f_{ISF}(t)$ from

$f_{scat}(t)$.

The following step was to calculate the kinetics for the RI of the ISF that occurs due to the partial replacement of water by glycerol. Such partial replacement and consequent variations in the VFs will induce changes in the scatterer density (ρ_s) inside the sample. Since μ_s is the product between the scattering cross section (σ_s) and ρ_s [40], the following equation must be considered to determine the time dependence for n_{ISF} [2, 39, 44]:

$$\bar{n}_{ISF}(\lambda,t) = \frac{n_{scat}(\lambda)}{\left(\sqrt{\frac{\mu_s(\lambda,t)\times d(t)}{\mu_s(\lambda,t=0)\times d(t=0)}}\times\left(\frac{n_{scat}(\lambda)}{n_{ISF}(\lambda)}-1\right)+1\right)}, \quad (13)$$

where $n_{scat}(\lambda)$ is the dispersion of scatterers as calculated by the Gladstone and Dale law (Eq. (9)), $n_{ISF}(\lambda)$ is the dispersion of the ISF in the untreated tissue (calculated with Eq. (7)). Sample thickness for the untreated tissue and during treatment are represented as $d(t = 0)$ and $d(t)$, respectively, and $\mu_s(\lambda, t = 0)$ and $\mu_s(\lambda, t)$ are the wavelength dependencies for the scattering coefficient for the untreated tissue and during treatment. The calculation of $\mu_s(\lambda, t = 0)$ was made using Eq. (4) and its kinetics during treatment were obtained by subtracting the unchanged $\mu_a(\lambda)$ to the kinetics of μ_t, which were calculated from the thickness and T_c kinetics using Eq. (3). All the results from these calculations are presented in Section 3.

3 Results and discussion

Considering the various experimental steps described in Section 2, we will present sequential results in this section, starting with the experimental data and calculation of the optical properties for the untreated muscle in Sub-section 3.1. The results that correspond to the OC-induced variations will be presented in Sub-section 3.2

3.1 Tc measurements and calculated optical properties for the natural muscle

As indicated in Section 2, we have recently used 10 colorectal muscle samples to acquire precise T_c spectra that show well-defined absorption bands for hemoglobin. Such accuracy and spectral quality depends on the blood content of the samples, which sometimes is low. Figure 1 presents the mean T_c spectrum for the human colorectal muscle that resulted from these measurements. The error bars in Fig. 1 represent the SD obtained from the 10 measurements.

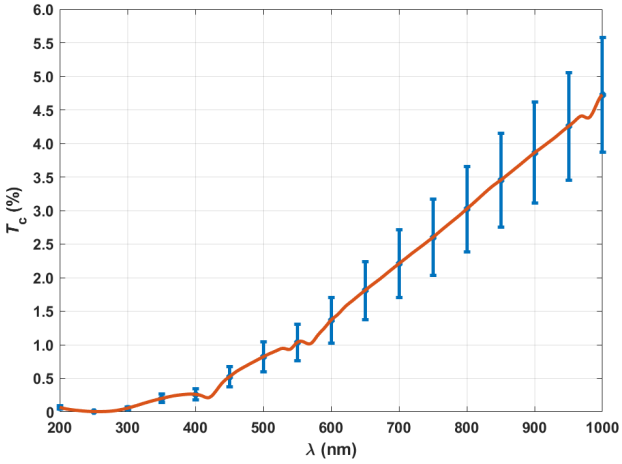


Fig. 1 Mean T_c spectrum of the human colorectal muscle.

As we can see from Fig. 1, T_c is very low in the UV range, and practically null between 200 and 300 nm. Considering the visible-NIR range, T_c increases almost linearly with wavelength, showing the absorption bands at 418 nm (Soret), 540 and 570 nm (Q-bands) and 980 nm (water).

Using the sample thickness of 0.5 mm and the mean spectrum presented in Fig. 1 in Eq. (3), we calculated $\mu_t(\lambda)$. Using the Curve Fitting Tool on MATLAB™, we recreated $\mu_s(\lambda)$ that better suits the calculated $\mu_t(\lambda)$. In this estimation for $\mu_s(\lambda)$, we used Eq. (4). Fig. 2 presents the calculated curves for $\mu_t(\lambda)$ and $\mu_s(\lambda)$.

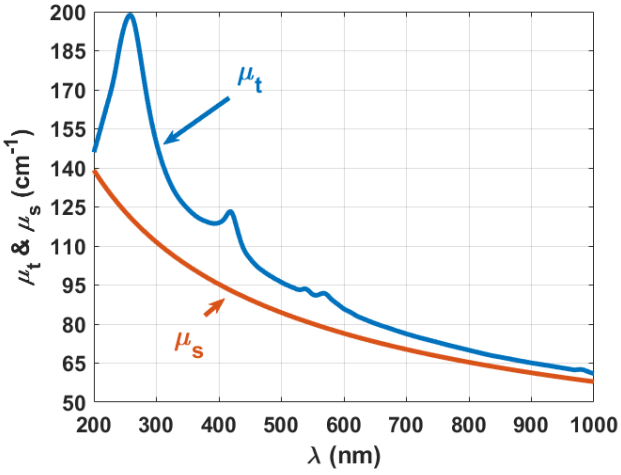


Fig. 2 Calculated $\mu_t(\lambda)$ and estimated $\mu_s(\lambda)$ for the native colorectal muscle.

The curve in Fig. 2 for $\mu_s(\lambda)$ is described as:

$$\mu_s(\lambda) = 84.41 \times \left(3.371 \times 10^{-5} \times \left(\frac{\lambda}{500(\text{nm})} \right)^{-4} + \right.$$
$$\left. + \left(1 - 3.371 \times 10^{-5}\right) \times \left(\frac{\lambda}{500(\text{nm})} \right)^{-0.5446} \right), \quad (14)$$

As we can see from Fig. 2, $\mu_s(\lambda)$ was constructed to be a little lower than $\mu_t(\lambda)$, so that the difference between the two represents $\mu_a(\lambda)$. After calculating such difference, we obtained $\mu_a(\lambda)$, which is presented in Fig. 3.

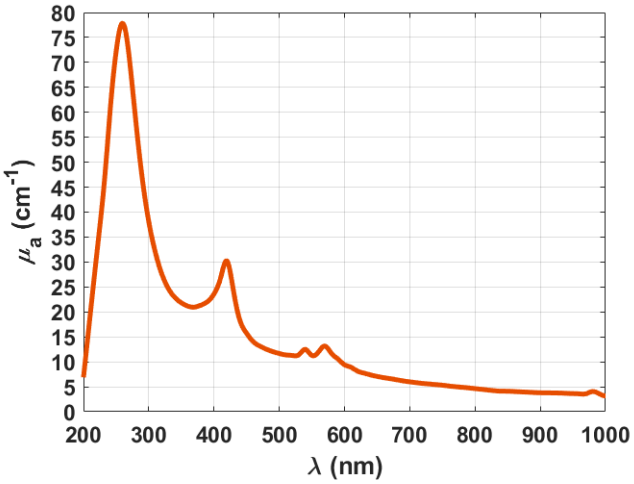


Fig. 3 $\mu_a(\lambda)$ for the native colorectal muscle.

The calculated $\mu_a(\lambda)$ presents the typical wavelength dependence for biological tissues and contains precise information about the main absorbers in the muscle. Fig. 3 shows the absorption band of DNA (260 nm), the Soret band (418 nm), the Q- bands (540 and 570 nm) and the absorption band of water (980 nm). With such detail in $\mu_a(\lambda)$ we see that the calculation through the BBL equation is precise, in opposition to traditional estimation methods, such as the inverse Adding-Doubling method, which is not able to detect absorption bands in the spectral range where scattering is strong (UV range) [31].

Using the data in Fig. 3, the muscle dispersion was calculated through K-K relations (Eqs. (5) and (6)). The result of this calculation and the previous smooth dispersion, which was calculated from experimental RI measurements in the visible-NIR range [44], are presented in Fig. 4 for comparison.

Both curves presented in Fig. 4 show good agreement in the visible-NIR range, but the one estimated through K-K relations provides more information, since it contains the spectral signatures of the major absorbers in the muscle. This curve was selected for further calculations.

The following step was to calculate the dispersions for the ISF and scatterers in the muscle. Such calculation procedure was made using Eqs. (7) to (9) and as described in Sub-section 2.4. The resulting dispersions are presented in Fig. 5, where the smooth dispersions, previously obtained [44], are also represented for comparison.

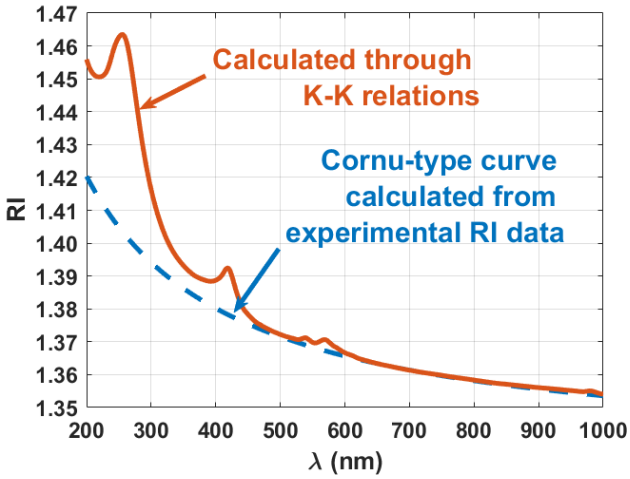


Fig. 4 Colorectal muscle dispersion curves.

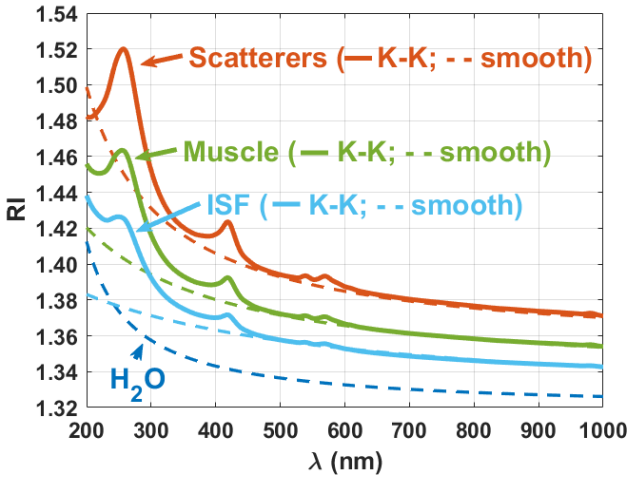


Fig. 5 Dispersion curves for the colorectal muscle and its components.

We can see from Fig. 5 that for the visible-NIR range, the dispersions calculated based on K-K relations have good agreement with their smooth correspondents. Such agreement indicates that such estimation for the dispersions of the ISF and scatterers is good and it provides more information about the spectral signatures that each dispersion has. As example, the K-K calculated dispersion for the ISF shows that ISF also contains some DNA and hemoglobin molecules – peaks at 260 and 418 nm. The content of these molecules is much stronger in scatterers, as expected, as seen by the magnitude of the peaks in the top dispersion in Fig. 5.

After obtaining the wavelength dependence for the optical properties that are necessary to calculate the dispersion kinetics, we will now present the results of such calculations.

3.2 Calculation of dispersion kinetics

After reconstructing the T_c spectra for all treatments from the OC efficiency data published in Ref. [37] and the mean T_c spectrum presented in Fig. 1, we initiated the calculations to obtain the dispersion kinetics.

The first step of this calculation was to obtain the kinetics for the VFs in each treatment. To perform such calculations, we used the mean thickness kinetics (mean of 3 studies for each treatment), presented in Fig. 6.

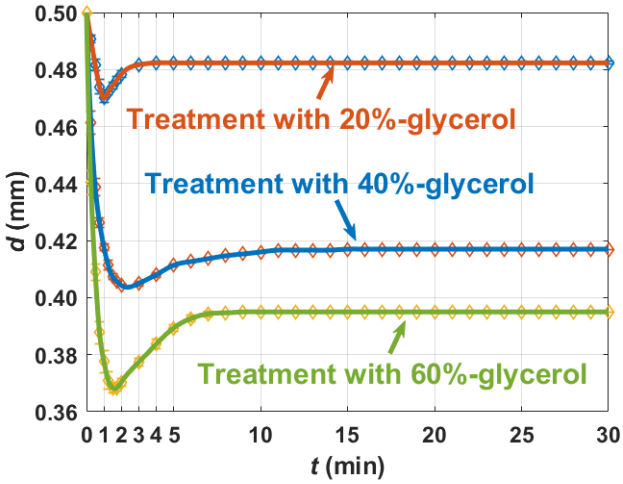


Fig. 6 Mean thickness kinetics during the treatments with 20%-glycerol, 40%-glycerol and 60%-glycerol.

The curves presented in Fig. 6 are smooth splines that were adjusted to the discrete experimental thickness data for each treatment. According to these curves, all treatments show a strong initial decrease of sample thickness, which is evidence of the fast dehydration mechanism. The magnitude of such thickness decrease rises with the glycerol concentration in the treating solution. After the initial thickness decrease, we see a smooth increase in sample thickness that lasts for different time intervals for each treatment. Such smooth increase is evidence of the OCA flux into the interstitial locations of the muscle to perform the RI matching mechanism. After that smooth increase, thickness stabilizes, showing that the effective net flux between the tissue and the treating solution has ended.

The mean data for each treatment in Fig. 6 was used in Eq. (12) to calculate $f_{scat}(t)$, which through the Gladstone and Dale law (Eq. (7)) allowed to calculate $f_{ISF}(t)$. The time dependence for the VFs in each treatment are presented in Fig. 7.

The graphs in Fig. 7 show that the major changes in the VFs occur within the first 5 min of treatment. The magnitude of these variations increases with the concentration of glycerol in the treatment solution and for the treatment with 60%-glycerol it indicates that $f_{scat}(t)$ grows above $f_{ISF}(t)$.

The calculated kinetics for the T_c spectra in each treatment also shows increasing behavior, as we can see from Fig. 8.

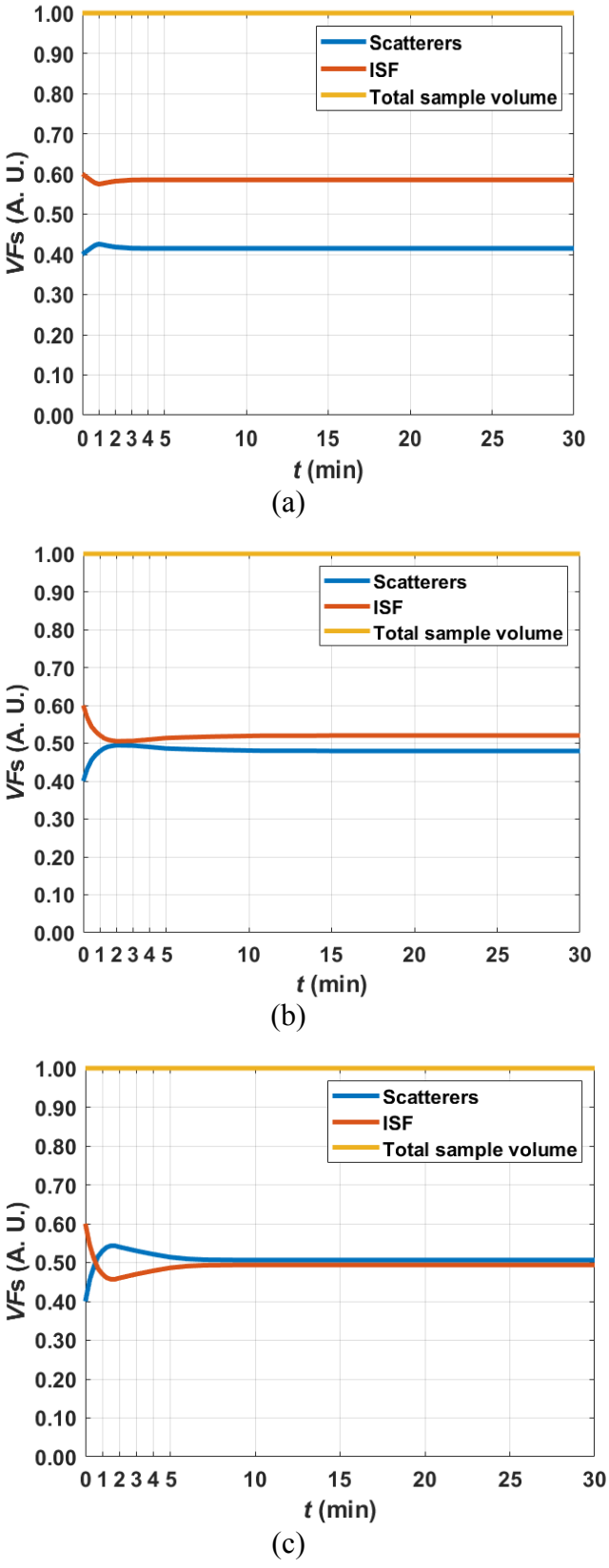
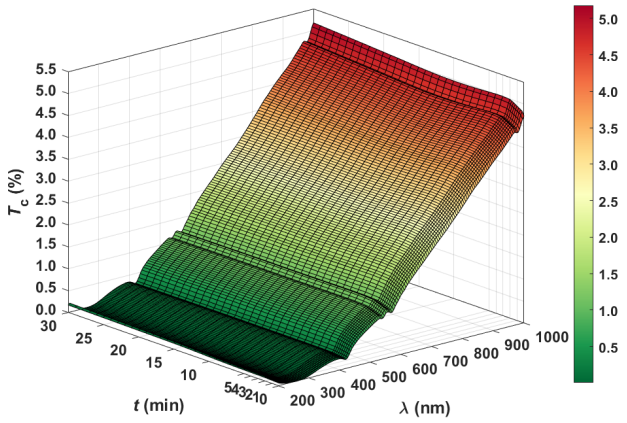
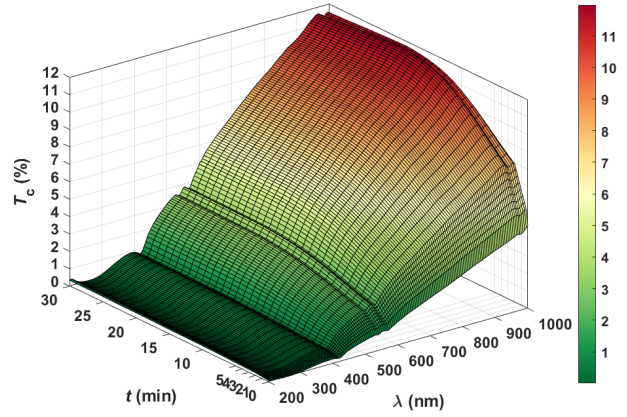


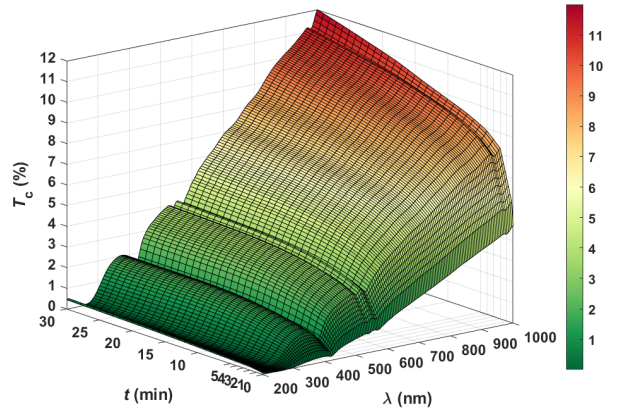
Fig. 7 Kinetics for the VFs for the treatments with: 20%-glycerol (a), 40%-glycerol (b) and 60%-glycerol (c).



(a)



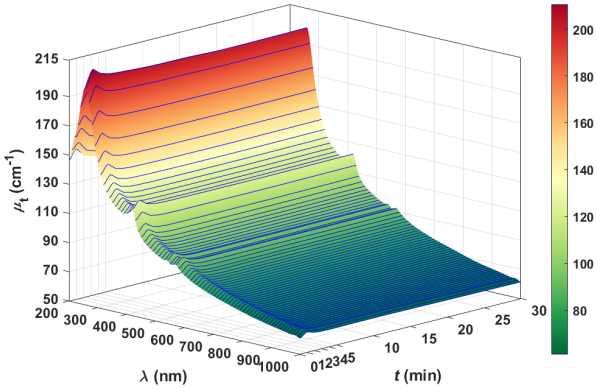
(b)



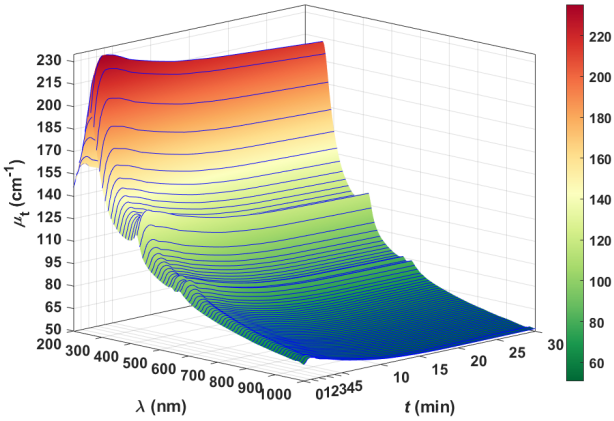
(c)

Fig. 8 Spectral T_c kinetics for colorectal muscle during treatments with: 20%-glycerol (a), 40%-glycerol (b) and 60%-glycerol (c).

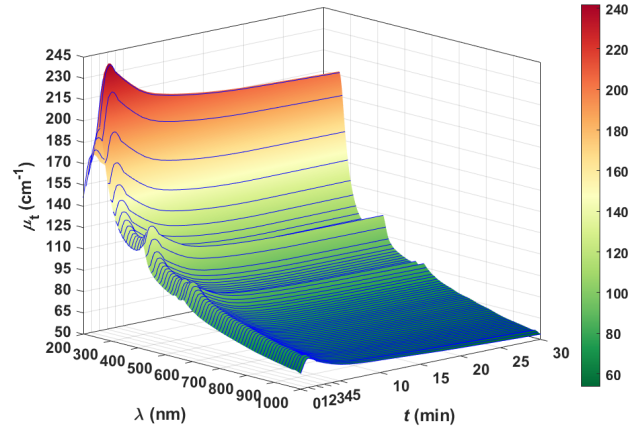
To calculate the time dependence for $\mu_t(\lambda)$ in the three treatments, we used the thickness kinetics data from Fig. 6 and the T_c kinetics data from Fig. 8 in the BBL equation (Eq. (3)). Fig. 9 presents such kinetics between 200 and 1000 nm.



(a)



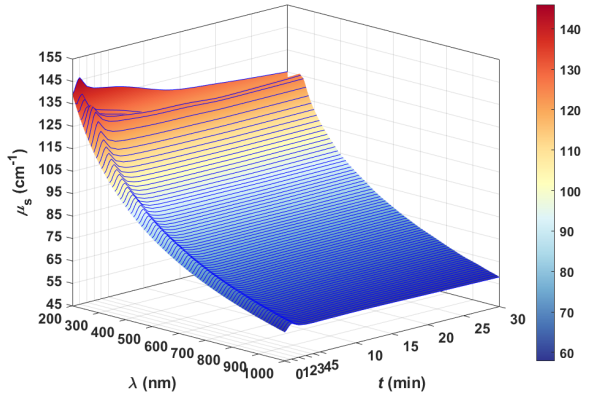
(b)



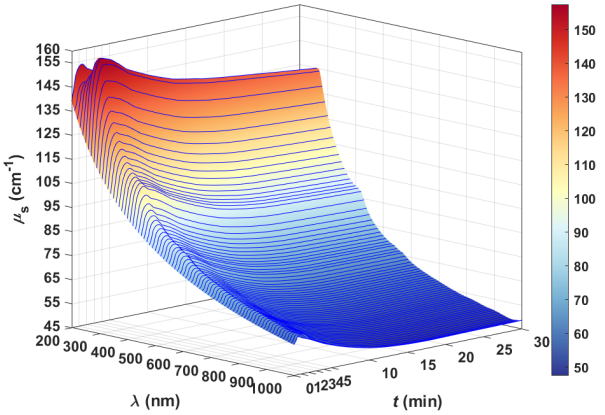
(c)

Fig. 9 Kinetics of $\mu_t(\lambda)$ for the treatments with: 20%-glycerol (a), 40%-glycerol (b) and 60%-glycerol (c).

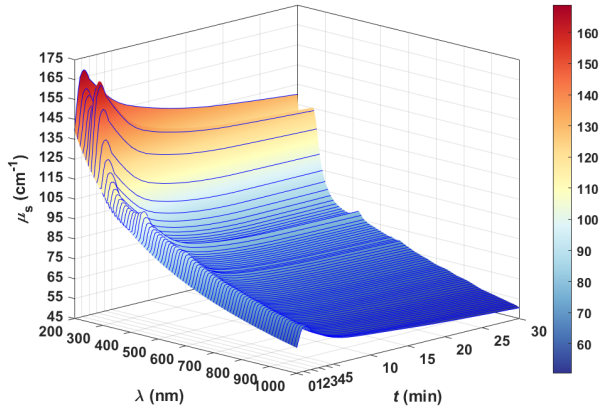
All graphs in Fig. 9 show a fast increase in $\mu_t(\lambda, t)$ at the beginning of the treatment, followed by a smooth decrease. Such behavior is observed for the entire spectral range, but with higher magnitude in the UV. The magnitude of these variations also grows from treatment to treatment with the increase of glycerol concentration in the treating solution.



(a)



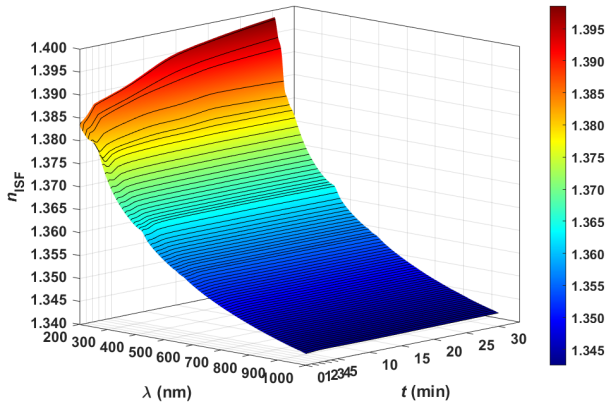
(b)



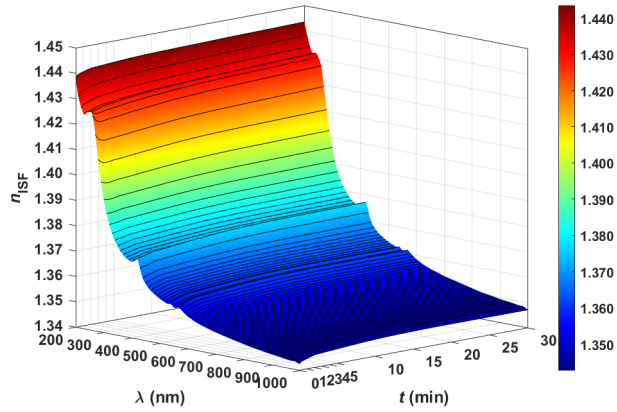
(c)

Fig. 10 Kinetics of $\mu_s(\lambda)$ for the treatments with: 20%-glycerol (a), 40%-glycerol (b) and 60%-glycerol (c).

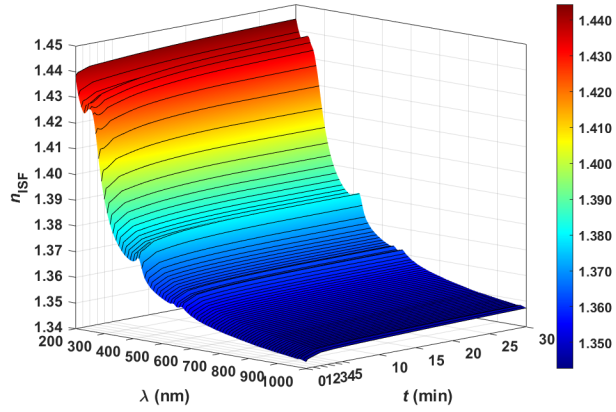
By subtracting the unchanged $\mu_a(\lambda)$ (presented in Fig. 3) to $\mu_t(\lambda, t)$, we obtained $\mu_s(\lambda, t)$. Those graphs are presented in Fig. 10.



(a)



(b)



(c)

Fig. 11 Kinetics of $n_{ISF}(\lambda)$ for the treatments with: 20%-glycerol (a), 40%-glycerol (b) and 60%-glycerol (c).

Similarly to what was observed in the kinetics of $\mu_t(\lambda)$, $\mu_s(\lambda,t)$ also shows a fast increase at the beginning of the treatment, which indicates the approach of tissue

scatterers as a result of dehydration. Such increase is followed by a smooth decrease as a result of the RI matching mechanism. Once again the magnitude of these variations grows with the glycerol concentration in the treating solution. For the treatments with 40%- and 60%-glycerol we see that these variations also occur for the wavelengths that correspond to the hemoglobin bands, with the later treatment showing the highest magnitude for these variations. Due to the presence of the absorption bands of proteins (200–230 nm) and DNA (260 nm), if we consider a particular time of treatment, no smooth decay is observed for the $\mu_s(\lambda)$.

Using the dispersion of scatterers (top curve in Fig. 5), the thickness kinetics data in Fig. 6 and the kinetics for $\mu_s(\lambda)$ in graphs of Fig. 10 in Eq. (13), the time dependence for $n_{ISF}(\lambda)$ was calculated for the three treatments. Fig. 11 presents the results of this calculation.

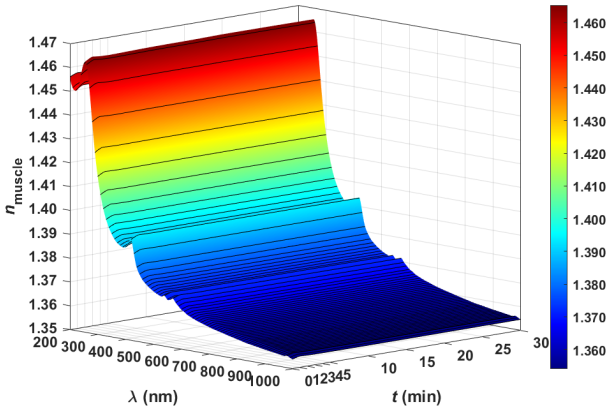
As a result of the partial replacement of water by glycerol in the interstitial locations, the average RI of the ISF increases during treatment. According to all graphs in Fig. 11, such RI matching is stronger in the UV range, as expected, especially for wavelengths between 200 and 320 nm (red and orange areas). A comparison between the graphs in Fig. 11 shows that such RI matching in the UV presents a growing magnitude with increasing glycerol concentration in the treating solution. Such information is important for the development of future diagnostic/treatment procedures that will work at UV wavelengths.

Finally, combining the scatterers dispersion in Fig. 5 with the data in the three graphs of Fig. 11 in the Gladstone and Dale law (Eq. (7)), we have calculated the RI kinetics for the whole muscle. The resulting graphs of this calculation are presented in Fig. 12.

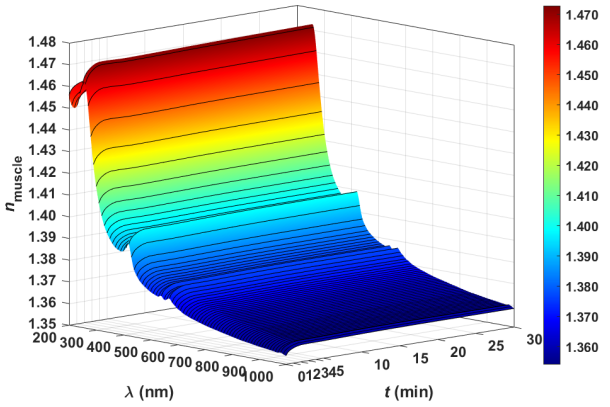
The kinetics presented in graphs of Fig. 12 are similar to the ones presented in graphs of Fig. 11, but now showing three clear stages: the dehydration mechanism is observed with the strong increase within the first min; a transition between the dehydration and RI matching mechanisms is observed in the following 3 min; and the RI matching mechanism dominates in the remaining 26 min. These graphs are clearer in showing that the magnitude in the RI increase is higher in the UV range and that such magnitude grows with increasing glycerol concentration in the treating solutions. Similar kinetics is seen for the absorption bands of proteins (200 nm), DNA (260 nm) and hemoglobin (418, 540, and 570 nm), meaning that the fraction of these biological molecules that were dissolved in the ISF are also subject of clearing.

4 Conclusion

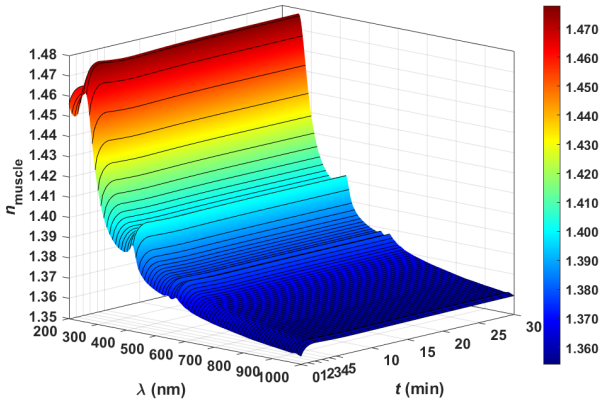
The RI kinetics of human colorectal muscle were calculated based only on thickness and T_c measurements made during OC treatments with different glycerol osmolarities. To evaluate the RI matching mechanism between 200 and 1000 nm, the three treatments used in this study were performed with aqueous solutions of glycerol, where the water content was higher (20%-glycerol), equal (40%-glycerol) or smaller (60%-glycerol) than the mobile water content in the muscle. As part of the calculations, the kinetics for $\mu_s(\lambda)$ were also obtained, showing a decrease over the time of treatment as a result of the RI matching mechanism (see Fig. 11).



(a)



(b)



(c)

Fig. 12 Kinetics of $n_{muscle}(\lambda)$ for the treatments with: 20%-glycerol (a), 40%-glycerol (b) and 60%-glycerol (c).

It was observed that the smooth decreasing wavelength dependence was kept unchanged in all

treatments for μ_s, n_{ISF} and n_{muscle} between ~270 and 1000 nm. For shorter wavelengths, no smooth decrease wavelength dependence was observed during treatments due to the presence of the absorption bands of proteins and DNA. The kinetics observed in this wavelength range for μ_s and n_{ISF} are also slightly different than what was observed for higher wavelengths, which indicates that glycerol has dissolved protein and DNA molecules located in the ISF. Increase in n_{ISF} and n_{muscle} at 418, 540, and 570 nm, especially for the treatments with 40%-glycerol and 60%-glycerol, shows that some hemoglobin in the ISF might also be cleared.

Considering the visible-NIR range and the treatment with 40%-glycerol, the kinetics of n_{ISF} presented the expected smooth-increasing time dependence, which indicates the unique glycerol flux into the interstitial locations as a result of the water balance between the solution and the mobile water in the muscle. For the other treatments, such time dependence also shows a global increase, but not with smooth kinetics due to the water unbalance between tissue and treating solution.

A comparison between the UV and visible-NIR ranges shows that the magnitude of the RI matching is higher in the UV and that such magnitude rises with the increase of glycerol in the treating solution.

Such results proof that native tissues have stronger light scattering properties in the UV range and that OC treatments through the RI matching mechanism are an effective way to reduce such scattering. Such information in conjunction with the discovery of two OC-induced windows in the UV range [37], opens the possibility to develop new diagnostic and treatment procedures with the use of UV light.

Disclosures

The authors declare that there are no conflicts of interest related to this article.

Acknowledgements

This research was supported by the Portuguese Grant FCT UIDB/04730/2020.

VVT was supported by the grant of the Russian Foundation of Basic Research #18-29-02060 MK.

References

1. V. V. Tuchin, I. L. Maksimova, D. A. Zimnyakov, I. L. Kon, A. H. Mavlutov, and A. A. Mishin, "Light propagation in tissues with controlled optical properties," Journal of Biomedical Optics 2(4), 401–407 (1997).
2. L. M. C. Oliveira, V. V. Tuchin, The Optical Clearing Method: A New Tool for Clinical Practice and Biomedical Engineering, Springer, Cham: Switzerland (2019).
3. L. Oliveira, M. I. Carvalho, E. Nogueira, and V. V. Tuchin, "Optical clearing mechanisms characterization in muscle," Journal of Innovative Optical Health Sciences 9(5), 1650035 (2016).
4. A. Yu. Sdobnov, M. E. Darvin, E. A. Genina, A. N. Bashkatov, J. Lademann, and V. V. Tuchin, "Recent progress in tissue optical clearing for spectroscopic application," Spectrochimica Acta Part A: Molecular and Biomolecular Spectroscopy 197, 216–229 (2018).
5. O. Semyachkina-Glushkovskaya, A. Abdurashitov, A. Dubrovsky, D. Bragin, O. Bragina, N. Shushunova, G. Maslyakova, N. Navolokin, A. Bucharskaya, V. V. Tuchin, J. Kurths, and A. Shirokov, "Application of optical coherence tomography for in vivo monitoring of the meningeal lymphatic vessels during opening of blood-brain barrier: mechanisms of brain clearing," Journal of Biomedical Optics 22(12), 121719 (2017).
6. T. Yu, Y. Qi, H. Gong, Q. Luo, and D. Zhu, "Optical clearing for multiscale biological tissues," Journal of Biophotonics 11(2), e201700187 (2018).
7. A. Yu. Sdobnov, V. V. Tuchin, J. Lademann, and M. E. Darvin, "Confocal Raman microscopy supported by optical clearing treatment of the skin – influence on collagen hydration," Journal of Physics D: Applied Physics 50(28), 285401 (2017).
8. D. Chen, N. Zeng, Q. Xie, H. He, V. V. Tuchin, and H. Ma, "Mueller matrix polarimetry for characterizing microstructural variation of nude mouse skin during optical clearing," Biomedical Optics Express 8(8), 3559–3570 (2017).
9. M. G. Ghosn, E. F. Carbajal, N. A. Befrui, V. V. Tuchin, and K. V. Larin, "Differential permeability rate and percent clearing of glucose in different regions in rabbit sclera," Journal of Biomedical Optics 13(2), 021110 (2008).
10. Q. L. Zhao, J. L. Si, Z. Y. Guo, H. J. Wei, H. Q. Yang, G. Y. Wu, S. S. Xie, X. Y. Li, X. Guo, H. Q. Zhong, and L. Q. Li, "Quantifying glucose permeability and enhanced light penetration in ex vivo human normal and cancerous esophagus tissues with optical coherence tomography," Laser Physics Letters 8(1), 71–77 (2011).
11. H. Ullah, E. Ahmed, and M. Ikram, "Monitoring of glucose levels in mouse blood with noninvasive optical methods," Laser Physics 24(2), 025601 (2014).
12. O. Zhernovaya, V. V. Tuchin, and M. J. Leahy, "Blood optical clearing studied by optical coherence tomography," Journal of Biomedical Optics 18(2), 26014 (2013).

13. P. Liu, Y. Huang, Z. Guo, J. Wang, Z. Zhuang, and S. Liu, "Discrimination of dimethyl sulfoxide diffusion coefficient in the process of optical clearing by confocal micro-Raman spectroscopy," Journal of Biomedical Optics 18(2), 20507 (2013).
14. L. M. Oliveira, M. I. Carvalho, E. Nogueira, and V. V. Tuchin, "The characteristic time of glucose Diffusion measured for muscle tissue at optical clearing," Laser Physics 23, 075606 (2013).
15. L. M. Oliveira, M. I. Carvalho, E. M. Nogueira, and V. V. Tuchin, "Diffusion characteristics of ethylene glycol in skeletal muscle," Journal of Biomedical Optics 20(5), 051019 (2015).
16. S. Carvalho, N. Gueiral, E. Nogueira, R. Henrique, L. Oliveira, and V. V. Tuchin, "Glucose diffusion in colorectal mucosa – a comparative study between normal and cancer tissues," Journal of Biomedical Optics 22(9), 091506 (2017).
17. K. V. Berezin, K. N. Dvoretski, M. L. Chernavina, V. V. Nechaev, A. M. Likhter, I. T. Shagautdinova, E. Yu. Stepanovich, O. N. Grechukhina, and V. V. Tuchin, "Studying the mechanism of tissue optical clearing using the method of molecular dynamics," Proceedings of SPIE 10336, 103360J (2017).
18. K. V. Berezin, K. N. Dvoretski, M. L. Chernavina, A. M. Likhter, V. V. Smirnov, I. T. Shagautdinova, E. M. Antonova, E. Yu. Stepanovich, E. A. Dzhalmuhambetova, and V. V. Tuchin, "Molecular modeling of immersion optical clearing of biological tissues," Journal of Molecular Modeling 24(2), 45 (2018).
19. L. Pires, V. Demidov, I. A. Vitkin, V. S. Bagnato, C. Kurachi, and B. C. Wilson, "Optical clearing of melanoma in vivo: characterization by diffuse reflectance spectroscopy and optical coherence tomography," Journal of Biomedical Optics 21(8), 081210 (2016).
20. D. Abookasis, T. Moshe, "Reconstruction enhancement of hidden object using speckle contrast projections and optical clearing agents," Optics Communications 300, 58–64 (2013).
21. D. Zhu, W. Lu, Y. Weng, H. Cui, and Q. Luo, "Monitoring thermal-induced changes tumor blood flow and microvessels with laser speckle contrast imaging," Applied Optics 46(10), 1911–1917 (2007).
22. Y. Zhang, H. Liu, J. Tang, Z. Li, X. Zhou, R. Zhang, L. Chen, Y. Mao, and C. Li, "Non-invasively imaging subcutaneous tumor xenograft by handheld Raman detector, with assistance of optical clearing agent," ACS Applied Materials & Interfaces 9(21), 17769–17776 (2017).
23. M. Oldham, H. Sakhalkar, T. Oliver, M. Y. Wang, J. Kirkpatrick, J. Cao, C. Badea, and M. Dewhirst, "Three-dimensional imaging of xenograft tumors using optical computed and emission tomography," Medical Physics 33(9), 3193–3202 (2006).
24. M. Oldham, H. Sakhalkar, T. Oliver, G. A. Johnson, and M. Dewhirst, "Optical clearing of unsectioned specimens for three-dimensional imaging via optical transmission and emission tomography," Journal of Biomedical Optics 13(2), 021113 (2008).
25. M. Wei, L. Shi, Y. Shen, Z. Zhao, A. Guzman, L. J. Kaufman, L. Wei, and W. Min, "Volumetric chemical imaging by clearing-enhanced stimulated Raman scattering microscopy," Proceedings of the National Academy of Sciences 116(14), 6608–6617 (2019).
26. T. Lagerweijt, S. A. Dusoswa, A. Negrean, E. M. L. Hendrikx, H. E. Vries, J. Kole, J. J. Garcia-Vallejo, H. D. Mansvelder, W. P. Vandertop, D. P. Noske, B. A. Tannous, R. J. P. Musters, Y. van Kooyk, P. Wesseling, X. W. Zhao, and T. Wurdinger, "Optical clearing and fluorescence deep-tissue imaging for 3D quantitative analysis of the brain tumor microenvironment," Angiogenesis 20(4), 533–546 (2017).
27. J. Hirshburg, B. Choi, J. S. Nelson, and A. T. Yeh, "Collagen solubility correlates with skin optical clearing," Journal of Biomedical Optics 11(4), 040501 (2006).
28. V. Hovhannisyan, P.-S. Hu, S.-J. Chen, C.-S. Kim, and C.-Y. Dong, "Elucidation of the mechanisms of optical clearing in collagen tissue with multiphoton imaging," Journal of Biomedical Optics 18(4), 046004 (2013).
29. I. Costantini, R. Cicchi, L. Silvestri, F. Vanzi, and F. S. Pavone, "In-vivo and ex-vivo optical clearing methods for biological tissues: review," Biomedical Optics Express 10(10), 5251–5267 (2019).
30. E. A. Genina, A. N. Bashkatov, and V. V. Tuchin, "Tissue optical immersion clearing," Expert Review of Medical Devices 7(6), 825–842 (2010).
31. I. Carneiro, S. Carvalho, R. Henrique, L. Oliveira, and V. Tuchin, "Measurement of optical properties of normal and pathological human liver tissue from deep-UV to NIR," Proceedings of SPIE 11363, 113630D (2020).
32. H. Ding, J. Q. Lu, W. A. Wooden, P. J. Kragel, and X. H. Hu, "Refractive indices of human skin tissues at eight wavelengths and estimated dispersion relations between 300 and 1600 nm," Physics in Medicine and Biology 51(6), 1479–1489 (2006).
33. Z. Deng, J. Wang, Q. Ye, T. Sun, E. Zhou, J. Mei, C. Zhang, and J. Tian, "Determination of continuous complex refractive index dispersion of biotissue based on internal reflection," Journal of Biomedical Optics 21(1), 015003 (2016).
34. S. Liu, Z. Deng, J. Li, J. Wang, N. Huang, R. Cui, Q. Zhang, J. Mei, E. Zhou, C. Zhang, Q. Ye, and J. Tian, "Measurement of the refractive index of whole blood and its components for a continuous spectral region," Journal of Biomedical Optics 24(3), 035003 (2019).
35. Y. Zhou, J. Yao, and L. V. Wang, "Tutorial on photoacoustic tomography," Journal of Biomedical Optics 21(6), 061007 (2016).

36. P. Brescia, Micro-volume purity assessment of nuclei acids using A260/A280 ratio and spectral scanning protein and nucleic acid quantification (accessed: May 2020).
37. I. Carneiro, S. Carvalho, R. Henrique, L. Oliveira, and V. Tuchin, "Moving tissue spectral window to the deep-ultraviolet via optical clearing," Journal of Biophotonics 12(12), e201900181 (2019).
38. A. Yeh, B. Choi, J. S. Nelson, and B. J. Tromberg, "Reversible dissociation of collagen in tissues," Journal of Investigative Dermatology 121, 1332–1335 (2003).
39. L. M. Oliveira, M. I. Carvalho, E. M. Nogueira, and V. V. Tuchin, "Skeletal muscle dispersion (400-1000 nm) and kinetics at optical clearing," Journal of Biophotonics 11(1), e201700094 (2018).
40. V. V. Tuchin, Tissue Optics: Light Scattering Methods and Instruments for Medical Diagnosis, 3rd ed., SPIE Press, Bellingham (2015).
41. S. L. Jacques, "Optical properties of biological tissues: a review," Physics in Medicine and Biology 58(11), R37–R61 (2013).
42. J. Grienger, H. Groβ, J. Newkammer, and M. Bär, "Determining the refractive index of human hemoglobin solutions by Kramers-Kronig relations with an improved absorption model," Applied Optics 55(31), 8951–8961 (2016).
43. O. Sydoruk, O. Zhernovaya, V. Tuchin, and A. Douplik, "Refractive index of solutions of human hemoglobin from the near-infrared to the ultraviolet range: Kramers-Kronig analysis," Journal of Biomedical Optics 17(11), 115002 (2012).
44. I. Carneiro, S. Carvalho, R. Henrique, L. Oliveira, and V. V. Tuchin, "Kinetics of optical properties of colorectal muscle during optical clearing," IEEE Journal of Selected Topics in Quantum Electronics 25(1), 7200608 (2019).
45. V. V. Tuchin, Optical Clearing of Tissues and Blood, SPIE Press, Bellingham (2006).
46. I. Carneiro, S. Carvalho, V. Silva, R. Henrique, L. Oliveira, and V. V. Tuchin, "Kinetics of optical properties of human colorectal tissues during optical clearing: a comparative study between normal and pathological tissues," Journal of Biomedical Optics 23(12), 121620 (2018).
47. L. Oliveira, A. Lage, M. Pais Clemente, and V. V. Tuchin, "Optical characterization and composition of abdominal wall muscle from rat," Optics and Lasers in Engineering 47, 667–672 (2009).
48. L. Oliveira, A. Lage, M. Pais Clemente, and V. V. Tuchin, "Rat muscle opacity decrease due to the osmosis of a simple mixture," Journal of Biomedical Optics 15(5), 055004 (2010).
49. K. M. Meek, S. Dennis, and S. Khan, "Changes in the refractive index of the stroma and its extrafibrillar matrix when the cornea swells," Biophysical Journal 85(4), 2205–2212 (2003).
50. K. M. Meek, D. W. Leonard, C. J. Connon, S. Dennis, and S. Khan, "Transparency, swelling and scarring in the corneal stroma," Eye 17(8), 927–936 (2003).
51. O. Zhernovaya, O. Sydoruk, V. V. Tuchin, and A. Douplik, "The refractive index of human hemoglobin in the visible range," Physics in Medicine and Biology 56(13), 4013–4021 (2011).
52. E. N. Lazareva, V. V. Tuchin, "Measurement of refractive index of hemoglobin in the visible/NIR spectral range," Journal of Biomedical Optics 23(3), 035004 (2018).
53. E. N. Lazareva, V. V. Tuchin, "Blood refractive index modeling in the visible and near infrared spectral regions," Journal of Biomedical Photonics & Engineering 4(1), 010503 (2018).
54. I. Yu. Yanina, E. E. Lazareva, and V. V. Tuchin, "Refractive index of adipose tissue and lipid droplet measured in wide spectral and temperature ranges," Applied Optics 57(17), 4839–4848 (2018).
55. M. Daimon, A. Masumura, "Measurement of the refractive index of distilled water from the near-infrared region to the ultraviolet region," Applied Optics 46, 3811–3820 (2007).

Optical Clearing of Human Skin Using Polyethylene Glycols

Kirill V. Berezin[1], Konstantin N. Dvoretskiy[2*], Vladimir V. Nechaev[3], Anatoliy M. Likhter[4], Ilmira T. Shagautdinova[4], and Valery V. Tuchin[1,5,6]

[1] Saratov State University, Saratov 410012, Russia
[2] Saratov State Medical University, Saratov 410012, Russia
[3] Saratov State Technical University, Saratov 410054, Russia
[4] Astrakhan State University, Astrakhan 414056, Russia
[5] Institute of Precision Mechanics and Control, Russian Academy of Sciences, Saratov 410028, Russia
[6] Tomsk State University, Tomsk 634050, Russia

*** e-mail:** dcn@yandex.ru

Abstract. Molecular docking and quantum chemistry (PM6 and DFT/B3LYP) methods have been used to investigate the interaction of a number of biological tissue immersion clearing agents (PEG200, PEG300 and PEG400) with collagen mimetic peptides $(GPH)_3$. Correlations between the rate (efficiency) of optical clearing and the energy of complex formation are established. © 2020 Journal of Biomedical Photonics & Engineering.

Keywords: molecular dynamics; quantum chemistry; immersion optical clearing.

Paper #3373 received 23 May 2020; revised manuscript received 11 Jun 2020; accepted for publication 12 Jun 2020; published online 27 Jun 2020. doi: 10.18287/JBPE20.06.020308.

1 Introduction

The use of modern methods of biomedical optics and photomedicine for the diagnosis and treatment of diseases is experiencing difficulties due to the fact that the skin and many other tissues have strong light scattering in the visible and near-infrared regions. The scattering is caused by the inhomogeneities of the refractive indices at the boundaries of various macromolecular structures, mainly, on collagen fibers, which are mainly responsible for the scattering of light in the skin [1]. These difficulties are overcome by introducing biocompatible molecular agents into the tissue, which contribute, to some extent, to its optical clearing [2–4]. Quite a lot of works was devoted to experimental studies of the optical clearing of various types of tissues *in vitro* and *in vivo* [5–11] that indicates the importance of the problem. Mathematical models of light propagation in strongly scattering tissues with absorption are discussed in Ref. [2]. Tuchina et al. [12] considered the effect of model diabetes on the optical clearing of the skin of laboratory mice. Wen et al. [13] explored the mechanism of optical clearing of the skin using glycerol as a clearing agent to improve second harmonic generation (SHG) imaging. However, the mechanisms of optical clearing at the molecular level are still not fully determined, and only a few works [1, 14–17] are devoted to the study of molecular processes responsible for the optical clearing of the skin. Yu et al. [18] present the results of studies of the dehydrating properties of clearing agents. The authors note that dehydration is only one of the possible mechanisms leading to better optical transparency of tissues. Conducting research in this area opens the way to understanding the essence of optical clearing processes at the molecular level, which, in turn, offers the use of new active clearing agents with desired properties.

In this regard, in order to establish a correlation between the rate (efficiency) of optical clearing of tissue and the parameter of intermolecular interaction (energy of complex formation), the interaction of a number of immersion clearing agents (polyethylene glycols) with collagen mimetic peptides $(GPH)_3$ using molecular docking and quantum chemistry methods (PM6 and DFT/B3LYP) is studied.

Due to its effectiveness, availability and biocompatibility, polyethylene glycol (PEG) can be successfully used as an immersion optical clearing agent [19, 20]. Also, PEG is actively used in medicine and cosmetology as a base for ointments, registered as a food additive E1521, applied as a solvent, extractant, preservative, as well as a strong osmotic.

2 Molecular Modeling

We used collagen mimetic peptide $(GPH)_3$ [21] that forms the basis of most of the regular domains of human collagen, as the molecular model of collagen. Such

relatively small synthetic peptides are often used for molecular simulation of collagens. The three-dimensional model of the peptide was constructed according to data from the Protein Data Bank (PDB) with the subsequent addition of hydrogen atoms and structure optimization by the molecular dynamics method [22]. We have considered three PEG molecules with a molecular weight of 200, 300 and 400 Da as immersion clearing agents (OCAs) for that experimental data on the efficiency of optical clearing (OC) are available in Refs. [19, 20]. The rate (efficiency) of OC of the skin was estimated in three spectral ranges using the expression

$$OC_{ef} = (\mu_{s0} - \mu_s(t))/\mu_{s0},$$

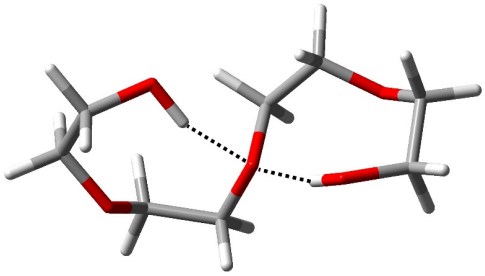
where μ_{s0} is the scattering coefficient at the initial time and $\mu_s(t)$ is the scattering coefficient value at time t of the optical clearing of the skin. Molecular simulation of the interaction of OCAs with collagen was carried out in two stages.

At the first stage, all the lowest energy conformers of the considered sugars in an isolated state were determined and calculated by the DFT/B3LYP/6-311+G(d,p) method [23, 24] using the Gaussian program [25]. The calculated geometrical parameters were later used in the simulation of these systems within the framework of classical molecular docking. The wavenumbers of vibrational transitions were also calculated, which turned out to be positive that additionally indicates the presence of molecular systems in local minima.

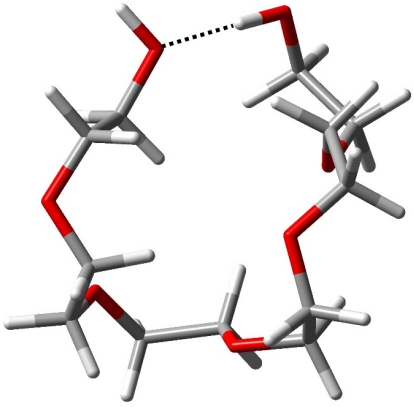
At the second stage, the minimal fragment of the mimetic peptide retaining a regular structure, that is, $((GPH)_3)_2$, consisting of 231 atoms, the structure of which was pre-optimized using the semi-empirical method PM6 [26], was used to estimate the intermolecular interaction energy of selected OCAs with collagen. This optimized structure of the collagen model was used for molecular docking with OCAs in the AutoDockVina software [27]. After carrying out molecular docking for each interacting system, the first ten most advantageous configurations were selected, which were further optimized by the semi-empirical PM6 method. Then, the total electron energy of the complexes was calculated by performing a single SCF procedure using the DFT/B3LYP/6-31G(d) method. A similar procedure was used to obtain the total electron energy values of the OCAs and the peptide fragment. The energy of intermolecular interaction was calculated as the difference between the total energies of the complex and the sum of the energies of its individual components. To find out the correlation with the efficiency of OC, we selected the highest values of the intermolecular interaction energies corresponding to the most probable structures of the complexes.

3 Results and Discussion

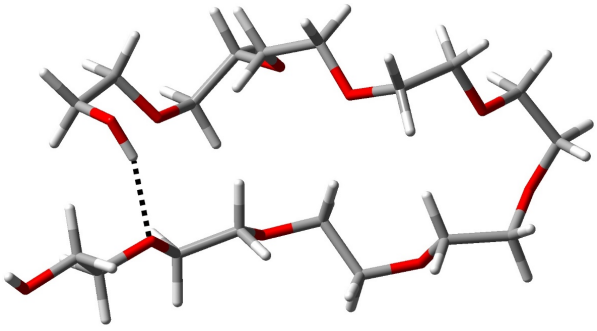
The spatial configurations of the lowest energy isolated conformers of PEGs calculated using the DFT/B3LYP/6 311+G(d,p) method are shown in Fig. 1. As can be seen, for all of the compounds presented, the most favorable in the isolated state are conformations in which hydroxyl groups are located as close to each other as possible, which often leads to the formation of intramolecular hydrogen bonds.



PEG200



PEG300



PEG400

Fig. 1 Spatial configurations of the lowest energy isolated conformers of optical clearing agents calculated by DFT/B3LYP/6 311+G(d,p) method. The dotted lines in the figure show intramolecular hydrogen bonds

At the second stage of the simulation, the energy of intermolecular interactions of OCAs with a fragment of the mimetic collagen peptide – $((GPH)_3)_2$, the spatial structure of which is shown in Fig. 2, was calculated.

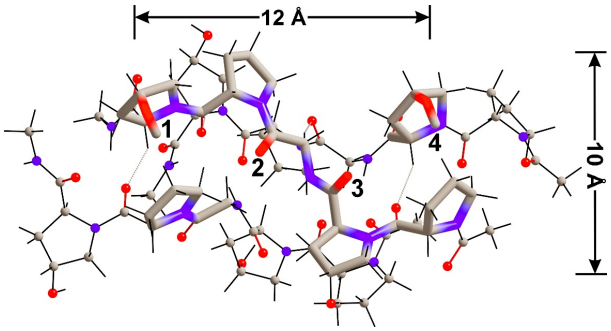
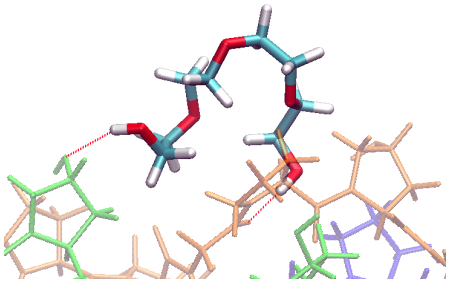
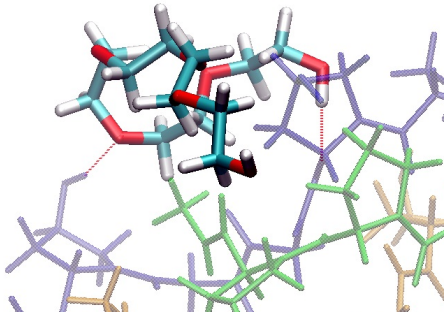


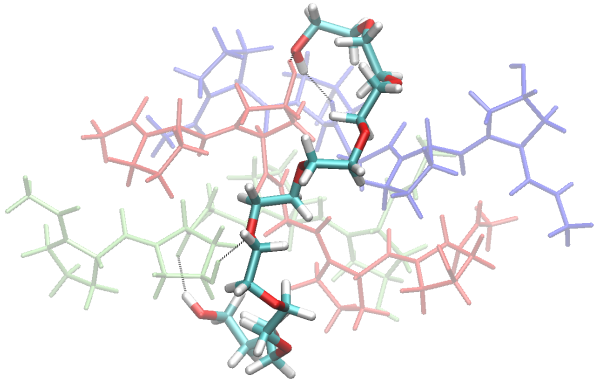
Fig. 2 Spatial structure of the mimetic peptide fragment – $((GPH)_3)_2$ optimized in the framework of the semi-empirical PM6 method. Numbers indicate the molecular groups involved in the formation of hydrogen bonds with optical clearing agents. The dotted lines in the Fig. show the hydrogen bonds between different α-chains.



PEG200



PEG300



PEG400

Fig. 3 Structure of the PM6-calculated hydrogen-bound complexes formed by a collagen fragment $((GPH)_3)_2$ and immersion optical clearing agents. The dotted line shows classic intermolecular hydrogen bonds.

Table 1 Lengths of hydrogen bonds and energy of intermolecular interactions between a collagen fragment $((GPH)_3)_2$ and various clearing agents calculated by the PM6/B3LYP/6-31G(d) method and experimental values of the rate (efficiency) of optical clearing.

Type of agent	Lengths of hydrogen bond, Å	ΔE	Efficiency of optical clearing
PEG200	2.04; 2.06	−42.41	0.31±0.10 [19]
PEG300	1.83; 1.95	−48.92	0.36±0.14 [20]
PEG400	1.84; 1.84; 1.93; 2.09	−73.91	0.42±0.10 [20]

The molecular capture pocket is a section of a peptide approximately 10×12 Å in size, in which there are four functional groups available for intermolecular binding: two carbonyl groups (one (2) on the glycine residue, the other (3) on the hydroxyproline residue of the same α-chain) and two alcohol groups (1 and 4) on the hydroxyproline residues of various α-chains (Fig. 2). When collagen interacts with low-molecular agents, a certain spatial adjustment of the molecular pocket occurs to form the largest number of possible hydrogen bonds.

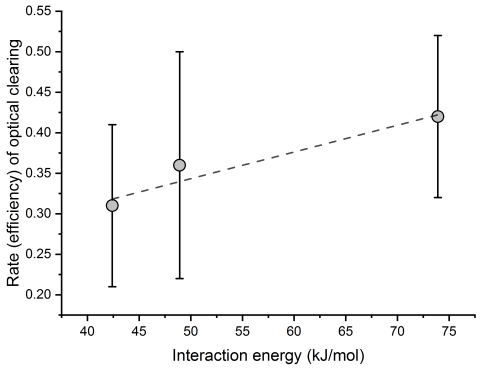


Fig. 4 The dependence of the efficiency of optical clearing of rat skin [19, 20] on the energy of interaction of the collagen peptide molecule with the molecules of clearing agents.

Fig. 3 shows the spatial structure of hydrogen-bound complexes formed by collagen fragments $((GPH)_3)_2$ and the OCAs. For convenience of discussion of the results obtained, Table 1 summarizes the quantitative parameters of intermolecular interactions (the values of the lengths of classical hydrogen bonds, formed according to the calculation between the active groups of the collagen molecular pocket and the hydroxyl groups of the OCAs, and the calculated energies of the intermolecular interactions). Fig. 3 also shows that the distance between the alcohol groups at the ends of the PEG400 molecule is already sufficient to form hydrogen bonds with different landing molecular pockets on the surface of the molecule. The energy of

this interaction is much greater than that of the shorter PEG200 and PEG300 molecules, which are able to form hydrogen bonds only within one molecular capture pocket. From the data it follows that the dependence of the efficiency of OC of the skin of *ex vivo* white laboratory rats [19, 20] correlates well with the interaction energy calculated by the PM6/B3LYP/6-31G method for the selected OCAs (Fig. 4). The linear correlation coefficient is 0.94. This suggests the fundamental importance of the post-diffusion stage, in which the interaction of collagen with OCAs occurs, and its effect on the OC of tissues takes place. The results of the study suggest that in the process of such an interaction, a partial replacement of water associated with collagen occurs. This leads to the destruction of the network of hydrogen bonds and, as a result, to the reversible process of dissolution of collagen fibrils, which in turn decreases their refractive index and matches it with the intercollagen medium. The higher the affinity of the OCA to collagen, the more effective is this process.

The next fundamental step to increase the efficiency of interaction may be the selection of a molecular agent with such structural characteristics that would allow it to interact with two or more molecular pockets of collagen at once. Such an active OCA can serve as a polymer-type molecular system consisting, for example, of six-membered monosaccharides connected by a mobile carbon–oxygen chain of such a length that saturated rings of sugar fall into the regions of the molecular pockets of collagen and interact with them through their hydroxyl groups. A significant increase in the size of molecules used as OCAs leads to an increase in the viscosity of a substance and, as a consequence, to a decrease in its diffusion coefficient in tissue and an increase in the time of its washing out from tissues. Therefore, the choice of the optimal OCA is a trade-off between the effectiveness of the OC and OCA diffusion time.

Thus, the construction of an adequate molecular model and finding the correlation described above for various optical clearing agents [7, 17, 28] allows one to predict the optical clearing potential of various molecular systems and select the most effective ones before expensive *ex vivo* and *in vivo* animal studies and further for practical use in medicine.

4 Conclusions

As a result of complex molecular modeling of the interaction of a number of immersion optical clearing agents with a mimetic collagen peptide $((GPH)_3)_2$ correlations between the rate (efficiency) of optical clearing and such a characteristic as the energy of intermolecular interaction of clearing agents with a fragment of a collagen peptide are established.

Disclosures

All authors declare that there is no conflict of interests in this paper.

Acknowledgments

V. V. Tuchin was supported by RFBR grant no 18-52-16025.

References

1. J. M. Hirshburg, Chemical agent induced reduction of skin light scattering: doctoral dissertation, Texas A&M University (2009).
2. V. V. Tuchin, Tissue Optics: Light Scattering Methods and Instruments for Medical Diagnostics, 3rd ed., PM254, SPIE Press, Bellingham, WA (2015).
3. D. Zhu, K. V. Larin, Q. Luo, and V. V. Tuchin, "Recent progress in tissue optical clearing," Laser & Photonics Reviews 7(5), 732-757 (2013).
4. E. A. Genina, A. N. Bashkatov, Y. P. Sinichkin, I. Yu. Yanina, and V. V. Tuchin, "Optical clearing of biological tissues: prospects of application in medical diagnostics and phototherapy [Review]," Journal of Biomedical Photonics & Engineering 1(1), 22-58 (2015).
5. K. V. Larin, M. G. Ghosn, A. N. Bashkatov, E. A. Genina, N. A. Trunina, and V. V. Tuchin, "Optical clearing for OCT image enhancement and in-depth monitoring of molecular diffusion," IEEE Journal of Selected Topics in Quantum Electronics 18(3), 1244-1258 (2012).
6. V. V. Tuchin, "Polarized light interaction with tissues," Journal of Biomedical Optics 21(7), 071114 (2016).
7. A. N. Bashkatov, K. V. Berezin, K. N. Dvoretskiy, M. L. Chernavina, E. A. Genina, V. D. Genin, and V. I. Kochubey, "Measurement of tissue optical properties in the context of tissue optical clearing," Journal of Biomedical Optics 23(9), 091416 (2018).
8. E. N. Lazareva, P. Dyachenko (Timoshina), A. Bucharskaya, N. Navolokin, and V. Tuchin, "Estimation of dehydration of skin by refractometric method using optical clearing agents," Journal of Biomedical Photonics & Engineering 5(2), 020305 (2019).
9. A. Yu. Sdobnov, M. E. Darvin, E. A. Genina, A. N. Bashkatov, J. Lademann, and V. V. Tuchin, "Recent progress in tissue optical clearing for spectroscopic application," Spectrochimica Acta Part A: Molecular and Biomolecular Spectroscopy 197, 216–229 (2018).

10. S. M. Zaytsev, Y. I. Svenskaya, E. V. Lengert, G. S. Terentyuk, A. N. Bashkatov, V. V. Tuchin, and E. A. Genina, "Optimized skin optical clearing for optical coherence tomography monitoring of encapsulated drug delivery through the hair follicles," Journal of Biophotonics 13(4), e201960020 (2020).
11. N. Sudheendran, M. Mohamed, M. G. Ghosn, V. V. Tuchin, and K. V. Larin, "Assessment of tissue optical clearing as a function of glucose concentration using optical coherence tomography," Journal of Innovative Optical Health Sciences 3(3), 169-176 (2010).
12. D. K. Tuchina, R. Shi, A. N. Bashkatov, E. A. Genina, D. Zhu, Q. Luo, and V. V. Tuchin, "Ex vivo optical measurements of glucose diffusion kinetics in native and diabetic mouse skin," Journal of Biophotonics 8(4), 332-346 (2015).
13. X. Wen, Z. Mao, Z. Han, V. V. Tuchin, and D. Zhu, "In vivo skin optical clearing by glycerol solutions: mechanism," Journal of Biophotonics 3(1-2), 44-52 (2010).
14. J. M. Hirshburg, K. M. Ravikumar, W. Hwang, and A. T. Yeh, "Molecular basis for optical clearing of collagenous tissues," Journal of Biomedical Optics 15(5), 055002 (2010).
15. W. Feng, R. Shi, N. Ma, D. K. Tuchina, V. V. Tuchin, and D. Zhu, "Skin optical clearing potential of disaccharides," Journal of Biomedical Optics 21(8), 081207 (2016).
16. K. N. Dvoretsky, K. V. Berezin, M. L. Chernavina, A. M. Likhter, I. T. Shagautdinova, E. M. Antonova, O. N. Grechukhina, and V. V. Tuchin, "Molecular Modeling of the Post-Diffusion Stage of Surface Bio-Tissue Layers Immersion Optical Clearing," Journal of Surface Investigation: X-ray, Synchrotron and Neutron Techniques 12 (5), 961-967 (2018).
17. K. V. Berezin, K. N. Dvoretski, M. L. Chernavina, A. M. Likhter, V. V. Smirnov, I. T. Shagautdinova, E. M. Antonova, E. Yu. Stepanovich, E. A. Dzhalmuhambetova, and V. V. Tuchin, "Molecular modeling of immersion optical clearing of biological tissues," Journal of Molecular Modeling 24(2), 45 (2018).
18. T. Yu, X. Wen, V. V. Tuchin, Q. Luo, and D. Zhu, "Quantitative analysis of dehydration in porcine skin for assessing mechanism of optical clearing," Journal of Biomedical Optics 16(9), 095002 (2011).
19. V. D. Genin, P. Rakotomanga, S. M. Zaytsev, E. A. Genina, E. N. Lazareva, G. Khairallah, M. Amouroux, C. Soussen, H. Chen, W. Feng, D. Zhu, A. N. Bashkatov, W. Blondel, and V. V. Tuchin, "Research and development of effective optical technologies for diagnostics in dermatology," Proceedings of SPIE 11065, 1106505 (2019).
20. D. K. Tuchina, V. D. Genin, A. N. Bashkatov, E. A. Genina, and V. V. Tuchin, "Optical clearing of skin tissue ex vivo with polyethylene glycol," Optics and Spectroscopy 120(1), 36-45 (2016).
21. K. Okuyama, K. Miyama, K. Mizuno, and H. P. Bächinger, "Crystal structure of (Gly-Pro-Hyp)9: implications for the collagen molecular model," Biopolymers 97(8), 607-616 (2012).
22. W. D. Cornell, P. Cieplak, C. I. Bayly, I. R. Gould, K. M. Merz, D. M. Ferguson, D. C. Spellmeyer, T. Fox, J. W. Caldwell, and P. A. Kollman, "A second generation force field for the simulation of proteins, nucleic acids, and organic molecules," Journal of the American Chemical Society 117(19), 5179-5197 (1995).
23. A. D. Becke, "Density - functional thermochemistry. III. The role of exact exchange," The Journal of Chemical Physics 98(7), 5648-5652 (1993).
24. C. Lee, W. Yang, and R. G. Parr, "Development of the Colle-Salvetti correlation-energy formula into a functional of the electron density," Physical Review B 37(2), 785-789 (1988).
25. M. J. Frisch, G. Trucks, H. B. Schlegel, G. E. Scuseria, M. A. Robb, J. R. Cheeseman, G. Scalmani, V. Barone, B. Mennucci,G. A. Petersson, H. Nakatsuji, X. Li, M. Caricato, X. Li, J. Bloino, H. P. Hratchian, A. F. Izmaylov, J. L. Sonnenberg, G. Zheng, M. Hada, and D. J. Fox, Gaussian09, Revision A.02, Gaussian Inc., Wallingford CT (2009).
26. J. J. P. Stewart, "Optimization of parameters for semiempirical methods V: Modification of NDDO approximations and application to 70 elements," Journal of Molecular Modeling 13(12), 1173-1213 (2007).
27. O. Trott, A. J. Olson, "AutoDock Vina: Improving the speed and accuracy of docking with a new scoring function, efficient optimization, and multithreading," Journal of Computational Chemistry 31(2), 455-461 (2010).
28. K. V. Berezin, K. N. Dvoretskii, M. L. Chernavina, V. V. Nechaev, A. M. Likhter, I. T. Shagautdinova, E. M. Antonova, and V. V. Tuchin, "Optical clearing of human skin using some monosaccharides in vivo," Optics and Spectroscopy 127(2), 352-358 (2019).

Optical Biopsy and Optical Pathology: Affordable Health Care Under Low-Resource Settings

Swathi Rao[1], Reena John[1], Ajeetkumar Patil[1], Unnikrishnan V. K.[1], Sajan D. George[2], Keerthilatha M. Pai[3], Ravikiran Ongole[4], Tom Devasia[5], V. B. Kartha[1], and Santhosh Chidangil[1*]

[1] Centre of Excellence for Biophotonics, Department of Atomic and Molecular Physics, Manipal Academy of Higher Education, Manipal, Karnataka 576104, India

[2] Centre for Applied Nanoscience, Department of Atomic and Molecular Physics, Manipal Academy of Higher Education, Manipal, Karnataka 576104, India

[3] Department of Oral Medicine and Radiology, Manipal College of Dental Sciences, Manipal, Manipal Academy of Higher Education, Manipal, Karnataka 576104, India

[4] Department of Oral Medicine and Radiology, Manipal College of Dental Sciences, Mangalore 575001, Manipal Academy of Higher Education, Manipal, Karnataka 576104, India

5 Department of Cardiology, Kasturba Medical College, Manipal Academy of Higher Education, Manipal, Karnataka 576104, India

* e-mail: santhosh.cls@manipal.edu

Abstract. In this paper the potential of optical spectroscopy based techniques for regular screening and early diagnosis of "Killer" diseases (various types of cancers, cardiovascular diseases, etc.) is discussed with focus on routine use under low-resource settings. A brief account of work carried out in our laboratory to design, assemble and optimize Laser Induced Fluorescence (LIF) based optical devices for routine screening, early diagnosis and discrimination of premalignant/malignant conditions in oral and other cancers is presented. An ultra-sensitive protein profiling system based on highly efficient High Performance Liquid Chromatograpy-Ultrasensitive Laser Induced Fluorescence (HPLC-LIF) detection, and its extensive use in monitoring various cancers, coronary conditions, gynecological problems etc. through protein profile pattern analyses of markers in body fluids is also discussed. © 2020 Journal of Biomedical Photonics & Engineering.

Keywords: optical pathology; laser induced fluorescence; HPLC-LIF; oral cancer; cardio vascular disease; principal component analysis.

Paper #3377 received 12 Jun 2020; accepted for publication 17 Jun 2020; published online 30 Jun 2020. doi: 10.18287/JBPE20.06.020309.

1 Introduction

As of March 2020, the estimated world population stands at >7.775 billion [1]. The 32 OECD (Organization of Economic Development and Cooperation) "developed" countries all together constitute only 15% of this, of which 81% live in urban areas [2] with universal accessibility and availability of complete health care. In contrast, the remaining more than 6 billion people of the world, in developing countries, live with grossly inadequate health care facilities. This has lead, combined with the huge disparity in Per Capita Income (eg. US >$56,000 vs India <$6900) to a situation in which routine health care has become a commodity almost unavailable and unaffordable for the bulk of the population. Whatever modern facilities required for advanced health care are mostly located in big towns and large cities, making it mandatory for a rural person to take leave from his daily job in the village, stay away for several days to visit a large hospital in the city, incurring considerable expenditure for stay and for expensive medical tests. Often, for many disease conditions repeated visits become necessary, and many times the person has to have support of additional manpower, to facilitate his stay and therapy. The small hospitals and health care

centers in rural areas have no facilities for regular screening for early detection of "Killer" diseases (coronary diseases, various types of cancer, tuberculosis, etc.), since such facilities (imaging techniques, detection of tumor markers, identification of drug-resistant pathogens, to mention a few) require costly equipment and experienced professionals (radiologists, pathologists) for routine operation, both of them unavailable in small rural hospitals. To cap all this, there is almost no awareness of the need for regular screening for major diseases for early detection and successful therapy. Finally, the rural population mostly consist of orthodox individuals, who are very reluctant to go for personally invasive diagnostic techniques like mammography, colposcopy, Trans-vaginal sonography, colonoscopy, etc., physical exposure to strangers, especially for women, being almost taboo. The total outcome of all these deficiencies is a humongous health care burden on the country in terms of manpower loss, economy, societal well-being, and human welfare index. In an analysis of global burden of disease study of 2015, India is ranked as 143rd, out of 188 countries worldwide, in health related sustainable development goals [3]. It is clear that to escape from this deplorable social, financial, psychological, and human welfare conditions, one has to have universal health care, characterized by ready availability, affordability, and acceptability; that is, a cost-effective health surveillance program, which can be executed without the need for highly-qualified medical professionals**.** with minimum personal intrusion, and which can be made available at a large number of locations, like rural health-care centers, small hospitals, and single-doctor clinics in small towns and villages.

2 Systems, Techniques, and Technology

Optical pathology and optical biopsy are uniquely positioned at present, to provide highly cost effective, non- or minimally- invasive, point-of-use or field deliverable diagnostic methods. Optical methods can provide unambiguous, objective diagnosis in many biomedical applications like detection of pathogens in samples or environment, screening and early detection of asymptomatic abnormal health conditions, diagnosis and staging of diseases, prognosis and follow up in therapy, imaging applications, drug cell interactions, clinical trials, etc.

Furthermore, most of the time, they require only minimally trained technicians for routine operation, eliminating the need for highly qualified professionals. Revolutionary advances in lasers and other light sources like LEDs, miniaturization of spectroscopic instrumentation with mini and micro spectrometers, high sensitivity state-of-the-art detectors, and efficient and fast data processing techniques, have made optodiagnostic systems highly cost effective, amenable to large scale production of inexpensive portable, miniature, or wearable configurations, usable at almost any location.

All optical biomedical systems depend on the interaction of radiation with the material at the point of incidence [4]. The interaction involves three processes; absorption, reflection, or scattering of photons. Absorption can give rise to further processes, in which the absorbed energy is released either as a different photon (giving fluorescence) or as thermal energy, giving a photothermal effect. If the incident radiation is not continuous, but pulsed or periodically interrupted, the thermal excitation and relaxation will lead to acoustic waves which effect is called the photo acoustic effect. Since absorption will depend on the energy levels of the atoms/molecules in the system, all these processes will be highly characteristic of the structure and composition of the material under study.

Reflection of radiation from a material can be of two types. Conventional regular (specular, mirror-like, directional) reflection, obeying the laws of reflection, or diffuse reflection in which the radiation enters into the medium, gets multiply scattered, and exits in all directions (nondirectional). In the process of multiple scattering in the medium, some of the radiation can be absorbed, depending on the composition of the material, and hence the diffusely reflected radiation, once again, will be characteristic of the material, and can thus be used for getting information on its structure and composition. If, instead of the multiply scattered light in the reflection method, one uses singly scattered light, then one can apply interferometric methods to get information on the tissue structure. This is the basis of imaging by Optical Coherence Tomography (OCT) [5].

Scattering can be elastic (without loss or gain of energy for the incident the photon) or inelastic with some energy transfer between the incident photon and atoms/molecules in the medium. Elastic scattering can be approximated by Mie theory and has been developed for many imaging applications [6, 7]. The inelastic scattering with energy exchange – Raman scattering – gives information on molecular characteristics, which can be used for many applications for *in vivo*, *ex vivo,* and *in vitro* diagnostic techniques [4].

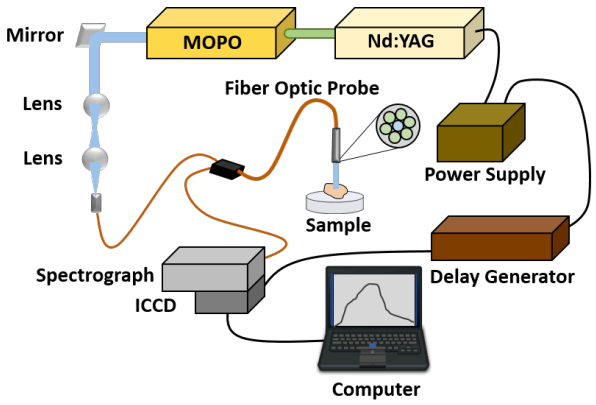


Fig. 1 Block diagram of the pulsed laser LIF setup.

In summary, for biomedical applications by optical techniques, the general instrumentation consists of an optical radiation source (laser, LED, lamp), a probe to direct the radiation to the sample and transmit the effect

produced on it (by absorption, fluorescence, reflection, or scattering) to a radiation detector and analyze the return signal through various data processing techniques. Schematic diagram of such a system is shown in Fig. 1.

The system, in this specific case comprises of a pulsed Nd-YAG laser, a 150 mm spectrograph and an ICCD detector, can be used only in the lab because of its size, and operational requirements like power supply, Pure N_2 gas for flushing, vibration isolation for optical components etc., because of these requirements it is not convenient for use in locations like small hospitals and clinics. We have used it extensively to develop *ex vivo* optical biopsy for various cancers, study of radiation and drug effects in radiotherapy and animal models, etc. [8–11].

A biopsy, by definition, "is a procedure to remove a piece of tissue or a sample of cells from your body so that it can be analyzed in a laboratory" [12]. Thus, conventional biopsy needs examination of the organ by a clinician or oncologist and removal of sample from visually suspect locations, depending on his judgment based on visual inspection. Often the process is highly subjective, may require removal of tissue samples from many locations, and prone to errors due to effects like "Field cancerization" [13], and mistakes due to "past pointing" etc., which can happen even with some experience. Also removal of tissue from suspect locations itself may lead to problems later. Further, the final decision as to the status of the sample is made by the pathologist, who again takes a decision based on visual examination and previous experience. With optical methods, an objective and unambiguous decision can be made by examination of multiple sites without the need for tissue removal and subsequent dangers. For such *in vivo* examinations the Nd-YAG-Spectrograph-ICCD model is unsuitable because it is bulky and also fairly expensive. Both these drawbacks were eliminated in the next version of our portable optical biopsy system, by replacing the Nd-YAG laser with a much smaller, low power, and much cheaper continuous wave He-Cd laser, a less expensive CCD system and a fiber optic probe for delivery of the laser radiation and collection of the resulting spectra. This is shown in Fig. 2, clearly illustrating its ease of use for routine *in vivo* studies at any location.

The system was evaluated by *in vivo* examination of ~380 subjects (133 normal, 155 oral premalignancy, and 92 oral malignancy) and recording a total of about 4000 fluorescence spectra from different sites – buccal mucosa, tongue lateral, tongue tip, tongue top, tongue bottom, lip underside, and palate – under normal, pre-malignant, and malignant conditions [14]. The system in Fig. 2 is compact, portable, and can be operated by a technician. By putting different fiber optic probes, it can be easily adapted for use in all types of endoscopic examinations, like gastroscopy, colonoscopy, colposcopy etc. The diagnostic conclusions are arrived at by statistical pattern analysis methods like Principal Component Analysis (PCA) and artificial Neural Network (ANN) [8–11], leading to highly objective decision making, with well defined statistical probability assigned to the decision [15]. Since no tissue removal is involved, a subject can be examined at as many locations as needed during any visit. Susceptible population groups (smokers, females, etc) can be called for regular periodic screening, since it is sufficiently cost effective for installation in small hospitals, clinics and community-health care centers.

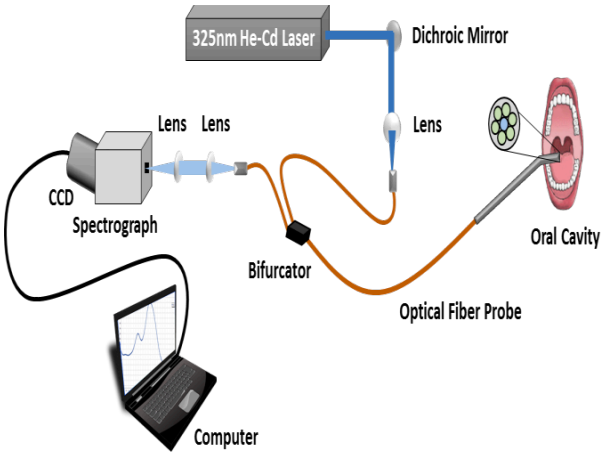




Fig. 2 Block diagram and the Photograph of the He-Cd laser based tabletop LIF system.

Even when facilities like that have shown in Fig. 2 become available in small town hospitals and clinics, regular health coverage by screening for the many types of cancers like oral, esophageal, cervical, etc. may not happen. The susceptible rural population, consisting of laborers, females busy with household chores, etc. usually pay very little attention to early symptoms of such diseases. Also they are often unaware of the need for such screening, and so neglect to have such examinations out of lack of leisure time or even sheer laziness. It is thus advantageous to have a system, which can be taken around to small health care camps, or which can be carried around by a health care worker for home visits. We achieved this easy translation ability by replacing the spectrograph-CCD combination with spectrograph-Photo Diode Array (PDA) unit, which can

be incorporated in a hand-held unit. This is shown in Fig. 3a, b. Typical fluorescence spectra recorded from induced mice skin cancer using the setup are shown in Figure 3c. The He-Cd laser can be easily replaced with an UV light emitting LED with 325 nm sharp radiation to make the system still smaller and cheaper.

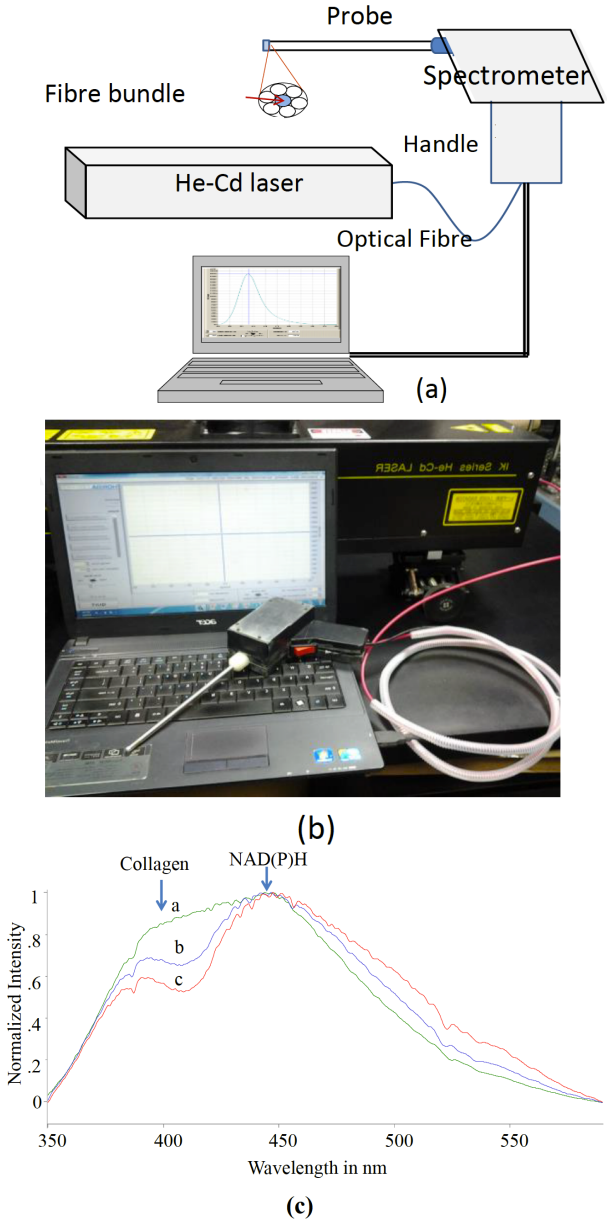


Fig. 3 Hand-held optical biopsy system for *in vivo* cancer screening**.** Typical autofluorescence spectra of healthy and cancer-induced mice skin recorded by using the system; (a) Healthy, (b) Premalignant, and (c) Malignant

The first requirement of the screening device was to show that its performance will be quite adequate for routine *in vivo* fluorescence spectroscopy. For this a detailed fluorescence spectroscopy study of squamous epithelial carcinogenesis in Swiss Albino mice was carried out. Swiss albino mice treated with 7,12-dimethylbenz(a)anthracene (DMBA) were used for this study. DMBA is a complete chemical cancirogen (initiator and promoter) and studies have shown that there is a consistent sequence of histological changes that transpire the DMBA treated epithelial layer of the mice skin lesion of Swiss Albino mice. The autofluorescence emission spectra at 325 nm excitation from DMBA treated animal skins and control animal skins were recorded (Fig. 3c) every week using the LIF system and the results were analyzed by statistical pattern analysis methods. Specificities and sensitivities, for discrimination between malignant and normal conditions have been calculated from the analysis and are found to be 89% and 91% respectively [16]. Showing that such a system is quite adequate to serve the purpose of screening and early diagnosis of cancers in organs accessible through endoscopic procedures.

It is very important to note that the same system, with minor modifications, can be adapted for other techniques of optodiagnostics applications, using Raman, Photo-acoustic, or Diffuse Reflection spectroscopy, in conditions like skin problems, arthritis, diabetes, etc.

3 “Killer” Diseases

According to a recent survey [17], the major “Killer” diseases in India (by percentage of total number of deaths) are cardiovascular diseases (25%), respiratory diseases (10%), Tuberculosis (10%), cancer (9%), digestive diseases (5%), diarrhea (5%), and malaria (3%).

There are several reasons for these diseases to dominate the ill-health status of countries like India. The easily available screening facilities in developed countries lead to early detection in the majority urban population. But in developing countries, the majority-rural population is not diagnosed at all in the early stages. The easy availability of early detection methods to the majority urban population lead to a twice-higher detection of incidence rate, more successful therapy, and consequent higher survival rate in developed countries, but leads to more or less similar death rates in both cases [18]. Currently, there are no screening methods routinely applied for the 70% rural population in countries like India. Methods like Mammography, colonoscopy, CT Scan, and even biopsy and histopathology, and Pap test are beyond the reach of this group, being available only at Multi-Specialty hospitals in big towns and cities. Almost always any type of cancer or cardiovascular diseases are diagnosed only after overt symptoms appear, by which time it is too late for successful therapy. The result of lack of routine screening for early detection is particularly seen in the various cancers, designated as “Number 2” Killer in almost all countries [19]. But, presumably due to inadequate records only being available in rural areas, it is greatly under-estimated as only the fourth killer in India [17]. Coronary diseases and various types of cancers are the two most important “Killer” diseases where adequate health care can considerably reduce the health care burden of the country. Below we discuss

how optical biopsy and optical pathology are extremely well tailored at present to meet this need.

One of the major causative factors for cardiovascular diseases is smoking. The use of tobacco (in the form of beedi) and consumption of alcohol (as toddy, desi-spirit, etc.) are relatively high in rural population, while cigarette use and foreign liquor consumption are higher in urban areas [20]. Physical inactivity and obesity, the other major causative factors, may not play a large role for the Indian rural population, which consist mostly of farm laborers, daily wage workers, and middle class people, all of whom have some minimal physical activity in their daily life. Smoking is also recognized as a major causative factor for lung and oral cancers. Optical biopsy and optical pathology can easily recognize quite early, changes induced in tissue and body fluids like saliva and blood by smoking, so that the subjects can be made aware of their health status by periodic observation through screening by optical methods. Fig. 4 shows the fluorescence spectra of oral buccal mucosa for normal, malignant, and smoker subjects. It is seen that in smokers there is a considerable decrease in relative fluorescence intensity in the 375–425 nm region. Excitation of tissue at 325 nm gives fluorescence in this region from collagen (386 nm) and pyridoxine-VitaminB_6, (406 nm) derivatives [21]. The decrease in intensity in this region can be attributed to a thickening of the epithelial layer (collagen decrease, 380 nm) and loss of Pyridoxine (Vitamin B_6, 405 nm).

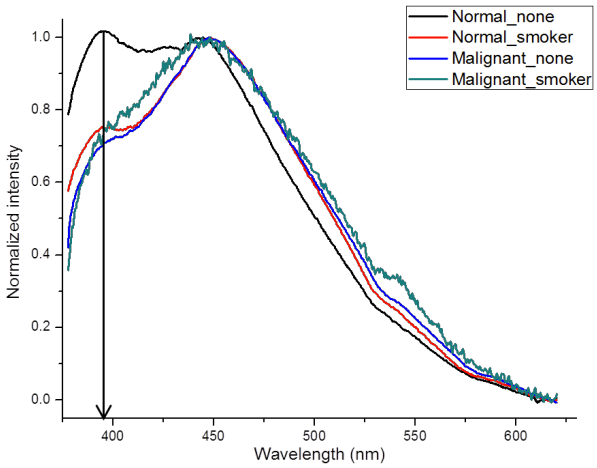


Fig. 4 Buccal Mucosa fluorescence spectra.

Vitamin B_6 (Pyridoxine 5'-phosphate) is needed in the production of many neurotransmitters (serotonin, norepinephrine). More important in the present context is the fact, that B_6 together with B_{12} and B_9 control the levels of Homocysteine, an amino acid associated with heart diseases, in the blood. A deficiency of B_6 in the diet thus poses a higher risk of heart disease [22, 23]. If the decrease in intensity is at least partly due to Pyridoxine, then it is clear that a periodic screening of smokers for signs of loss of pyridoxine intensity can be used to caution them about possible heart problems.

Fig. 4 also shows that the *in vivo* fluorescence spectra are quite suitable for discrimination between normal and malignant conditions. This is further illustrated in Fig. 5, where the fluorescence differences between normal, pre-malignant, and malignant conditions for buccal mucosa are shown. As mentioned earlier, we have employed PCA and ANN to develop screening and diagnostic methods for early detection of pre-malignant and malignant conditions at the different sites of oral cavity by this method of optical biopsy [8–10, 14, 16]. The method of laser induced fluorescence works very well for the detection of malignant conditions of breast and cervical tissues. Similar to oral tissue, excitation at 325 nm is also quite suitable for the discrimination of disease conditions in breast and cervical tissues based on their fluorescence characteristics (Fig. 6).

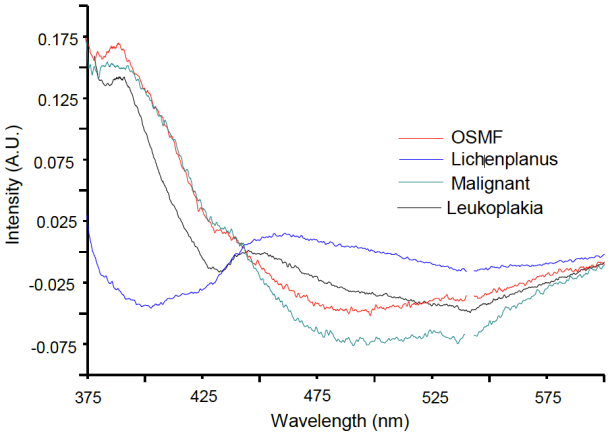


Fig. 5 "Difference Spectra" – Normal Buccal Mucosa – (minus) Buccal Mucosa under Different Clinical conditions.

It is appropriate to mention here that, for discriminating between normal and malignant tissue conditions, one can make use of the differences in tissue conditions in the two states. Since the tissue structure, components, and environment of the fluorescing molecular species will be quite different in the two cases, fluorescence, which is highly sensitive to these parameters, will be determined to a very large extent by the intermolecular interactions and environments of the fluorescing molecule. This changes the relaxation processes of the excited molecule, causing drastic changes in excited state lifetimes of the molecular species under investigation. Thus, time resolved fluorescence emission will have different time dependence in the two cases, and may be a very good method for discrimination between normal and malignant or other disease conditions. This is illustrated in Fig. 7 in the case of breast tissue. It is seen that the fluorescence at 400 nm, arising from Pyridoxine/Collagen, decay very fast in malignant condition, whereas it shows an initial increase and a very slow decay rate afterwards, for normal tissue.

It is well recognized that a host of biochemical reactions precede/accompany the onset of any disease.

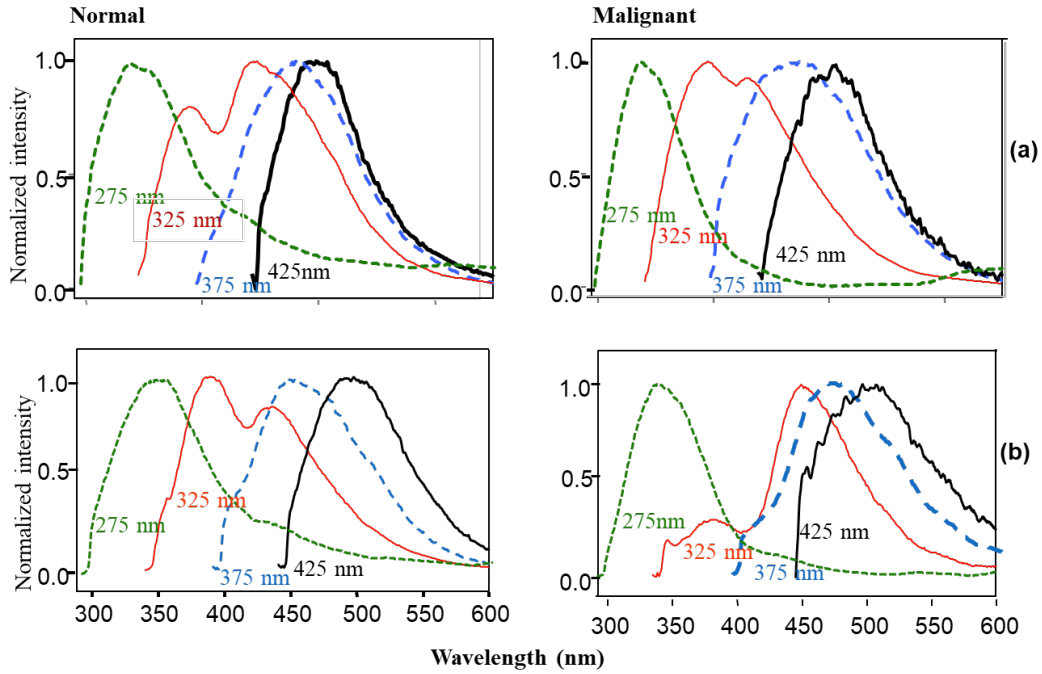


Fig. 6 Fluorescence spectra of normal and malignant breast (a) and cervical tissues (b) at different excitation wavelength.

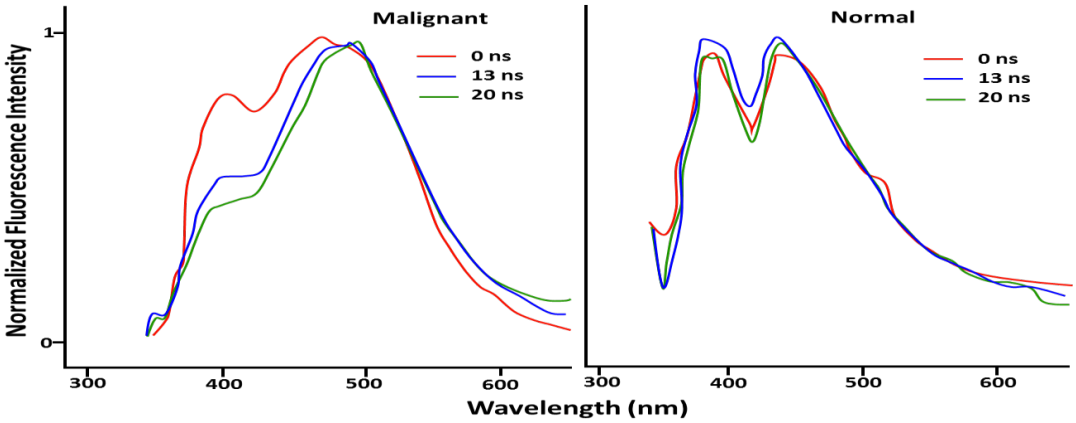


Fig. 7 Breast tissue; Time dependence of fluorescence: excitation 325 nm.

Changes continue to take place during progression of the disease, and also in regression during therapy. These changes will be reflected in the cellular components, and circulating body fluids, as in the case of tissue sites. We have shown that protein profiling of body fluids, cytological specimens, and biopsy tissue samples provide unambiguous markers, which can discriminate between normal and disease conditions. They can be used for screening, early detection, staging, and follow-up for deciding efficacy of therapy. Having seen a direct connection between smoking and coronary diseases (and oral cancer), and tissue fluorescence, it should be interesting to look at protein profiles of body fluids under similar situations. We have developed an ultra-sensitive protein profiling system (Fig. 8) based on highly efficient High Performance Liquid Chromatograpy–Ultrasensitive Laser Induced Fluorescence (HPLC-LIF) for this. The details of the system and its extensive use in monitoring various cancers (oral, cervical, ovarian, breast, urinary bladder, colon, etc.), coronary conditions, gynecological problems, etc. are described elsewhere [24–30]. Here we will illustrate the capabilities of the system with a few results.

In view of the changes observed in oral tissue (Fig. 4), it will be informative to see whether similar striking changes happen in the tissue homogenates, body fluids in potentially malignant and malignant conditions. Figs. 9 and 10 show protein profiles recorded using the HPLC-LIF system (separation column was reverse phase biphenyl and mobile phase: water/acetonitrile/TFA), of oral tissue homogenates (normal and malignant), and saliva under normal, pre-malignant, and malignant conditions to different sites in the oral cavity.

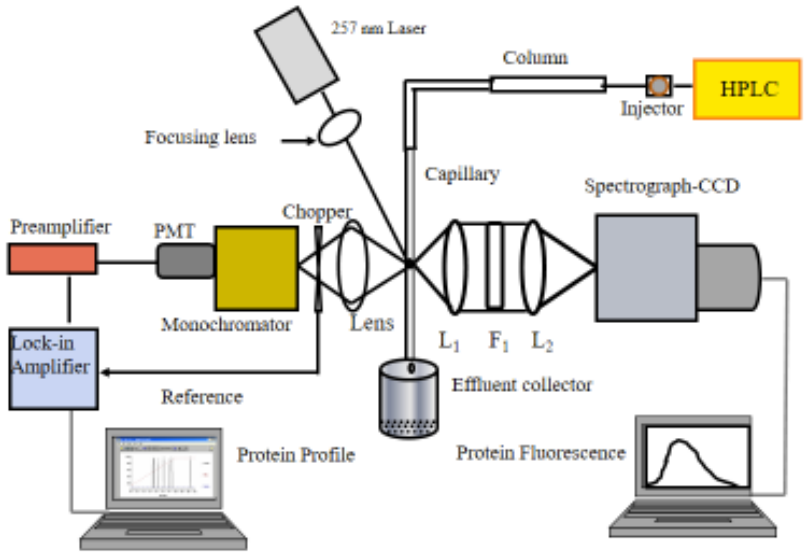


Fig. 8 Block diagram of the locally assembled HPLC-LIF system.

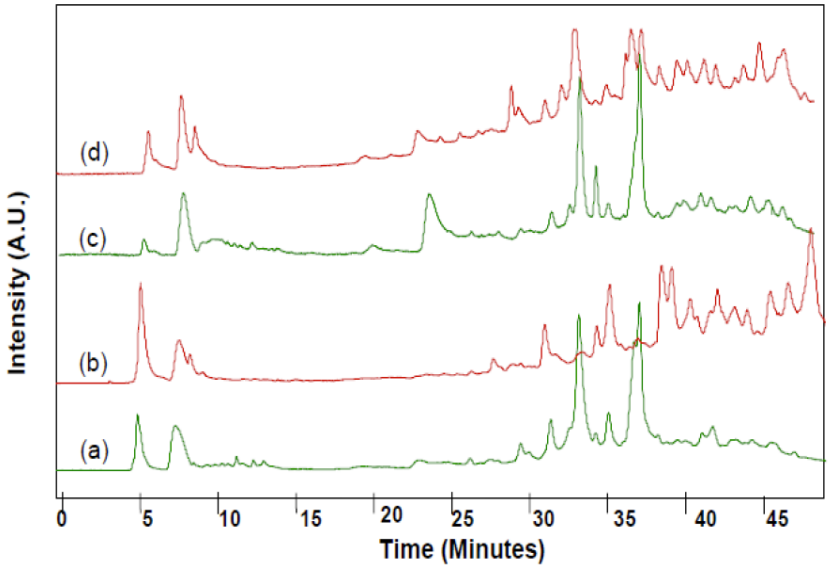


Fig. 9 Protein profiles oral tissue homogenates of (a) Male normal (55 Years); (b) Male malignant (55 Years); (c) Male normal (62 years) and (d) Male malignant (62 years).

It is seen that there are substantial changes from the normal saliva under all conditions, showing that drastic changes have taken place in the functioning of the associated organs. We have standardized the protein profile pattern analysis method for screening, early detection, and monitoring of oral cancer by PCA of salivary samples, with high sensitivity and specificity [24].

Blood, which circulates all over the body, collects many bio-molecules produced in different organs, and also serves as a distributor for molecular species like anti-bodies, antigens, immunoreaction products and many other molecules. We have investigated the protein profile of blood in many different conditions, normal, smoker, various malignancies, cardiovascular diseases, diabetes, etc. Fig. 11 shows typical chromatograms of serum from normal, smoker, oral premalignant and malignant subjects.

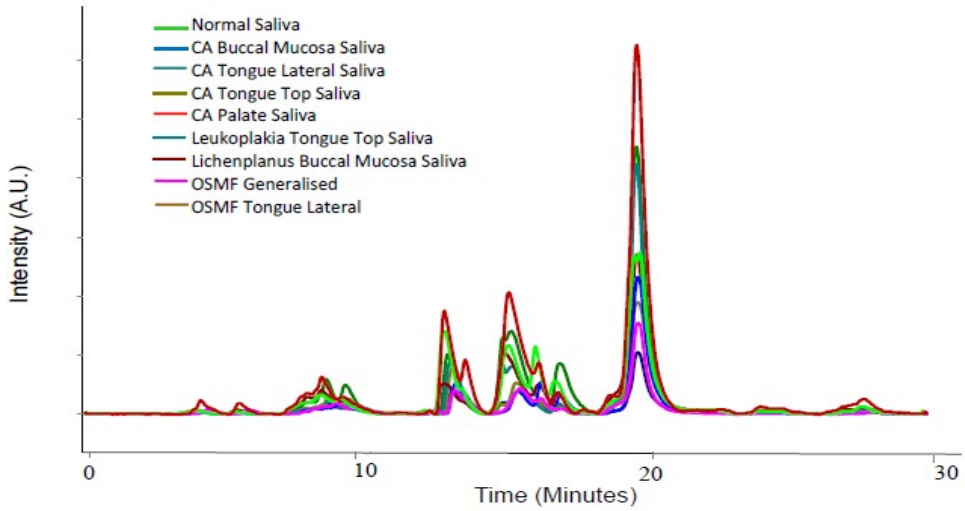


Fig. 10 Protein profiles human saliva: Normal saliva, Cancer of buccal mucosa, cancer of tongue lateral, cancer of tongue top; cancer of palate and some other potentially malignant cases.

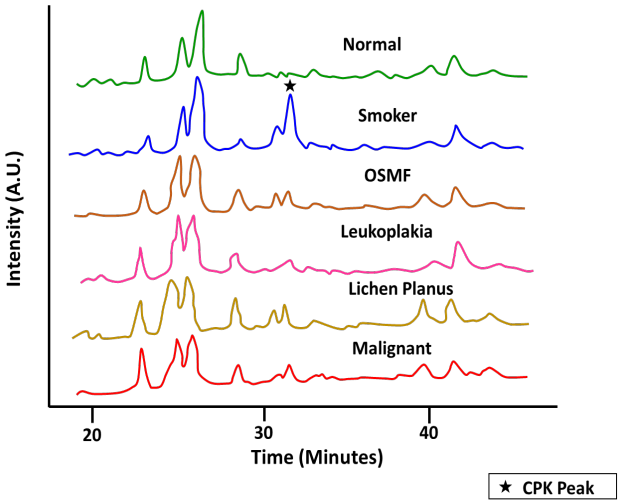


Fig. 11 HPLC-LIF Protein profiles of serum samples.

We have identified many of the peaks here, including transferrin, ferritin, HSA, I_GG, and CPK, by co-injection of pure compounds as well as SDS Page of the collected fractions. PCA of the serum protein profiles have been shown to be highly suitable for screening, early detection, staging, and follow-up in therapy [27–30] for many cancers and other abnormal conditions.

It is seen from Fig. 11 that CPK (peak ~32 min), which is present in extremely small amounts in normal serum – our detection limit for CPK is about 7 fmol [31] – increases to very large values in smokers, and is also high in pre-malignant and malignant conditions of the oral cavity. Fig. 12 shows a plot of relative intensities of CPK peaks in a number of samples with reference to a standard peak, which had remained more or less same in all samples.

The levels of CPK, together with other proteins like Troponin I (TnI) and Troponin T (TnT) are linked with injury of the heart muscle [32–35]. An injury of heart muscle like that from a heart attack, leads to an increase in their levels in the bloodstream. This is supported by protein profile study of serum samples after ischemic heart disease, shown in Fig. 13. The observation of CPK levels in serum of smokers can thus provide a method for screening and diagnosis of coronary problems.

The change in the relative intensities of HSA and CPK illustrate the "catastrophic" change in CPK in Ischemic Heart Disease.

In many cancers often biopsy samples are obtained by procedures like brush biopsy, fine needle aspiration, or by mechanical removal of cellular samples. These cytological samples are then processed and examined by a pathologist, under a microscope. Diagnosis and staging of the disease is arrived at by visual observation of morphological or biomolecular changes. Thus, the results are subjective to the experience of the pathologist, and are prone to other problems like "Fatigue Factor" arising from need to observe large number of samples over long periods. Also, during early stages of the disease, the number of cells in abnormal condition may be quite small and may be missed leading to "False Negative" results. On the other hand, often changes may take place due to reasons other than the suspected disease, and this may lead to "False positive" diagnosis. Such problems can be minimized by optical pathologic techniques like "Spectral Histopathology" and "Spectral cytopathology", and ultrasensitive HPLC-protein profiling, which can detect presence of even extremely small number of abnormal cells in a collection with very large number of normal cells. We have standardized such protein profiling method of cellular samples, for, screening, early diagnosis, staging and follow-up in therapy [26, 36]. Especially noteworthy is the fact that the protein profile

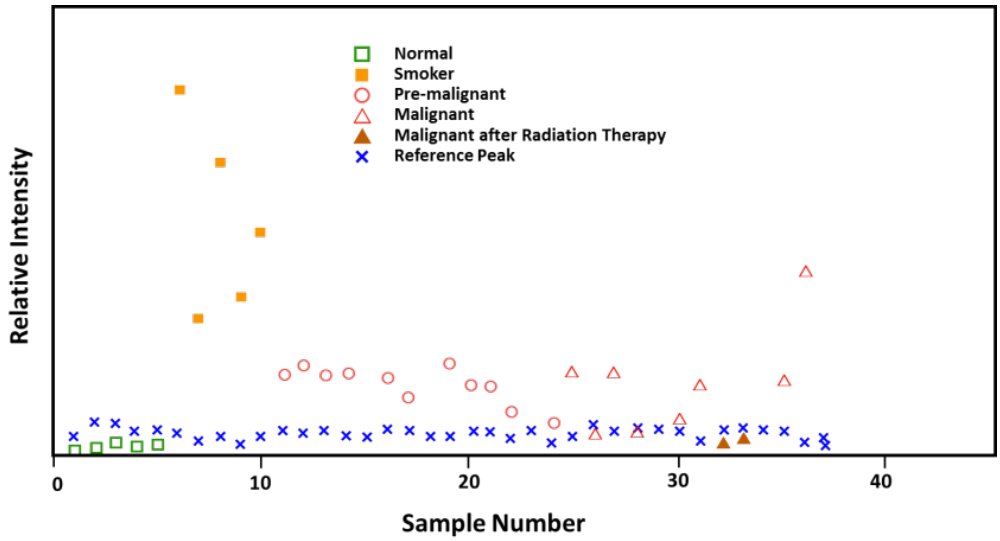


Fig. 12. Relative Intensity of CPK in Serum samples of different conditions.

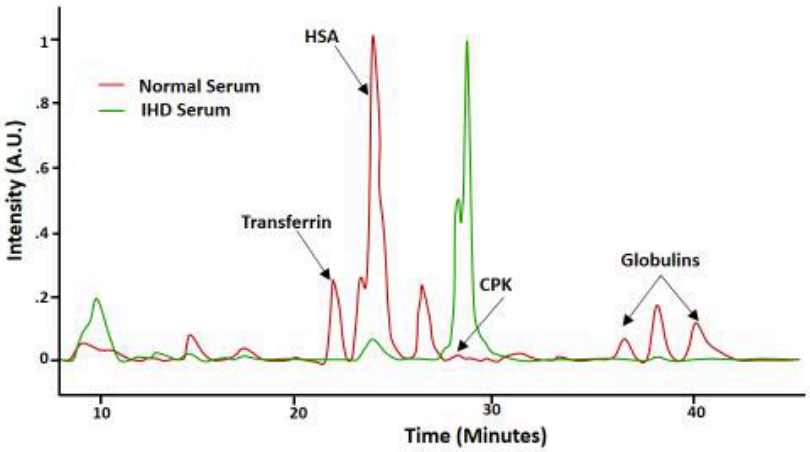


Fig. 13 HPLC-LIF Protein Profiles of Serum in Ischemic Heart Disease.

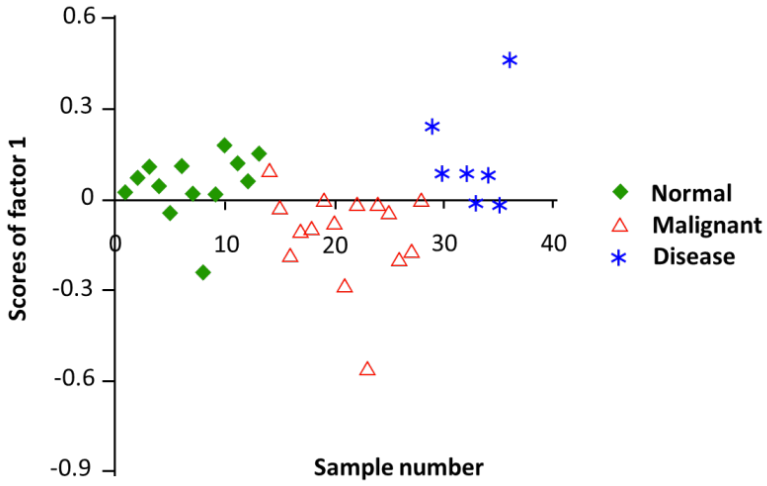


Fig. 14 PCA Scores for factor 1: Cytological Samples from Cervix.

study could discriminate other disease conditions from malignancy, as shown in Figure 14, where the scores of Factor 1 from PCA of serum protein profiles are plotted against sample number. It is seen that subjects having diseases of cervix other than cervical cancer (erosion of cervix, nabothian cyst, polycystic ovary, etc.), are separated out from subjects with cervical cancer.

4 Conclusion

It is clear from the results presented above and the various work referred to in the text, that advances in optical instrumentation, data processing techniques, and development of efficient analytical methods based on ultrasensitive spectroscopy techniques, have made Optical Biopsy and Optical Pathology acceptable and affordable for the majority-rural population in developing countries, satisfying the requirements of many health care needs like screening, early detection, diagnosis, and therapy follow-up in many disease-conditions. The techniques can be made universally available in resource limited settings in developing countries, especially because of advantages like cost-effective instrumentation, which can be made easily portable, and which can be operated by trained technicians without the need for highly qualified medical professionals like clinicians, radiologists, oncologists, and pathologists. Also diagnostic decision-making being done with objective statistical methods, minimizing possible human errors like false positive and false-negative conclusions, over-diagnosis (as in most imaging methods), and errors that can arise from multiple choices. Methods like serum protein profile are minimally (personally) invasive making it acceptable to all levels of population. Also, collection, storage, transportation, processing etc. for blood samples are highly standardized and, thus, it is quite convenient for large scale screening operations. Thus, it is highly desirable to encourage the acceptance of Optical Biopsy and Optical Pathology techniques as routine technology to provide affordable health care to the 70% of the rural population in developing countries like India, who at present survive with grossly inadequate health care facilities. It should also be emphasized that such rural health care can in effect provide much better successful therapy by the multispecialty hospitals in big towns and cities, since they get the opportunity to start treatment at early stages, of suspect-subjects, screened and referred to them by the local hospitals, clinics and health care units.

Disclosures

The authors declare that there are no conflicts of interest related to this article.

Acknowledgement

Authors are thankful to VGST, Govt. of Karnataka, BRNS, DST, DBT, Govt. of India and Manipal Academy of Higher Education for financial support for the Optical Pathology research initiatives. Swathi Rao and Reena John are thankful to Dr. TMA Pai Ph.D. Scholarship and Govt. of Karnataka Minority Scholarship respectively.

References

1. "World Population Prospects: The 2019 Revision," United Nations Population Division (accessed April 4, 2020).
2. OECD Health Statistics 2020 (accessed May 17, 2020).
3. GBD 2015 SDG Collaborators, "Measuring the health-related Sustainable Development Goals in 188 countries: a baseline analysis from the Global Burden of Disease Study 2015," The Lancet 388(10053), 1813–1850 (2016).
4. V. B. Kartha, Santhosh C., Biomedical Spectroscopy, (Chapter 1, and References therein), Manipal University Press, Manipal, India (2014).
5. A. F. Fercher, W. Drexler, C. K. Hitzenberger, and T. Lasser, "Optical coherence tomography – principles and applications," Reports on Progress in Physics 66, 239–303 (2003).
6. S. L. Jacques, "Optical properties of biological tissues: a review," Physics in Medicine and Biology 58(11), R37–R61 (2013).
7. V. V. Tuchin, "Light scattering study of tissues," Physics Uspekhi 40(5), 495–515 (1997).
8. B. K. Manjunath, J. Kurien, L. Rao, C. Murali Krishna, M. S. Chidananda, K. Venkatakrishna, and V. B. Kartha, "Autofluorescence of oral tissue for optical pathology in oral malignancy," Journal of Photochemistry and Photobiology B: Biology 73(1–2), 49–58 (2004).
9. S. M. Chidananda, K. Satyamoorthy, L. Rai, A. P. Manjunath, and V. B. Kartha, "Optical diagnosis of cervical cancer by fluorescence spectroscopy technique," International Journal of Cancer 119(1), 139–145 (2006).
10. V. B. Kartha, J. Kurien, K. M. Pai, L. Rao, L. Rai, K. K. Mahato, C. M. Krishna, and C. Santhosh, "Diagnosis at the molecular level: Analytical Laser spectroscopy for clinical applications," Chapter in Photo/Electrochemistry & Photobiology in the Environment, Energy and Fuel, S. Kaneco (Ed.), Research Signpost, Trivandrum, 153–221 (2005).
11. R. Jyothi Lakshmi, M. Alexander, J. Kurien, J. G. R. Solomon, P. Umadevi, M. S. Vidyasagar, and V.B. Kartha, "Laser spectroscopy studies of radiation effects on animal models and human systems," Chapter in

Photo/Electrochemistry & Photobiology in the Environment, Energy and Fuel, S. Kaneco (Ed.), Research Signpost, Trivandrum, 105–151 (2005).
12. Biopsy: Types of biopsy procedures used to diagnose cancer, Mayo Clinic Staff (accessed 16/07/2016).
13. P. Holmstrup, P. Vedofte, J. Reibel, and K. Stoltze, "Oral pre-malignant lesions: is a biopsy reliable?" Journal of Oral Pathology & Medicine 36(5), 262–266 (2007).
14. A. Patil, V. K. Unnikrishnan, R. Ongole, K. M. Pai, V. B. Kartha, and S. Chidangil, "Non-Invasive in vivo Screening of Oral Malignancy," Modern Technologies in Medicine 10(1), 15–26 (2018)
15. V. K. Unnikrishnan, A. Patil, R. Bernard, K. K. Mahato, K. M. Pai, R. Ongoleetal, "Oral Cancer Screening in Rural India-Report on *in vivo* Device Test of 349 Subjects at Manipal and Mangalore," Philips Research, Technical Note MU-PR-TN/LIF-02/2007 (2007).
16. C. E. Metz, "Basic Principles of ROC Analysis," Seminars in Nuclear Medicine 8(4), 283–298 (1978).
17. What's Killing India? Knowing Top 10 Killer Death Diseases in India, icicilombard.com (accessed Aug 06, 2013).
18. A. Jemal, F. Bray, M. M. Center, J. Ferlay, E. Ward, D. Forman, "Global Cancer Statistics," CA: A Cancer Journal for Clinicians 61, 69–90 (2011).
19. Global Cancer Facts and Figures, 3rd Edition, American Cancer Society, Atlanta, Georgia (2015).
20. Household Consumption of Various Goods and Services in India, 2011–12, NSS Report No. 558, Ministry of Statistics and Programme Implementation, Government of India, June (2014).
21. N. Ramanujam, "Fluorescence spectroscopy *In Vivo*," Chapter in Encyclopedia of Analytical Chemistry, R.A. Meyers (Ed.), John Wiley & Sons, 20–56 (2000).
22. Vitamin B6 (Pyridoxine), University of Maryland Medical Centre (accessed 8/5/2015).
23. H. McNulty , K. Pentieva, L. Hoey, and M. Ward, "Homocysteine, B-vitamins and CVD," Proceedings of the Nutritions Society 67(2), 232–237 (2008).
24. A. K. Patil, K. S. Choudhari, V. K. Unnikrishna, N. Shenoy, R. Ongole, K. M. Pai, V. B. Kartha, and C. Santhosh, "Salivary protein markers: a noninvasive protein profile-based method for the early diagnosis of oral premalignancy and malignancy," Journal of Biomedical Optics 18(10), 101317 (2013).
25. S. Bhat, A. Patil, L. Rai, V. B. Kartha, and S. Chidangil, "Application of HPLC Combined with Laser Induced Fluorescence for Protein Profile Analysis of Tissue Homogenates in Cervical Cancer," The Scientific World Journal 2012, 976421 (2012).
26. S. Bhat, A. Patil, L. Rai, V. B. Kartha, and C. Santhosh, "Protein profile analysis of cellular samples from the cervix for the objective diagnosis of cervical cancer using HPLC-LIF," Journal of Chromatography B 878(31), 3225–3230 (2010).
27. A. Patil, V. Prabhu, K. S. Choudhari, V. K. Unnikrishnan, S. D. George, R. Ongole, K. M. Pai, K. Jayarama Shetty, S. Bhat, V. B. Kartha, and C. Santhosh, "Evaluation of high-performance liquid chromatography laser-inducedfluorescence for serum protein profiling for early diagnosis of oral cancer", Journal of Biomedical Optics, 15(6), 067007 (2010).
28. L. Rai, P. Kumar, K. K. Mahato, V. B. Kartha, and C. Santhosh, "Serum protein profile study of normal and cervical cancer subjects by high performance liquid chromatography with laser-induced fluorescence," Journal of Biomedical Optics 13(5), 054062 (2008).
29. S. K. Singh, R. L. Martis, S. Bhat, A. Rani, P. Kushtagi, L. Rai, V. B. Kartha, and C. Santhosh, "Protein Profile Study of Clinical Samples of Ovarian Cancer using High Performance Liquid Chromatography-Laser Induced Fluorescence (HPLC-LIF)," Proceedings of SPIE 6092, 60920N (2006).
30. V. K .Venkatakrishna, B. Kartha, K. M. Pai, C. M. Krishna, O. Ravikiran, J. Kurian, M. Alexander, and G. Ullas, "HPLC-LIF for Early Detection of Oral Cancer," Current Science 84(4), 551–557 (2003).
31. A. Patil, K. S. Choudhari, V. Prabhu, V. K. Unnikrishnan, S. Bhat, K. M. Pai, V. B. Kartha, and C. Santhosh, "Highly Sensitive High Performance Liquid Chromatography-Laser Induced Fluorescence for Proteomics Applications," International Scholarly Research Notices 2012, 643979 (2012).
32. J. F. Portales, J. A. García Robles, J. J. Candil, E. P. David, J. R. Rey Blas, L. Pérez de Isla, Ó. D. Castro, and J. Almendral, "Utility of the Serum Biochemical Markers CPK, CPK MB Mass, Myoglobin, and Cardiac Troponin T in a Chest Pain Unit. Which Marker Determinations Should Be Requested and When?" Revista Española de Cardiología 55(9), 913–920 (2002).
33. Cardiac Enzyme Studies:Test Overview WebMD Medical Reference from Healthwise (acessed August 7, 2015).
34. F. Fischbach, D. M. Bunning III, A Manual of Laboratory and Diagnostic Tests, 9th ed., Wolters Kluwer Health, Philadelphia (2015).
35. N. Sujatha, L. Rai, P. Kumar, B. R. Krishnanand, K. K. Mahato, S. D. George, V. B. Kartha, S. C, "Protein profile study of Pap smear and tissue of cervix by High Performance Liquid Chromatography-Laser Induced Fluorescence," Proceedings of SPIE 6441, 64410B (2007).

1540 nm LIBS Investigation of Healthy and Pathological Human Nails

Andrey V. Belikov, Sergey N. Smirnov, Anastasia D. Tavalinskaya*, and Victoria S. Pomazanova
ITMO University, 49 Kronverksky Pr., Saint Petersburg 197101, Russia

***e-mail:** ntavalin@gmail.com

Abstract. The paper discusses the possibility of using laser-induced breakdown spectroscopy (LIBS) as a method for the diagnosis of human nail onychomycosis. LIBS spectra obtained with excitation of plasma on the surface of healthy and onychomycotic nails by pulses of Q switched Yb, Er: Glass laser radiation with a wavelength of 1540 nm were compared for the first time. The spectrum of onychomycotic nail contained unique lines additional to characteristic spectral lines of healthy nails. These additional lines disappeared after 90 days of sample storage in air at room temperature 20 ± 3 °C. © 2020 Journal of Biomedical Photonics & Engineering.

Keywords: LIBS; onychomycosis; Yb, Er: Glass laser; nail; diagnostics; spectrum.

Paper #3369 received 18 May 2020; revised manuscript received 19 Jun 2020; accepted for publication 25 Jun 2020; published online 30 Jun 2020. doi: 10.18287/JBPE20.06.020310.

1 Introduction

Laser-induced breakdown spectroscopy (LIBS) is a technology for fast remote chemical analysis based on the excitation of plasma on the surface of a sample by a short laser pulse and the study of its spectral composition. LIBS technology is applicable to many samples, including metals, semiconductors, glasses, biological tissues, and others. The accuracy of LIBS allows one to quantitatively characterize the elemental composition with high spatial and temporal resolution, as well as detect substances at their relatively low concentration – from 2 ppm [1, 2]. The ability to identify chemical elements is limited only by the spectral resolution of the used spectrometer (usually ≈0.3 nm). LIBS analysis compares favorably with many other analysis technologies: it is sensitive to elements with a low atomic number, unlike, for example, X-ray Fluorescence analysis, and it is sensitive to trace concentrations of materials, unlike, for example, Prompt Gamma Neutron Activation Analysis [3]. The extremely short time required for sample preparation is also an advantage of LIBS analysis. Of particular interest is the spectral region from 180 to 850 nm, which includes the spectral lines of most of the known elements [4].

Onychomycosis is a widespread fungal disease of the nails. Early rapid diagnosis and treatment of onychomycosis are very important. If treatment is not done on time, the infection can progress penetrating deeper into the nail and destroying it. In addition to aesthetic discomfort, onychomycosis can be a cause of pain during walking, which limits a person's ability to work. For diabetics, mycoses can provoke the appearance of ulcers or secondary infection by bacteria [5, 6]. When detecting onychomycosis, the remoteness of the analysis performed is very important in order to avoid contact with the affected tissue and to eliminate infection of medical personnel. Traditional diagnosis of onychomycosis requires extraction of the sample and its study in the laboratory, which takes considerable time and does not exclude contact with the affected biological tissue [7]. An optical diagnostic method is also possible. Traditionally, the color of the nail is analyzed [8, 9]. Healthy and onychomycotic nails have different optical properties, as fungi contain unique chromophores. For example, one of these chromophores is a polysaccharide chitin present only in fungal cell walls. Spectral studies are being carried out. In Ref. [10], the absorption spectra of healthy and onychomycotic nails were measured. Trichophyton rubrum showed a unique absorption peak at 415 nm. This peak most likely corresponds to mitochondrial cytochrome absorption. However, in medical practice when diagnosis of onychomycosis the spectral methods are not currently widely used. All this necessitates the search for new effective remote sensing methods as one of which LIBS analysis can be considered.

The nail consists of a large number of chemical elements, 26 of which relate to essential and structural

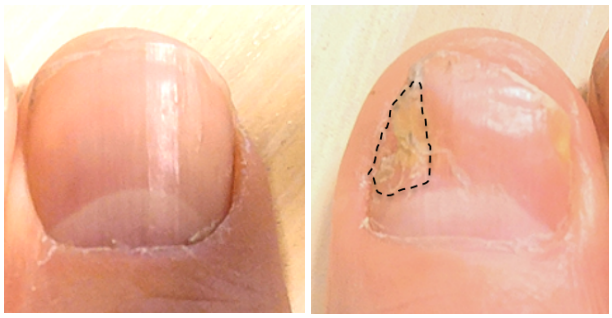
micro- and macroelements (Cl, I, B, V, Fe, K, Ca, Co, Si, S, Li, Mg, Mn, Cu, Mo, Na, Ni, Se, P, Cr, Zn, O, N, C, H, F), the rest are toxic [10]. The 82 emission lines belonging to the atomic and ionic lines of 13 elements – Al, C, Ca, Fe, H, K, Mg, N, Na, O, Si, Sr, and Ti – can be identified in the LIBS spectrum of the nail [11–14]. LIBS analysis does not require sample extraction, as it can be performed *in vivo*. Elemental analysis of nails can be used not only for the diagnosis of nail diseases, but also for detecting an imbalance of elements and the presence of pathological processes in the human body as a whole [14, 15]. In the latter case, an analysis of the intensities ratios of emission lines in the LIBS spectra can serve as an indicator of the level of a pathology. Using the LIBS technology, it is possible to identify various types of fungi and bacteria [16, 17]. For example, the Candida LIBS spectrum reveals the elements C, N, H, O, and CN [17]. Thus, depending on the type of pathogen, the spectrum of the onychomycotic nail can probably change.

A difference was found [14] in the LIBS spectra of normal and pathological nails when analyzing the intensities of calcium, sodium, and potassium lines. To excite the plasma, the radiation of a frequency-doubled Nd: YAG laser ($\lambda = 532$ nm) was used, which is the main drawback, because does not exclude damage to the eyes of the doctor and patient during LIBS excitation at this wavelength. The radiation of a Yb, Er: Glass laser ($\lambda = 1540$ nm), in contrast to the radiation of frequency-doubled Nd: YAG laser ($\lambda = 532$ nm), belongs to the eye-safe spectral range, since the radiation of this laser is absorbed by hydrated tissues of the anterior segment of the eye and does not reach the more sensitive retina [18–20]. In this regard, 1540 nm LIBS analysis can be an effective, remote and safe method for diagnosing a wide range of diseases, including the diagnosis of onychomycosis.

The main goal of this work was to study the possibility of using the radiation of a compact Q-switched Yb, Er: Glass laser ($\lambda = 1540$ nm) for LIBS detection of the nail region affected by onychomycosis.

2 Materials and Methods

The *in vitro* study involved one sample of healthy fingernail and one sample of onychomycotic human fingernail obtained from the same volunteer in order to avoid the influence of physiological, genetic and other factors when comparing the spectra obtained from a healthy and diseased nail. The 30 healthy human fingernail samples obtained from 5 other volunteers were also investigated. After separation from the nail, samples were stored in a dark place at a temperature of 20 ± 3 °C for no more than 24 h for the spectral measurements just after extraction and 90 days for the measurements after longer storage. Photos of the healthy fingernail and the onychomycotic fingernail of the same volunteer before their separation from the nail are shown in Fig. 1.

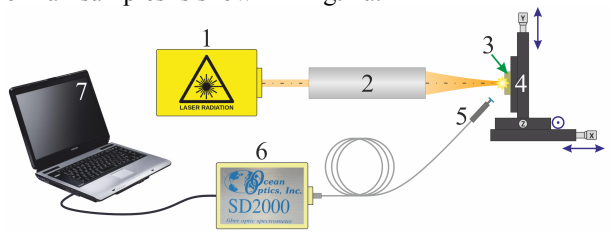


(a) (b)

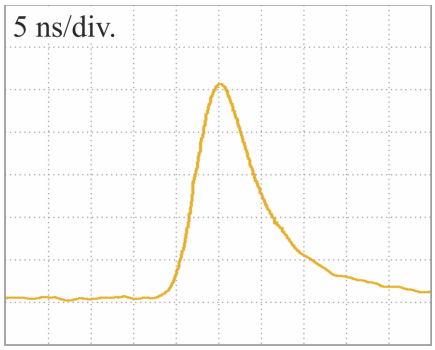
Fig. 1 Photos of healthy (a) and onychomycotic (b) fingernail of the same volunteer (dashed line marks the border of onychomycotic area)

During the LIBS investigation, the laser beam was focused on the dorsal layer of the nail plate. The change of the nail plate color, its delamination and crumbling are typical signs of onychomycosis. The area of the nail affected by onychomycosis usually becomes white or yellowish [8, 9]. Thus, the color serves as an indicator of the presence of infection in the nail. For present LIBS analysis, a sample of a nail affected by onychomycosis was taken from a region having a yellow color (this region is indicated by a dashed line in Fig. 1b).

The scheme of experimental setup for LIBS analysis of nail samples is shown in Fig. 2a.



(a)



(b)

Fig. 2 Scheme of the experimental setup (a): 1 – Yb, Er: Glass-laser, 2 – focusing system, 3 – nail sample, 4 – sample positioning system, 5 – receiving fiber of spectrometer, 6 – fiber-optic spectrometer, 7 – computer; (b) oscillogram of Yb, Er: Glass-laser pulse.

Plasma was excited on the surface of human nail plate samples by pulses of passively Q-switched Yb, Er: Glass laser (Nela Ltd., Russia) with a wavelength of 1540 nm. The laser pulse energy was $E = 2.40 \pm 0.05$ mJ, the pulse duration was $\tau = 8$ ns (FWHM) (Fig. 2b). The radiation intensity on the surface of the nail plate reached 1.4×10^{10} W/cm^2 and was close to the radiation intensity of neodymium lasers commonly used for LIBS analysis [15]. The emission spectra of laser-induced plasma were recorded using a "USB-2000" (OceanOptics, Inc., USA) fiber-optic spectrometer with spectral resolution of 1.5 nm. This model has the ability to external trigger by a TTL signal. The start of the spectrometer was synchronized with a laser pulse exciting the plasma. The laser pulse was detected by a photodiode placed in the laser housing, which triggered the pulse generator. The signal from the pulse generator with duration of 2 μs and a delay of 10 μs relative to the laser pulse was used as an external hardware trigger. The "SpectraSuite" (OceanOptics, Inc., USA) software package was used to control the spectrometer. The integration time 10 ms was set in this program and the spectral signal was recorded within this period after laser exposure.

Radiation from the plasma plume was captured by the receiving fiber of a spectrometer with a core diameter of 125 μm. The input end of the receiving fiber was located at ~10 mm from the sample surface at an angle of ~45° to its normal line. A thin (~200 μm) silica glass plate was placed in front of the input fiber end preventing it from being contaminated by particles of an erosion plume leaving the nail surface. Spectra collection was performed by averaging the spectra obtained as a result of exposure to ten consecutive laser pulses.

The emission spectra of laser-induced plasma excited on the surface of healthy nail samples were recorded just after extraction. The spectra of the nail sample affected by onychomycosis were recorded both just after extraction and after 90 days of longer storage. The intensity of the obtained spectra was normalized (normalized intensity) to the line of air N+O at a wavelength of 500 nm, which was chosen as the reference, since air is always present during the experiment, in addition, it does not change significantly its composition under laboratory conditions.

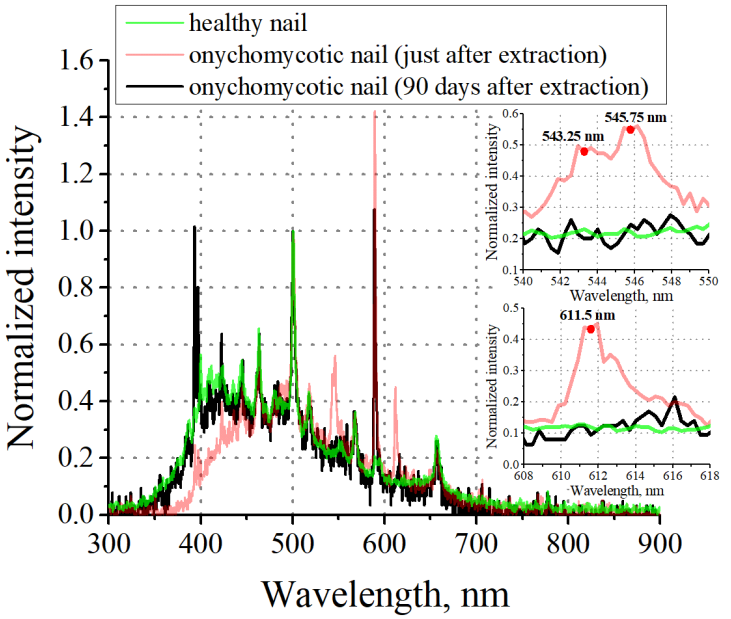
3 Results and Discussion

The emission spectra of the plasma induced by the radiation Q-switched Yb, Er: Glass laser with a wavelength of 1540 nm on the surface of healthy nail samples just after extraction, as well as the nail affected by onychomycosis, just after extraction and after 90 days of longer storage are presented in Fig. 3a. The LIBS spectrum of a healthy nail shown in Fig. 3a was obtained by averaging the spectra of healthy nails of all volunteers studied just after extraction. It should be noted that the LIBS spectra of healthy nails of all volunteers did not have any significant differences between themselves.

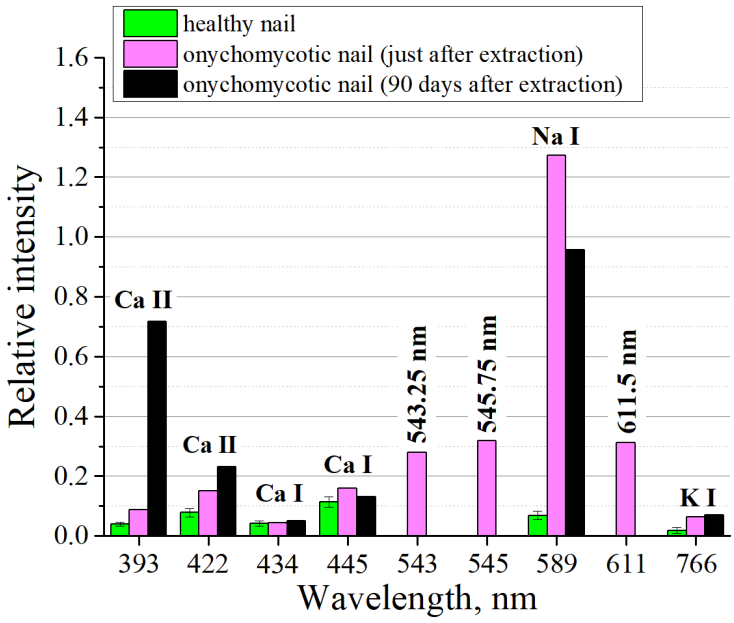
It can be seen that the LIBS spectra of human nail samples contain a continuous component of the emission of plasma electrons, as well as lines of individual chemical elements against its background. The presence of a continuous component is due to the fact that the spectrum was recorded immediately after laser irradiation. The contribution of the continuous component to the recorded spectrum may be reduced by introducing a time delay between the moment the laser exposure begins and the moment the spectrum is recorded [21]. This is relevant in the case when the continuous component of the spectrum does not allow resolving the lines of elements. In our case, the lines of the elements were well resolved against the background of the continuous spectrum.

It can be seen that the main elements in the LIBS spectra of healthy nails are Ca II (393 nm), Ca I (423 nm, 434 nm, 445 nm), Na (589 nm) and K (766 nm). The intensities of the lines of these elements in the spectra of healthy and onychomycotic nails differ from each other. We have not observed the shift of these spectral lines in transition from healthy to onychomycotic nail. In Ref. [22], the LIBS spectra of nails of people of different age and sex were studied. The results show that the line intensities of Ca, Al, Ti, P and K elements are higher among women, and Mg and Na – for men. It was found that the intensity of the lines of Ca and K decreases with increasing age for both sexes. As in our study, in Ref. [22] authors no shift of spectral lines is observed.

In addition, the unique lines at 543.25, 545.75, and 611.5 nm (see Fig. 3b) may be found in the spectrum of just extracted onychomycotic nail, while the intensity of these lines in the LIBS spectrum of just extracted healthy nails is at the level of the continuous component of the emission of plasma electrons. Taking into account the resolution of the "USB-2000" (OceanOptics, Inc., USA) fiber-optic spectrometer, these three lines can be correlated with the following elements: 543.25 ± 0.75 nm – S, Mg, Fe, Cu, Mn, I, V, **Br**, P; 545.75 ± 0.75 nm – S, Mn, Fe, Cu, N, Mg, Ca, Cl, **As**, I, V, P, and 611.5 ± 0.75 nm – S, Mn, Cu, Cl, S, Zn, Fe, Cu, N, Al, Ca, **Br, Cd, As**, V [23]. Elements missing in a healthy nail are highlighted in bold. Fungi can collect elements that are nutrients for them, as it was shown for Candida [24]. These elements include S, Cu, Zn, ammonium, Al, Ca, Mg, Fe, Br, Cd, As, I, Mn, Se, V, sulfates, phosphates, and chlorides in small amounts [25–27]. In Ref. [28], samples of healthy and onychomycotic toenails were analyzed by using an inductively coupled plasma-optical emission spectrophotometer to detect the difference in concentrations of such trace elements as Cr, Cu, Fe, Mg, Mn, Se, and Zn. The study showed that Mg, Mn, and Zn levels were significantly changed in toenails with onychomycosis compared to healthy controls, but the difference in Mg levels was the only element independent of age, sex, and smoking [28]. Thus, the unique lines found in our study in LIBS spectrum of onychomycotic nails are difficult to final identify. This



(a)



(b)

Fig. 3 Typical 1540 nm LIBS spectra of samples of a healthy nail, a nail affected by onychomycosis just after extraction and the same nail after 90 days of longer storage (a), and a histogram of the relative intensity of the spectral lines of the elements containing in these samples (b).

identification may be performed in the future using a higher-resolution spectrometer and more amount of onychomycotic nail samples.

Fig. 3b shows a histogram of the relative intensity of the spectral lines of the elements contained in the samples of a healthy nail, a just extracted nail affected by onychomycosis and the same nail after 90 days of longer storage. Relative intensity was determined by subtracting the value of normalized intensity of the continuous component of the spectrum at the wavelength of the element's line from the value of the normalized intensity of this line. There are no standard deviation bars in Fig. 3b for onychomycotic nail because only one sample of onychomycotic nail was used in the study, and based on the results of measuring the spectrum from one sample, it is impossible to conduct a standard statistical study on the effect of possible differences between samples on the measurement results. In the experiment with this one sample, we did not register statistical differences in the LIBS spectra obtained in different regions of the sample surface.

LIBS spectra obtained in different regions of the sample surface.

It is seen that for the just extracted nail affected by onychomycosis relative intensity of the Ca II (393 nm), Ca I (423 nm), Ca I (445 nm) lines are 2.2, 1.9 and 1.4 times higher than the relative intensity of these lines in LIBS spectrum of healthy nails, respectively. The intensity of the Ca I line (434 nm) in the spectrum of a healthy nail is equal to the intensity of this line in the spectrum of the onychomycotic nail just after extraction. The intensity of the Na (589 nm) and K (766 nm) lines in the spectrum of the just extracted onychomycotic nail is higher than the intensity of this line in the LIBS spectrum of a just extracted healthy nail by 18.6 times and 3.3 times, respectively. The unique lines in the spectrum of onychomycotic nail just after extraction have the same relative intensity equal to 0.31 a.u. The presence of the unique lines in the spectrum may indicate the presence of the vital products of the fungus in the sample.

After 90 days of longer storage the unique lines were not detected in the LIBS spectrum of the sample affected by onychomycosis. This may be due to the death of the fungus as a result of sample storage, since in the extracted nail plate it does not receive enough nutrients to support vital activity. The intensity of Ca I lines at wavelengths of 423 nm and 434 nm increased as a result of longer storage, but not much – by 1.54 and 1.16 times, respectively, and at a wavelength of 445 nm – decreased by 1.2 times. The intensity of K line (766 nm) remained practically unchanged. The intensity of the Na line (589 nm) decreased by 1.3 times as a result of longer storage. It is also worth noting that the Ca II line's intensity (393 nm) increased by 8 times in the spectrum of the onychomycotic sample after 90 days of longer storage, which may be due to dehydration of the nail plate.

4 Conclusion

Pilot LIBS detection of onychomycosis with excitation of plasma on the surface of nail with eye-safe radiation of compact Q-switched Yb, Er: Glass laser with a wavelength of 1540 nm was performed. The difference was found in the LIBS spectra of a healthy and onychomycosis-affected nail plate *in vitro*. Based on the data obtained, an original method and apparatus for the early rapid diagnosis of fungal diseases of the nail may be developed. During the transition to *in vivo* studies, the main limitations may be associated with the contribution of the nail surface – its relief, curvature and purity (the presence of foreign substances, including residues of solvents, drugs, cosmetics, etc.) will affect the measurement result. In addition, it will be possible to encounter the variance in measurement results when scanning the surface of the nail. All these features can influence the result of the LIBS spectrum registration. Under *in vivo* conditions, these features are difficult to control, which will most likely require additional research and improvement of the measurement technique.

Disclosures

All authors declare that there is no conflict of interests in this paper.

References

1. R. C. Wiens, S. K. Sharma, J. Thompson, A. Misra, and P. G. Lucey, "Joint analyses by laser-induced breakdown spectroscopy (LIBS) and Raman spectroscopy at stand-off distances," Spectrochimica Acta Part A: Molecular and Biomolecular Spectroscopy 61(10), 2324–2334 (2005).
2. J. Thompson, R. C. Wiens, D. A. Cremers, J. Barefield, and C. Wetteland, "The suitability of Laser Induced Breakdown Spectroscopy for determining the compositions of extraterrestrial material," Lunar and Planetary Science XXXV (2004).
3. D. Body, B. L. Chadwick, "Optimization of the spectral data processing in a LIBS simultaneous elemental analysis system," Spectrochimica Acta Part B: Atomic Spectroscopy 56(6), 725–736 (2001).
4. R. C. Wiens, S. K. Sharma, J. R. Thompson, A. K. Misra, and P. G. Lucey, "Joint analyses by laser-induced breakdown spectroscopy (LIBS) and Raman spectroscopy at stand-off distances," Spectrochimica Acta Part A: Molecular and Biomolecular Spectroscopy 61(10), 2324–2334 (2005).
5. B. E. Elewski, "Onychomycosis," American journal of clinical dermatology 1(1), 19–26 (2000).
6. P. Rodgers, M. Bassler, "Treating onychomycosis," American family physician 63(4), 663–673 (2001).
7. R. K. Scher, A. Tavakkol, B. Sigurgeirsson, D. G. Armstrong, B. C. Markinson, and B. E. Elewski, "Onychomycosis: diagnosis and definition of cure," Journal of the American Academy of Dermatology 56(6), 939–944 (2007).
8. Yu. V. Sergeev, A. Yu. Sergeev, Onychomycosis. Fungal infections of the nails, Geotar-medicine, Moscow (1998). ISBN 5–88816–040–7 [In Russian].
9. C. Carney, A. Tosti, R. C. Daniel, R. Scher, P. A. Rich, J. DeCoster, and B. E. Elewski, "A new classification system for grading the severity of onychomycosis: Onychomycosis Severity Index," Archives of dermatology 147(11), 1277–1282 (2011).

10. A. K. Gupta, K. A. Foley, and S. G. Versteeg, "Lasers for onychomycosis: current status," Journal of cutaneous medicine and surgery 21(2), 114–116 (2017).
11. W. W. Harrison, G. G. Clemena, "Survey analysis of trace elements in human fingernails by spark source mass spectrometry," Clinica Chimica Acta 36(2), 485–492 (1972).
12. M. Garland, J. S. Morris, B. A. Rosner, M. J. Stampfer, V. L. Spate, C. J. Baskett, W. C. Willett, and D. J. Hunter, "Toenail trace element levels as biomarkers: reproducibility over a 6-year period," Cancer Epidemiology and Prevention Biomarkers 2(5), 493–497 (1993).
13. D. E. Vance, W. D. Ehmann, and W. R. Markesbery, "Trace element content in fingernails and hair of a nonindustrialized US control population," Biological trace element research 17(1), 109–121 (1988).
14. M. Bahreini, B. Ashrafkhani, and S. H. Tavassoli, "Discrimination of patients with diabetes mellitus and healthy subjects based on laser-induced breakdown spectroscopy of their fingernails," Journal of biomedical optics 18(10), 107006 (2013).
15. S. Hamzaoui, R. Khleifia, N. Jaïdane, and Z. B. Lakhdar, "Quantitative analysis of pathological nails using laser-induced breakdown spectroscopy (LIBS) technique," Lasers in medical science 26(1), 79–83 (2011).
16. A. P. Flores, A. K. F. Sanchez, A. Villarreal, F. G. R. Sauz, L. P. Cabrera, and T. F. Reyes, "The potential of compact LIBS system with multi-pulse Nd:YAG laser for bacteria identification," Journal of Biomedical Science and Engineering 8(03), 207 (2015).
17. S Manzoor, L. Ugena, J. Tornero-Lopéz, H. Martín, M. Molina, J. J. Camacho, and J. O. Cáceres, "Laser induced breakdown spectroscopy for the discrimination of Candida strains," Talanta 155, 101–106 (2016).
18. M. J. Myers, J. D. Myers, B. Guo, C. Yang, C. R. Hardy, J. A. Myers, A. G. Myers, and S. M. Christian, "Non-invasive in-situ detection of malignant skin tissue and other abnormalities using portable LIBS system with fiber spectrometer and eye-safe erbium glass laser," Proceeding of SPIE 6863, 68630W (2008).
19. J. Taboada, J. M. Taboada, D. J. Stolarski, J. J. Zohner, L. J. Chavey, H. M. Hodnett, G. D. Noojin, R. J. Thomas, S. S. Kumru, and C. P. Cain, "100-megawatt power Q-switched Er-glass laser," Proceeding of SPIE 6100, 61000B (2006).
20. D. De Luca, I. Delfino, and M. Lepore, "Laser safety standards and measurements of hazard parameters for medical lasers," International Journal of Optics and Applications 2(6), 80–86 (2012).
21. M. J. Myers, J. D. Myers, J. T. Sarracino, C. R. Hardy, B. Guo, S. M. Christian, J. A. Myers, F. Roth, and A. G. Myers, "LIBS system with compact fiber spectrometer, head mounted spectra display and hand held eye-safe erbium glass laser gun," Proceeding of SPIE 7578, 75782G (2010).
22. H. A. Harun, R. Zainal, and Y. M. Daud, "Analysing human nails composition by using laser induced breakdown spectroscopy," Sains Malaysiana 46(1), 75–82 (2017).
23. NIST Atomic Spectra Database Lines Form.
24. M. Kieliszek, A. M. Kot, A. Bzducha-Wróbel, S. BŁażejak, I. Gientka, and A. Kurcz, "Biotechnological use of Candida yeasts in the food industry: a review," Fungal Biology Reviews 31(4), 185–198 (2017).
25. W. A. Mosher, D. H. Saunders, L. B. Kingery, and R. J. Williams, "Nutritional requirements of the pathogenic mold Trichophyton interdigitale," Plant Physiology 11(4), 795 (1936).
26. A. J. Pirzada, P. Iqbal, W. Shaikh, T. Kazi, and U. Ghani, "Studies on the elemental composition and anti fungal activity of medicinal plant Lippia nodiflora L against skin mycosis," Journal of Pakistan Association of Dermatology 15(2), 113–118 (2016).
27. G. A. Marzluf, "Regulation of sulfur and nitrogen metabolism in filamentous fungi," Annual review of microbiology 47(1), 31–55 (1993).
28. E. Kilinc, B. Buturak, and F. A. Alkan, "Level of Trace Elements in Serum and Toenail Samples of Patients with Onychocryptosis (ingrown toenail) and Onychomycosis," Journal of Trace Elements in Medicine and Biology 61, 126509 (2020).

Temperature Dependencies of the Aggregation Properties of RBC in Dextran Solutions *In Vitro*

Petr B. Ermolinkiy[1*], Anastasia I. Maslyanitsina[1], Andrei E. Lugovtsov[1,2], and Alexander V. Priezzhev[1,2]

[1] Department of Physics, M.V. Lomonosov Moscow State University, 1 Leninskie Gory, Moscow 119991, Russia
[2] International Laser Center, M.V. Lomonosov Moscow State University, 1 Leninskie Gory, Moscow 119991, Russia

***e-mail:** peter.ermolinskiy@biomedphotonics.ru

Abstract. The process of reversible spontaneous aggregation of red blood cells (RBC), as well as the process of their shear stress induced disaggregation, both affect hemorheology and blood microcirculation in the human body. The aim of this work is to estimate the influence of temperature on the aggregation properties of RBC suspended in PBS dextran solutions *in vitro*. Laser method based on diffuse light scattering was used to estimate the RBC aggregation properties. The results demonstrate a clear dependence of the critical shear stress aggregation parameter of RBC in PBS dextran solutions on temperature. These results would help to better understand the process of RBC aggregation. © 2020 Journal of Biomedical Photonics & Engineering.

Keywords: RBC aggregation; temperature; erythrocytes; diffuse light scattering; dextran; critical shear stress.

Paper #3372 received 23 May 2020; revised manuscript received 17 Jun 2020; accepted for publication 18 Jun 2020; published online 25 Jun 2020. doi: 10.18287/JBPE20.06.020501.

1 Introduction

Processes of red blood cells (RBC) aggregation and disaggregation strongly influence the viscosity of blood in vessels and have a general impact human health [1, 2]. Aggregation properties of blood may be changed due many factors: alteration of blood plasma composition, change in blood temperature, injection of different synthetic macromolecules, RBC aging, pathological alterations, and others [2, 3]. The mechanisms of RBC aggregation, as well as the influence of these factors on it, are not fully understood so far. At the present, there exist two main hypotheses explaining the RBC aggregation process: the "Bridging" model and the "Depletion" model [2, 4, 5]. There is still no evidence that would fully confirm or completely refute any one of these models. There exist some suggestions that the RBC aggregation process can be described as a combination of both models [6]. The development of the RBC aggregation models is vital for clearer predicting the changes of the microrheologic properties of blood due to the alterations of concentration of plasma proteins, temperature, etc. The aggregation properties of blood change due to many socially significant diseases [2]. That is why the new knowledge about RBC aggregation process can be used for the development of future clinical applications.

Dextrans are synthetic macromolecules with molecular weights from 3 to 2000 kDa [7]. Dextran solutions are widely used both in clinical practice to adjust viscosity of blood, in the synthesis of drug-delivering nanoparticles [8], and in experimental studies of RBC aggregation [2, 9]. Thermodynamic parameters of polymer solutions (including dextran solutions) are strongly dependent on temperature [10]. Therefore, the temperature should inevitably influence the aggregation properties of RBC in these solutions. If we consider *in vivo* conditions, the temperature of the patient's body can alter due to pathologies, and dextran injections can lead to slightly different effects under different temperatures accordingly. The influence of temperature on the processes of RBC aggregation and disaggregation in different solutions, e.g. in dextran solutions, has not been studied in detail so far. However, it is known that *in vitro* aggregation properties of RBC in autologous plasma are dependent on the temperature [3, 11].

The aim of this work is to estimate the influence of temperature on the RBC aggregation properties in

solutions of dextran of different molecular weights and concentrations *in vitro*.

2 Materials and Methods

The laser aggregometry technique was used to estimate the aggregation properties of RBC in dextran solutions at different temperatures [12, 13]. It is based on measuring the intensity of diffuse light scattering from a blood sample and is implemented in the slit-flow type system RheoScan (Rheomeditech, Seoul, Korea) [14]. In more detail, this technique and measured parameters are described in Refs. [3, 13, 15]. Briefly, RheoScan allows to measure kinetics of scattered light and to relate them to the RBC aggregation and disaggregation parameters. One of these parameters is critical shear stress (CSS) that characterizes the shear stress required to balance the process of aggregates formation and aggregates destruction, and therefore CSS is related to the hydrodynamic strength of the RBC aggregates. In this work, only the CSS parameter was measured.

Blood from one healthy individual was drawn using venipuncture technique and was stabilized by EDTA anticoagulant. RBCs were separated from the plasma using standard protocols, then they were suspended and washed in PBS 3 times at 600g for 3 min. Washed RBC were suspended in dextran solutions (PBS + dextran) at hct = 0.4. In this work, dextran macromolecules with different molecular weights (70, 150, 500 kDa) were used and suspended in PBS at various concentrations (10 mg/ml to 100 mg/ml). Prepared samples were incubated for 40 min at room temperature (22 ℃). After that, the blood samples were placed for 5 min into the RheoScan measurement chamber that was preheated up to 30, 37, or 40 ℃ and then measurements were conducted. The temperature of the RheoScan measurement chamber was maintained. Each sample corresponds to one temperature. All experiments were carried out during 5 h after blood drawing. This time period on its own is not sufficient to cause any significant CSS changes.

3 Results and Discussion

Fig. 1 shows the CSS values measured for 3 different temperatures (30, 37, 40 ℃) and for the dextrans of 3 different molecular weights (70, 150 and 500 kDa) and 4 concentrations (10, 30, 60 and 100 mg/ml). The bell shaped dependencies of CSS on dextran concentration are observed in all cases. The graphs shift horizontally at different temperatures. In particular, for dextran 150 kDa (Fig. 1b) the increase in temperature corresponds to shifting to the left, so that the maximum CSS is reached at lower concentration. In the case of dextran 70 kDa and dextran 500 kDa (Fig. 1a and Fig. 1c), the trends are different. The maximum CSS values for 37 and 40 ℃ are almost the same and differ from the one at 30 ℃. Thus, the molecular weights influence the way how CSS changes under different temperatures. These results mean that there is a nonlinear dependence of CSS parameter on dextran molecular weight, its concentration and the temperatures of the sample. Also, it means that there may be complex influence of combination of these 3 factors (dextran molecular weight, dextran concentration, and temperature) on the RBC aggregation properties.

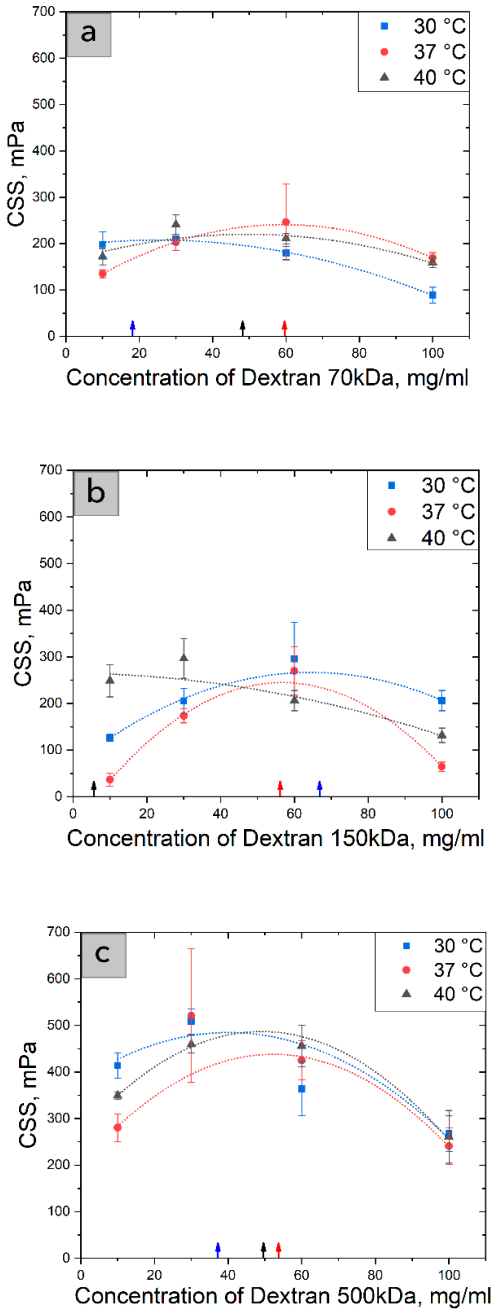


Fig. 1 CSS at different temperatures and concentrations of dextran (a) 70, (b) 150 and (c) 500 kDa. Bars represent standard deviations. Each point is an average of at least 5 measurements. Dotted lines are parabolic approximations of experimental data. Colored arrows on horizontal scale correspond to the maximum CSS values.

Dextran 70 kDa is widely used in clinical practice, namely 6–7.5% dextran 70 kDa solutions are commonly used for injections to control blood viscosity [16]. Therefore, a more accurate observation of CSS changes was made for dextran 70 kDa. Results in Fig. 2 show CSS as a function of temperature for 50 mg/ml concentration of dextran 70 kDa. Interestingly, the minimum CSS values are observed at 30 ℃. This also indicates that there is a complex dependence of CSS on temperature.

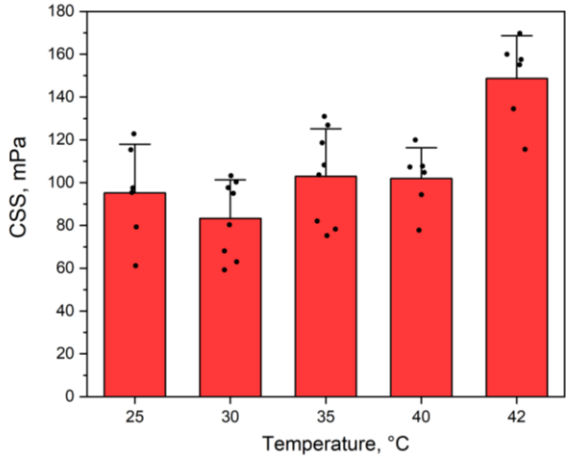


Fig. 2 CSS at different temperatures of dextran 70 kDa solution at concentration of 50 mg/ml. Bars represent standard deviations. Each point corresponds to the one measurement.

In future, it is planned to relate the obtained results with one of the aggregation models. The temperature dependencies of these models are not presented explicitly and need to be developed. The thermodynamic parameters of dextrans depend on temperature, therefore the temperature influences the adsorption of dextran macromolecules on RBC membrane in the case of the "Bridging" model. Also, temperature influences the osmotic pressure in the case of the "Depletion" model. That is why these kinds of results could verify one of the RBC aggregation models in the future.

4 Conclusion

In this work, the aggregation of RBC was studied by assessing the critical shear stress (CSS) that characterizes the hydrodynamic strength of the aggregates. The results show a dependence of CSS in dextran solutions on the temperature changes *in vitro*. In particular, the bell shape dependence of CSS on dextran concentration changes under different temperatures and different molecular weights of dextrans. For example, the concentration of dextran 150 kDa that corresponds to the maximum CSS value is lower for 40 ℃ than for 30 ℃. These observations mean that there is a non-linear effect of dextran concentration, dextran molecular weights and temperature on RBC aggregation properties. In future, the fundamental knowledge about RBC aggregation can be used in the development of new methods of patient treatment in order to control the viscosity of blood and rheological parameters.

Disclosures

All authors declare that there is no conflict of interests in this paper.

Acknowledgments

This work was supported by the Russian Foundation for Basic Research grant #19-52-51015.

References

1. A. N. Yaroslavsky, I. V. Yaroslavsky, "Optics of blood," Chapter 2 in Handbook of Optical Biomedical Diagnostics, V. V. Tuchin (ed.), Volume 1: Light-Tissue Interaction, Second edition, SPIE PRESS, Bellingham, Washington, USA, 161–220 (2016).
2. O. Baskurt, B. Neu, and H. J. Meiselman, Red Blood Cell Aggregation, CRC Press, Boca Raton, USA (2012).
3. P. B. Ermolinkiy, A. N. Semenov, A. E. Lugovtsov, C. Poeschl, U. Windberger, E. Kaliviotis, and A. V. Priezzhev, "Effect of different macromolecules on viscous and microrheologic properties of blood at various temperatures," Proceeding of SPIE 11065, 1106507 (2019).
4. D. E. Brooks, "Mechanism of red cell aggregation," Chapter in Blood Cells, Rheology and Aging, D. Platt (Ed.), Springer, Berlin, Heidelberg, 158–162 (1988).
5. Z. W. Zhang, B. Neu, "Role of macromolecular depletion in red blood cell adhesion," Biophysical Journal 97(4), 1031–1037 (2009).
6. R. Fantoni, A. Giacometti, and A. Santos, "Bridging and depletion mechanisms in colloid-colloid effective interaction: A reentrant phase diagram," The Journal of Chemical Physics 142(22), 224905 (2015).
7. T. Heinze, T. Liebert, B. Heublein, and S. Hornig, "Functional polymers based on dextran," Chapter in Polysaccharides II, D. Klemm (Ed.), Springer-Verlag Berlin Heidelberg, New York, 199–293 (2006).
8. I. Wasiak, A. Kulikowska, M. Janczewska, M. Michalak, I. A. Cymerman, A. Nagalski, P. Kallinger, W. W. Szymanski, and T. Ciach "Dextran nanoparticle synthesis and properties," PLoS ONE 11(1), e0146237 (2016).

9. N. Antonova, P. Riha, and I. Ivanov, "Experimental evaluation of mechanical and electrical properties of RBC suspensions under flow. Role of RBC aggregating agent," Clinical Hemorheology and Microcirculation 45(2–4), 253–261 (2010).
10. A. Gunner, G. Kibarer, "The important role of thermodynamic interaction parameter in the determination of theta temperature, dextran/water system," European Polymer Journal 37(3), 619–622 (2001).
11. M. Singh, J. F. Stoltz, "Influence of temperature variation from 5°C to 37°C an aggregation and deformability of erythrocytes," Clinical hemorheology and microcirculation 26(1), 1–7 (2002).
12. A. V. Priezzhev, K. Lee, N. N. Firsov, and J. Lademann, "Optical study of RBC aggregation in whole blood samples and single cells," Chapter in Handbook of Optical Biomedical Diagnostics, V. V. Tuchin (Ed.), Volume 2: Methods, Second edition, SPIE PRESS, Bellingham, Washington, USA, 5–36 (2016).
13. S. Shin, J. H. Nam, J. X. Hou, and J. S. Suh, "A transient, microfluidic approach to the investigation of erythrocyte aggregation: The threshold shear-stress for erythrocyte disaggregation," Clinical Hemorheology and Microcirculation 42(2), 117–125 (2009).
14. V. N. Lopatin, A. V. Priezzhev, and A. D. Aponasenko, Methods light scattering in the analysis of dispersed biological media, Fizmatlit, Moscow, Russia (2004) [in Russian]. ISBN 5-9221-0547-7.
15. A. N. Semenov, A. E. Lugovtsov, K. Li, A. A. Fabrichnova, Y. A. Kovaleva, and A. V. Priezzhev, "Applying methods of diffuse light scattering and optical trapping for assessing blood rheological parameters: erythrocytes aggregation in diabetes mellitus," Izvestiya of Saratov University. New series. Series Physics 17(2), 85–97 (2017) [in Russian].
16. A. Gray, J. Wright, V. Goodey, and L. Bruce, Injectable drugs guide, Pharmaceutical Press. Royal pharmaceutical society, London, UK (2011).